06

annual progress

HEAVY VEHICLE SYSTEMS OPTIMIZATION PROGRAM

FreedomCAR and Vehicle Technologies Program

Less dependence on foreign oil today, and transition to a petroleum-free, emissions-free vehicle tomorrow.

U.S. Department of Energy
Energy Efficiency and Renewable Energy
Bringing you a prosperous future where energy is clean, abundant, reliable, and affordable

FreedomCAR & Fuel Partnership

21st CENTURY TRUCK PARTNERSHIP

U.S. Department of Energy
FreedomCAR and Vehicle Technologies Program
1000 Independence Avenue, S.W.
Washington, DC 20585-0121

FY 2006

Annual Progress Report for Heavy Vehicle Systems Optimization Program

Submitted to:
U.S. Department of Energy
Energy Efficiency and Renewable Energy
FreedomCAR and Vehicle Technologies Program
Advanced Vehicle Technology Analysis and Evaluation

Lee Slezak, Technology Manager

CONTENTS

CONTENTS (CONT.)

I. AERODYNAMIC DRAG REDUCTION

I.A. DOE Project on Heavy Vehicle Aerodynamic Drag

Project Principal Investigator: R. C. McCallen
Lawrence Livermore National Laboratory
P.O. Box 808, Livermore, CA 94551-0808
(925) 423-0958, e-mail: mccallen1@llnl.gov

Principal Investigator: K. Salari
Co-Investigators: J. Ortega, P. Castellucci
Lawrence Livermore National Laboratory
P.O. Box 808, Livermore, CA 94551-0808
(925) 424-4635, e-mail: salari1@llnl.gov

Principal Investigator: W. D. Pointer
Co-Investigators: J. Chang, S. Singh, E. Dringenberg
Argonne National Laboratory
9700 S. Cass Avenue, NE-208, Argonne, IL 60439
(630) 252-1052, e-mail: dpointer@anl.gov

Principal Investigator: F. Browand
Co-Investigators: C. Radovich, T. Merzel, D. Plocher
Aerospace & Mechanical Engineering, University of Southern California
RRB 203, Los Angeles CA 90089-1191
(213) 740-5359, e-mail: browand@spock.usc.edu

Principal Investigator: J. Ross
Co-Investigators: B. Storms
NASA Ames Research Center
MS 260-1, Moffett Field, CA 94035
(650) 604-6722, e-mail: jcross@mail.arc.nasa.gov

Technology Development Manager: Lee Slezak
(202) 586-2335, e-mail: Lee.Slezak@EE.DOE.GOV

Technical Program Manager: Jules Routbort
(630) 252-5065, e-mail: routbort@anl.gov

Contractor: Lawrence Livermore National Laboratory, Argonne National Laboratory,
NASA Ames Research Center
Contract No.: W-7405-ENG-48, W-31-109-ENG-38, DE-AI01-99EE50559

Objective

Class 8 tractor-trailers consume 11-12% of the total US petroleum use.[1] At high way speeds, 65% of the energy expenditure for a Class 8 truck is in overcoming aerodynamic drag. The project objective is to improve fuel economy of Class 8 tractor-trailers by providing guidance on methods of reducing drag by at least 25%. A 25% reduction in drag would present a 12% improvement in fuel economy at highway speeds, equivalent to about 130 midsize tanker ships per year. Specific goals include:

- Provide guidance to industry in the reduction of aerodynamic drag of heavy truck vehicles.
- Develop innovative drag reducing concepts that are operationally and economically sound.
- Establish a database of experimental, computational, and conceptual design information, and demonstrate the potential of new drag-reduction devices.

Approach

- Develop and demonstrate the ability to simulate and analyze aerodynamic flow around heavy truck vehicles using existing and advanced computational fluid dynamics (CFD) tools.
- Through an extensive experimental effort, generate an experimental data base for code validation and for understanding of key drag producing flow characteristics
- Provide industry with design guidance and insight into flow phenomena from experiments and computations.
- Investigate aero devices (e.g., base flaps, tractor-trailer gap stabilizer, underbody skirts and wedges, blowing and acoustic devices), provide industry with conceptual designs of drag reducing devices, and demonstrate the full-scale fuel economy potential of these devices.

Accomplishments

- Organized and lead a very successful annual DOE Heavy Vehicle Working Group Meeting with active industry participation. The objective of these annual meetings is to provide a forum for reviewing industry needs, presenting new drag reduction concepts, discussing project direction, and identifying areas of collaboration between industry and DOE supported R&D participants from National Labs, universities and other research organizations. Participants comprised major industrial representatives: Freightliner, PACCAR, Kenworth, International, Cummins, Michelin, Eaton, along with small company representation: Laydon, Aerovolution, Aero Industries, Mach Zero Associates.Highlights of the meeting were
  - Interest in new flow conditioning concept of a “bleeding flow” device for trailer base and tractor base.
  - Identified need for experimental and computational methods for evaluation of design options, e.g., optimization methods and tools
  - Importance of vehicle integration for achieving goal to double vehicle efficiency, e.g., geometry/shaping, power source/drive-train, tire/road
- New flow conditioning concept of “bleeding-flow” device has been shown computationally to provide significant gap flow and trailer base drag reduction. Plans are to perform reduced-scale tests at NASA and full-scale tests at NRC
- Providing a consistent, realistic, comprehensive assessment of the energy balance when evaluating devices like with the “bleeding flow” device is needed. Consider and report:
  - energy used by active features
  - weight of all components
  - Impact of design on fleet operation in terms of dollars saved per ton hauled in addition to changes in drag coefficient or fuel use rate.
  - Yaw-averaged drag values when evaluating design changes.

---

[1] U.S. DOE, Transportation Energy Data Book, 24th Edition, http://cta.ornl.gov/data/new_for_edition24.sht ,
U.S. DOT, FHA, Highway Statistics, 2002

Representatives from (left to right) Freightliner, PACCAR, Kenworth, International, and Cummins take advantage of opportunity during meeting to form a breakout group to discuss common interests

Participants from (left to right) Michelin USA, Mach Zero Associates, Michelin International Office, Freightliner, International, NASA, and Eaton during formal presentations by government, industry, and DOE Aero Team

- Tractor and trailer underbody experiments at NASA show small improvement in tractor drag with the use of tractor belly pans or with the covering of cross ribs under the trailer. Experiments also showed that trailer side skirts are still the most promising drag reduction approach.

- Evaluation of the impact of small changes in radiator or grille dimensions has revealed that the total drag is not particularly sensitive to those changes.

- A preliminary computation of the effect of wet roads on rolling resistance indicates a significant impact on fuel economy.
- Spray experiments at USC in collaboration with Michelin have demonstrated the effect of tire treatments as a possible spray mitigation options.

Future Direction

- Getting devices on road
  - From understanding of key flow mechanisms, develop less obtrusive and optimized device concepts
  - Demonstration wind tunnel, track, and road tests by leveraging work with National Research Council of Canada, TMA/DOE, and seek collaborative demonstrations with fleet owners and operators
- Economic/duty cycle evaluation with PSAT (ANL's system model)
  - Provide mechanistic data: strong variation in drag per yaw, speed, geometry/devices, environment, etc
- Develop and transfer technology and information to industry
  - Perform full-scale wind tunnel experiments of bleeding flow device in collaboration with tractor manufacturer
  - Contouring the tractor hood reduces the grille area, also reducing coolant flow. In addition, underhood exhaust gas recirculation to meet EPA 2007 regulation requires more underhood cooling. With industry encouragement, we are including underhood flow in aerodynamic drag computations to provide insight into the coupled flow phenomena.
  - Identified need for experimental and computational methods for evaluation of design options for improved efficiency, e.g., optimization methods and tools.
  - Experiments at USC in collaboration with Michelin will provide some guidance on methods to minimize wet road effect on rolling resistance.
- Leverage Program work and seek funding from other agencies.

Introduction

The following reports on the findings and accomplishments for fiscal year 2005 in the project's three focus areas

- Drag reduction devices
- Experimental testing
- Computational modeling

Detailed reports from each participating organization are provided in the appendices. Included are experimental results by NASA and USC, and complimentary computations by LLNL, ANL in Appendices A through D.

Drag Reduction Devices and Future Plans

There are three areas identified for aero drag reduction and several drag reduction devices have been investigated

- **Tractor-Trailer Gap**
  Stabilizing devices, cab extenders
- **Wheels/Underbody**
  Skirts/wedge and lowboy trailer
- **Trailer Base**
  Boattail plates, base flaps, rounded edges, and pneumatics

Over 12% increase in fuel economy is possible, e.g.,

> 4% trailer base-flaps
> 6% trailer skirts
> <u>2%</u> gap splitter plate
> 12% Total

Unfortunately, these devices have operational and maintenance issues. With our understanding of the key flow mechanisms, we are developing less obtrusive and optimized innovative design concepts using computational fluid dynamics and experiments. In addition, to getting devices on the road, consequences with aerodynamic improvements need to be addressed.

Addressing these consequences of aerodynamic improvements is an important task in getting devices on the road. Our efforts in the development of device concepts and device optimization will accomplish this. These issues are also of interest to other government agencies (e.g., DOT and EPA) and industry (i.e., Michelin is providing partial support for experiments at USC). The rolling resistance and splash and spray effort will continue to receive complimentary support from industry and we will actively seek joint government funding.

Acknowledgments

This work was performed under the auspices of the U.S. Department of Energy by University of California, Lawrence Livermore National Laboratory under Contract W-7405-Eng-48. This work has been completed under the auspices of the U.S. Department of Energy by the University of Chicago as Operator of Argonne National Laboratory (“Argonne”) under Contract No. W-31-109-ENG-38.

I.B. Heavy Vehicle Flow Conditioning: Application to the Tractor/Trailer Gap and Trailer Base

Kambiz Salari, Jason Ortega, Paul Castelucci
Lawrence Livermore National Laboratory
7000 East Ave, L-098, Livermore, CA 94551
(925) 423-0958, fax: 925-422-3389, e-mail: mccallen1@llnl.gov

Technology Development Manager: Lee Slezak
(202) 586-2335, e-mail: Lee.Slezak@EE.DOE.GOV

Technical Program Manager: Jules Routbort
(630) 252-5065, e-mail: routbort@anl.gov

Contractor: Lawrence Livermore National Laboratory
Contract No.: W-7405-ENG-48

Objective

The goal of this study is to reduce the aerodynamic drag of a heavy vehicle by bleeding low speed air into the tractor/trailer gap and into the trailer wake.

Approach

To alleviate the aerodynamic drag that arises from the flow separating off the trailer base and from cross-flow in the tractor/trailer gap, a low speed bleeding flow is introduced into the trailer wake and into the tractor/trailer gap, respectively. The idea to pursue this method of drag reduction came out of discussions with the fleets regarding their needs and operational concerns about the present drag reduction devices and methodologies. Numerical simulations are performed on two representative heavy vehicle geometries. The aerodynamic drag coefficients are computed for various bleeding speeds and bleeding areas. Wind tunnel experiments will be conducted to validate the computational results. In preparation for these experiments, a reduced-scale heavy vehicle wind tunnel model is fabricated with a rapid-prototyping technique.

Accomplishments

I. Bleeding flow into the tractor/trailer gap and into the trailer wake is shown to reduce the aerodynamic drag

The computational fluid dynamics (CFD) simulations demonstrate that bleeding air from the trailer base reduces the aerodynamic drag coefficient of a heavy vehicle by as much as 0.03-0.05. When the bleeding flow is applied to the tractor/trailer gap, the reduction in the drag coefficient ranges from 0.06-0.35, depending on the heavy vehicle geometry and the vehicle yaw angle.

II. Wind Tunnel Experiments to Validate the Bleeding Flow Results

To confirm the effectiveness of bleeding flow into the trailer wake or into the tractor/trailer gap, wind tunnel experiments will be performed on a reduced-scale heavy vehicle model at NASA Ames in FY07. Given our collaboration with Freightliner and our upcoming full-scale tests in the Freightliner wind tunnel in FY07, we selected a Freightliner Columbia tractor for testing in the NASA Ames wind tunnel. The Columbia model is fabricated using a selective laser sintering (SLS) rapid-prototyping technique, which will allow a performance comparison of tractor/trailer gap bleeding, traditional side extenders, a complete gap sealer, traditional base flaps, and trailer base bleeding. Through these wind tunnel experiments, we will gain a deeper understanding into the physics behind tractor/trailer and tractor base bleeding.

Near Term Directions

- Pursue a deeper understanding into the drag reduction performance of base bleeding
- Approach industry, fleets, and third party manufacturers for performing road tests with the base bleeding concept
- Conduct wind tunnel measurements on a reduced-scale heavy vehicle model at NASA Ames
- Perform CFD simulations to model the base bleeding flow physics
- Collaborate with Freightliner and the National Research Council (NRC) of Canada to make full-scale aerodynamic drag measurements of a heavy vehicle with a bleeding flow

Far Term Directions

- Collaborate with industry and the fleets to devise additional drag reduction concepts that can integrate heavy vehicles and lead to a reduction in fuel usage
- Understand underbody flow and thermal management

Motivation and Background

In November 2005, LLNL members of the Heavy Vehicle Aerodynamic Drag project spoke with Mr. Marty Fletcher of US Xpress at the 2005 SAE Commercial Vehicle Engineering conference regarding industry's perspective of heavy vehicle drag reduction devices. During the conversation that ensued, Mr. Fletcher expressed his concerns about the current and proposed devices for drag reduction. In particular, Mr. Fletcher explained the maintenance issues he had been experiencing with tractor side extenders and similar concerns he had regarding the proposed trailer base flaps. One of his suggestions was to investigate the feasibility of using air injection to condition the flow in the tractor/trailer gap and in the trailer wake, thus mitigating these sources of aerodynamic drag. The potential advantage this technique is that it would eliminate the large, easily damaged structural surfaces present in the side extenders and base flaps designs. Based upon this recommendation, we initiated a study to determine if air injection could be utilized as a means for reducing heavy vehicle aerodynamic drag.

A review of the literature demonstrated that there have been two main approaches in using air injection to reduce the aerodynamic drag of a bluff body, such as a heavy vehicle. The first is to fabricate peripheral slots around the base of the bluff body and to inject air through these slots (Freund & Mungal, 1994). Straight or curved plates are positioned adjacent to these slots so that the high-speed jets turn the separating shear layers into the wake and, thereby, increase the trailer base pressure. Employing this method on a full-scale heavy vehicle, Engler (2004) showed that it is possible to reduce the fuel usage by as much as 4% (not considering the fuel consumption to run a required blower or compressor). The second approach is to bleed air over a large portion of the bluff body base. Wood (1964, 1967) and Bearman (1967) showed that sufficient base bleed can increase base pressure and reduce the base drag. Furthermore, Yao & Sandham (2002) found that bleeding air over a large area at a low velocity is much more effective in reducing the drag than bleeding over a small area at a high velocity. Since large area bleeding had not been applied to heavy vehicles, the LLNL members decided upon applying the latter approach to the tractor and trailer bases as a means of reducing heavy vehicle drag.

Computational Simulations

To evaluate the effectiveness of base bleeding, computational fluid dynamics simulations are performed on two full-scale heavy vehicle geometries (Figure 1). The first geometry (Figure 1a), labeled MGTS, is a representation of a cab-over-engine tractor, while the second (Figure 1b), labeled GCM, is a representation of a conventional tractor. Due to the simplified nature of the MGTS and GCM, their gap geometries differ slightly from that of a full-scale heavy vehicle. For example, the

MGTS has a thin plate that covers a portion of the gap bottom, while the GCM has a completely closed gap bottom.

Trailer base bleeding is tested on the GCM by specifying an area over the trailer base (Figure 2) that injects air into the downstream direction. Several bleeding flowrates are defined for each bleeding area. Additionally, the GCM is positioned at 0 degrees relative to the freestream velocity, U_{inf}, for the trailer base bleeding simulations. Tractor base bleeding is tested on both the MGTS and the GCM by injecting air over the entire tractor base (Figure 3). For the GCM, the vehicle is yawed at 7 degrees relative to the freestream velocity to simulate the vehicle traveling within a crosswind. For the MGTS, yaw angles of 0 and 7 degrees are investigated. Additionally, a performance comparison is made on the MGTS with traditional tractor side extenders, which have been shown in previous experiments and simulations to be effective in reducing the drag when the vehicle operates within a crosswind. A commercial CFD code (STARCD, www.cd-adapco.com) is used to solve for the velocity, pressure, and turbulent quantities about the two heavy vehicle geometries.

The simulations demonstrate that both trailer and tractor base bleeding are effective in reducing the heavy vehicle drag coefficient, C_d. Figure 4 shows the drag coefficient as function of the bleeding area and bleeding flow rate for trailer base bleeding on the GCM. It is evident that a greater reduction in drag is achieved at the higher bleeding flowrates. Figure 5 shows that the two largest bleeding areas alter the structure of the separated wake by displacing it in the downstream direction. A similar phenomenon has been observed by Wood (1967), Bearman (1967), Yao & D. Sandham (2002), and Sevilla & Martinez-Bazan (2004).

Figures 6 and 7 show the drag coefficients for the tractor base bleeding configurations. On the MGTS, it is evident that tractor base bleeding is more effective at reducing the drag at both yaw angles than the traditional side extenders. Since bleeding flow is computationally introduced on the trailer or tractor base by means of a simple boundary condition, it is not possible to get a proper estimate of the actual power requirements needed to produce the bleeding flow. However, our future full-scale wind tunnel experiments at NASA Ames and Freightliner will help provide us with this information.

Figure 8 highlights the physical mechanism by which tractor base bleeding functions. It can be seen that without tractor base bleeding there is a significant cross flow from the freestream into the gap between the tractor and trailer. As the cross flow exits on the leeward side of the vehicle, it does not remain attached to the trailer, but separates massively. When tractor base bleeding is introduced, very little freestream flow enters the gap and the massive separation bubble is dramatically reduced. Analysis of the pressure over the tractor base and trailer front demonstrates that tractor base bleeding reduces the drag primarily by increasing the pressure over the tractor base (Figure 9).

Since simulating the separated wake of the trailer and tractor/trailer gap poses a challenge for Reynolds averaged Navier-Stokes (RANS) turbulence models, LLNL is currently developing a hybrid turbulence model that utilizes a RANS model near the vehicle surface and a large eddy simulation (LES) model farther away from the surface. When complete, this advanced turbulence model will allow for a more accurate performance evaluation of devices, such as trailer base flaps and side extenders, that are typically located near massively separated flow regions.

Wind Tunnel Experiments to Validate the Bleeding Flow Results

While the CFD results show promise for the tractor and trailer base bleeding concepts, it is necessary to confirm these findings with experimental measurements. To achieve this, we will conduct a wind tunnel study at NASA Ames during FY07. Measurements will be made on a scale representation of a Freightliner tractor that employs both tractor and trailer base bleeding. To ensure that the tractor properly characterizes the full-scale vehicle, we corresponded with Mr. Matt Markstaller at Freightliner. The CAD model was then fabricated with a SLS method that captures the fine-scale details of an actual Columbia tractor (Figure 10). The trailer component of the model will be designed and fabricated at NASA Ames, who is providing its

3' x 4' low-speed wind tunnel for aerodynamic testing in FY07.

References

1. Bearman, P.W. 1967 The effect of base bleed on the flow behind a two-dimensional model with a blunt trailing edge, *Aero. Quart.*, **18**, 207-224.

2. Englar, R.J. 2004 Pneumatic heavy vehicle aerodynamic drag reduction, safety enhancement, and performance improvement, *The Aerodynamics of Heavy Vehicles: Trucks, Buses, and Trains, Lecture Notes in Applied and Computational Mechanics*, **19**, 277-302.

3. Freund, J.B. & Mungal, M.G. 1994 Drag and wake modification of axisymmetric bluff bodies using Coanda blowing, *J. Aircraft*, **31**(3), 572-78.

4. Sevilla, A. & Martinez-Bazan, C. 2004 Vortex shedding in high Reynolds number axisymmetric bluff-body wakes: local linear instability and global bleed control, *Phys. Fluids*, **16**(9), 3460-3469.

5. Wood, C.J. 1964 The effect of base bleed on a periodic wake, *J. Roy. Aero. Soc.*, **68**, 477-482.

6. Wood, C.J. 1967 Visualization of an incompressible wake with base bleed, *JFM*, **29**(2), 259-272.

7. Yao, Y.F. & Sandham, N.D. 2002 Direct numerical simulation of turbulent trailing-edge flow with base flow control, *AIAA J.*, **40**(9), 1708-1716.

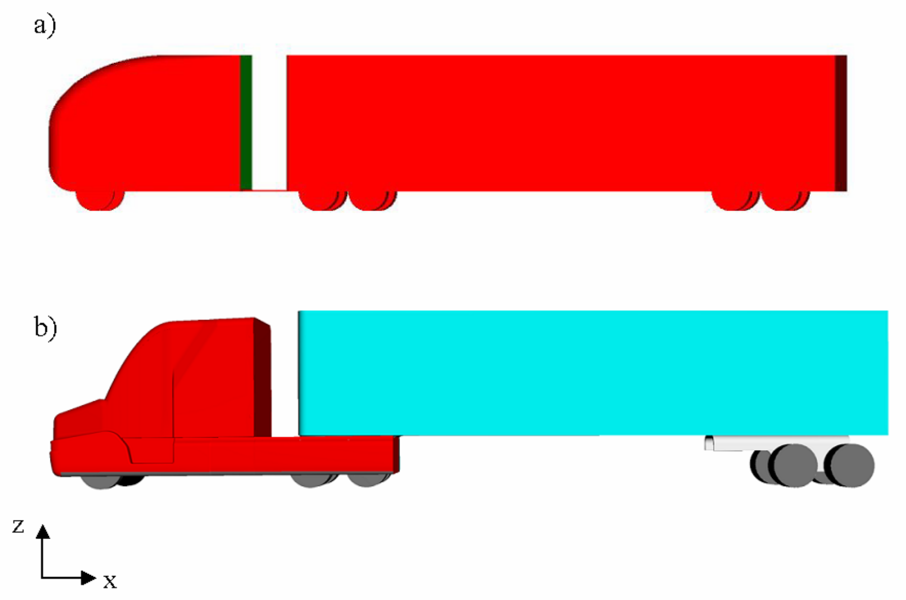

Figure 1. a) MGTS and b) GCM heavy vehicle geometries used for testing the tractor and trailer base bleeding concept

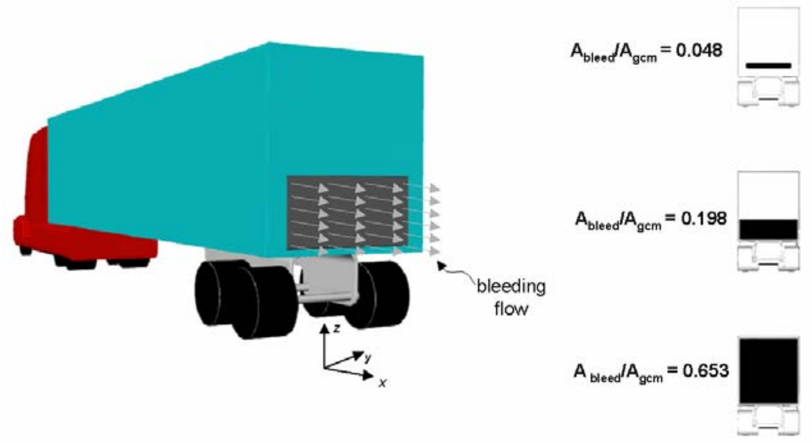

Figure 2. Trailer base bleeding areas on the GCM. A_{bleed} denotes the bleeding area and A_{GCM} the cross-sectional area of the GCM vehicle

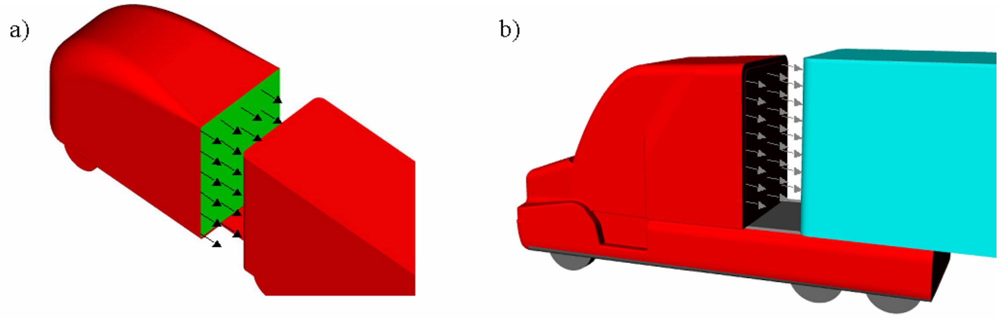

Figure 3. Location of tractor base bleeding for the a) MGTS and b) GCM

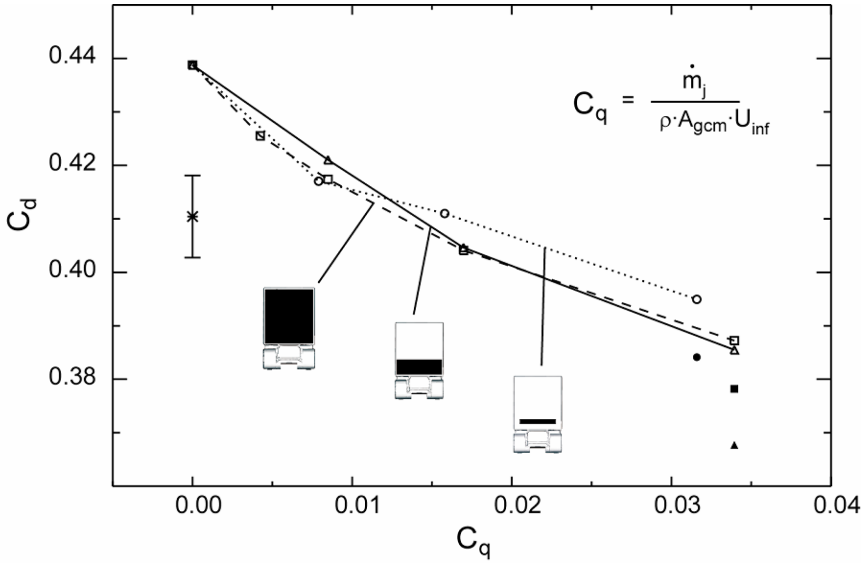

Figure 4. Drag coefficient as a function of bleeding area and bleeding coefficient, C_q, for trailer base bleeding on the GCM, where m_j is the bleeding mass flowrate and ρ the density of air

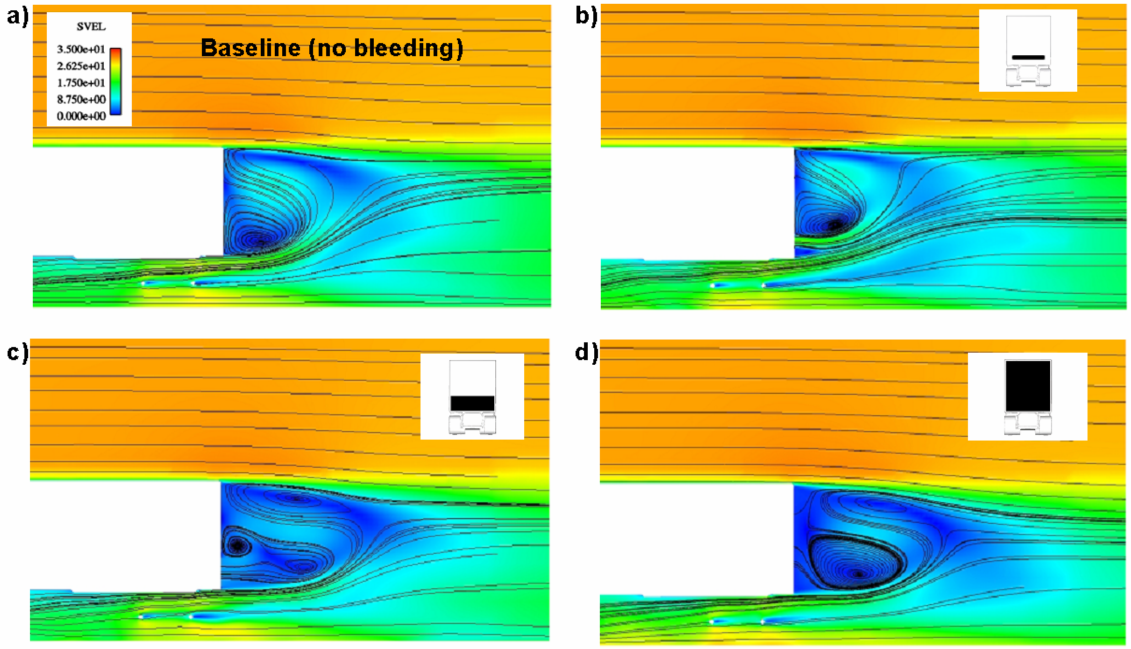

Figure 5. Mid-plane velocity magnitude (color contours) and velocity streamlines in the wake of GCM a) without and b-d) with trailer base bleeding ($C_q \approx 0.03$)

Yaw angle	0° yaw		7° yaw	
	C_D	ΔC_D	C_D	ΔC_D
Baseline	**0.401**		**0.496**	
Cab extenders	**0.393**	**-0.008**	**0.457**	**-0.039**
Flow conditioning	**0.344**	**-0.057**	**0.400**	**-0.096**

Figure 6. Drag coefficients for tractor base bleeding ($C_q = 0.05$) on the MGTS at 0 and 7 degrees yaw

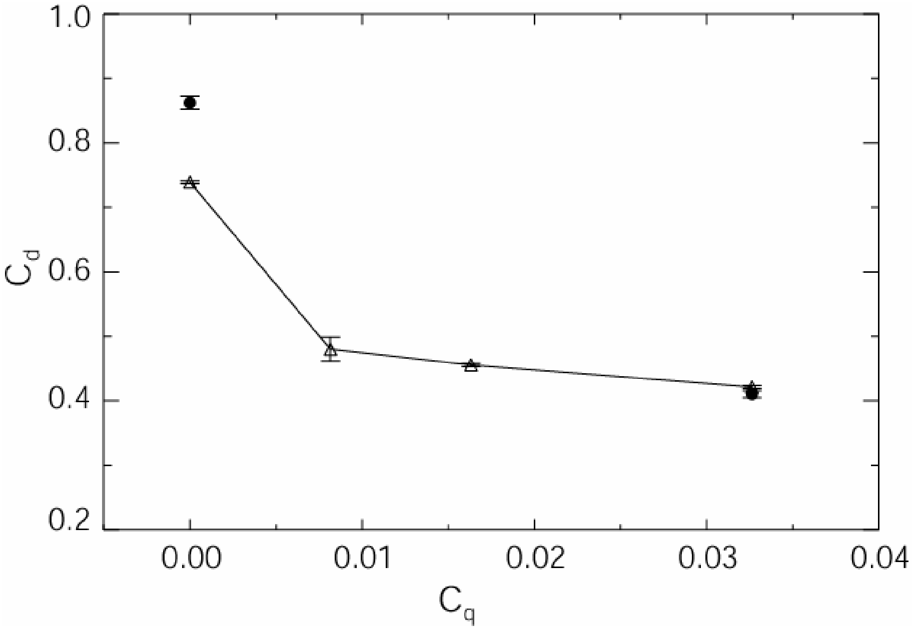

Figure 7. Drag coefficients as a function of the bleeding coefficient, C_q, for tractor base bleeding on the GCM at 7 degrees yaw

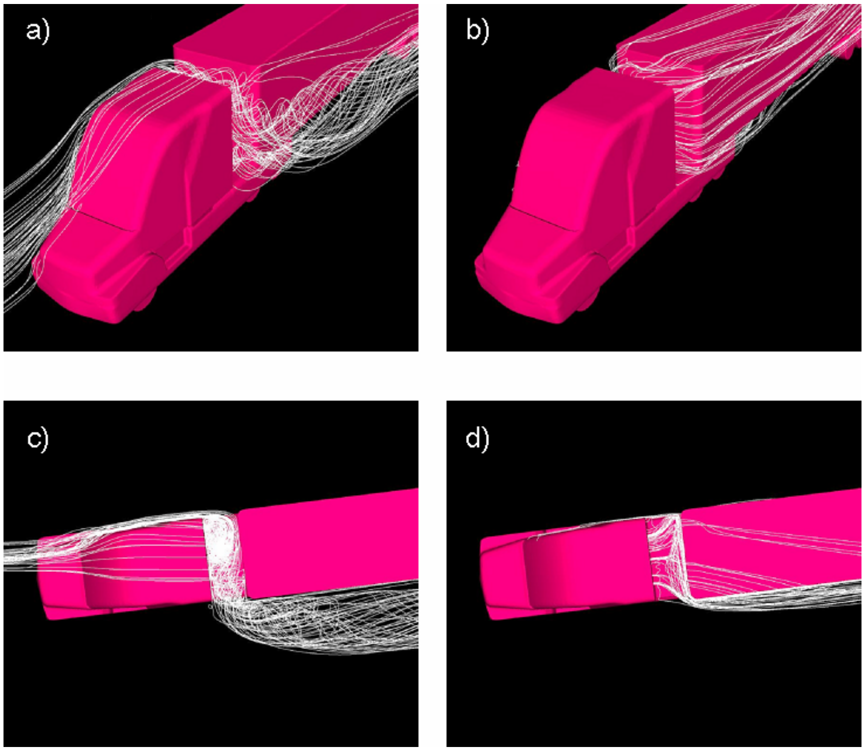

Figure 8. Velocity streamlines in the gap of the GCM a,c) without and b,d) with tractor base bleeding

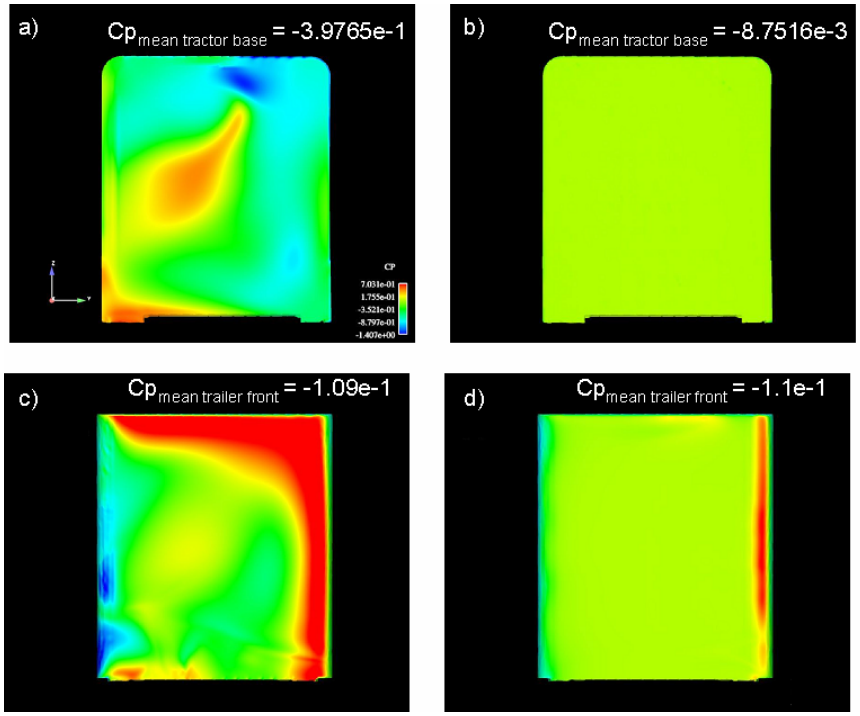

Figure 9. Pressure distribution over the a,b) tractor base and c,d) trailer front a,c) without and b,d) with tractor base bleeding on the GCM. $C_p = p/(\frac{1}{2}\rho U_{inf}^2)$ is defined to be the pressure coefficient, where p is the pressure

Figure 10. Wind tunnel model (1:20 scale) for testing the tractor and trailer base bleeding concepts at NASA Ames in FY07

I.C. Experimental Measurement of the Flow-field of Heavy Trucks

Principal Investigator: Fred Browand
Aerospace & Mechanical Engineering, University of Southern California
RRB 203, Los Angeles CA 90089-1191
(213) 740-5359, fax: (213) 740-7774, e-mail: browand@spock.usc.edu

Technology Development Manager: Lee Slezak
(202) 586-2335, e-mail: Lee.Slezak@EE.DOE.GOV

Technical Program Manager: Jules Routbort
(630) 252-5065, e-mail: routbort@anl.gov

Contractor: Lawrence Livermore National laboratory
Subcontract No.: B545349

Objective

- Improve the performance of heavy trucks by reducing aerodynamic drag, rolling resistance, and by increasing safety.

Approach

- Water spray from heavy truck tires is an important safety issue. The spray decreases the rearward visibility of the truck drivers. For automobiles in the immediate vicinity, spray obscures the roadway on either side of the truck. We study the fundamental mechanisms of spray formation.
- Water on the roadway also increases the rolling resistance of tires by the momentum expended to move the water out of the way. No direct measurements of rolling resistance are presently available in the literature, but we estimate the change in rolling resistance due to water on the roadway to be significant.

Accomplishments

- **Preliminary tests illuminate the mechanisms of spray formation.**
  For the first time, the complex process of spray formation from rolling tires has been documented in the laboratory. Visualizations reveal the major mechanism of break-up to be the result of the instability of thin sheets of water that form between the roadway and the tire.
- **Propose modifications to the apparatus for the study of rolling resistance on a wet roadway.**
  In the laboratory apparatus two tires are rolled in contact with one another. One tire simulates the presence of the road surface. Water is injected from a specially designed injector placed just upstream of the contact patch. The speed of the injected water jet is the peripheral speed of the tires. Sensors can be added to the apparatus to measure change in the rolling force as water is applied.

Future Direction

- Initiate a program of rolling resistance measurement using the newly constructed apparatus. Continue study of tire spray formation, and methods to mitigate spray.

Changes in Rolling Resistance Due to a Wet Roadway

We can estimate the magnitude of the additional force felt by a tire due to the water as it rolls over a flooded road. In a coordinate system moving with the vehicle, the water on the roadway represents an oncoming flow which is diverted laterally and brought to rest at a stagnation point at the front of the tire. The order of magnitude of the force exerted by the flow on the two front tires in this process is

$$F = \rho U^2 (t \times W),$$

where ρ is the density of water, U is the velocity, t is the depth of the water and W is the width of the tires. Substituting representative values for these variables, we see a vehicle traveling 27 $\mathrm{m\,s^{-1}}$ (60 mph), with $t = 3$ mm (1/8 inch) and $W = 8$ cm (3 1/8 inches) must overcome an additional resistance of about 175 N (40 lbs.)—the same order of magnitude as the rolling resistance. Experiments with an airplane taxiing on a flooded runway show an additional resistance due to the water of about 10-11% of the airplane's weight.[2] This additional resistance due to displacing water can be added to the rolling resistance and aerodynamic drag as forces that the vehicle's engine must work against to maintain forward motion.

Continuing in a reference frame moving with the vehicle, we could treat the roadway not as a solid surface, but as an imaginary plane between the rolling tire and its image located below the surface. The layer of water still flows toward the tire at a speed U, producing the resistance force described above.

Our plans are to measure this additional force using the tire spray apparatus at USC (Fig. 1). That machine consists of two tires, each hung from a pendulum arm so the tire treads touch. The pendulum arms are then loaded with a side force pressing the tires together to form a tire patch. This geometry is the same as that in the image view of the problem except the plane of symmetry is now vertical. One tire is driven by a motor while the other rotates due to its contact with the other tire.

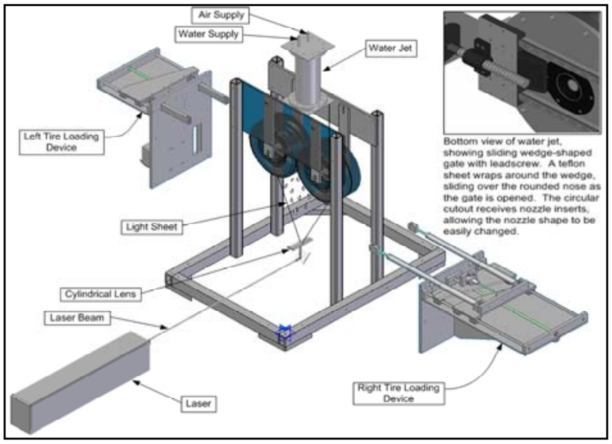

Figure 1.

It is important in this configuration that the water is delivered to the tire patch at the circumferential speed of the tire. To do this, a water jet was designed and built. The jet exits through a sharp-edged opening in the bottom of a cylindrical tank, producing a glassy-smooth laminar jet. The speed of the jet is controlled by setting the depth of water and the air pressure in the tank while the volume of the flow is controlled through the size of the nozzle.

To measure the force on the non-driven tire load cells will be inserted into the pendulum arms (Fig. 2). With the tires spinning at constant speed, the jet will be turned on. The difference in force measured before the flow and during the flow will be the additional resistance resulting from the tire pushing the water out of its path.

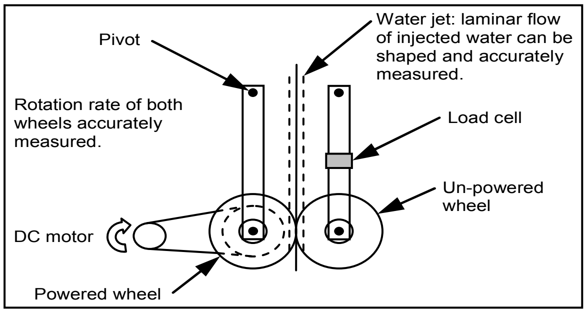

Figure 2.

---

[2] Adnan Cepic, "Hydroplaning of H-type aircraft tires," *SAE Transactions* **113** part I (SAE paper 2004-01-3119), pp. 1599-1606, 2004.

Spray From Rolling Tires

A continuing part of the project has been looking at spray from a tire rolling over a wet surface. This has been done using illumination both from a laser and via backlighting—shining a bright light on a glass plate mounted behind the tires then looking at the spray from the front. The laser offers the advantage of a very short exposure, about 5 ns, and the limitation of a low framing rate. Backlighting has limitations imposed by the brightness of the light and the characteristics of the video camera, in our case typical exposures of 6 µs and framing rates of about 1600 frames/s.

Fig. 3 is a frame from a movie using backlighting and looking at the 25 cm long region downstream of the tire patch formed between a smooth tire on the bottom and a single-grooved tire on the top. Most prominent is the sheet of water extending between the tire groove and the smooth tread of the opposite tire. Also prominent are the ridges of disturbed water extending through the sheet between the tires.

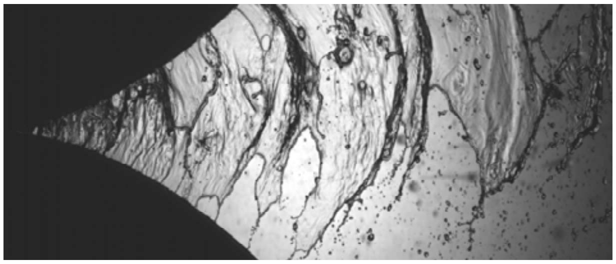

Figure 3.

Looking at these frames more closely one can identify holes developing in the sheets (Fig. 4) and clearly see the texture of another sheet behind. This growing hole in the sheet of water with another sheet behind becomes even clearer when several frames are viewed in succession.

The flow downstream of the tire patch, then, is made up of sheets of water coming from different locations across the tire groove, with thicker bands of water with a rougher surface extending between the two tires. These bands have a preferred spacing. As this pattern moves downstream, the preferred spacing becomes larger and both the sheets and bands separate from the tire surfaces. The sheets form holes which grow until there is only a thin string of water separating adjacent holes. This thin string then breaks down into small droplets. The preferred spacing of the bands decreases with speed and less sheet formation.

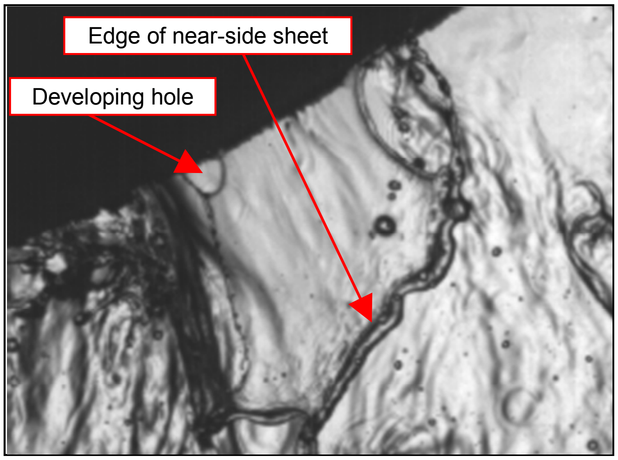

Figure 4.

Several different treatments were applied to the spray system. Depending on the treatment, the flow could be made rougher, with less sheet formation at a particular speed or smoothed dramatically as in Fig. 5.

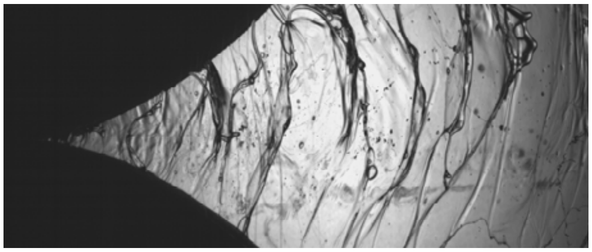

Figure 5.

I.D. Aerodynamic Drag Reduction of the Underbody of a Class-8 Tractor-Trailer

Principal Investigator: Bruce L. Storms
AerospaceComputing, Inc.
M/S/260-1
NASA Ames Research Center
Moffett Field, CA 94035
(650) 604-1356, fax: (650) 604-4511, e-mail: bstorms@mail.arc.nasa.gov

Field Project Manager: James C. Ross
NASA Ames Research Center
M/S/260-1
Moffett Field, CA 94035
(650) 604-1356, fax: (650) 604-4511, e-mail: james.c.ross@nasa.gov

Technology Development Manager: Lee Slezak
(202) 586-2335, e-mail: Lee.Slezak@EE.DOE.GOV

Technical Program Manager: Jules Routbort
(630) 252-5065, e-mail: routbort@anl.gov

Contractor: NASA Ames Research Center
Contract No.: DE-AI01-99EE50559

Objective

- To investigate the contributions of the tractor and trailer underbody to overall aerodynamic drag.
- To test configurations and devices resulting in aerodynamic drag reduction

Approach

- Fabricate a 1:20-scale model with a realistic tractor-trailer geometry including significant underbody detail.
- Measure the forces and moments and surface pressure distribution in the 32- by 48-Inch Wind Tunnel. Measurements were made at various yaw angles to study the influence of crosswind and to calculate wind-averaged drag coefficients. Several drag-reduction concepts were studied in order to document their potential benefit.

Accomplishments

- Small-scale study completed of aerodynamic effects of tractor-trailer underbody.
  - Detailed experimental results were presented for several configurations of interest with several tractor and trailer add-on devices to demonstrate the potential of underbody modifications.
    - Separate measurements of underbody fairings on the tractor and trailer yielded wind-averaged drag reduction of 0.018 for two configurations. A floor plate blocking vertical flow in the tractor-trailer gap resulted in a drag reduction of 0.021. Trailer side skirts proved to be the most effective trailer-underbody device, reducing the wind-averaged drag by 0.073.
    - The estimated annual fuel savings per truck was calculated assuming a typical use of 240,000 km/yr. The smooth trailer underbody and side skirts yielded an estimated savings of 1653 and 6586 liters/yr.

For the relatively small drag reduction of the smooth underbody configuration, the annual monetary savings for a 5,000 truck fleet (assuming a fuel cost of $0.83/liter) would be close to $7 million.

– The results of the study were presented at the SAE 2006 Commercial Vehicle Engineering Conference in Chicago, IL on November 1st (paper number SAE-2006-01-3532)

Future Direction

- Additional studies of aerodynamic drag reduction of tractor-trailer gap and trailer base.

Introduction

For a typical heavy vehicle at a highway speed of 110 km/hr, the energy required to overcome aerodynamic drag is about 65% of the total expenditure (which includes rolling friction, transmission losses, and accessories). By altering the vehicle shape, it has been estimated that modern truck drag coefficients may be reduced by up to 50% resulting in an annual national fuel savings of eleven billion liters (Ref. 1). This large potential savings coupled with increasing fuel costs have spurred renewed interest in heavy-vehicle aerodynamics.

A significant number of experimental studies of heavy-truck geometries were conducted in the 1970's and 1980's (Ref. 2). The resulting first-generation drag-reduction technology currently in use includes cab shaping, cab-mounted deflectors, trailer front-end fairings, cab side extenders, and body front-edge rounding. The cab deflectors and side extenders accounted for the majority of the wind-averaged drag reduction reducing the pre-1980 drag level by about 25%. Other drag-reduction technologies that are not widely used include tractor-trailer gap seals, trailer side skirts, and rear boat-tailing. Each of these technologies produce a reduction of the wind-averaged drag coefficient between 0.03 and 0.10 which is about one-half the benefit of the first-generation technologies. However, the benefits of these devices are additive and the resulting net reduction is relatively large.

The aerodynamic drag reduction and fuel savings of various tractor and trailer modifications was previously summarized in Ref. 3. Since fuel consumption is the quantity of interest for commercial operators, a derivation of fuel consumption as a function of drag coefficient and road speed was provided. For trailer base flaps and skirts, the ranges of wind-averaged drag reduction were listed as 0.03 – 0.09 and 0.04 – 0.07, respectively.

More recently, a series of experimental and computational studies was funded by the Department of Energy (DOE), Office of Heavy Vehicle Technology. With the goal of CFD validation, the experimental efforts have focused on simplified geometries at 1:8-scale and below. Early experiments (Refs. 4-6) focused on the simplified geometry of the Ground Transportation System (GTS) model representative of a class-8 tractor-trailer with a cab-over-engine design. A 1:8-scale GTS model with no tractor-trailer gap and no wheels was first studied with the addition of several ogival boattails and slants to the base of the trailer (Ref. 4). The largest overall drag reduction of 10% was obtained by a 2.4-m ogive configuration (full scale). The addition of boattail plates to the same model resulted in a 19% drag reduction and PIV measurements behind the trailer document a significant reduction in the wake size due to the flow turning provided by the plates (Ref. 5). Variation of the tractor-trailer gap on a 1:15-scale model at zero yaw revealed relatively constant drag on the tractor while the trailer drag increased by a factor of three as the gap was increased from zero to 1.55*A**0.5 (Ref. 6).

Also part of the DOE effort, the Generic Conventional Model (GCM) of the current study was tested in two different facilities at the National Aeronautics and Space Administration's (NASA) Ames Research Center. This geometry included a tractor-trailer gap and a simplified conventional tractor geometry (detailed below). In the 7- by 10-Ft Wind Tunnel, measurements were made at a Reynolds number of 1.1 million. Of particular interest are the detailed PIV data in the tractor-trailer gap with and without side extenders and in the trailer wake with and without boattail plates (Ref. 7).

A large subset of the configurations tested in the 7- by 10-Ft Tunnel were duplicated in the 12-Ft Pressure Tunnel to determine the effects of Reynolds number variation (Ref. 8). For all configurations, Reynolds number effects were evident at high yaw angles (greater than 8 deg) where there was a significant reduction in drag at lower Reynolds numbers. However, this difference did not significantly affect the computation of the wind-averaged drag coefficients (at highway speeds) which employs data at lower yaw angles.

The goal of the present study is to investigate the potential for drag reduction by geometric modifications of the underbodies of both the tractor and trailer. Large fairings were first attached to the underbodies and gap region to determine the upper limits of possible drag reduction. More practical fairings were subsequently tested for comparison.

Experimental Setup

The experiments were conducted in the 48- by 32-Inch Subsonic Wind Tunnel in the Fluid Mechanics Laboratory at NASA Ames Research Center (Fig. 1). This facility is an open-circuit, in-draft wind tunnel with flow supplied by a single-stage centrifugal compressor acting as a vacuum source. The compressor runs at constant speed while mass flow (and hence, speed) through the test section is controlled by means of a variable-area sonic throat. When running, the compressor fan draws ambient laboratory air through a pleated filter, which prevents the entry of dust and foreign materials into the tunnel. Immediately downstream of the pleated filter are a stainless steel honeycomb and four progressively smaller open-area screens for flow conditioning. The 9:1 contraction leads to the wind tunnel test section, which is approximately 1.2 m wide, 0.81 m tall, and 3.05 m long. The side-walls and roof of the test section are constructed of thick Plexiglas. Directly above the test section is a constant pressure plenum that houses a 3-axis traverse to which various flow sensors, cameras, lighting, or other equipment can be attached. In addition, the test section floor contains a remote-controlled rotating yaw platform. The flow exits from the test section through a contraction into the sonic throat. The design maximum velocity in the test section is 52 m/s, corresponding to a Reynolds Number of approximately 3.5 million per meter. The freestream turbulence levels of the empty test section in the longitudinal, lateral, and vertical directions are approximately 0.15%, 0.1%, and 0.1%, respectively. The flow speed and static pressure reference was provided by a pitot-static probe located at $x/w = 3.1$, $y/w = 4.9$, and $z/w = -3.7$.

A three-view drawing of the baseline tractor-trailer configuration is shown in Fig. 2. This 1:20-scale model is representative of a class-8 tractor-trailer with a standard aero package. The tractor was fabricated by stereolithography from a publicly available geometry of the Kenworth T600A. This unvalidated geometry definition included a full-scale height mismatch between the tractor roof fairing and the top of the trailer of 38 cm (the actual height of the tractor is unknown due to the proprietary nature of the design). Apart from a standard aero package with cab side extenders and wheel fairings, this geometry includes significant underbody detail as shown in Fig. 3. A 0.4-mm trip wire was located at the front of the model (visible in Fig. 4) to ensure turbulent flow on the tractor. A simplified engine block was also included with the approximate external dimensions of a typical engine. To simulate flow through the engine compartment, a flow-through front grill with a porosity of 60% was included to approximate the pressure drop across the radiators.

The trailer geometry was chosen to be representative of modern U.S. designs. The trailer measures 13.7 m in length (full scale) with rounded front vertical edges (20-cm full-scale radius). The underbody includes details of cross-members, landing gear, undercarriage, and other significant components (Fig. 3). This geometry was provided by SOLUS with input from Great Dane. The tractor-trailer gap for this study was held constant at the full-scale equivalent of 1 m (0.39w).

A photograph of the baseline tractor-trailer configuration installed in the 48- by 32-Inch Wind Tunnel test section is shown in Fig. 4. The model was attached to the model-support hardware by two 1.9-cm vertical posts. The posts were non-metric (i.e., their aero loads were not measured by the balance) with 3 mm of clearance as they passed through the trailer floor. Since there was no moving ground plane, the model was mounted with its wheels 5.4 mm above the ground plane (to account for the tunnel floor boundary layer) and centered laterally in the tunnel. The center of rotation of the model was located 39.5 cm aft of the tractor front bumper. The model frontal area of 0.025 m2 gives a solid blockage of 2.5%. The overall model loads were measured with a six-component balance (1.9-cm Task balance Mark XV) that was mounted inside the trailer. The manufacturer-specified accuracy of the internal balance in the axial (drag) direction was ± 0.33 N, but the experimental results suggest significantly greater accuracy as detailed in the subsequent discussion.

The model was instrumented with 9 pressure taps on the tractor and 66 taps on the trailer. The surface pressures were measured with an electronically scanned pressure system and time averaging yielded an uncertainty in the calculated pressure coefficients of ±0.002 at Re = 430,000. The model was yawed through a range of angles between ±14 degrees.

Results and Discussion

The results presented below detail the body-axis drag (axial force) for the tractor-trailer combination. This drag coefficient represents the force along the axis of the vehicle in the direction of travel. No wall corrections were applied to the data and all coefficients were calculated based on the dynamic pressure from a pitot-static probe adjacent to the model. Without wall corrections, the computed drag coefficients will differ from those of the equivalent model in free air. However, the measured differences between configurations should be representative of the effects of the associated geometric modifications.

Using the variation of drag with yaw angle, wind-averaged drag coefficients ($\bar{C}_D$) were computed using the SAE Recommended Practice (Ref. 9). This practice assumes that the mean wind speed in the United States of 11.2 km/hr has an equal probability of approaching the vehicle from any direction. This mean wind speed and the vehicle velocity were used to calculate a weighted average based on the variation in drag coefficient over a range of yaw angles. The wind-averaged drag coefficients reported in this paper were computed for a highway speed of 90 km/hr.

Except where noted, the data presented below are from the measurements conducted in the 48- by 32-Inch Wind Tunnel at a Reynolds number of 430,000 and all data were acquired for increasing yaw angle.

A. Baseline Configuration

Prior to the force and pressure measurements, tufts were applied to the sides of the baseline trailer to provide flow visualization (tufts did not adhere to the tractor due to the nature of the nylon material). Although the test Reynolds number of 430,000 is well below the critical value for this configuration (estimated at 1 million), no large-scale separation was observed on the trailer sides for yaw angles between ± 10 deg. This suggests that the trip wire and relatively complicated tractor geometry resulted in turbulent downstream flow.

A comparison of the baseline drag curve to that of previously tested configurations is presented in Figure 5. Relative to the 1:8-scale GCM configuration tested at Re = 1.1 million (Ref. 8), the drag curve of the 1:20-scale model was significantly higher and exhibited a larger increase with increasing yaw. This result is expected due to the significantly more complicated tractor geometry, the added trailer underbody detail, and the previously noted height mismatch between the tractor and trailer. Relative to a more realistic geometry with a 1:10-scale White Road Boss tractor tested at NRC (Ref. 10), there was relatively good agreement at zero yaw with increasing difference at higher yaw angles. The difference at yaw is possibly a result of the added detail (and corresponding drag) of the current 1:20-scale trailer underbody. There was also some observed asymmetry between positive and negative yaw angles. Data acquired for decreasing yaw (opposite the standard rotation) indicated minimal hysteresis, so the drag-curve asymmetry is likely related to small asymmetries in the tractor geometry and/or the facility flow.

During the course of this wind-tunnel study, measurements of the baseline configuration were made four times over a three-day period to demonstrate repeatability. The resulting drag curves (Fig. 6) indicate that the repeatability is on the order of the symbol size, or approximately ±0.003, for yaw angles between ± 5 deg. For larger angles, the repeatability was about twice this value, or ±0.006. To account for the observed drag-curve asymmetry, the drag coefficients at corresponding positive and negative yaw angles were averaged for the computation of wind-averaged drag. For these four repeat runs, the repeatability of the wind-averaged drag coefficients was ±0.002.

B. Tractor Underbody Fairings

Two underbody fairings, or belly pans, were studied on the tractor (Fig. 7). Although impractical, a full tractor fairing was tested to determine the maximum drag reduction possible. This fairing was a simple flat plate that extended from the front bumper to the rear axle, enclosing and/or shielding the engine compartment and underbody components. In addition, a partial tractor fairing was tested that was identical to the full fairing, but only extended to the rear of the cab. The resulting drag curves (Fig. 8) indicate that the benefit of the tractor fairings is the greatest for yaw angles between ± 5 deg, resulting in wind-averaged drag reduction of 0.015 and 0.018 for the partial and full fairings, respectively.

C. Tractor-Trailer Gap Fairings

An image of the baseline tractor-trailer gap is shown in Figure 9. This geometry allows for flow between the underbody and the tractor-trailer gap region. The effect of sealing the bottom of the gap to vertical flow was investigated with the addition of full- and partial-width gap-floor plates (Fig. 10). The effect of the floor plates on the drag curves is shown in Figure 11. Relative to the baseline, both floor-plates provided reduced drag, especially for yaw angles between ± 5 deg where cross flow is less important. At yaw angles between ± 2 deg, the partial floor plate was more effective than the full-width plate. At higher angles, the full-width floor plate was more effective. The resulting wind-averaged drag reductions for the partial- and full gap-floor plates were 0.011 and 0.021, respectively. These results indicate the benefit of blocking or reducing the vertical flow through the tractor-trailer gap.

D. Trailer Underbody Fairings

The effect of the trailer underbody detail was studied by covering the structural cross members with a simple flat-plate fairing that simulated a sandwich-type construction (Fig. 12). In addition, trailer side skirts were mounted on the underbody with a full-scale length and ground clearance of 4 m and 0.3 m, respectively (Fig. 13). The effects of the smooth underbody and side skirts on the drag curves are presented in Figure 14. The smooth trailer underbody marginally reduced the drag at all yaw angles and yielded a wind-averaged drag reduction of 0.018. Admittedly, the conversion of existing trailers to a smooth-underbody configuration is unpractical due to weight and cost considerations. However, if the floor of the trailer was designed to include a sandwich construction, these penalties could likely be avoided. The trailer side skirts were considerably more effective yielding a wind-averaged drag reduction of 0.073. This value is at the upper end of the range reported previously (Ref. 3) most probably due to the higher fidelity of the current underbody geometry. The combined effect of the tractor and trailer fairings was not measured.

E. Surface Pressure Distributions

Static surface pressures were measured on the back of the tractor, the front and back of the trailer, and on the side of the trailer. The pressure distributions along the vertical model centerline and on the left side of the trailer are presented in Figures 15-22 for selected configurations at yaw angles of 0, 10, and –10 deg. In general, the same trends were observed for the off-centerline pressure-tap rows. The graphs are organized by location of the geometry modifications: 1) tractor fairing and gap-floor plates, and 2) smooth trailer underbody and trailer side skirts. Each graph includes the associated baseline for comparison.

Due to internal structural details of the model tractor, only four pressure taps were installed along the vertical row at the model centerline. In addition, these taps are only on the lower two-thirds of the tractor base (the top of the trailer is at approximately $z/w = 1.5$). The gap-floor plate produced the greatest change in the tractor pressure distributions (Fig. 15) by reducing the vertical gradient and associated vertical flow. Except at zero yaw, the tractor underbody fairing reduced the pressure on the tractor base (resulting in increased tractor drag). As expected the trailer modifications had little effect on the tractor pressure distributions (Fig. 16).

On the front of the trailer (Fig. 17), the effect of the height mismatch is observed as a relatively high pressure at pressure tap second from the top (near the region of flow stagnation on the trailer face). The gap-floor plate had the greatest effect at zero yaw where it significantly reduced pressures (and corresponding drag) over most of the trailer face. The tractor fairing resulted in only a margin decrease in pressure at zero yaw, and both modifications had a relatively small effect at ± 10 deg. Again, the trailer modifications had little effect on the trailer-front pressure distributions (Fig. 18).

On the left side of the model, a row of pressure taps ran the length of the trailer at half-height. The pressure distributions indicate a minimal effect (mostly near the front) of the tractor fairing and gap-floor plate (Fig. 19). Relative to the baseline, the smooth trailer underbody and trailer side skirts generated marginally higher and lower pressures on the trailer side, respectively (Fig. 20).

On the base of the trailer, the effects of the tractor underbody fairing and gap-floor plate were marginal (Fig. 21). The effects of the trailer smooth underbody and side skirts, however, were significant. At zero yaw, both modifications provided a significant increase in pressure for the entire distribution. At ± 10 deg yaw, the side skirts produced a greater pressure increase (and associated drag reduction) especially on the lower half of the base (Fig. 22). The difference between the pressure distributions of the smooth underbody and trailer skirts, however, is not enough to account for the significantly greater drag reduction of the side skirts. Apart from the increased base pressures, it should also be noted that the trailer side skirts effectively shield the rear boggies and trailer undercarriage, thereby reducing the drag on these underbody components.

F. Estimated Fuel Savings

The estimated annual fuel savings per truck was calculated using the methodology presented in Ref. 3 and assuming a typical use of 240,000 km/yr. For the configurations presented above, a summary of the measured wind-averaged drag reduction and estimated annual fuel savings is presented in Table 1. The smooth trailer underbody and side skirts yielded an estimated savings of 1653 and 6586 liters/yr. For the relatively small drag reduction of the smooth underbody configuration, the annual monetary savings for a 5,000 truck fleet (assuming a fuel cost of $0.83/liter) would be close to $7 million.

Table 1. Summary of drag reduction and estimated fuel savings per truck (based on 240,000 km/yr)

Configuration	**Wind-avg drag ΔC_D, 90 km/hr**	**Fuel savings Liters/yr**
Part Tractor Fairing	–0.015	1359
Full Tractor Fairing	–0.018	1635
Partial Floor Plate	–0.011	948
Full Floor Plate	–0.021	1912
Smooth Trailer UB	–0.018	1653
Trailer Side Skirts	–0.073	6586

Conclusions

Experimental measurements were obtained of a 1:20-scale class-8 tractor-trailer model in the NASA-Ames 48- by 32-Inch Subsonic Wind Tunnel. Data were acquired at a Reynolds number of 430,000 for yaw angles between ±14 deg. Forces, moments, and surface pressures were measured to detail a baseline configuration representative of a modern aero package with and without underbody and gap fairings.

Separate measurements of underbody fairings on the tractor and trailer yielded wind-averaged drag reduction of 0.018 for both configurations. A floor plate blocking vertical flow in the tractor-trailer gap resulted in a drag reduction of 0.021. Smaller fairings provided less benefit. As in previous studies, trailer side skirts proved to be the most effective trailer-underbody device, reducing the wind-averaged drag by 0.073. An estimation of the annual fuel savings is provided for each configuration.

References

1. McCallen R., Flowers, D., Dunn, T., Owens, J., Leonard, A., Brady, M., Brownad, F., Hammache, M., Salari, K., Rutledge, W., Ross, J., Storms, B., Heineck, J.T., Driver, D., Bell, J., Zilliac, G., Walker, S., "Aerodynamic Drag of Heavy Vehicles (Class 7-8): Simulation and Benchmarking," 2000-01-2209, SAE Gov/Industry Meeting, Washington, D.C., June 19-21, 2000.

2. Cooper, K. R., "Truck Aerodynamics Reborn – Lessons from the Past," SAE Paper 2003-01-3376, November 2003.

3. Cooper, K., "The Wind Tunnel Testing of Heavy Trucks to Reduce Fuel Consumption," SAE Paper 821285, November 1982.

4. Croll, R. H., Gutierrez, W. T., Hassan, B., Suazo, J. E., and Riggins, A. J., "Experimental Investigation of the Ground Transportation Systems (GTS) Project for Heavy Vehicle Drag Reduction," SAE Paper 960907, February 1996.

5. Storms, B.L., Ross, J.C., Heineck, J.T., Walker, S.M., Driver, D.M. and Zilliac, G.G., "An Experimental Study of the Ground Transportation System (GTS) Model in the NASA Ames 7- by 10-Foot Wind Tunnel." NASA/TM-2001-209621, February 2001.

6. Hammache, M., Michaelian, M., and Browand, F. "Aerodynamic Forces on Truck Models, Including Two Trucks in Tandem," SAE Paper 2002-01-0530, March 2002.

7. Heineck, J. T., Walker, S. M., and Satran, D., "The Measurement of Wake and Gap Flows of the Generic Conventional Truck Model (GCM) using Three-Component PIV," The Aerodynamics of Heavy Vehicles: Trucks, Buses and Trains, Monterey-Pacific Grove, CA, Dec. 2002.

8. Storms, B. L., Satran, D. R., Heineck, J. T., and Walker, S. M., "A Study of Reynolds Number Effects and Drag-Reduction Concepts on a Generic Tractor-Trailer," AIAA Paper 2004-2251, June 2004.

9. "SAE Wind Tunnel Test Procedure for Trucks and Buses," SAE J1252 JUL81, SAE Recommended Practice, July 1981.

10. Cooper, K. R and Leuschen, J., "Model and Full-Scale Wind Tunnel Tests of Second-Generation Aerodynamic Fuel Saving Devices for Tractor-Trailers," SAE Paper 2005-01-3512, November 2005.

Nomenclature

A = tractor-trailer frontal area = w*h
C_D = body-axis drag coefficient = D / q*A
$\bar{C}_D$ = wind-averaged drag coefficient
D = body-axis drag
q = test-section dynamic pressure = $\frac{1}{2}\rho U^2$
Re = Reynolds number = U*w / ν
U = free-stream velocity
w = truck width
x = axial distance from front bumper
y = lateral distance from model centerline
z = vertical distance from bottom of bumper
ν = kinematic viscosity
ρ = air density
ψ = yaw angle (positive nose right)

Figure 1. NASA Ames 48- by 32-Inch Subsonic Wind Tunnel (Inlet at left, plenum chamber above with doors open, test section below)

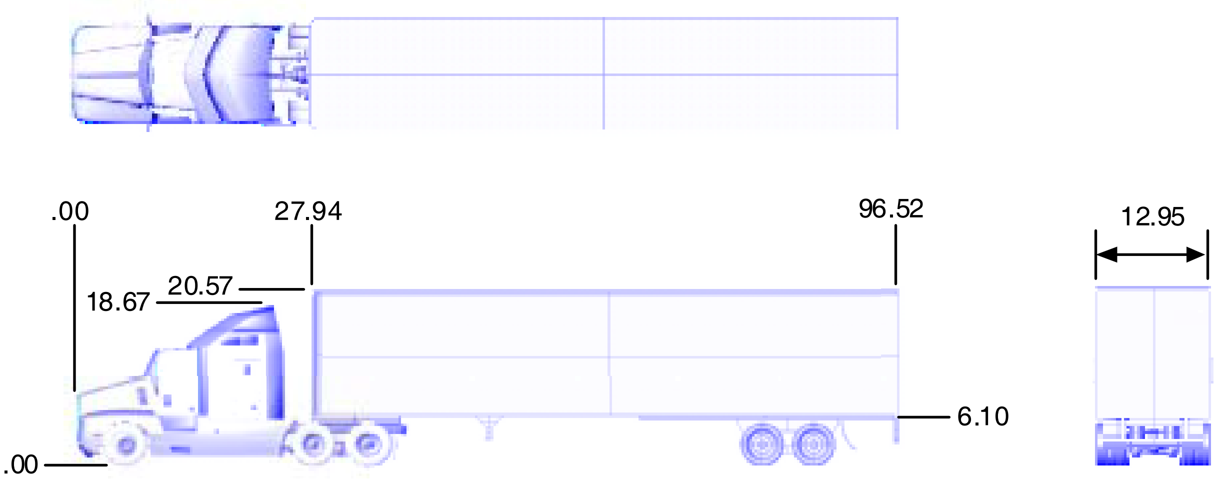

Figure 2. Three-view drawing of baseline tractor-trailer configuration (measurements in cm). Note height mismatch between tractor and trailer due to inaccuracies in the publicly available CAD geometry.

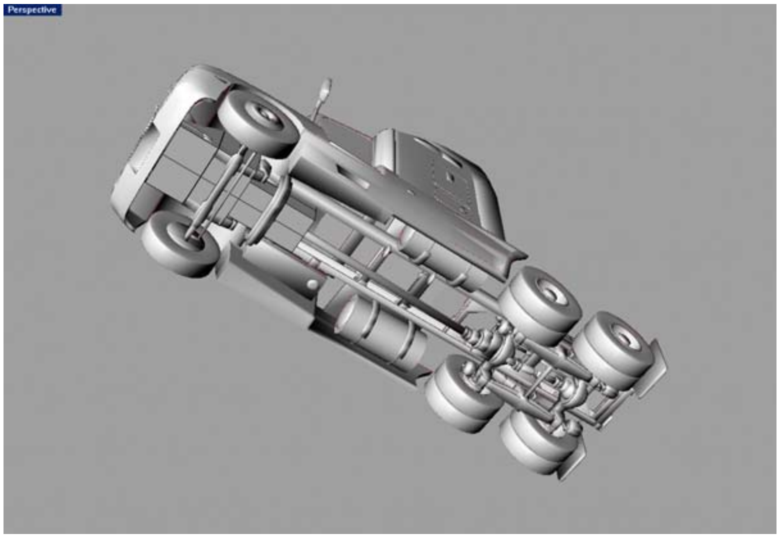

Figure 3. View of tractor underbody detail including simplified engine block

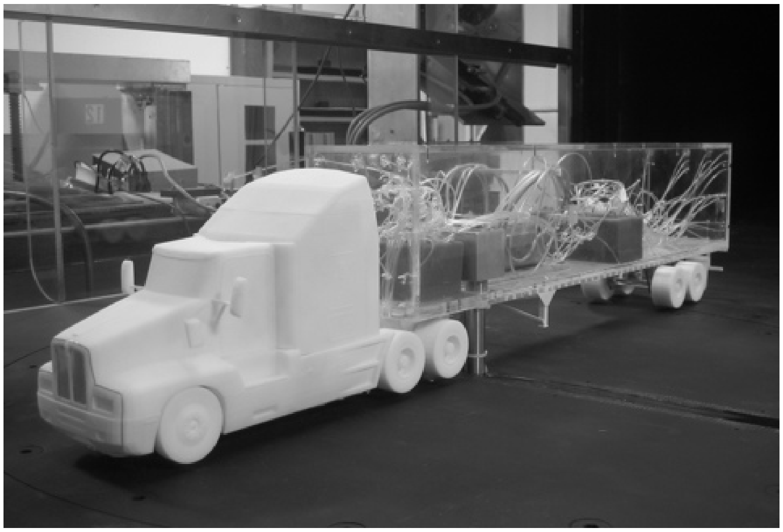

Figure 4. 1:20-scale model installed in the 48- by 32-Inch Wind Tunnel test section. The trip wire is visible as a dark line at the front of the tractor.

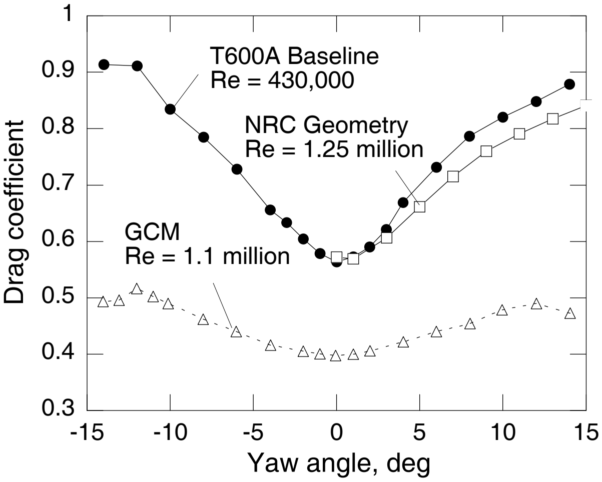

Figure 5. Drag curves of current and previous configurations

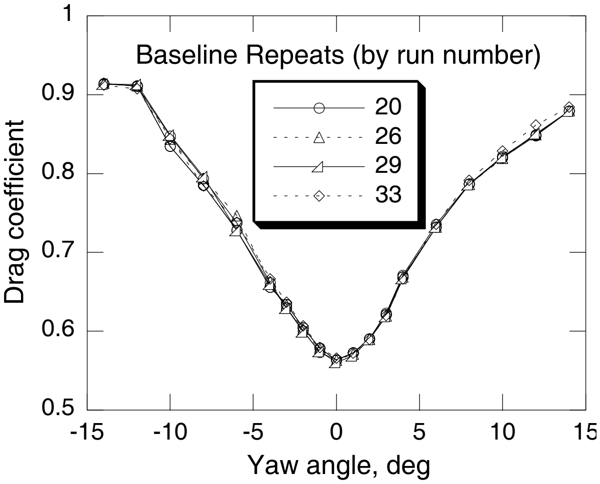

Figure 6. Drag curves for baseline repeats

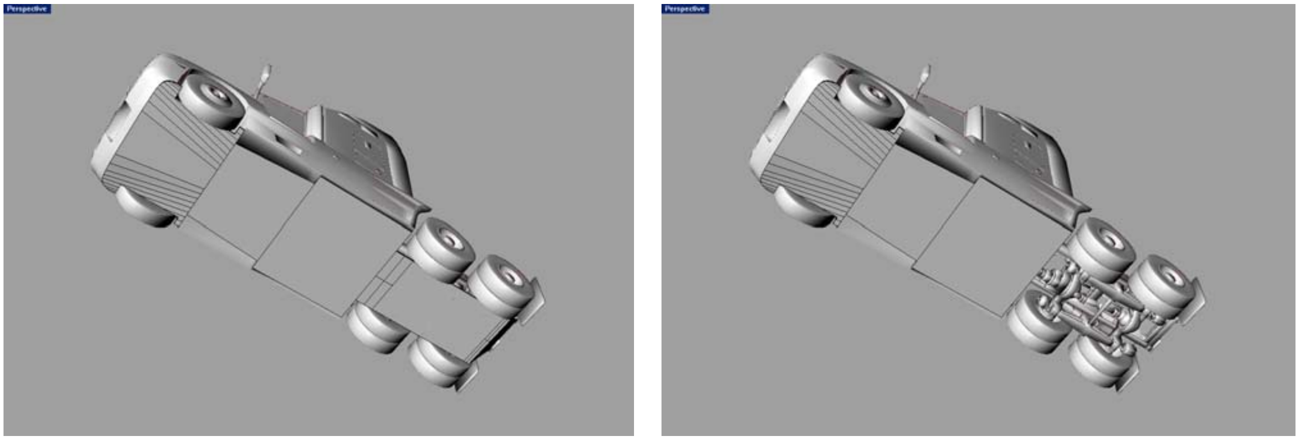

Figure 7. Full and partial underbody fairings on the tractor

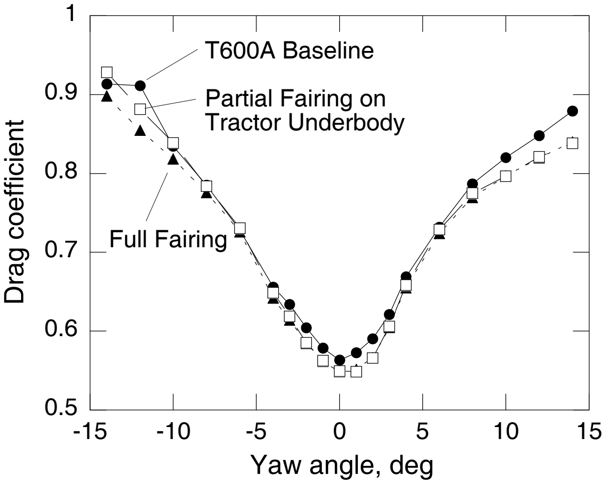

Figure 8. Effect of tractor underbody fairings on drag curve

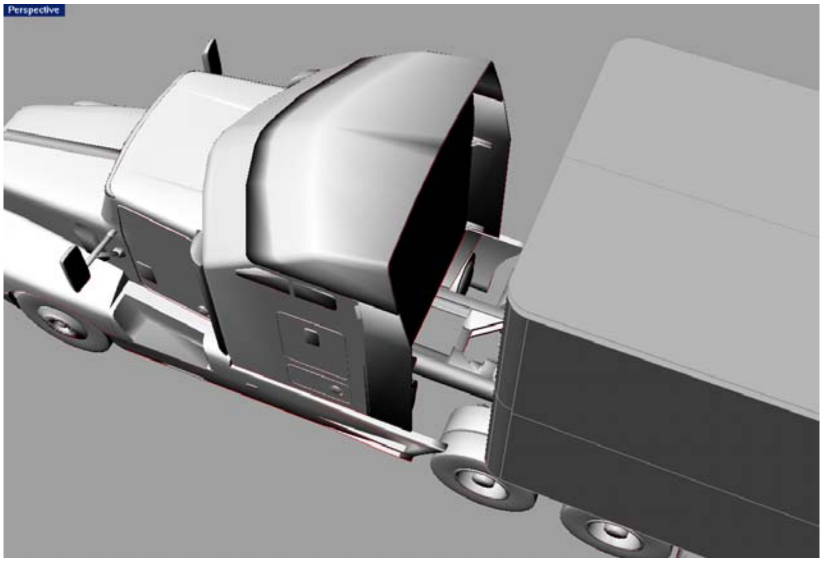

Figure 9. View of tractor-trailer gap (tractor-trailer separation = 1 m full-scale)

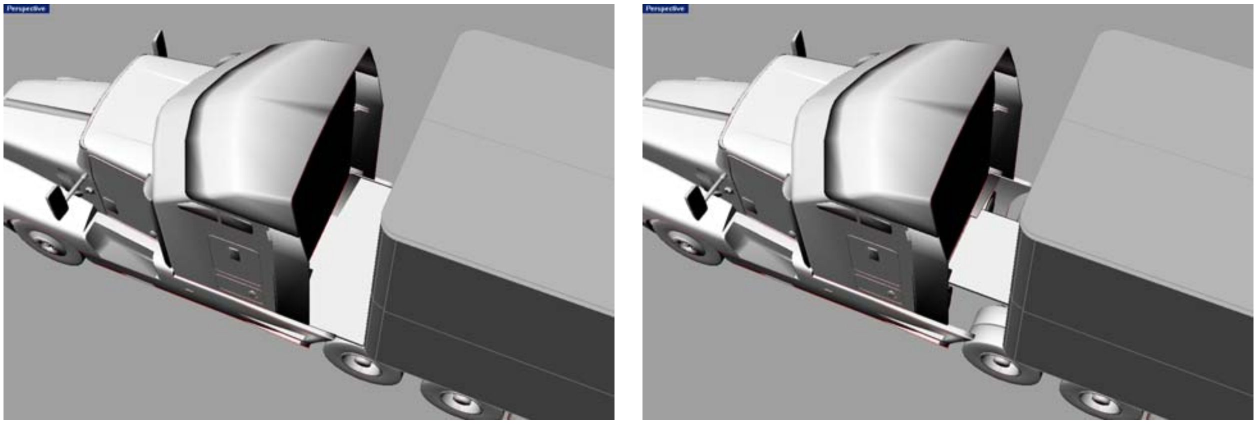

Figure 10. Full and partial floor plates in the tractor-trailer gap

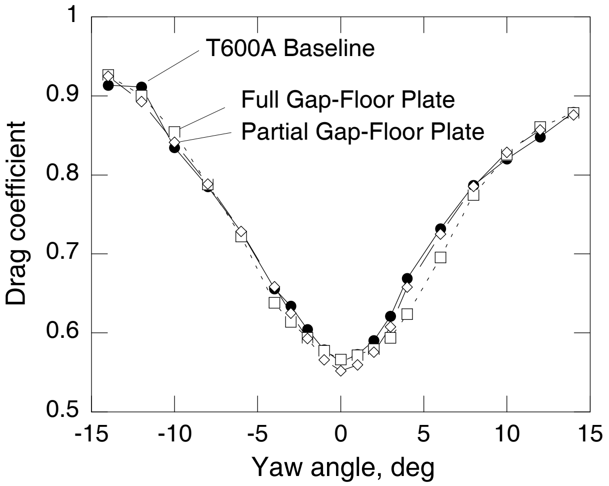

Figure 11. Effect of tractor-trailer gap-floor plates on drag curve

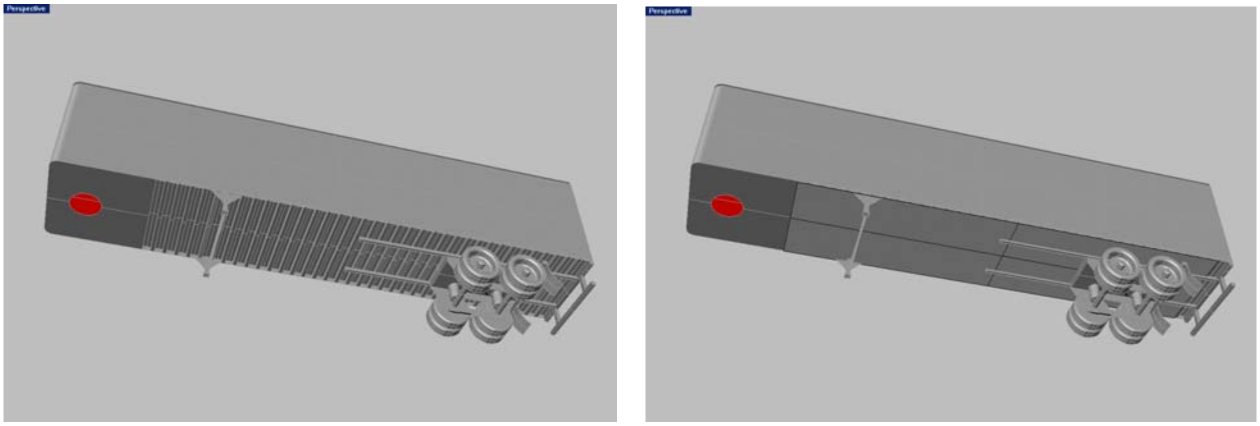

Figure 12. Trailer underbody with and without simple fairing

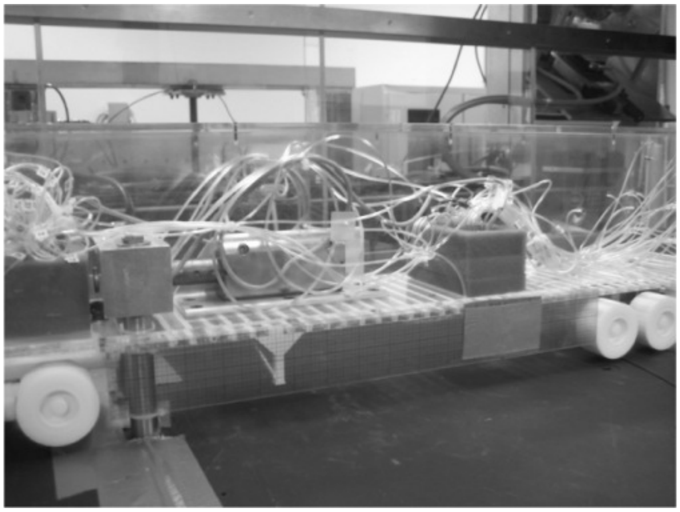

Figure 13. Trailer side skirts mounted on trailer underbody

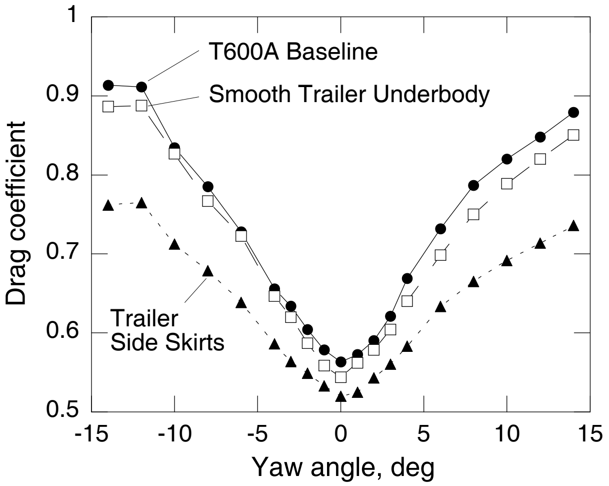

Figure 14. Effect of smooth trailer underbody and side skirts on drag curve

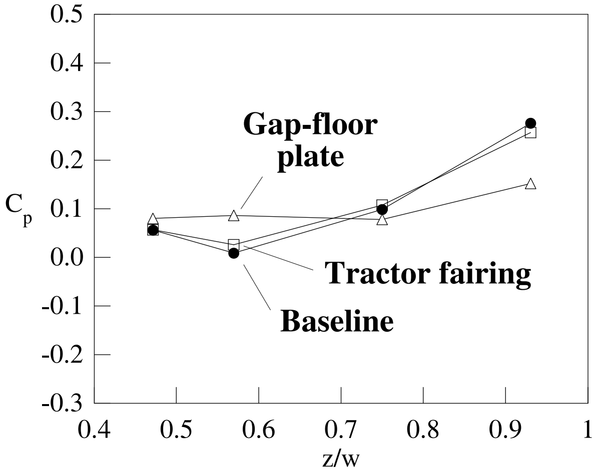

a) Ψ = 0°

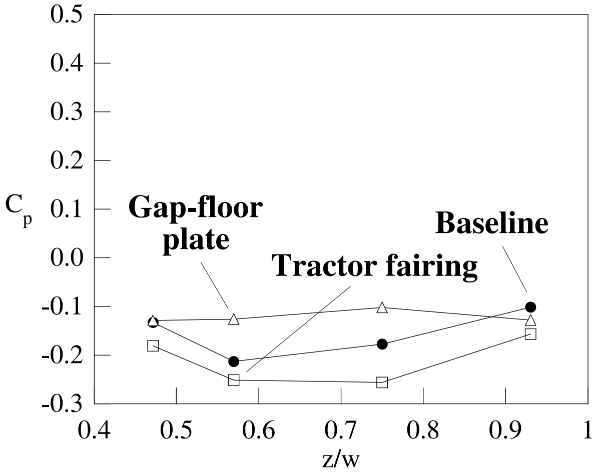

b) Ψ = 10°

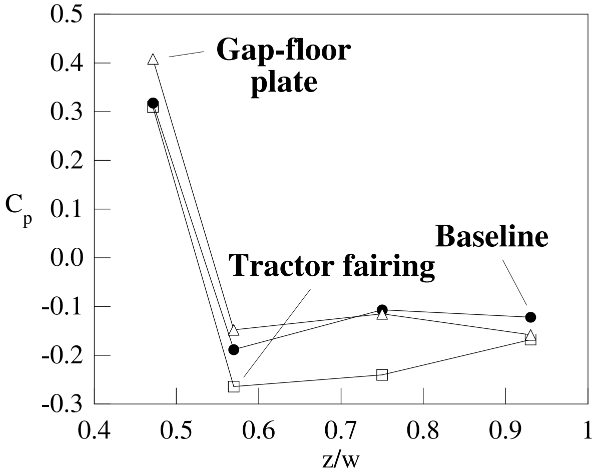

c) Ψ = -10°

Figure 15. Effect of full trailer fairing and gap-floor plate on tractor-base centerline pressure coefficients

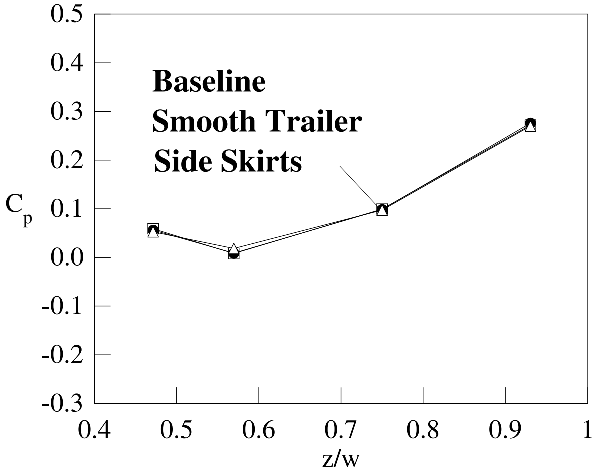

a) Ψ = 0°

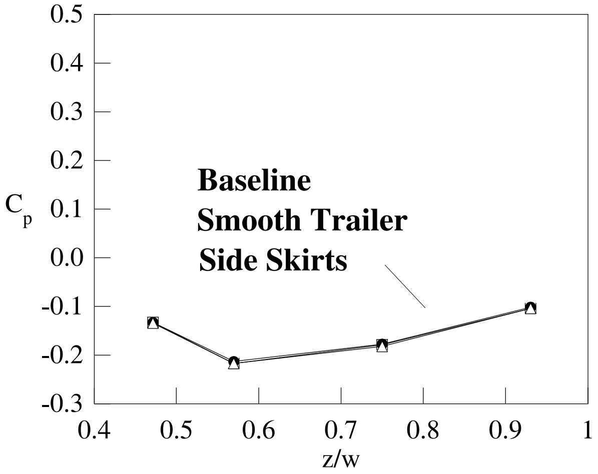

b) Ψ = 10°

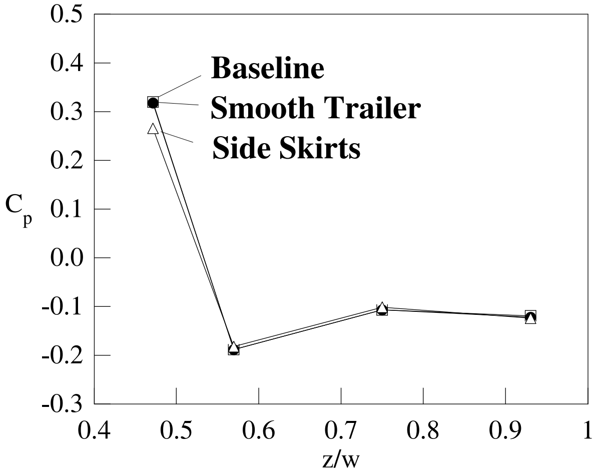

c) Ψ = -10°

Figure 16. Effect of smooth trailer underbody and side skirts on tractor-base centerline pressure coefficients

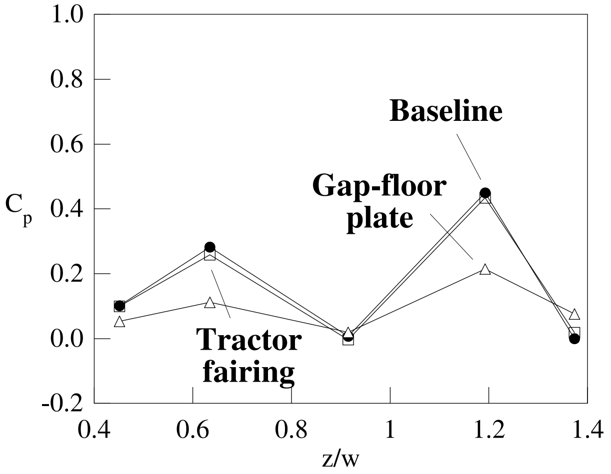

a) Ψ = 0°

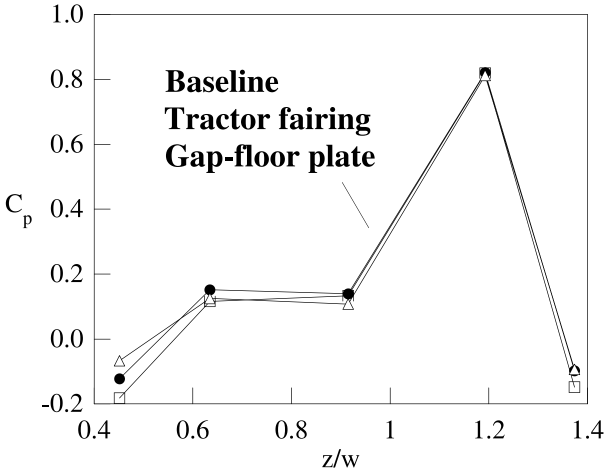

b) Ψ = 10°

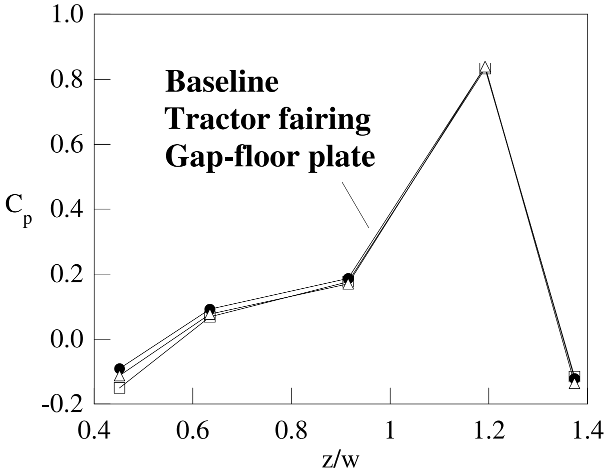

c) Ψ = -10°

Figure 17. Effect of full trailer fairing and gap-floor plate on trailer-front centerline pressure coefficients

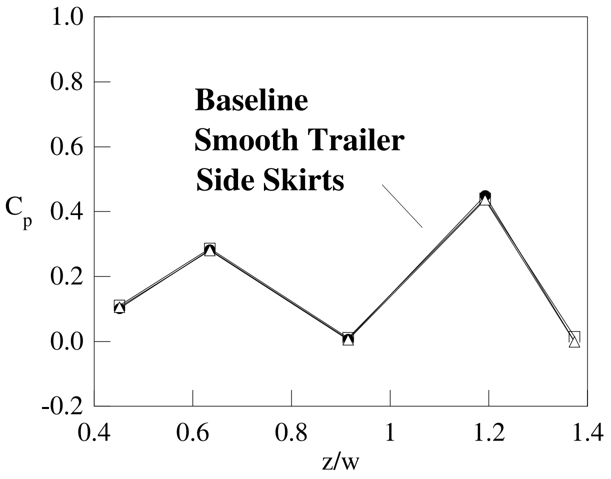

a) Ψ = 0°

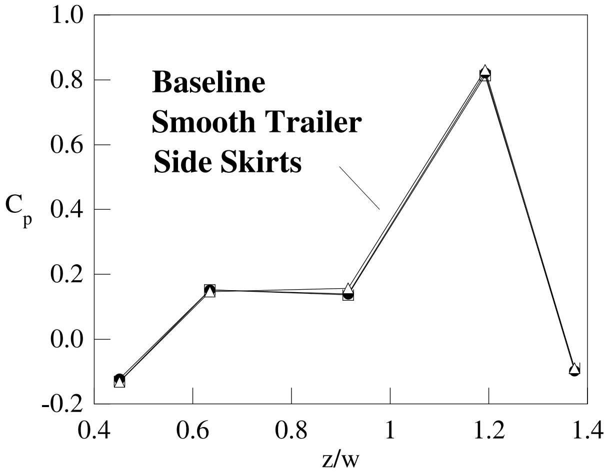

b) Ψ = 10°

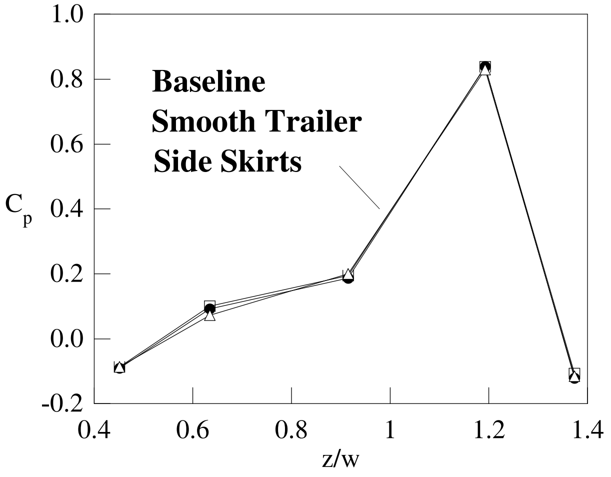

c) Ψ = -10°

Figure 18. Effect of smooth trailer underbody and side skirts on trailer-front centerline pressure coefficients

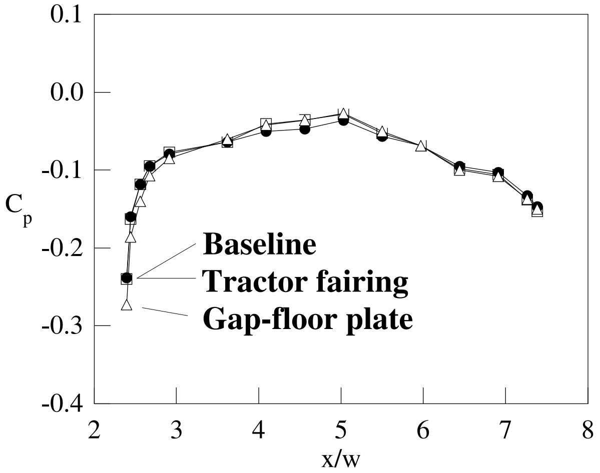

a) Ψ = 0°

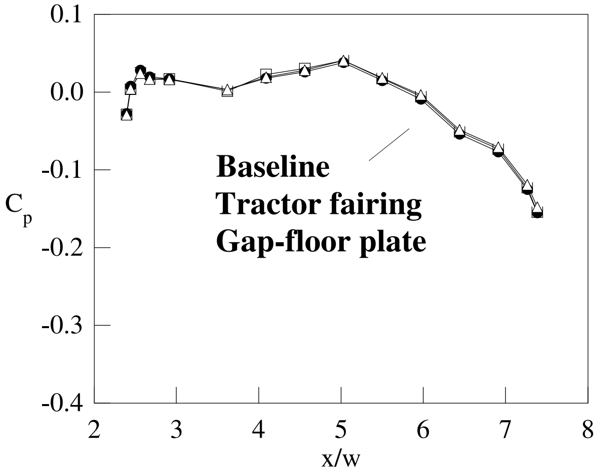

b) Ψ = 10°

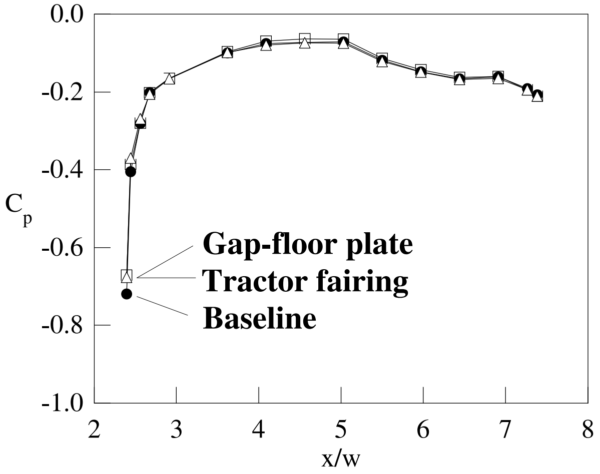

c) Ψ = -10°

Figure 19. Effect of full trailer fairing and gap-floor plate on trailer left-side centerline pressure coefficients

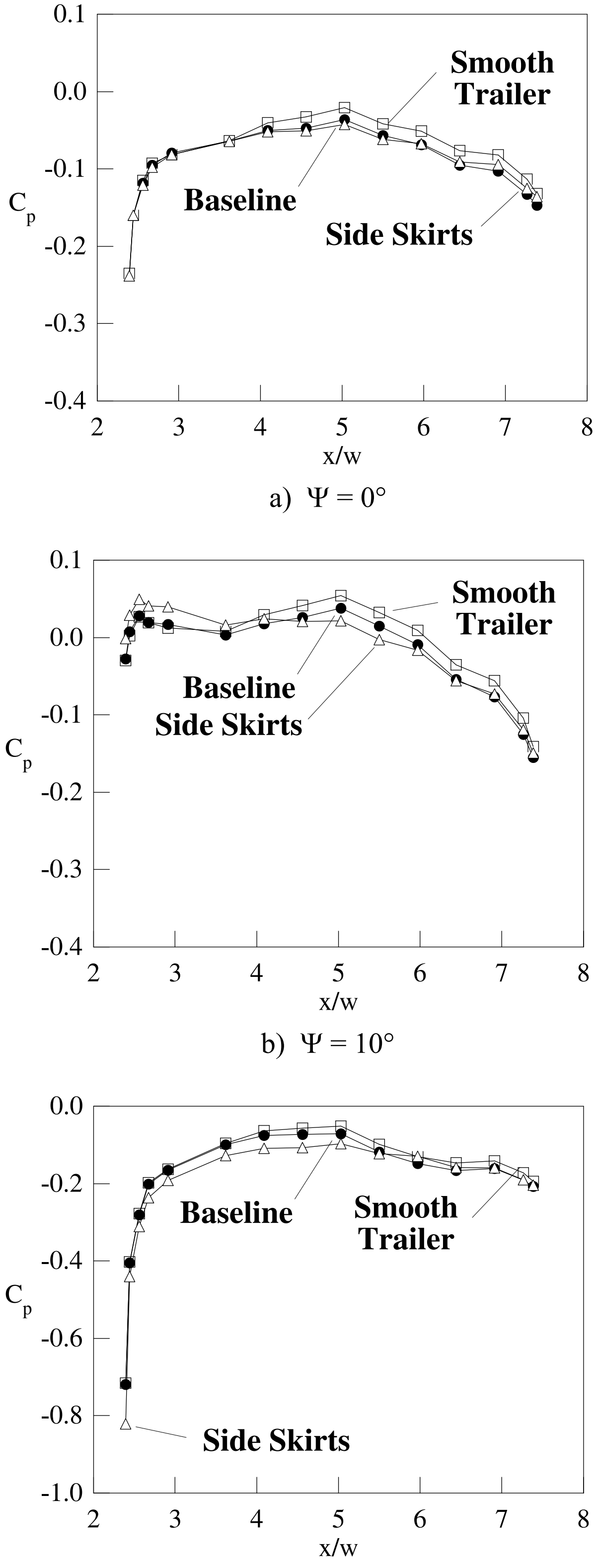

a) Ψ = 0°

b) Ψ = 10°

c) Ψ = -10°

Figure 20. Effect of smooth trailer underbody and side skirts on trailer left-side centerline pressure coefficients

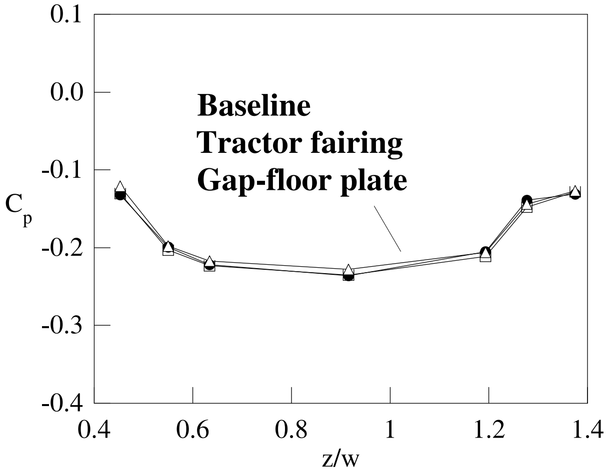

a) Ψ = 0°

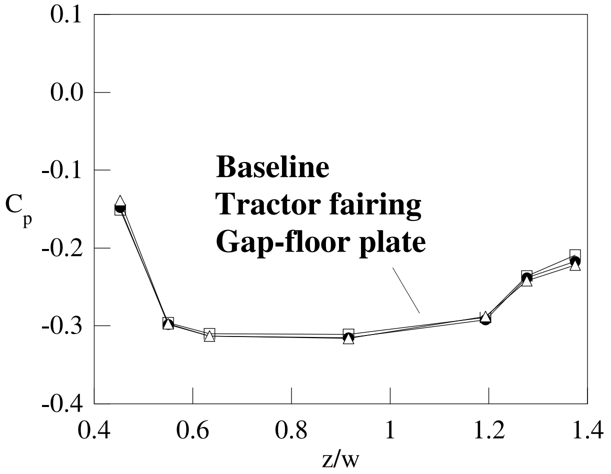

b) Ψ = 10°

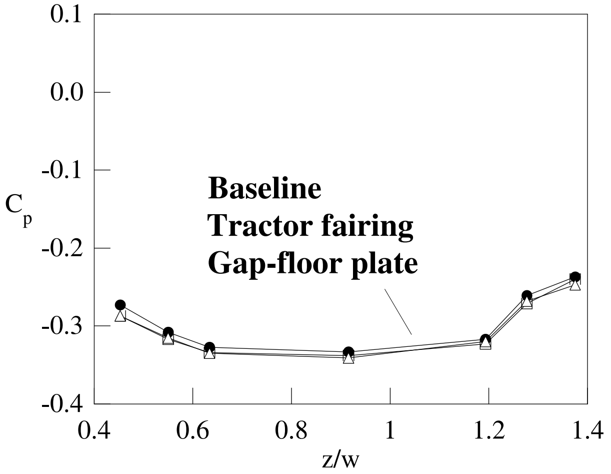

c) Ψ = -10°

Figure 21. Effect of full trailer fairing and gap-floor plate on trailer-base centerline pressure coefficients

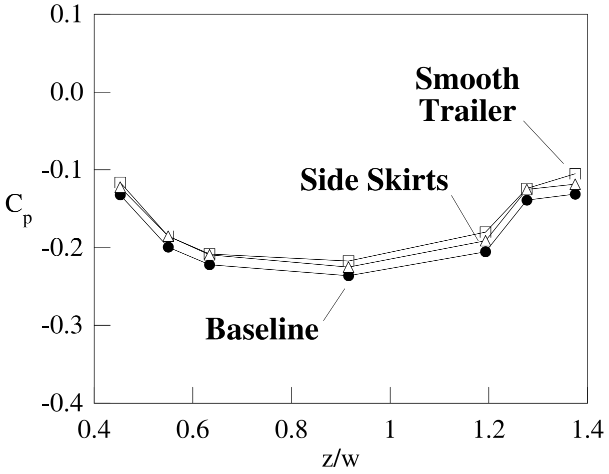

a) Ψ = 0°

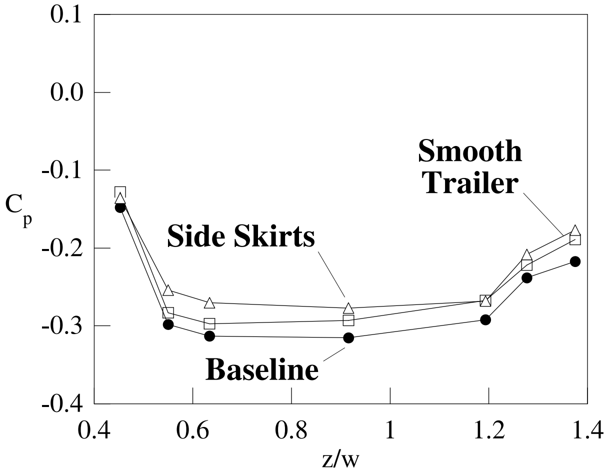

b) Ψ = 10°

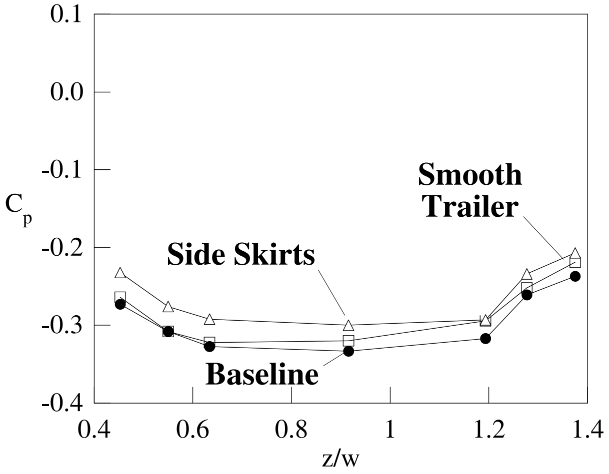

c) Ψ = -10°

Figure 22. Effect of smooth trailer underbody and side skirts on trailer-base centerline pressure coefficients

I.E. Commercial CFD Code Validation for External Aerodynamics Simulations of Realistic Heavy-Vehicle Configurations

W. David Pointer, J. Chang, S. Singh, E. Dringenberg
Argonne National Laboratory
9700 S Cass Avenue, NE-208, Argonne, IL 60439
(630) 252-1052, fax: (630) 252-4500, e-mail: dpointer@anl.gov

Technology Development Manager: Lee Slezak
(202) 586-2335, e-mail: Lee.Slezak@EE.DOE.GOV

Technical Program Manager: Jules Routbort
(630) 252-5065, e-mail: routbort@anl.gov

Contractor: Argonne National Laboratory
Contract No.: W-31-109-ENG-38

Objective

- Evaluate capabilities in standard commercial computational fluid dynamics (CFD) software for the prediction of aerodynamic characteristics of a conventional U.S. Class 8 tractor-trailer truck.
- Develop practices and procedures for the application of commercial CFD software in the design process of Class 8 vehicles.
- Apply practices and procedures to evaluation of geometric modifications and drag-reducing devices to assess potential energy savings

Approach

- Develop computational models of simplified vehicles based on the Generic Convention Model geometry used in experiments completed in the NASA Ames Laboratory's 7 ft. by 10 ft. wind tunnel.
- Compare the predictions of the computational models with experimental measurements of vehicle aerodynamic drag force and pressure field distributions.

Accomplishments

- Experimental measurements and computational predictions of the vehicle drag coefficient agree within less than 1 percent in the best case simulations at zero yaw and within less than 5% at higher yaw angles. Experimental measurements and computational predictions of the pressure distribution along the surface of the vehicle agree well everywhere except the rear faces of the cab and the trailer.
- Confirmed applicability of the practices and procedures to the evaluation of devices which modify the wake flow at the rear of the trailer.
- Confirmed difficulty in applying this methodology to configurations which result in a significant increase in the relative importance of the base drag acting on the rear faces of the trailer.
- Established that small changes in radiator width or height do not significantly impact the drag coefficient if all other dimensions are held constant.
- Established that the flow into the underhood through the radiator does not significantly impact the drag losses.

Future Direction

- Work with team members in the development of an integrated approach to development of the next generation heavy vehicle transportation

---

Abstract

With rising oil prices, the issue of energy economy in transportation is getting much attention. At the same time, new emissions standards for tractor-trailer vehicles introduce additional challenges for the manufacturers to achieve improvements in vehicle fuel economy. As part of the U.S. Department of Energy Office of FreedomCAR and Vehicle Technologies' Heavy Vehicle Aerodynamic Drag Consortium, Argonne National Laboratory is applying commercial computational fluid dynamics (CFD) software to facilitate energy efficiency improvements through improved aerodynamic design of tractor-trailer vehicles. Early investigations sought to establish the validity of this approach by evaluating the sensitivity of the predictions of drag coefficients and surface pressure distributions for the standard configuration of the GCM to the size and structure of the computational mesh and the selection of turbulence model. Current assessments are focusing on the ability to predict the change in the drag coefficient when drag reduction devices are employed and the application of the code to design studies.

Modeling Strategy

This program has provided guidance for the use of commercial CFD software in heavy vehicle design, including the expected impact of grid resolution and structure on prediction accuracy, the impact of the RANS turbulence model formulation selected, the impact of considering only half of a vehicle to speed up initial simulations. The experience developed by this program provides generic advice for the application of a commercial CFD software package to the prediction of heavy vehicle aerodynamic drag coefficients. Since this market is currently dominated by finite volume formulations, the guidelines will focus upon software using this methodology.

Selection of Commercial CFD Software

All simulations completed as part of this program have used the commercial CFD code Star-CD.[1] The Star-CD software was selected for this purpose largely the code offers a great deal of the flexibility in computational mesh development with the ability to utilize polyhedral "cut" cells and recognize both integral and arbitrary interfaces between regions of the computational domain. Furthermore, user subroutines allow the user to implement significant modifications to most features of the code if such modifications are needed. It is anticipated that the applicability of the general observations on modeling strategy extends to other commercial CFD codes using the finite volume methodology.

Selection of Tractor Trailer Geometry

The Generic Conventional Model[1] (GCM), developed by NASA Ames Research Center for scaled wind tunnel testing, is a generalized representation of a conventional U.S. tractor-trailer truck, as shown in Figure 1. The 1/8th scale model is approximately 2.5 m long by 0.3 m wide by 0.5 m high. The studies contained herein consider experiments that were completed in the NASA Ames 7ft. by 10 ft. wind tunnel. Instrumentation included a force balance, 476 steady pressure transducers, 14 dynamic pressure transducers, and three-dimensional Particle Image Velocimetry (PIV). Data was collected at various Reynolds number values and yaw angles. The initial studies presented herein consider only the case using the standard configuration of the GCM with a vehicle-width based Reynolds number of Re = 1.15 million. Measurements using alternate configurations with add on devices will be used to evaluate whether computational modeling guidelines developed based upon these studies are sufficiently general to be applied in the evaluation of the aerodynamic characteristics of other vehicles under different operating conditions.

Figure 1. Generic Conventional Model (GCM)

Computational Model

The computational model employed in these studies was developed using the ES-Aero tool for aerodynamic drag simulation that is available as part of the Star-CD software package. The surface of the standard configuration GCM is defined using approximately 500,000 triangular surface elements based upon CAD data representations taken from optical scans of the actual model. A computational domain, which as external dimensions that are based on the cross-sectional dimensions of the wind tunnel, is developed based upon this surface definition using a semi-automated process that begins by creating a hexahedral mesh that is successively refined in smaller zones around vehicle, with integral cell coupling employed at the interfaces between zones. The dimensions of hexahedral elements that make up the zone immediately surrounding the vehicle are specified by user as the near vehicle cell size. The mesh elements near the vehicle surface are then further refined based upon local surface features identified by the user or selected automatically based on curvature or gap width. The user specifies a minimum allowable cell size that limits the refinement of the mesh in this step.

Using this locally refined hexahedral mesh, the original surface is “wrapped” by projecting the hexahedral mesh onto the original surface. The “wrapped” surface definition is then volumetrically expanded to create a subsurface which is used to cut away the portions of the locally-refined hexahedral mesh that fall inside the vehicle. A brick and prism cell extrusion layer is then created to fill the gap between the sub-surface and the “wrapped” surface. In this way, the polyhedral cut cells are removed some distance from the surface, and a consistent y^+ value between approximately 20 and 200, can be maintained regardless of grid resolution, insuring that the computational meshes are suitable for the turbulence models used in these studies. A final step further refines the wake region and the underbody region in order to better capture a steady state representation of important flow features. An example of the mesh construction of the computational domain used in the GCM simulations is shown in Figure 2.

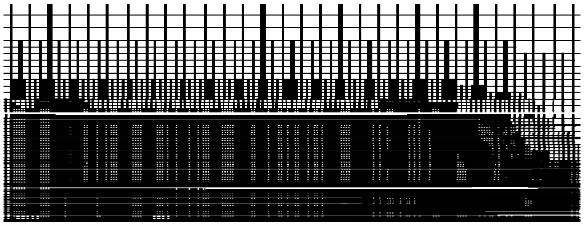

Figure 2. Example of computational mesh structure used in the simulation of the aerodynamic characteristics of the Generic Conventional Model (GCM)

Using locally-refined, face-coupled computational domains with substantial numbers of non-hexahedral cells makes the standard practice of evaluating grid convergence by uniformly refining the entire mesh in all directions intractable. In the computational meshes used in these studies, two separate parameters determine the size of the mesh. Mesh sensitivity analyses included in these studies examine the effects of changes in the near-vehicle cell size and minimum cell size parameters on the prediction of the drag coefficient. However, this is not equivalent to the traditional grid convergence study because the grid is not uniformly refined in all directions throughout the domain and the vehicle surface definition cannot be exactly maintained for all models since the final surface definition is dependent upon the local refinement of the computational mesh.

Computational Requirements

Models are constructed using a 64-bit 2.8GHz Xeon Linux workstation with 8 GB of RAM. The construction of the most coarsely-meshed models included in this study, from IGS formatted CAD data to final model, requires approximately 3 hours and peak memory usage is approximately 1.0 GB. The most finely-meshed models requires approximately 12 hours and the peak memory usage is approximately 5 GB. Since the automated mesh wizard included with the software package is used, little intervention is required by the user during this process. As with any software, initial models created by a novice user will likely require a larger initial time investment. All models employed in these studies are used as supplied from the automated tool with no manual repair or modification.

The Nuclear Engineering Division maintains a Beowulf cluster for performing engineering mechanics, fluid dynamics, and reactor engineering analyses. The cluster consists of three front-end (i.e., control) nodes and seventy-five compute nodes. One of the front-end nodes is a 32-bit servers contains dual Athlon MP 2.2GHz processors and 4 GB of memory. The two remaining front ends are 64-bit front-end servers: one with dual Itanium2 processors and 24 Gigabytes of memory, the other with dual Xeon processors and 8 gigabytes of memory. The cluster's file server provides nearly 1 Terabyte of home file system space. Each of the 75 compute nodes has a 3.2 GHz Pentium IV processor with 2 GB of memory. All of the machines in the cluster are interconnected via Gigabit Ethernet. All of the systems run RedHat Enterprise Linux.

Brief Summary of Prior Results

Initial studies focused on establishing the validity of commercial CFD software for the prediction of the aerodynamic characteristics of a tractor-trailer vehicle. This previous effort included a mesh sensitivity study considering the effect of near vehicle cell size and minimum cell size on the accuracy of aerodynamic characteristics as well as the impact of turbulence model selection and the use of half vehicle versus full vehicle models. Additional studies have examined the ability to predict the impact of cross-winds on aerodynamic performance.

Computational Mesh Sensitivity

A series of studies have been completed to evaluate sensitivity of the predictive accuracy to selection of the two primary characteristic dimensions of the generated computational mesh: the near vehicle cell size and the minimum cell size. The near-vehicle cell size defines the dimensions of the cells in the region of tunnel-aligned hexahedral brick cells closest to the model surface. The minimum cell size is the limit applied to the automatic refinement of the region immediately adjacent to the vehicle surface and defines the smallest cell that can be used to capture local surface characteristics.

To assess the impact of the near-vehicle cell size, a series of parametric simulations was completed specifying near-vehicle cell sizes between 6mm and 10 mm for the 1/8th scale GCM. Results, summarized in table 1, indicate that the drag coefficient can be predicted with acceptable accuracy using a near vehicle cell size of 6 mm. Furthermore, coarser meshes using near vehicle cell sizes as large as 12 mm can likely be used for initial coarse evaluations and trending.

Based on these results, an additional study was completed to evaluate the impact of the minimum cell size. The default minimum cell size in the previous study was 1/8 the near-vehicle cell size. In this study the minimum cell size was reduced to determine whether the same computational accuracy observed in the 6mm case could be achieved using a smaller number of computational cells. When the minimum cell size in the 8 mm case was reduced from 1 mm to 0.5 mm, the accuracy of the drag coefficient prediction improved from 4.2 percent error to 1.0 percent error. This level accuracy was achieved using 30% fewer computational cells than in the most refined model in the near-vehicle cell size study.

Turbulence Model Effects

In all simulations completed for the computational mesh sensitivity studies, the high Reynolds number k-ε turbulence model was used in conjunction with a standard logarithmic wall function for the prediction of turbulent kinetic energy and eddy diffusivity. While the high Reynolds number k- ε turbulence model is a robust general purpose turbulence model, the strong adverse pressure gradients and large flow recirculation regions associated with the GCM geometry may limit the applicability of steady state RANS modeling strategies. Using the computational mesh with a near vehicle cell size of 8 mm and a near wall cell size limit of 0.5 mm, simulations of the aerodynamic characteristics of the GCM model were repeated using five steady RANS turbulence models and their associated wall functions: 1) the standard high-Reynolds number k-ε model with logarithmic wall function, 2) the Menter k-ω SST model, 3) the renormalization group (RNG) formulation of the k-ε model, 4) the Chen formulation of the k-ε model, and 5) the quadratic formulation of the k-ε model. Drag coefficients predicted using each of the selected steady-RANS turbulence models are shown in Table 2. Comparisons of the predicted pressure coefficient distributions when using the selected turbulence models are shown in Figure 3. The differences in the predicted drag coefficient are largely a result of localized discrepancies in the surface pressure coefficient predictions in the regions of separated flow, with the largest discrepancies appearing in the underbody region just behind the tractor.

Yaw Angle Effects

The effects of cross-winds on the vehicle performance are evaluated by rotating the model in the wind tunnel to introduce an effective yaw angle between the wind direction and the vehicle direction. In the wind tunnel experiments, yaw angles between 14 degrees and -14 degrees were considered. In the experiments, a low drag state is observed at low yaw angles. For yaw angles greater than 3 degrees a higher drag state was observed, where large flow separation zones begin to form along the leeward side of both the tractor and trailer, introducing significant turbulent instability into the flow field. The instability is further exacerbated by the formation of a highly turbulent jet through the gap between the tractor and trailer which washes over the logical separation points on the leeward side of the trailer, extending the separation zone.

Using this data for comparison, a series of simulations were completed to evaluate the effects of the computational mesh parameters on predictive accuracy at yaw angles greater than zero. Results of the mesh sensitivity study are summarized in Figure 4. These studies show that the transition between the high and low drag state can be accurately captured using the methodology developed for the GCM at zero yaw angle. Furthermore, the studies demonstrate that the aerodynamic coefficients of the vehicle can be predicted within a few percent error when sufficient resolution is used near the vehicle surface. Additional simulations included in this study indicate that little difference in drag coefficient predictions is observed for cases using the 8mm near vehicle cell size when the minimum cell size is further reduced from 0.5 mm to 0.25 mm.

Table 1. Effects of Near-Vehicle Cell Size Parameter on Accuracy of Drag Coefficient Prediction

Near-Vehicle Cell Size (mm)	Predicted Drag Coefficient	Error in Drag Coefficient
experiment	0.398	
16	0.449	12.0
12	0.441	10.3
10	0.418	4.9
8	0.415	4.2
6	0.405	1.7

Table 2. Results of evaluation of two-equation turbulence models for prediction of drag coefficients for the GCM geometry

Turbulence Model	Predicted Drag Coefficient	Percent Error in Prediction
Experiment	0.398	--
High-Reynolds Number k-epsilon Model	0.402	1.0
Menter k-ω SST model	0.401	0.8
RNG model	0.389	2.3
Chen's model	0.3919	1.61
Quadratic model	0.3815	4.32

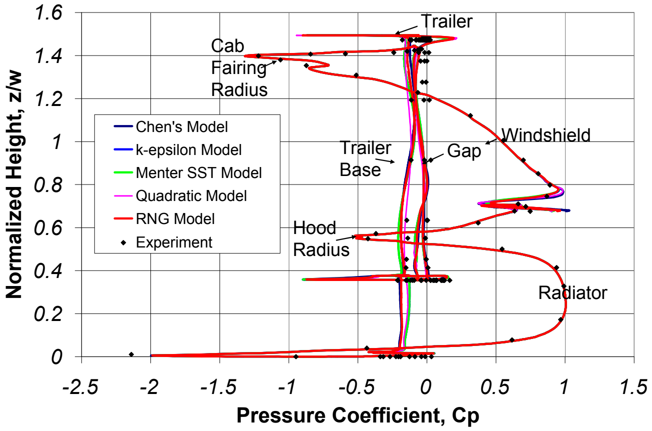

Figure 3. Comparison of predicted pressure coefficient distributions on the vehicle surface with experimental data for selected turbulence models

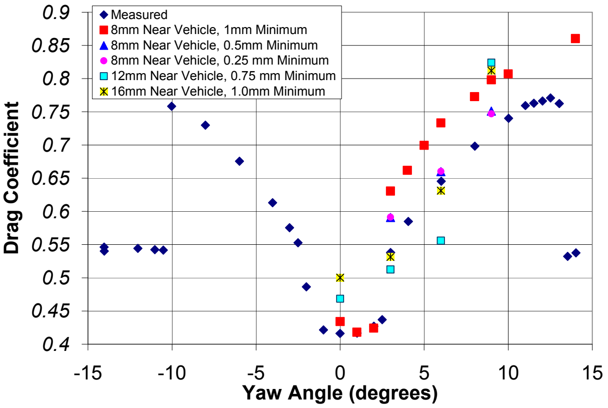

Figure 4. Comparison of drag coefficient predictions as a function of yaw angle and mesh size parameters

Prediction of Changes in Aerodynamic Characteristics

Building on the foundation of prior studies, the practices and procedures developed through the analyses of baseline GCM geometry have been applied to studies for a number of alternative configurations. These studies include the evaluation of add on devices, the assessment of impacts of radiator size and an investigation of the impacts of flow through the grille on drag coefficients.

"GTS" Configuration of the GCM

As an initial application of the modeling strategy to alternative configurations, simulations were completed for the so-called "GTS" configuration of the GCM geometry, shown in Figure 5. This configuration includes a full fairing between the tractor and trailer and a belly box under the trailer. While this configuration is not practical for deployment, it does provide a very low drag test of the predictive capability of the CFD models. Using the baseline meshing strategy with a near vehicle cell size of 8 mm and a minimum cell size of 0.5 mm, simulations were completed using 4 different steady RANS turbulence models: the standard high-Reynolds number k-epsilon model, the Chen model, the RNG model, and the Quadratic model. Results are summarized in Figure 6. The error between predicted and measured coefficients ranges from approximately 10 to 30 percent. Additional studies examining mesh refinement sensitivity show little change in predictions with additional refinement near the vehicle surface or in the model as a whole. Examination of detailed flow and surface pressure results indicate that the larger error may be a consequence of the extremely low drag coefficient and the increasing importance of the base drag at the rear of the trailer. Prior studies have shown that the largest error in computational predictions when using this approach occurs at base of the trailer. For very low drag coefficient configurations, more advanced turbulence modeling strategies should be investigated.

Figure 5. "GTS" configuration of the GCM, with full gap fairing and trailer belly box

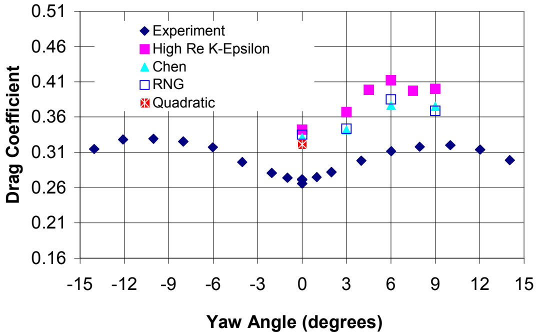

Figure 6. Drag coefficient predictions for the "GTS" configuration of the GCM, as a function of yaw angle and turbulence model selection

Ogive Boattail

Working with a commercial partner, Aerovolutions Inc., a CAD geometry based on the GCM with a commercially-marketed inflatable ogive boat tail device attached to the trailer was developed, as shown in Figure 7. Simulations using this geometry were completed using three different computational mesh configurations. Results are summarized in Table 3. When compared with results for the standard configuration of the GCM using comparable mesh densities, a drag coefficient reduction of 7% is expected, which would correspond to a fuel savings of 3.5%. These predictions are consistent with claims based on wind tunnel and road tests by Aerovolution.

Figure 7. Modified GCM geometry with ogive boat tail

Table 3. Summary of drag coefficient predictions for the GCM geometry with ogive boat tail

Near Vehicle Cell Size	Near Wall Cell Size	Drag Coefficient
12 mm	2 mm	0.4179
8 mm	1 mm	0.4116
8 mm	0.5 mm	0.3975

The impact of the device on the wake behind the vehicle is quite dramatic, with the wake closing shortly behind the vehicle rather than many vehicle lengths downstream, as shown in the comparison between results with and without the device in Figure 8. While this effect should improve driving conditions a vehicle length downstream, as with most trailer boat tail devices, the more energetic turbulence in the reduced-length wake may negatively impact driving conditions for passenger cars near the rear of the vehicle.

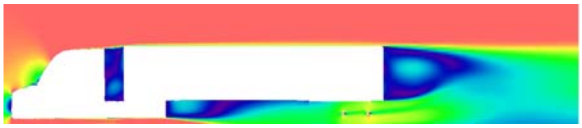

(a) Standard GCM

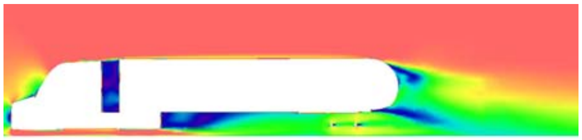

(b) GCM + Boat Tail

Figure 8. Comparison of velocity magnitude predictions for the standard GCM geometry and for the modified GCM geometry with ogive boat tail

Changes in Radiator/Grille Dimensions

To meet more restrictive EPA emissions requirements, manufacturers are likely to substantially redesign engine cooling packages to reject more of the engine heat that is currently carried away by the exhaust. An increase in radiator size is likely to result. To quantify the potential impact of this change on drag related parasitic energy losses, a series of modified GCM geometries have been developed with modified radiator or grille dimensions. In these simulations, the grille is completely closed and flow through the engine compartment is neglected. However, the effect of flow through the radiator has been quantified in other studies to be discussed in the following section.

Four different parametric cases have been considered: a 10 percent increase in the height of the radiator, a 10 percent reduction in the height of the radiator, a 10 percent increase in the width of the radiator and 10 percent reduction in the width of the radiator. In all cases, the hood angles are adjusted to be compatible with the modified grille dimensions and all other dimensions are maintained so that any observed change in performance can be directly attributed to the change in radiator size. All models use the baseline mesh parameters, with a near vehicle cell size of 8.0 mm and a minimum cell size of 0.5 mm. Results for the modified geometries at yaw angles of 0 and 6 degrees are summarized in Table 4. No significant change in drag coefficient is observed for any of the four cases. Review of detailed pressure and force distributions, such as those seen in Figure 9, confirms that high pressure areas on the grill are simply relocated to or from the windshield or the sides and top of the hood.

Table 4. Impact of changes in radiator/grille dimensions on drag coefficient

Configuration	Drag @ 0° Yaw	Drag @ 6° Yaw
Nominal	0.4061	0.7861
Height + 10 %	0.4041	0.8208
Height – 10 %	0.4022	0.8105
Width + 10 %	0.4097	0.7423
Width – 10 %	0.4097	0.7392

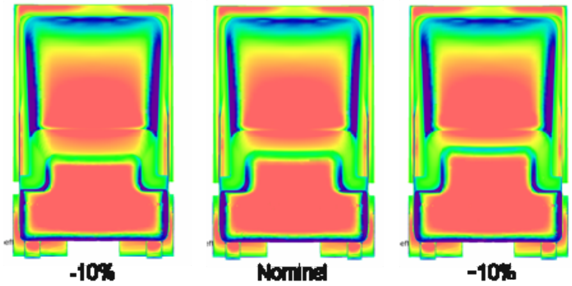

Figure 9. Response of surface pressure distribution to changes in radiator height

Effects of Flow through Radiator/Grille

In all prior simulations, the effect of the flow of air through the grille and radiator has been neglected on the assumption the radiator is so dense that it essentially appears as a solid surface to the impinging flow. To evaluate the effect of the underhood flow, a modified GCM geometry was developed with an open grille, as shown in Figure 10. An additional outlet boundary condition was placed at the back of the open space behind the grille, and the radiator was represented by a porous baffle between the grille and the outlet. The radiator was assumed to have a porosity of 33% and the outlet condition was specified based on the ratio of the areas of the new outlet to the primary outlet.

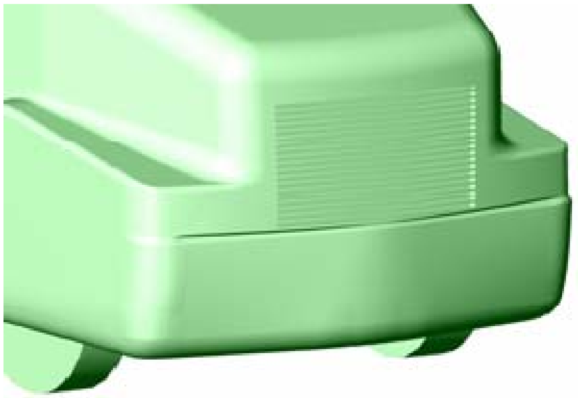

Figure 10. Modified GCM geometry with open grille and flow-through radiator

Simulations of the modified geometry at zero degrees yaw were completed using a computational mesh based on the baseline mesh parameters, so that the near vehicle cell size was 8 mm and the minimum cell size was 0.5 mm. The standard high-Reynolds number k-epsilon model was specified. The predicted drag coefficient for this case was 0.4115, which is a 1.2 percent increase over the standard configuration when compared to simulations using comparable computational mesh density. Since this value is within the anticipated error of the calculation, the change in configuration does not result in a statistically significant change in aerodynamic performance.

Conclusions

The studies described herein provide a demonstration of the applicability of the experience developed in the analysis of the standard configuration of the Generic Conventional Model. The modeling practices and procedures developed in prior efforts have been applied directly to the assessment of new configurations including a variety of geometric modifications and add-on devices. Application to the low-drag "GTS" configuration of the GCM has confirmed that the error in predicted drag coefficients increases as the relative contribution of the base drag resulting from the vehicle wake to the total drag increases and it is recommended that more advanced turbulence modeling strategies be applied under those circumstances. Application to a commercially-developed boat tail device has confirmed that this restriction does not apply to geometries where the relative contribution of the base drag to the total drag is reduced by modifying the geometry in that region. Application to a modified GCM geometry with an open grille and radiator has confirmed that the underbody flow, while important for underhood cooling, has little impact on the drag coefficient of the vehicle.

Furthermore, the evaluation of the impact of small changes in radiator or grille dimensions has revealed that the total drag is not particularly sensitive to those changes. This observation leads to two significant conclusions. First, a small increase in radiator size to accommodate heat rejection needs related to new emissions restrictions may be tolerated without significant increases in drag losses. Second, efforts to reduce drag on the tractor requires that the design of the entire tractor be treated in an integrated fashion. Simply reducing the size of the grille will not provide the desired result, but the additional contouring of the vehicle as a whole which may be enabled by the smaller radiator could have a more significant effect.

Acknowledgments

This work has been completed under the auspices of the U.S. Department of Energy by the University of Chicago as Operator of Argonne National Laboratory ("Argonne") under Contract No. W-31-109-ENG-38. The authors would like to acknowledge the generous support of DOE program manager Lee Slezak and the entire Heavy Vehicle Aerodynamics Team.

References

1. Star-CD, CD-adapco group, Melville, NY.

2. Satran, D., “An Experimental Study of the Generic Conventional Model (GCM) in the NASA Ames 7-by-10-Foot Wind Tunnel,” United Engineering Foundation Conference on the Aerodynamics of Heavy Vehicles: Trucks, Buses, and Trains, United Engineering Foundation, New York, 2002.

3. W. David Pointer, Tanju Sofu, and David Weber, “Development of Guidelines for the Use of Commercial CFD in Tractor-Trailer Aerodynamic Design,” 2005 SAE Commercial Vehicle Engineering Conference, Chicago, IL, November 2005. (SAE Paper No. 05CV-120).

4. W. David Pointer, “Evaluation of Commercial CFD Code Capabilities for Prediction of Heavy Vehicle Drag Coefficients,” *Proceedings of the 2004 AIAA Fluid Dynamics Conference and Exhibition*, Portland, Oregon, June 2004. (AIAA-2004-2254)

I.F. Test, Evaluation, and Demonstration of Practical Devices/Systems to Reduce Aerodynamic Drag of Tractor/Semitrailer Combination-Unit Trucks

Principal Investigator: Robert M. Clarke
Truck Manufacturers Association
1225 New York Avenue, NW, Suite 300
Washington, DC 20005
(202) 638-7825, fax: (202) 737-3742, e-mail: robertmclarke@truckmfgs.org

DOE Project Officer: Keith Carrington
National Energy Technology Laboratory
Morgantown, WV 26505
(304) 285-4456, e-mail: keith.carrington@netl.doe.gov

DOE Technology Development Area Specialist: Lee A. Slezak
Office of FreedomCAR and Vehicle Technologies
U.S. Department of Energy
1000 Independence Ave., S.W.
Washington, D.C.
(202) 586-2335, fax: (202) 586-2476, e-mail: lee.slezak@ee.doe.gov

Field Technical Manager: Jules L. Routbort
(630) 252-5065, fax: (630) 252-4289, e-mail: jules.routbort@anl.gov

Participants
Scott Smith, Karla Younessi, Freightliner LLC
Ronald Schoon, International Truck and Engine Corporation
Justin Clark, Conal Deedy, Volvo Technology of America (Volvo Trucks, Mack Trucks)

Contractor: Truck Manufacturers Association, 1225 New York Avenue, NW, Suite 300,
Washington, DC 20005
Contract No.: DE-FC26-04NT42117

Objective

- To reduce aerodynamic drag of tractor/semi trailer combination trucks through development, test, and demonstration of aerodynamic aids and systems of aerodynamic aids from the viewpoint of manufacturability and practicality for over-the-road use.

Approach

- Pursue complimentary research paths for aerodynamic devices and systems.
  - Research areas include the effect of mirror design on truck aerodynamics; the effect of aerodynamic treatments of tractor trailer gap, trailer side, and trailer wake on truck aerodynamics; the effect of trailer aerodynamics, trailer gap enclosure, and trailer gap flow control on truck aerodynamics; and the effect of vehicle underside design and management of tractor-trailer air flows on truck aerodynamics.

- Phase I: Conduct preliminary testing and analysis on a wide range of candidate devices and systems to determine effectiveness of such devices and establish promising sets of devices for further research. This testing will involve both full-size vehicles and scale models in wind tunnels and real-world driving tests. Computational fluid dynamics will also be used to establish effects of aerodynamic devices on truck aerodynamics.
- Phase II: Construct prototype devices for installation on full-size Class 8 trucks for testing in wind tunnels or in real-world environments (potentially in fleet applications). This testing will quantify the optimal fuel economy benefits achievable through the use of these devices and systems in terms of a percentage improvement relative to a similar baseline truck and trailer.

Accomplishments

- Completed eleven different types of simulations of several commercial mirror configurations establishing the effect of rear-view mirror design options and the constraints on truck aerodynamics. The latest computational fluid dynamics (CFD) tools were used to correlate the wind tunnel tests performed on a full-scale class 8 tractor. Freightliner added testing of mirror “soiling” (water management) and found that a benefit of improving mirror drag is an improvement in safety during rainy driving conditions. As the air flow around the mirror becomes more efficient, fewer rainwater droplets become deposited on the mirror surface where they obscure the driver's view. As a result of the drag force measurements, it was found that there is a potential for a 2-3 percent drag reduction with well-designed mirrors. An added benefit to the trucking industry is that these research methods can be duplicated and utilized, not only for testing mirrors, but with testing of other devices currently in use or for potential use on a tractor. (Freightliner)
- Developed experimental aerodynamic trailer in conjunction with Great Dane and Wal-Mart. Through track testing (SAE Type II fuel economy test), demonstrated a 7 percent fuel economy improvement with this trailer. Designed a trailer forebody aerodynamic device that demonstrated a 2 percent fuel economy improvement in track testing (SAE Type II fuel economy test). Designed prototype variable-length side extenders to close the tractor-trailer gap, and demonstrated 1 percent fuel economy improvement in track testing (SAE Type II fuel economy test). (International)
- Completed tuning tests of individual aerodynamic devices (trailer gap enclosure, trailer boat tail, side strakes, side skirts, and vortex generators) to determine most promising devices. Completed SAE Type II fuel economy testing of various combinations of trailer gap enclosures, side skirts, and boat tails: fuel economy benefits of between 1 percent and 8 percent were demonstrated. (Mack)
- Completed SAE Type II fuel economy testing of combinations of add-on aerodynamic devices (smooth underbody device, trailer gap up-flow prevention device, optimized roof extension to shorten the trailer gap, and trailer bogie deflectors). Fuel economy benefits of between 1 percent and 2.3 percent were demonstrated in track testing. (Volvo)

Future Direction

- Current project (Phase I and Phase II work) has been nearly completed. A no-cost time extension through April 2007 was granted to ensure sufficient time for completion of final reporting. Because of favorable weather conditions, International conducted additional testing of its devices and systems late in 2006 and early in 2007, the results of which will be included in the final report.

Introduction

Class 8 heavy-duty trucks represent over three-quarters of the total diesel fuel use for trucks in the United States each year, transporting vital goods to destinations across the country. At highway speeds for these trucks, aerodynamic drag is a major part of total horsepower needs for driving the truck down the highway, and reductions in aerodynamic drag can yield measurable benefits in fuel economy with relatively inexpensive and simple devices. The goal of this project is to examine a number of aerodynamic drag devices and systems and determine their effectiveness in reducing aerodynamic drag of Class 8 tractor/semitrailer vehicles, thus contributing to DOE’s goal of reducing petroleum use for transportation.

Project Team

The project team represents virtually all of the key heavy truck manufacturers in the United States, along with the management and industry expertise of the Truck Manufacturers Association as the lead investigative organization. The Truck Manufacturers Association (TMA) is the national trade association representing the major North American manufacturers of Class 6-8 trucks (GVWRs over 19,500 lbs). Four major truck manufacturers are participating in this project with TMA: Freightliner, LLC; International Truck and Engine Corporation; Mack Trucks Inc.; and Volvo Trucks North America, Inc. Together, these manufacturers represent over three-quarters of total Class 8 truck sales in the United States. These four manufacturers pursued complementary research efforts in order to provide a wide range of potential aerodynamic improvements to on-highway trucks.

Project Structure and Roles

The project work has been separated into two phases to be conducted over a period of two years. In Phase I, initial screening of aerodynamic devices and systems was conducted to focus research and development attention on devices that offer the most potential. This screening was done through full-size vehicle testing, scale model testing, and computational fluid dynamics analysis. In Phase II, the most promising devices were installed on full-size trucks and their effect on fuel economy will be determined, either through on-road testing or full-size wind tunnel testing.

As noted above, the participating manufacturers conducted complementary research and development of aerodynamic aids. In particular, Freightliner is working on outside mirrors; International is looking at tractor trailer gap, trailer side, and trailer wake effects on truck aerodynamics; Mack is examining trailer aerodynamics, trailer gap enclosure, and trailer gap flow control; and Volvo is working on vehicle underside design and management of tractor-trailer air flows. All of the manufacturers are working with devices and systems that offer practical solutions to reduce aerodynamic drag, accounting for functionality, durability, cost effectiveness, reliability, and maintainability.
A layout of the project team members and their roles and responsibilities is illustrated in Figure 1.

Project Activities

Phase II activities of the four truck manufacturers are described in more detail below, organized by truck manufacturer.

Freightliner: The overall objectives of this work are to assess the fuel-efficiency performance benefit that might be achieved with advanced mirror technology relative to current baseline technologies; outline the appropriate design processes associated with effective aerodynamic mirror development to be shared throughout industry; and develop realistic technology that can be readily implemented in the near-term.

In Phase II, Freightliner studied the effects of differing mirror systems on the aerodynamic drag of the vehicle, both through Freightliner's wind tunnel and through computational fluid dynamics analysis. These tests were performed on a full-size Freightliner Century Class S/T conventional Class 8 sleeper cab truck with a raised sleeper roof, one of Freightliner's most advanced current production truck designs. All tests were done in Freightliner's company wind tunnel located in Portland, Oregon. This tunnel has the capability of accommodating a full-size Class 8 truck in its 12,000 square foot facility. The Freightliner Wind Tunnel features a unique and efficient design that differs from those of traditional automotive and aviation wind tunnels. Standard building materials were used in innovative ways to build the structure. The power section is revolutionary as well, using ten industrial blower fans; all synchronized by computer, in place of what would typically be one large custom-designed and built fan. The fans have a combined 2500 horsepower capability and process over 2.5 million cubic feet per minute (CFM) of air. This allows for test section wind speeds of over 65 mph.

Freightliner studied three types of mirror systems: the "Aero" mirror offered as standard equipment on the test truck; an aerodynamic mirror with a single mounting post (versus the double mounting post of the standard aero mirror); and a "West Coast" style mirror with a complex multi-strut mounting system.

In the wind tunnel, Freightliner determined aerodynamic drag force due to mirrors (as percent of total vehicle drag), flow visualization with smoke, and water management visualization. In the CFD world, information was collected on aerodynamic drag force due to mirrors (as percent of total vehicle drag), surface pressures, flowfield streamlines, and flowfield velocity magnitude.

Results of the analysis of various mirror configurations and their contribution to total vehicle drag appear in Figure 2. Note that the “Aero” mirror offers the best overall performance, and the single-post mirror offers the least favorable performance. The primary reasons for this are: a) The mounting structure for single post mirrors has a bigger cross section and causes a larger wake and b) The mirror housing is in the path of the A-pillar and cowl vortex. Comparing the Aero mirrors and the West Coast styled mirrors, the West Coast mirrors have a higher drag because: a) the complex multi-strut mounting system causes a combined larger wake and b) the sharp edges with rectangular face on the on the West Coast mirror housing increases drag.

Figure 3 illustrates another aspect of the mirrors and their effect on the vehicle flowfield. The figure shows the differing flow around the vehicle for two different mirror configurations. Note that these mirrors produce different wake structures as a result of their differing configurations, and also note that the effect of the mirror wake propagates to the trailer flow field, highlighting the wide ranging effect of mirrors on aerodynamics.

All of these results highlight the importance of integrating the mirrors into the vehicle flowfield, treating the mirror and vehicle as a system. Depending on yaw angle and design, mirrors can contribute up to 7 percent of total vehicle drag.

International: International focused its effort on trailer side, trailer wake, and tractor-trailer gap technologies for reducing aerodynamic drag. In Phase II, International planned to develop full-scale prototypes from each area of focus, producing “proof of concept” hardware suitable for on-road vehicle fuel economy testing. International planned to use SAE J1321 Type II fuel economy testing protocols to establish benefits of the hardware tested.

For the trailer side and trailer wake work, International determined in Phase I that trailer skirts and base plates were most beneficial in reducing aerodynamic drag. In Phase II, International worked to secure a partnership with a major trailer manufacturer to further develop these technologies, and was successful in working with Great Dane.

Great Dane and International worked with a major customer (Wal-Mart) to produce an experimental aerodynamic trailer based on the Phase I data. Several trailer designs were considered, and the final design chosen featured an aft taper, straight side skirts, a reduction of 12 inches in height versus a standard trailer, and a load floor lowered by 16 inches. This trailer is pictured in Figure 4.

The aft taper on this trailer is structural (versus the movable flexible base flaps more commonly demonstrated), Wal-Mart’s standard roll-up door opening was not reduced in size. The side skirts are equipped with a mechanism to lower them at 35 mph for maximum aerodynamic benefit, and to retract them upward below 35 mph to minimize the potential for damage when maneuvering. Because the trailer’s standard ride height is 12 inches lower than a standard trailer (representing an 8% reduction in frontal area), a maxi-lift suspension is employed to raise the trailer to a standard dock height when exchanging cargo. In initial tests of this trailer with a standard International over-the-road tractor, a fuel economy improvement of 6.8% was achieved. Additional tuning testing on this trailer was conducted in December 2006 and January 2007.

In addition to the experimental Great Dane trailer work, International also tested two other aerodynamic concepts on full-scale vehicles. The first of these was a trailer forebody device designed to be affixed to the front of a trailer: it has no moving parts, accommodates the trailer swing clearance, and was estimated to have a 3-4 percent drag reduction opportunity based on Phase I testing. The second device was a set of variable length side extenders, which closes the gap between the tractor and trailer. The side extenders designed here had both fixed and movable sections: the movable section deploys at higher vehicle speeds to close the gap between the tractor and trailer, and stows at lower speeds to account for the trailer swing clearance. Even in the fully-deployed position, a gap of 4 to 6 inches between the extender and the trailer is required to account for relative movement of the tractor and trailer in highway travel. These extenders were forecast to have a 3 percent drag reduction opportunity in Phase I testing.

The trailer forebody device is shown in Figure 5. The device, which is the subject of a current patent application by International, provided a 2% fuel economy improvement in on-road vehicle testing (SAE Type II tests). This device was tested by itself in this work: it was not tested in combination with other devices to determine potential synergistic effects.

The variable-length side extenders are shown in Figure 6. These side extenders are envisioned to operate in a "hands-free" automatic mode with an actuation system that is the subject of a patent application. Because of resource constraints, the actuation system was not built, but the extenders themselves were tested and achieved a 1% fuel economy improvement in SAE Type II testing. Again, these side extenders were tested in isolation, separate from other aerodynamic devices.

Mack: In Phase II, Mack pursued practical analysis and testing of several devices (and combinations of devices) to improve the aerodynamics of the tractor-trailer combination truck, with a focus on the tractor-trailer gap and trailer aerodynamics. Testing for these devices took place using the current Mack Vision CX Class 8 tractor and a standard van trailer provided by Great Dane.

Prior to committing resources to full SAE Type II fuel economy testing, Mack conducted a series of tuning tests on the devices using a portable data logger to determine fuel usage from the vehicle ECU. The tuning tests were run on a public highway route in Greensboro, North Carolina. The purpose of these tuning tests was to gauge relative fuel economy improvements for these devices and to prioritize the devices for SAE Type II testing based on these fuel economy improvements. The final set of aerodynamic devices selected for SAE Type II testing included a trailer gap enclosure (side enclosure) designed by Mack, trailer side skirts provided by Freight Wing, and a boat tail provided by Clarkson University and Composite Factory Inc. in both 2 foot and 4 foot lengths.

Mack conducted its SAE Type II fuel economy testing at the Transportation Research Center test track in East Liberty, Ohio. The testing included the following combinations of the side enclosure, the side skirts, and the boat tail (2 foot and 4 foot).

1. Side enclosure only.
2. Side enclosure and side skirts.
3. Side enclosure and 4 foot boat tail.
4. Side enclosure, side skirt and 2 foot boat tail.
5. Side enclosure, side skirt, and 4 foot boat tail.

Figure 7 is a photo of the test truck and trailer equipped with the side enclosure, trailer side skirts, and boat tail. Figure 8 summarizes the results from the SAE Type II testing for the five technology combinations. The most effective combination was the combination of the side enclosure, side skirt, and four-foot boat tail, which achieved a fuel economy improvement of just over 8 percent. Shortening the boat tail by two feet to make the boat tail more practical still provided good results in combination with the side enclosure and side skirts, achieving 7.75 percent fuel economy improvement. Combinations of the side enclosure and either the side skirts or boat tail achieved fuel economy improvements of about 4-5 percent.

Mack examined the trailer gap enclosure (side enclosure) as part of this project, studying it both through on-road testing and CFD analysis. Mack determined that this device alone can achieve a 1% fuel economy improvement, and could be offered as OEM equipment on tractors. An automatic stow and deploy mechanism is needed, but is not at a development phase to be offered as production equipment at this time.

Volvo: Volvo pursued practical analysis and testing of practical devices to address the tractor and trailer underside aerodynamics and the tractor-trailer gap aerodynamics. Testing for this phase used several current-model Volvo VN series Class 8 trucks with both partial aerodynamic packages (no fairings beneath the cab to cover the fuel tanks, battery boxes, and so forth) and full aerodynamic packages (all OEM fairings in place).

Volvo focused its Phase II efforts on devices that could be simple add-ons to existing vehicles, including trailer gap devices (side deflectors), adjustable roof extenders, smooth tractor underside devices, deck closures, and trailer bogie deflectors. Trailer gap devices are simple and inexpensive yet effective, and adjustable roof extenders adapt to various trailer gap conditions. It is potentially easy to integrate a smooth underside concept, and a deck closure (behind the cab and between the tractor and trailer) can be provided with little effort. Bogie deflectors provide a simple alternative to full trailer skirts (though they are probably less effective than full skirts). Photos of the smooth tractor underside device, the bogie deflector, and the deck enclosure are shown in Figure 9.

In Phase II, Volvo performed tuning tests on these devices to obtain relative indicators of concept effectiveness. These tuning tests were performed on public roads, using fuel usage data from the engine ECU. Once tuning tests were complete, Volvo tested combinations of these devices at the Transportation Research Center test track in East Liberty, Ohio (a photo of the test truck with several aerodynamic devices is shown in Figure 10). Several combinations of devices were tested to determine fuel economy effects, as listed in Figure 11. The four major configurations included the total combination with all devices, a combination excluding the bogie deflector, a combination excluding the trailer gap devices and bogie deflector, and a combination excluding the smooth underside and bogie deflector.

As Figure 11 shows, Volvo demonstrated a 2.3 percent fuel savings by introducing a smooth underbody panel concept; influencing the interaction between the underside and trailer gap flows; shortening the effective trailer gap with add-on devices; and adding a unique trailer bogie deflector. Volvo measured an incremental 1.0 percent fuel savings by introducing a unique trailer bogie deflector. They measured a 1.0 percent fuel savings by introducing the underside and deck closure concepts, and a 1.0 percent fuel savings by introducing the trailer gap and deck closure concepts. Finally, Volvo measured a 1.3 percent fuel savings by introducing the underside, trailer gap and deck closure concepts.

End of Project Display/Demonstration: The demonstration was held on November 14, 2006 outside the DOE Forrestal Building with the display of the trucks and trailers used in the Phase I and II research for the benefit of DOE and other agency management, as well as for DOE staff and the general public. Several dignitaries were in attendance to make remarks about the importance of the aerodynamic project and its results to the attendees and press representatives at the even. Speaking attendees included Robert Clarke (President, Truck Manufacturers Association), Pat Charbonneau (Vice President of Government Relations for International Truck and Engine Corporation), David Rodgers (DAS for Technology Development for DOE EERE), and Congressman David Hobson from Ohio. The OEMs participating in the event developed press releases within their own public relations organizations describing their achievements, and the event received coverage from Transport Topics and other trade press. The photos in Figure 12 illustrate the trucks and technologies that were on display at the event.

Summary

The four truck manufacturers performed testing and analysis on a number of areas of the tractor-semitrailer combination with an eye toward aerodynamic improvements. Technologies were identified for the tractor and trailer that could provide combined fuel economy benefits of 1 percent to 8 percent.

Conclusions

Freightliner: Several mirror design parameters (frontal area, shape, alignment, and placement in the flowfield) are important. For instance, mirror housing should be curved and placed appropriately with respect to the A-pillar and cowl vortex. Mirror mounting structure should have a minimal number of struts, since together they form a complex system with a larger wake. Finally, the mirrors and cab should be designed as one integrated system. With well-designed mirrors, there is the potential to reduce aerodynamic drag by 2 to 3 percent, and on up to 6 percent if mirrors were eliminated altogether. CFD simulations and wind tunnel testing are complementary tools that should be used together to develop vehicles and accessories. These tools provide repeatable results with defined parameters that avoid the differing environmental impacts with on-the-road vehicles in a field test.

International: An experimental trailer design incorporating advanced aerodynamic features, developed in conjunction with a trailer manufacturer and a major customer, achieved on-road fuel economy improvements of 7 percent when connected to a standard International Class 8 tractor. A trailer forebody device designed by International can achieve a 2 percent fuel economy improvement, while movable side extenders to close the tractor-trailer gap can achieve a 1 percent fuel economy improvement. International felt that further tuning changes in the experimental trailer design could improve its performance.

Mack: The addition of side enclosures (tractor-trailer gap enclosures), trailer side skirts, and a boat tail to a standard tractor-van trailer combination can improve fuel economy of this vehicle by up to 8 percent. Shortening the boat tail by half still offered nearly the same fuel economy performance (7.75 percent). Side enclosures alone improved fuel economy by 1%.

Volvo: Moderate yet significant benefits were achieved with simple add-on devices which do not require complex solutions and can produce minimal operating concerns. Fuel savings of 1 percent to 2.3 percent were demonstrated through the addition of a smooth underbody concept, a trailer bogie deflector, side extenders and roof extenders, and tractor deck enclosures.

Publications

A combined Phase I technical report was provided to the Department of Energy detailing the work done in the first year of the project. The Truck Manufacturers Association presented an overview of the project at the 21st Century Truck Partnership session at the 2006 SAE Commercial Vehicle Engineering Congress and Exhibition in Chicago, Illinois. Additionally, International published a technical paper on their Phase I work at the 2006 SAE Commercial Vehicle Congress (*Practical Devices for Heavy Truck Aerodynamic Drag Reduction,* 2006-01-3531).

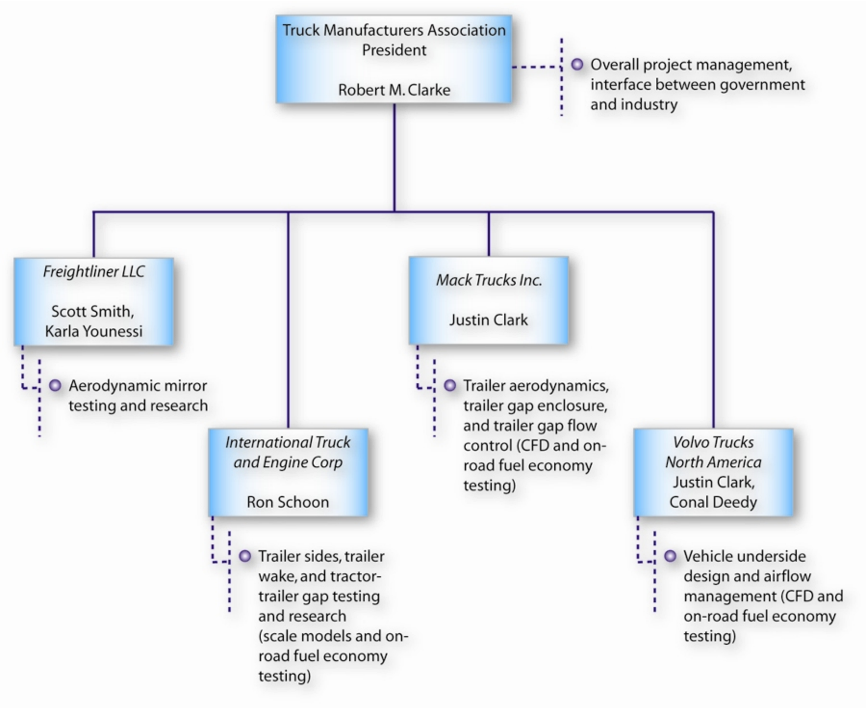

Figure 1. Project roles and responsibilities

"Aero" Mirror

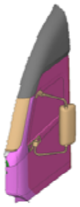

	-6°	0°	+ 6°
EFD	3.2%	4.5%	2.4%
CFD	3.5%	3.0%	1.8%

Single-Post Mirror

	-6°	0°	+ 6°
EFD	5.4%	5.9%	0.8%
CFD	4.1%	5.9%	3.7%

"West Coast" Mirror

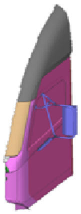

	-6°	0°	+ 6°
EFD	5.5%	7.0%	2.1%
CFD	3.8%	3.7%	2.8%

Figure 2. Aerodynamic drag due to mirrors (as percent of total vehicle drag) from freightliner testing

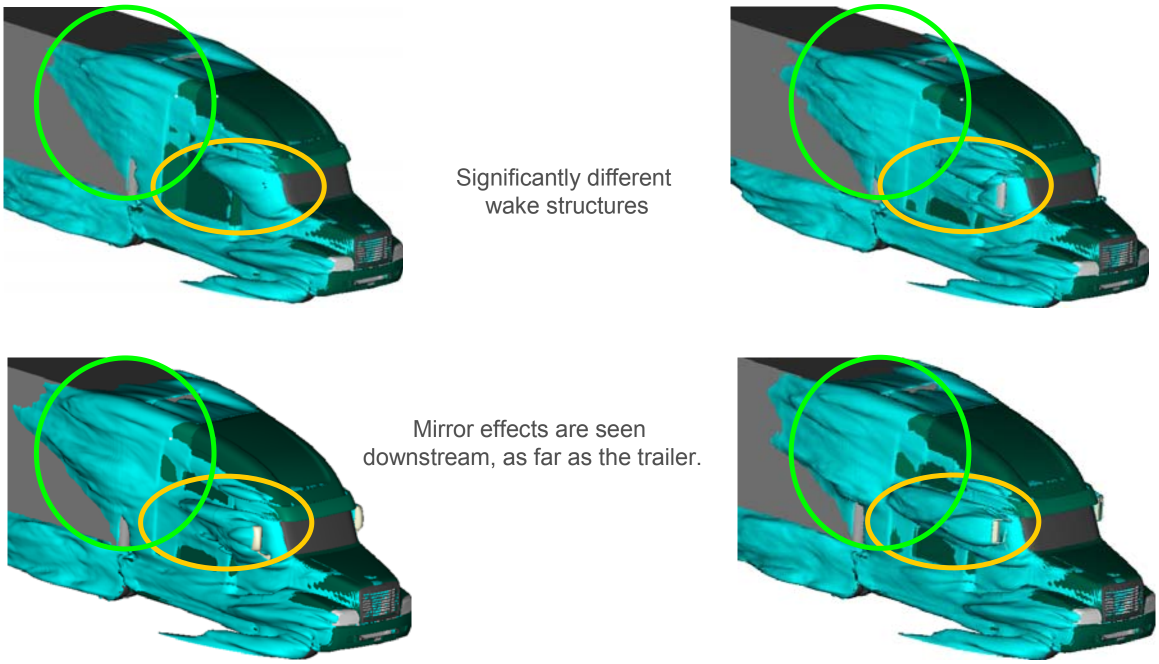

Significantly different wake structures

Mirror effects are seen downstream, as far as the trailer.

Figure 3. Freightliner CFD simulations showing mirror effects on wake structures for two different mirror systems

Figure 4. Experimental aerodynamic trailer developed in conjunction with Great Dane and Wal-Mart

Figure 5. Trailer forebody device developed by International

Figure 6. Variable length side extenders developed by International, in deployed position

Figure 7. Mack tractor-trailer combination including side enclosures, trailer skirts, and 2 foot boat tail

Figure 8. Results of Mack track testing of device combinations

Device Combination	Fuel Economy Improvement Relative to Baseline
Side enclosure, 4 foot boat tail, and trailer side skirts	8.01%
Side enclosure, 2 foot boat tail, and trailer side skirts	7.75%
Side enclosure and 4 foot boat tail	4.73%
Side enclosure and trailer side skirts	4.14%
Side enclosure	1.06%

Figure 9. Volvo smooth tractor underside concept (left), trailer bogie deflector (center), and deck enclosure (right)

Figure 10. Volvo test truck at TRC

Figure 11. Device combinations tested by Volvo and fuel economy improvements

Device Combination	Fuel Economy Improvement Relative to Baseline
Smooth underbody panel concept, trailer gap up-flow prevention (deck closure), trailer gap with add-on devices (side deflectors and roof extender), and trailer bogie deflector	2.3%
Smooth underbody panel concept, trailer gap up-flow prevention (deck closure), trailer gap with add-on devices (side deflectors and roof extender)	1.3%
Smooth underbody panel concept, trailer gap up-flow prevention (deck closure)	1.0%
Trailer gap up-flow prevention (deck closure), trailer gap with add-on devices (side deflectors and roof extender)	1.0%

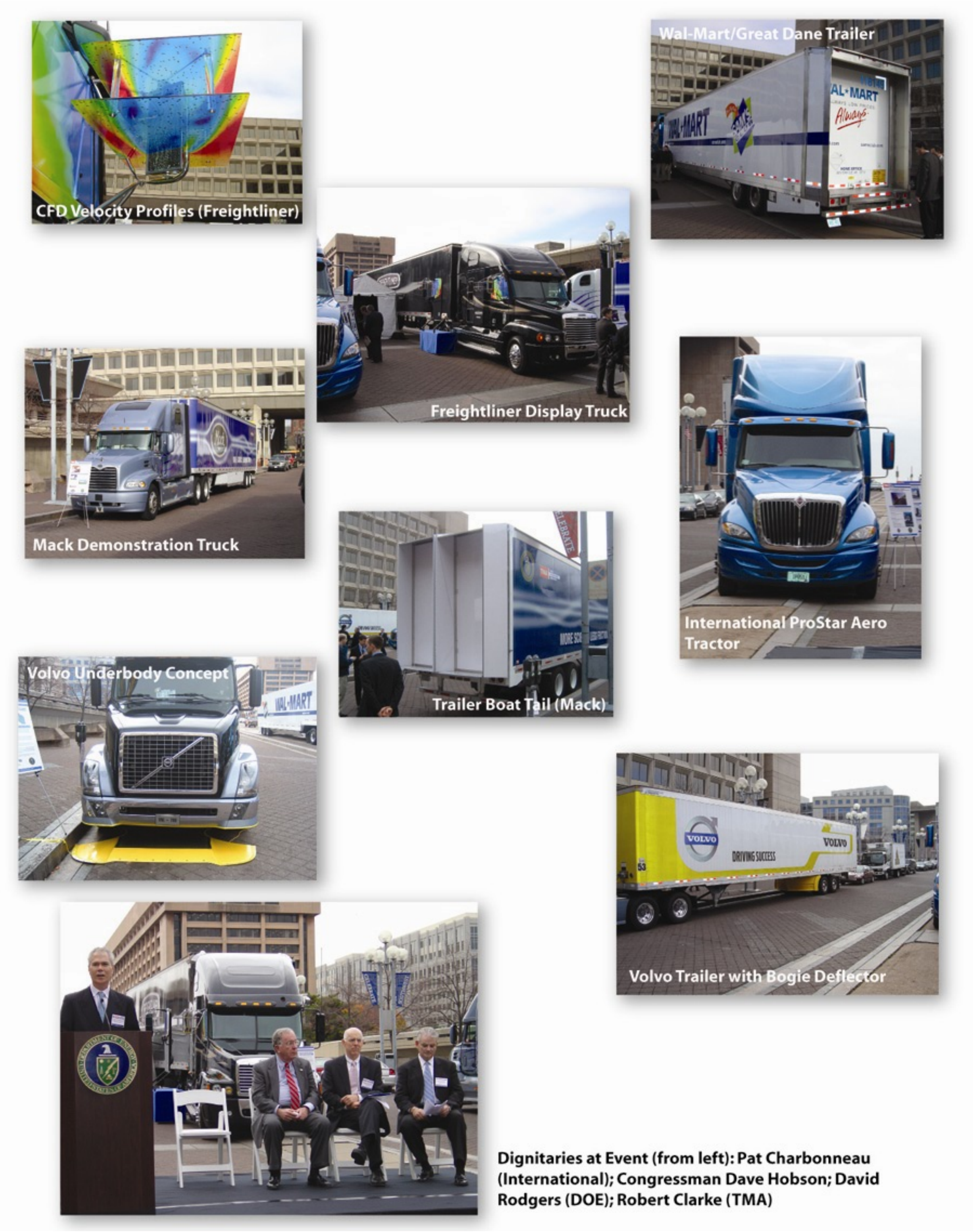

Figure 12. End-of-Project display at the Department of Energy

II. THERMAL MANAGEMENT

II.A. Efficient Cooling in Engines with Nucleate Boiling

Principal Investigator: W. Yu
Argonne National Laboratory
9700 South Cass Avenue, Building 212, Argonne, IL 60439
(630) 252-7361, fax: (630) 252-5568, e-mail: wyu@anl.gov

Technology Development Manager: Lee Slezak
(202) 586-2335, e-mail: Lee.Slezak@hq.doe.gov

Technical Program Manager: Jules Routbort
(630) 252-5065, e-mail: routbort@anl.gov

Contractor: Argonne National Laboratory
Contract No.: W-31-109-ENG-38

Objectives

- Investigate potential of two-phase flow in engine cooling applications.
- Determine limits on two-phase heat transfer (occurrence of critical heat flux or flow instability).

Approach

- Experimentally determine heat transfer rates and critical heat fluxes in small channels with water and 50% ethylene glycol in water mixture.
- Perform experiments over a concentration range of ethylene glycol in water.
- Experimental determine heat transfer characteristics for subcool flow boiling of water and ethylene glycol/water mixtures.
- Perform experiments with alternative fluids.

Accomplishments

- Completed experimental tests and data analysis for the two-phase pressure gradients and boiling heat transfer coefficients of horizontal flows to water and ethylene glycol/water mixtures.
- Developed a new procedure to analytically calculate the boiling temperature along the test section and subsequently the local heat transfer coefficients using ideal mixture and equilibrium assumptions along with Raoult's law.
- Developed a pressure drop correlation modified from the Chisholm's correlation with a concentration factor to better predict pressure drops for ethylene glycol/water mixtures.
- Developed a general correlation of boiling heat transfer coefficients modified from the Argonne's boiling heat transfer correlation with a concentration factor for the prediction of boiling heat transfer rates of flow boiling in small channels including refrigerants, water, and ethylene glycol/water mixtures.

- Fabricated a new vertical experimental test section, calibrated the instruments attached to the test section, modified the test facility and test monitoring program for vertical flow boiling tests. Completed single-phase calibration tests for vertical flow boiling on the nucleate boiling test facility.

Future Directions

- Continue systematical two-phase heat transfer experiments of water and ethylene glycol/water mixtures with vertical flows to provide essential information for nucleate-boiling cooling system design.
- Study the impact of vertical vs horizontal flows on two-phase heat transfer.
- Experimentally determine heat transfer characteristics for subcool flow boiling of water and ethylene glycol/water mixtures.
- Perform systematic experiments with alternative fluids.

Introduction

Analyses of trends in the transportation development sector indicate that future engine cooling systems will have to cope with greater heat loads because of more powerful engines, more air conditioning, more stringent emissions requirements, and additional auxiliary equipment. Moreover, there is considerable interest in reducing the size of the cooling systems to obtain a better aerodynamic profile. To meet these conditions, it is necessary to design cooling systems that occupy less space, are lightweight, have reduced fluid inventory, and exhibit improved performance. Among various new cooling systems proposed by researchers, the nucleate-boiling cooling system has high potential to meet these challenges. Order-of-magnitude higher heat transfer rates can be achieved in nucleate boiling cooling systems when compared with conventional, single-phase, forced-convective cooling systems. However, successful design and application of nucleate-boiling cooling systems for engine applications requires that the critical heat flux and flow instabilities not be reached. Therefore, a fundamental understanding of flow boiling mechanisms under engine application conditions is required to develop reliable and effective nucleate boiling cooling systems.

Cooling engine areas such as the head region often contain small metal masses that lead to small coolant channels. This geometry, in turn, leads to low mass flow rates in order to minimize pressure drop. Although significant research has been performed on boiling heat transfer and the critical heat flux phenomenon, results applicable for engine cooling systems are limited. It is the purpose of the present study to investigate the characteristics of coolant boiling, critical heat flux, and flow instability under conditions of small channel and low mass fluxes.

The test apparatus used in this investigation was designed and fabricated to study boiling heat transfer, critical heat flux, and flow instability of flowing water, ethylene glycol, and aqueous mixtures of ethylene glycol at high temperatures (up to 250° Celsius [C]) and low pressure (<345 Kilopascal [kPa]). Figure 1 shows a schematic of the apparatus. It is a closed-loop system that includes two serially arranged pumps with variable speed drives, a set of flowmeters, an accumulator, a preheater, a test section, and a condenser. The flowmeter set, including various types and sizes, was chosen to cover a large range of flow rates and was calibrated with a weighing-withstop-watch technique. The estimated uncertainty in the measurements of flow rates was ±3%. The bladder-type accumulator allows for stable control of the system pressure. The preheater provides a means to set the inlet temperature of the test section at various desired levels. Both the preheater and test section were resistance-heated with controllable direct current (DC) power supplies. Provisions were made to measure temperatures along the test section for calculating heat transfer coefficients. The pressures and temperatures at the inlet and outlet of the test section were also measured. Pressure transducers and thermocouples were calibrated against known standards. The estimated uncertainty in the

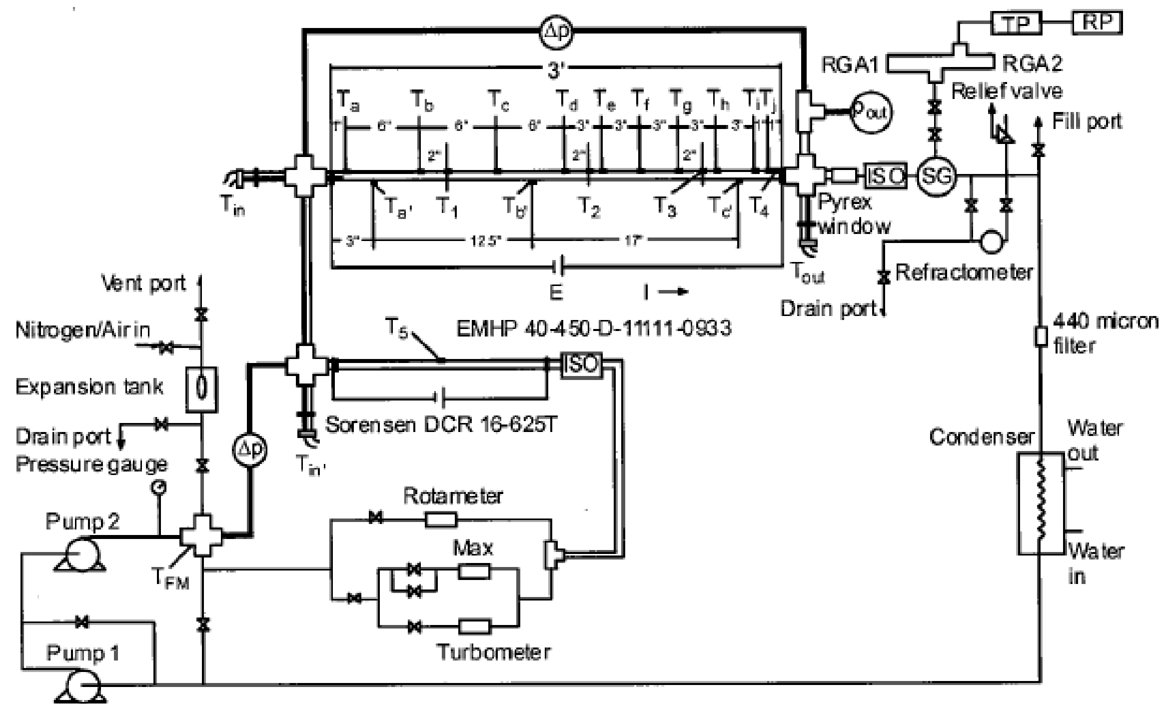

Figure 1. Schematic diagram of nucleate-boiling cooling test apparatus

measurements of pressures and temperatures were ±3% and ±0.2°C, respectively. As a safety precaution, both the preheater and test section were provided with high-temperature limit interlocks to prevent them from overheating. After leaving the test section, the two-phase flow was condensed into a single-phase flow, which returned to the pumps to close the system.

A data acquisition system consisting of a computer and a Hewlett-Packard multiplexer was assembled to record outputs from all sensors. A data acquisition program, which includes all calibration equations and conversions to desired engineering units, was written. The data acquisition system provides not only an on-screen display of analog signals from all sensors and graphs of representative in-stream and wall-temperature measurements but also a means of recording temperature measurements and pertinent information such as input power, mass flux, outlet pressure, pressure drop across the test section, and outlet quality for further data reduction.

Results and Discussion

Both experimental tests and data analysis for two phase boiling heat transfer of horizontal flows to water and ethylene glycol/water mixtures have been completed. The main results are reported below.

Boiling Curve

Figure 2 shows the heat flux as a function of wall superheat for boiling of water and ethylene glycol/water mixtures in small channels. As can be seen from Figure 2, generally, the saturation boiling in small channels can be divided into three regions, namely convection-dominant-boiling region, nucleation-dominant-boiling region, and transition boiling region. Both convective heat transfer and boiling heat transfer exist in all three regions, but their proportions are different in these three regions. In the convection-dominant-boiling region, the wall superheat is low, usually less than a few degrees centigrade. Although there is boiling heat transfer, the dominant mechanism is convective heat transfer. As a result, the mass quality and heat transfer rate are quite low comparing with those in the other two regions. In the nucleation-dominant-boiling region, the wall superheat is higher than that in the convection-dominant-boiling region but lower than certain upper limits that depend on mass flux. Opposite to the convection-dominant-boiling, the boiling heat transfer in the nucleation-dominant boiling is so developed that it becomes dominant and the heat transfer rate is much higher than that in convection-dominant boiling. As can be seen from Figure 2, the heat flux in this region is independent of mass flux and can be predicted with a power-law function of wall superheat. This characteristic was used in correlating the heat transfer data. In the transition-boiling region, the wall superheat is relatively high. The heat flux in this region is also high and close to the critical heat flux. The boiling in this region is unstable and a small change in the heat flux will result in a big change in wall superheat. If the heat flux increases further, it is possible for the system to reach the critical point producing an undesirably large jump in the wall superheat.

The above discussion shows that the nucleation dominant boiling is desired in engineering applications for both high heat transfer rate and stable flow boiling without reaching the critical point.

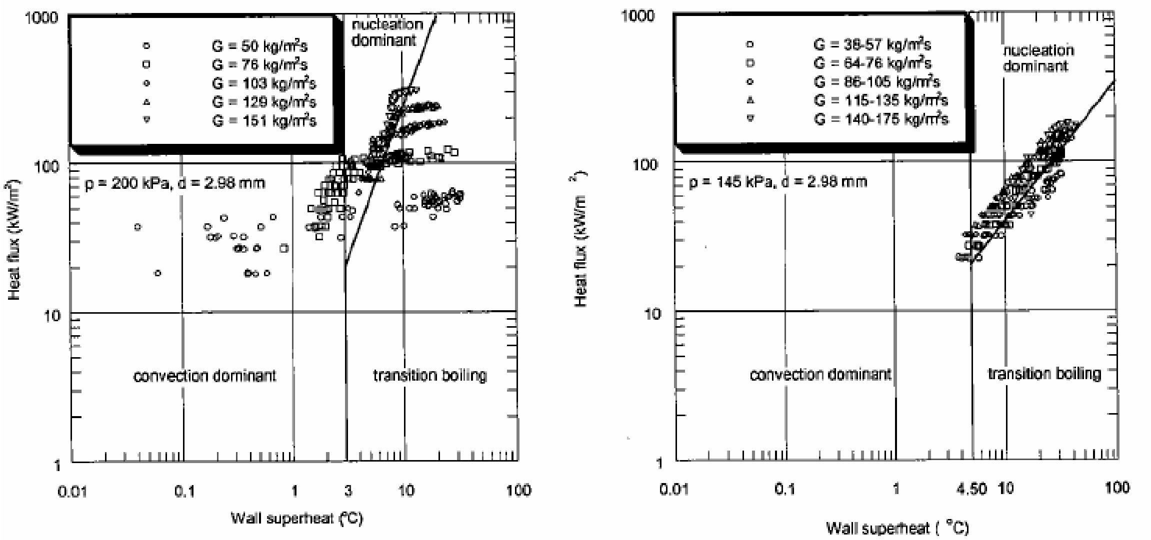

(a) water

(b) 40/60 ethylene glycol/water mixture

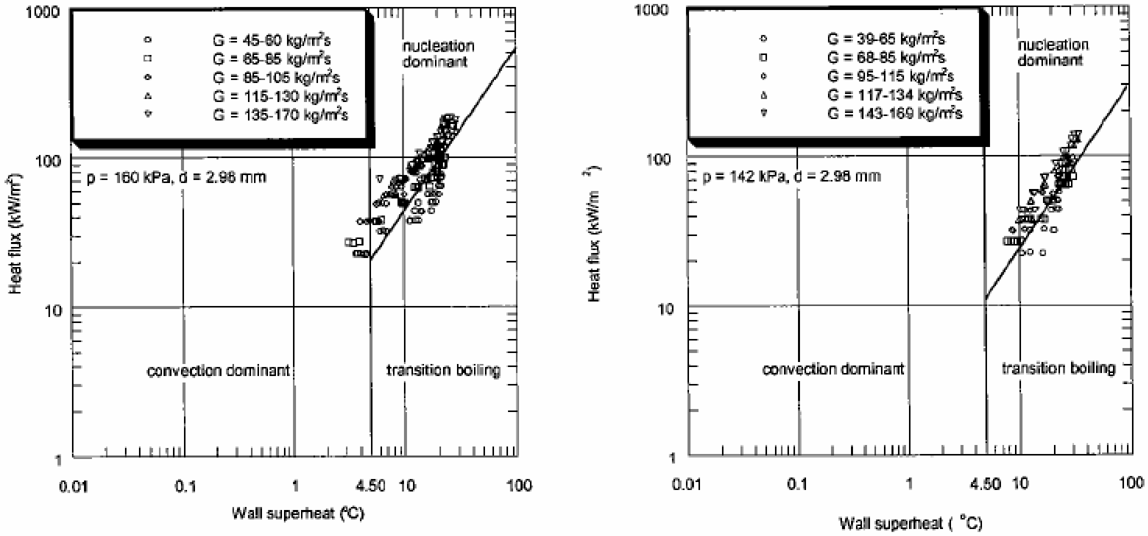

(c) 50/50 ethylene glycol/water mixture

(d) 60/40 ethylene glycol/water mixture

Figure 2. Heat flux as a function of wall superheat

Two-Phase Pressure Drop

The concept of two-phase multipliers proposed by Lockhart and Martinelli and the correlation of those multipliers by Chisholm was used to compare with the present experimental data. As can be seen from Figure 3, the experimental data are in reasonable agreement with the Chisholm predictions both in values and trends, although the Chisholm correlation slightly overpredicts the experimental data.

To better predict the experimental data and to take the concentration factor into account, the constant parameter $C = 12$ in Chisholm's correlation was modified into a function of the volume concentration v of ethylene glycol/water mixtures and Chisholm's correlation becomes

$$\phi_{FL}^2 = 1 + \frac{12[1 - 2.8v(1-v)]}{X} + \frac{1}{X^2} .$$

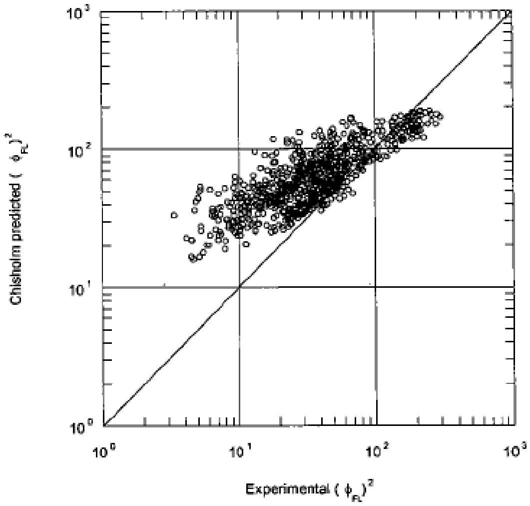

Figure 3. Two-phase frictional pressure gradient

This correlation has a feature that it reduces to Chisholm's correlation for both pure water ($v = 0$) and pure ethylene glycol ($v = 1$). In figure 4, the experimental data is compared with the predictions of the modified Chisholm's correlation. This modification improves the predictions both in values and trends.

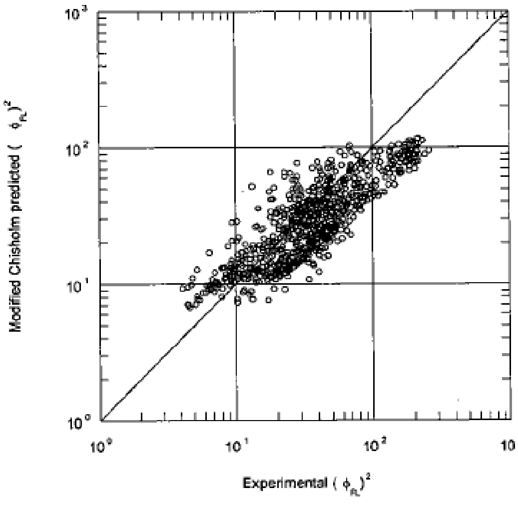

Figure 4. Two-phase frictional pressure gradient

Estimation of Local Temperature

To calculate local boiling heat transfer coefficients of an ethylene glycol/water mixture, the water vapor mass fractions, mixture vapor mass qualities, and mixture temperatures along the experimental test section must be determined. Researchers have used various approaches in making these determinations. Perhaps the simplest approach is to assume that the mixture boiling temperature is constant along the test section and equal to the mean of the zero quality temperature and the temperature at the test section outlet. This approach is not conducive to the determination of local heat transfer coefficients along the length of the test section as in the present study. Accuracy can be increased by assuming a linear mixture temperature distribution along the test section. Still another approach is to utilize a mixture equation of state such as the hard sphere equations. However, ideal mixture and equilibrium assumptions along with Raoult's law are sufficient to calculate the boiling temperature along the test section and subsequently the local heat transfer coefficients. This approach was developed and adopted in this study. Assuming an ideal mixture and applying Raoult's and Dalton's laws to the ideal mixture, one has the following equations for determine the water vapor mass fraction F_v, mixture vapor mass quality x, and mixture temperature T_m

$$F_v = \frac{9p_W(p_m - p_{EG})}{31p_m(p_W - p_{EG}) - 22p_W(p_m - p_{EG})}$$

$$x = \frac{31F_m(p_W - p_{EG}) - (9 + 22F_m)(p_m - p_{EG})}{31F_v(p_W - p_{EG}) - (9 + 22F_v)(p_m - p_{EG})}$$

$$T_{mi} = T_{mo} - \frac{\dot{q}/\dot{m} + \left[F_{vi} i_{fgWi} + (1 - F_{vi}) i_{fgEGi}\right] x_i - \left[F_{vo} i_{fgWo} + (1 - F_{vo}) i_{fgEGo}\right] x_o}{\left[F_m C_{pWl} + (1 - F_m) C_{pEGl}\right]}$$

where p is the pressure, T is the temperature, F is the mass fraction, x is the mass quality, C_p is the specific heat, i_{fg} is the latent heat of vaporization, $\dot{q}$ is the heat transfer rate, and $\dot{m}$ is the mass flow rate.

Heat Transfer Coefficient

In the present study, the nucleation-dominant boiling data have the following characteristics.

(a) Although both convective heat transfer and nucleate boiling heat transfer exist, the dominant heat transfer mechanism is nucleate boiling. Since nucleate boiling heat transfer rate is much higher than convective heat transfer, the latter can be neglected.

(b) As shown in figure 2, the boiling heat transfer is dependent on heat flux but almost independent of mass flux, which means that, for a certain fluid, the boiling heat transfer coefficient can be expressed as a function of heat flux.

(c) The heat transfer coefficients have different dependence on heat flux for different fluids. Therefore, to get a general correlation for boiling heat transfer coefficients, it is necessary to include fluid properties in the correlation.

(d) Argonne researchers employed the dimensionless parameter combination form of Boiling number, Weber number, and liquid-to-vapor density ratio in developing different predicted correlations for boiling heat transfer coefficients to different fluids, and the predicted results are quite good.

Based on the above facts, we extended the property term to including liquid-to-vapor viscosity ratio and were able to correlate boiling heat transfer data for water, 50/50 ethylene glycol/water mixture, refrigerant 12, and refrigerant 134a.

$$h = 135000(BoWe_l^{0.5})^{0.5}\left[(\rho_l/\rho_v)^{-0.5}(\mu_l/\mu_v)^{0.7}\right]^{-1.5}$$

In the above equation the Boiling number Bo and the Weber number We_l are defined respectively by $Bo = q''/(Gi_{fg})$ and $We_l = G^2D/(\rho_l\sigma)$, where ρ is the density, μ is the viscosity, G is the mass flux, D is the diameter, and σ is the surface tension. For this equation to be used for the predictions of experimental data of ethylene glycol/water mixtures with concentrations other than 50/50, we further modified the above correlation with a concentration correction factor, which reduces to 1 for concentrations $v = 0$ and $v = 0.5$. The new correlation can be expressed as

$$h/h^* = \left[1 + 6v(v - 0.5)\right](BoWe_l^{0.5})^{0.5}\left[(\rho_l/\rho_v)^{-0.5}(\mu_l/\mu_v)^{0.7}\right]^{-1.5}$$

where h^* is a characteristic heat transfer coefficient of 135 kW/m^{2}K above all of the data.

Figure 5 shows the experimental data and the predicted values obtained with the correlation for all fluids. The predictions of the equation are in good agreement with the experimental data, and most of the predictions are within ±30% of the experimental data. It should be noted that the comparisons are only for the data within the nucleation-dominant-boiling region. The success of the correlation in predicting the heat transfer coefficients of all fluids boiling in small channels is directly related to the trend, as presented in figure 2, that the heat transfer data are heat flux but not mass flux dependent. The fact that the equation is also heat flux but not mass flux dependent is in accordant with the experimental data.

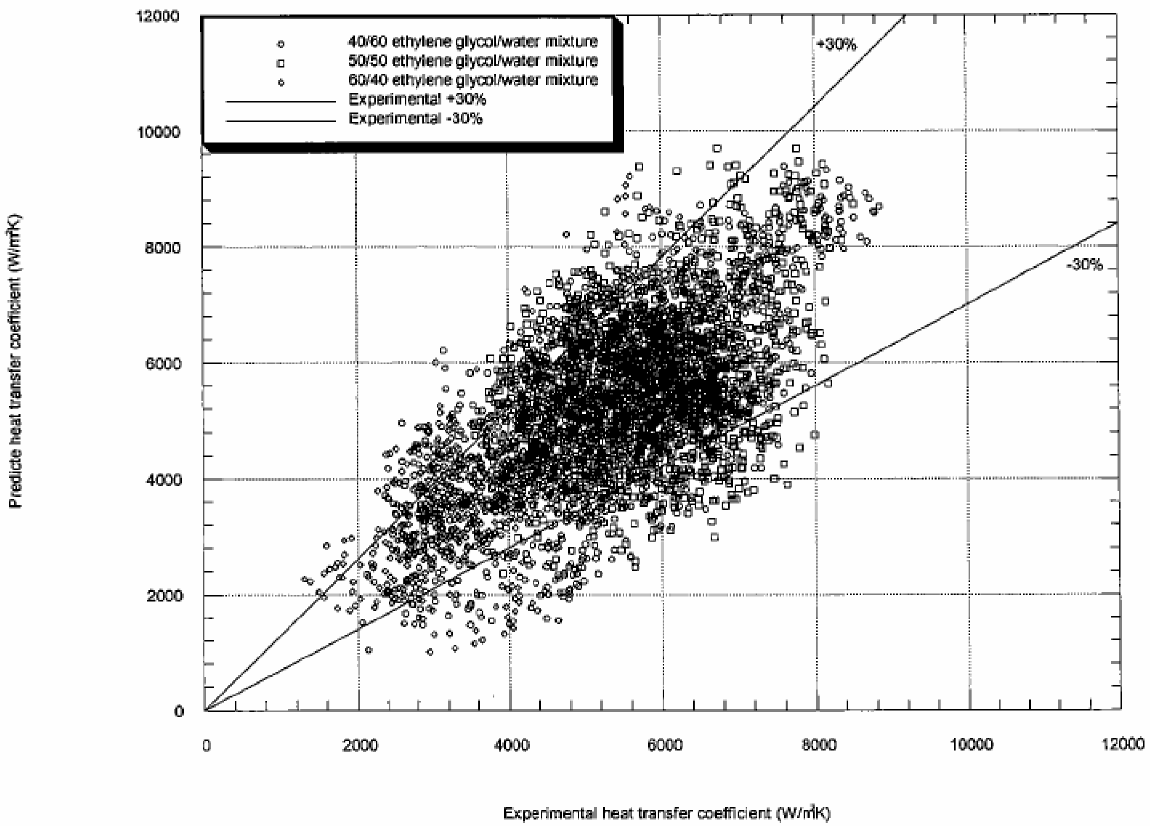

Figure 5. Heat transfer coefficient comparisons (nucleation-dominant-boiling region)

Vertical Flow Boiling Heat Transfer

In the applications of engine cooling, both horizontal and vertical flows exist. Therefore, it is necessary to investigate the impact of vertical flows vs horizontal flows on two-phase heat transfer. During the FY 2006, we have fabricated a new vertical experimental test section, the design of which is similar to the existing horizontal experimental test section. The instruments attached to the vertical test section including thermocouples and pressure transducers were calibrated against the NIST traceable thermocouple and standard device to ensure accurate measurements of temperatures and pressures. The test facility and test-monitoring program were also modified to adapt to both horizontal and vertical flow tests. Figure 6 shows a picture of the vertical test section before insulated. Single-phase tests for vertical flow have also been carried out on the test facility and the results are compared to the predictions of the Gnielinski equation in Figure 7. It can be seen that all experimental data are within 20% range of the predictions, which serves as a validation of the vertical test section and data reduction process. During the FY 2007, systematical vertical flow tests will be performed. We are planning using water and

Figure 6. Vertical experimental test section

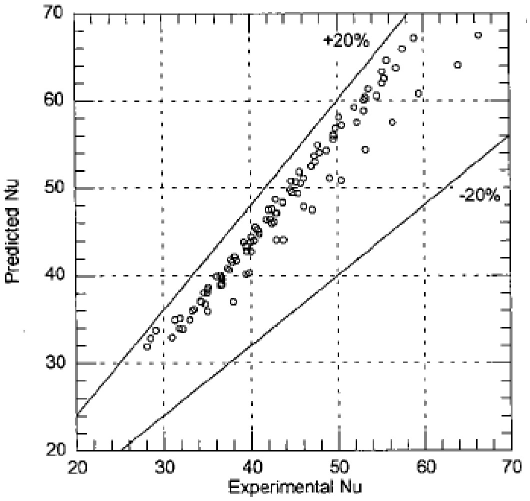

Figure 7. Single-phase Nusselt number

ethylene glycol/water mixtures two-phase boiling heat transfer experiments of vertical flows. The tests are expected to provide essential information for the design of nucleate-boiling cooling systems.

Conclusions

Excellent progress has been made on the experiments and analysis for this project.

(a) A new procedure has been developed that can analytically calculate the boiling temperature along the test section and subsequently the local heat transfer coefficients using ideal mixture and equilibrium assumptions along with Raoult's law. This procedure can be easily used for designing flow boiling cooling systems.

(b) Two-phase frictional pressure gradients of ethylene glycol/water mixtures follow similar trends as those of water. The results are in reasonable agreement with the predictions of Chisholm's correlation. A modification has been made to Chisholm's correlation, which reduces to Chisholm's correlation for concentrations $v = 0$ and $v = 1$. This modified Chisholm's correlation improves the predictions of pressure drop data of ethylene glycol/water mixtures.

(c) The experiments show a very high heat transfer rate with ethylene glycol/water mixtures, which is a positive result for engine cooling applications. A general correlation has been developed based on data of water, ethylene glycol/water mixtures (concentrations 40/60, 50/50, and 60/40), and refrigerants. This correlation predicts the experimental data quite well, and most of the predicted values are within ±30% of the experimental data.

(d) It was found that the boiling heat transfer of ethylene glycol/water mixtures is mainly limited by flow instability rather than critical heat fluxes that are usually the limits for water boiling heat transfer. Tests show that stable long-term two-phase boiling flow is possible for ethylene glycol/water mixtures as long as the mass quality is less than a certain critical value (approximately <0.2). The heat transfer rate at this mass quality is significantly higher than that of conventional, single-phase, forced-convective heat transfer.

(e) The single-phase tests on the vertical flow have confirmed the validation of the vertical test section and data reduction process. During the FY 2007, systematical vertical flow tests will be performed. We are planning using water and ethylene glycol/water mixtures for two-phase boiling heat transfer experiments of vertical flows. The tests are expected to provide essential information for the design of nucleate-boiling cooling systems.

Published Papers

1. W. Yu, D. M. France, J. R. Hull, and J. L. Routbort, Forced Convective Boiling Heat Transfer to Ethylene Glycol/Water Mixtures inside a Small Horizontal Tube, submitted to the International Journal of Multiphase Flow, 2006

2. W. Yu, D. M. France, V.-K. V. Ramamoorthy, and J. R. Hull, Small-Channel Flow Boiling of One-Component Fluids and an Ethylene Glycol/Water Mixture, Experimental Heat Transfer, 18 (4), pp. 243-257, 2005.

II.B. Nanofluids for Thermal Control Applications

Principal Investigator: S.U.S. Choi, Co-worker: Wenhu Yu
Argonne National Laboratory
9700 South Cass Avenue, Building 212, Argonne, IL 60439
(630) 252-6439, fax: (630) 252-5568, e-mail: choi@anl.gov

Technology Development Manager: Lee Slezak
(202) 586-2335, fax: (202) 586-2476, e-mail: Lee.Slezak@hq.doe.gov

Technical Program Manager: Jules Routbort
(630) 252-5065, e-mail: routbort@anl.gov

Contractor: Argonne National Laboratory
Contract No.: W-31-109-ENG-38

Objectives

- Exploit the unique properties of nanoparticles to develop heat transfer fluids with ultrahigh thermal conductivity.
- Characterize the thermal properties and heat transfer performance of nanofluids.
- Develop nanofluid technology for vehicle thermal control
- Reduce the size and weight of heavy vehicle cooling systems by >10%.

Approach

- Measure the thermal conductivity of nanofluids.
- Measure the heat transfer coefficient of nanofluids.
- Develop models of nanofluids for cooling system performance simulation.
- Conduct radiator and cooling tests in collaboration with truck companies, radiator manufacturers, and coolant manufacturers.

Accomplishments

- Developed new capabilities to measure the heat transfer coefficient of nanofluids.
- Developed new capabilities thermal conductivity measurements of nanofluids (from room temperature to 100°C).
- Measured the thermal conductivity of alumina nanofluids as a function of temperature and particle size consistent with the theoretical conjecture that the Brownian motion of nanoparticles is one of the key mechanisms of the thermal conductivity enhancement with increasing temperature and decreasing nanoparticle size.
- Developed and improved nanofluid models which account for the arrangement of nanoparticles.
- Measured the thermal conductivity of alumina-oil based nanofluids as a function of temperature and particle volume concentration and found that alumina-oil based nanofluids have a potential to reduce or eliminate the negative temperature dependence of the thermal conductivity of the base oil.

- Conducted single-phase tests with the pure base fluid (ethylene glycol) in the Nanofluid Heat Transfer Test Facility and showed a good agreement with the predictions of the Gnielinski equation. This served as a validation of the test section instruments and data reduction procedure.

Future Directions

- Produce well-characterized nanofluids.
- Conduct nanofluid flow and heat transfer experiments in laminar and turbulent flows.
- Modify the one-step nanofluid production procedure for a larger quantity of nanofluids.
- Refine models of nanostructure-enhanced and nanoparticle-mobility-enhanced thermal conductivity of nanofluids for cooling system performance simulation.
- Conduct cooling tests in collaboration with truck companies, radiator manufacturers, and coolant manufacturers.
- Develop comprehensive model of enhanced thermal conductivity of nanofluids

---

Introduction

The ever-increasing heat rejection requirements due to trends toward more power output and stringent emission requirements for engines bring cooling to the forefront issue. The conventional method to increase heat rejection rates is to use extended surfaces such as fins. However, current designs have already stretched this technology to its limits. Furthermore, conventional heat transfer fluids used in today's thermal control of vehicles, such as lubricants and engine coolants, are inherently poor heat transfer fluids. Therefore, a strong need exists for innovative concepts to achieve ultrahigh-performance cooling in thermal control systems for vehicles.

Scientists have tried adding particles to fluids to improve thermal conductivity for more than a century. However, studies of thermal conductivity of suspensions have been confined to millimeter- or micrometer-sized particles. The major problem with the use of such large particles is the rapid settling of these particles in fluids. Other problems are abrasion and clogging. To overcome these problems, Argonne has pioneered nanofluids by uniformly and stably suspending nanometer-sized particles in fluids. Nanofluids are nanotechnology based heat transfer fluids engineered by dispersing a very small quantity (preferably <1% by volume) of nanoparticles in conventional heat transfer fluids.

The potential benefits of using nanofluids include:

- Improve heat transfer of engine coolants and oils
- Reduce radiator and heat exchanger size and weight, thereby decreasing the vehicle frontal area, reducing the wind-averaged drag coefficient, increasing fuel efficiency
- Reduce heat transfer fluid inventory
- Reduce pumping energy in existing systems

The goal of the project is to reduce the size and weight of heavy vehicle cooling systems (radiator, oil cooler, pump, fan, etc.) by >10%, despite the higher cooling demands of higher-power engines and exhaust gas recirculation. Nanofluids are among the most promising coolants for the transportation industry. However, the ways in which the nanoparticles in these nanofluids generate enhanced properties are not completely understood. Therefore, to achieve this goal for the industry, both basic understanding of the mechanisms of enhanced thermal conductivity and stability of nanofluids and development of nanofluid technology are required. Consequently, the main objectives of the project are the following: (1) explore and exploit the unique properties of nanoparticles to develop heat transfer fluids with high thermal conductivity, (2) characterize the thermal conductivity and heat transfer behavior of nanofluids, (3) determine the basic mechanisms of enhanced thermal conductivity and stability of nanofluids, (4) experimentally determine heat transfer rates and pressure drops in flowing nanofluids, (5) develop and validate new models for nanofluids, (6) develop nanofluid technology for increasing the thermal transport of engine coolants and lubricants, and (7) conduct cooling tests in conjunction with industry.

Approach

Our approach to overcoming the poor heat transfer rates of conventional heat transfer fluids is to significantly increase the thermal conductivity of the liquids. An attractive method in that regard is the use of a suspension of solid nanoparticles in a liquid. Solids with thermal conductivities orders of magnitudes higher than those of the base liquids are chosen. For example, the thermal conductivity of copper at room temperature is about 3,000 times greater than that of engine oil. In fact, numerous theoretical and experimental studies of the effective thermal conductivity of dispersions that contain solid particles have been conducted since Maxwell's theoretical work was published about 100 years ago. However, studies on thermal conductivity of suspensions have been confined to millimeter- or micrometer-sized particles. The major problem with the use of such large particles is the rapid settling of these particles in fluids. Another problem is the abrasive nature of the suspension. In contrast, use of nanoparticles has the potential to produce the increased thermal conductivity sought in heat transfer fluids without the problems of settling and abrasion. Maxwell's concept of enhancing the thermal conductivity of fluids by dispersing solid particles in them is old, but what is innovative with the concept of nanofluids is the idea that size matters in nanofluids for suspension stability (gravity is negligible) and for dynamic thermal interactions.

The ANL nanofluid team has developed two techniques to make nanofluids: the single-step direct evaporation method, which simultaneously makes and disperses the nanoparticles directly into the base fluid, and the two-step method, which first makes nanoparticles and then disperses them into the base fluid. Although the two-step technique works well for oxide nanoparticles, it is not as effective for metal nanoparticles such as copper. For nanofluids containing high conductivity metals, the single-step direct evaporation technique is preferable to gas condensation processing. Nanoparticles agglomerate before dispersion and agglomerates settle rapidly. However, our innovation was dispersing nanoparticles into fluids before agglomeration by a single-step method.

ANL has already produced oxide and carbon nanotube nanofluids by the two-step technique and metal nanofluids by the single-step technique. In particular, it was demonstrated that stable suspensions can be achieved by maintaining the particle size below a threshold level.

We have made and used the transient hot wire apparatus to measure the thermal conductivity of nanofluids at room temperature. However, recent studies show the importance of measuring the temperature-dependent thermal conductivity of nanofluids. Therefore, new capabilities to measure the thermal conductivity of nanofluids from room temperature to 100°C have been developed. The thermal conductivity of oxide nanofluids with low particle concentrations (<1 % by volume) was measured as a function of temperature, particle volume concentration, and particle size using the transient hot wire method.

A major focus in nanofluids has been on their thermal conductivity. However, a new focus will be on the flow and heat transfer of nanofluids. We believe that it is critical to characterize the flow and heat transfer behavior of nanofluids in tubes in order to explain and exploit nanoparticle size-, shape-, and concentration-dependent pressure drop and heat transfer coefficient of nanofluids in tubes. For example, theories of flow in tubes or porous materials have been developed at the macroscopic level. However, we believe that it is vital to connect the structure and mobility of nanoparticles at the nano- or micro-scale to the properties of nanofluids measured at the macroscopic level. Therefore, we have developed new capabilities to measure the heat transfer coefficient of nanofluids.

We plan to conduct cooling tests with radiator manufacturers, and coolant manufacturers in order to demonstrate nanofluid technology for vehicle thermal control applications.

Results and Discussion

Thermal conductivities of alumina-oil based nanofluids were experimentally studied. Experimental measurements were performed at four particle volume concentrations of 1%, 2%, 3%, and 4% with temperature range from ambient to 90°C by the transient hot-wire method. As can be seen in Figure 1, the thermal conductivity enhancements of the alumina-oil based nanofluids have a linear temperature and nonlinear particle volume concentration trend. This trend translates into the improvement of the thermal conductivity of the base fluid, especially at higher temperature, and in the present study, there is of a 15% enhancement at 4% particle volume concentration and 80°C.

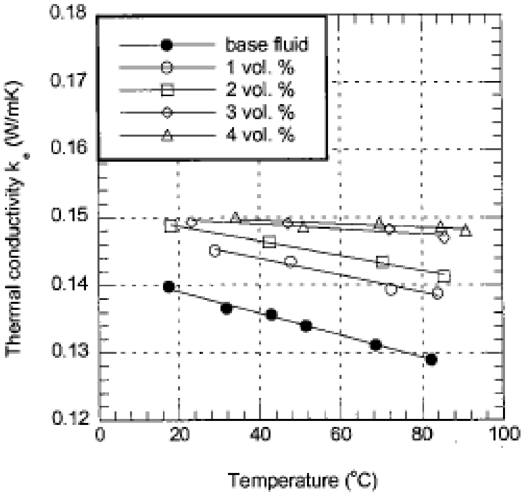

Figure 1. Thermal conductivity of alumina-oil nanofluids as a function of temperature

The results also suggest that alumina-oil based nanofluids have potential to reduce or eliminate the negative slope of the thermal conductivity of the base oil in respect to the temperature.

We have completed the design and construction of the Nanofluid Heat Transfer Test Facility, as shown in figure 2, for measuring heat transfer rates of a variety of flowing nanofluids under various flow conditions. The new Nanofluid Heat Transfer Test Facility has been carefully scrutinized for instrument accuracy, data acquisition process, and test procedure. The Nanofluid Heat Transfer Test Facility has been filled with ethylene glycol for initial tests and shake-down purposes. Single-phase pressure-drop and heat transfer testing has begun at room temperature and at an elevated temperature of 100°C. During the first tests, it was found that it was necessary to make some modifications to the Test Facility. Transparent reservoirs were added to the pump suction and discharge to allow visual confirmation of proper fluid fill level in the system. An additional electrical isolation tube was added to the flow circuit to insure that there is no current leakage through the differential pressure transducer across the test section. The test facility pump was reconfigured and test procedures changed in a manner to increase its precision over a long time period. Finally, a high accuracy flow meter was put in parallel with the test facility flow meter for use only when base fluids, and not nanofluids, are the test fluids.

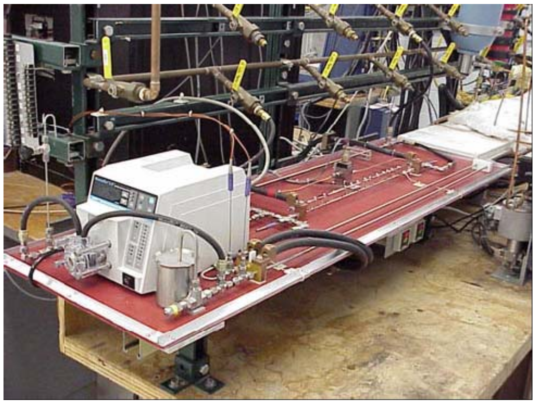

Figure 2. Picture of nanofluid heat transfer test facility

With these modifications in place, the test section pressure transducers were recalibrated (to NIST standards) and shake-down testing was resumed. Special attention is being given to the test facility pump and flow meter specially selected for nanofluid use.

Systematical single-phase tests with the pure base fluid (ethylene glycol) have been carried out on the Test Facility. The results (figure 3) show good agreement with the predictions of the Gnielinski equation and all the experimental data are within ±20% range of the predictions. The single-phase tests validated the test system designs, instrument calibrations, and data reduction process.

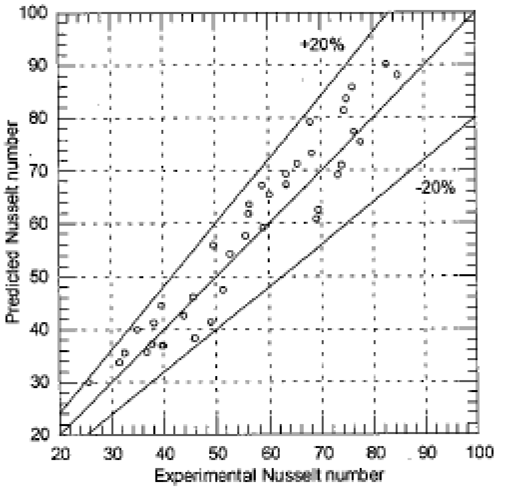

Figure 3. Comparison of single-phase Nusselt number

In 2005, we measured temperature-dependent thermal conductivities of nanofluids with 11-nm-, 47-nm-, and 150-nm-sized alumina nanoparticles at 1 and 4 vol.% concentration to delineate the effects of the nanoparticle size and nanofluid temperature. Figure 4 shows the measured thermal conductivity data normalized to the base fluid conductivity at each specified temperature (symbols) and the corresponding empirical correlations (curves) for different nanoparticle sizes and volume concentrations. It is clear that the nanofluid conductivity increases with increasing nanofluid temperature and with decreasing nanoparticle size. The results are consistent with the theoretical conjecture that the Brownian motion of nanoparticles is one of the key mechanisms of the thermal conductivity enhancement with increasing temperature and decreasing nanoparticle size.

Motion of the nanoparticles can be divided into two parts: the short-wavelength Brownian motion, which cannot be easily controlled by thermal fields, and the long-wavelength electrophoretic motion, which can be controlled with the AC electric voltage, frequency, and zeta potential. A theoretical analysis of the motion of nanoparticles in nanofluids and developed a theoretical model for controlling the motion of these nanoparticles by means of an AC electric field. We have measured the effect of nanoparticle motion induced by an AC electric field on the thermal conductivity of alumina nanofluids. The results indicate a very large improvement in the thermal conductivity under an AC electric field over that without the AC field.

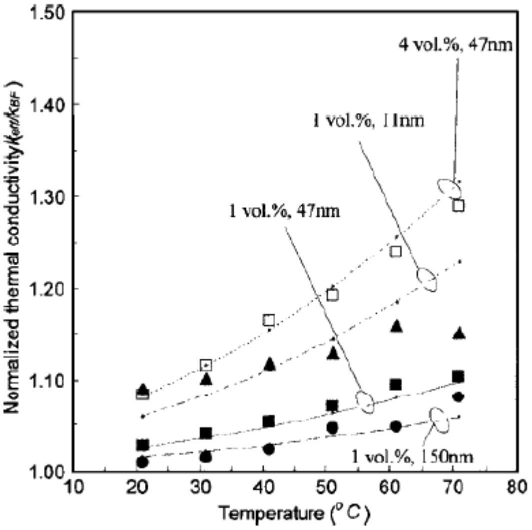

Figure 4. Temperature dependence of the thermal conductivity enhancement of three different nanofluids with 11-nm, 47-nm, and 150-nm sized Al_2O_3 nanoparticles at 1 and 4 vol. % concentration, normalized by the thermal conductivity of the base fluid at the specific temperature. Symbols represent experimental data, and the corresponding curves represent empirical correlation. At a fixed concentration, nanofluid conductivity increases with decreasing nanoparticle size and increases with increasing temperature. It should be noted that the gradually accelerating temperature dependence with increasing temperature is manifested as a slightly nonlinear function of temperature.

The theoretical investigation of the effective thermal conductivities of nanofluids is important in both predicting and designing nanofluids with effective thermal conductivities. We have developed a thermal-conductivity model for nanofluids that is based on the assumption that monosized spherical particles are uniformly dispersed in the liquid and are located at the vertexes of a simple cubic lattice, with each particle surrounded by a liquid layer having a thermal conductivity that differs from that of the bulk liquid. Figure 5 shows the thermal conductivity ratio k_e^* as a function of the volume concentration for four k_p^* values, where where k_p^* is the ratio of the thermal conductivity of the nanoparticle to that of the base fluid. It is obvious that the thermal conductivity ratio k_e^* is a nonlinear function of the volume concentration with an increase pattern that curves convex-upwards. This significantly affects the effective thermal conductivities of mixtures; it indicates that even at very low volume concentrations, the effective thermal conductivities of mixtures could be enhanced compared with base liquids. A comparison of predicted thermal conductivity values and experimental data shows that the predicted values are much higher than the experimental data, a finding that could indicate that there is a potential to further improve the effective thermal conductivities of nanofluids with more uniformly dispersed particles. Furthermore, this model nanofluid with a cubical arrangement of nanoparticles gives a more practical upper limit of thermal conduction than a model nanofluid with a parallel arrangement of nanoparticles.

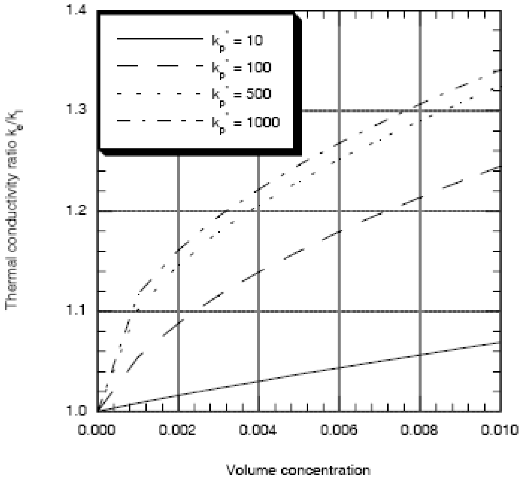

Figure 5. The thermal conductivity ratio as a function of the volume concentration for four *kp** values where *kp** is the ratio of the thermal conductivity of the nanoparticle to that of the base fluid

Future Directions

Future work will focus on the following four major tasks.

Produce and Characterize Nanofluids Containing Nanoparticles Less than 10 nm

Our experimental and theoretical studies show that particle size is of primary importance in the development of stable and high conductivity nanofluids. Size matters for achieving suspension stability and dynamic thermal interactions.

Because the thermal conductivity of nanofluids increases much more dramatically with decreasing particle size, particularly when the particle diameter is on the order of 1 nm, it should be possible to design nanofluids at the molecular and nanoscale level to create unprecedented thermal properties at the macroscopic level. For this technology to become a reality, new techniques are needed for manufacturing nanoparticles smaller than 10 nm. We will produce nanofluids containing nanoparticles less than 10 nm using one-step physical and chemical methods and characterize them. A small-angle scattering technique using x-rays from the Advanced Photon Source at ANL will be developed to measure particle size and size distributions.

Conduct Nanofluid Flow and Heat Transfer Experiments in Laminar and Turbulent Flow

We will explore the flow characteristic and measure the heat transfer coefficient of nanofluids in tubes. We will then relate enhanced thermal conductivity and flow characteristic to enhanced heat transfer coefficient of nanofluids. Control tests will be conducted with base fluids as the test fluids. Subsequently, nanofluid flow and heat transfer experiments will be conducted. The flow and heat transfer data for nanofluids will be used to determine whether the flow and heat transfer correlations developed for homogeneous fluids could be applied to nanoparticle dispersions with various aspect ratios.

Modify the One-step Nanofluid Production System for a Larger Quantity of Nanofluids

The largest barrier to industrial applications of nanofluids is scale-up of production techniques. Finding a way to produce small (1-10 nm) nanoparticles cheaply and disperse them without agglomeration is the key hurdle to commercialization. As a first step toward production scale-up, we will investigate the possibility of producing more nanofluids using one-step methods.

Refine Models of Nanostructure-enhanced and Nanoparticle-mobility-enhanced Thermal Conductivity of Nanofluids

We have developed simple models of nanostructure enhanced and nanoparticle-mobility-enhanced thermal conductivity of nanofluids. However, much is still unknown about the mechanisms of the anomalous thermal behavior of nanofluids. Therefore, we need to understand the fundamentals of energy transport in nanofluids. As we discover new energy transport mechanisms that are missing in existing theories, we will refine the simple models or develop a new model of energy transport in nanofluids integrating new mechanisms. The ultimate goal would be the theoretically based design of nanofluids for transportation applications.

Conclusions

Argonne scientists have created nanotechnology based, next-generation fluids that may revolutionize heat transfer. By suspending nanophase materials like copper or carbon nanotubes in liquids such as water, ethylene glycol, or engine oil, researchers can improve the ability to transfer heat by up to 100%. Improved oils and coolants would make possible more efficient engines and smaller and lighter cooling systems. Such engines and cooling systems would reduce aerodynamic drag and parasitic energy losses, improve fuel savings, and reduce damage to the emissions.

Published Papers

1. J.Y. Min, S.P. Jang, and S.U.S. Choi, "Motion of Nanoparticles in Nanofluids due to Brownian Force," submitted to *Physical Review Letters*, 2006.
2. S.P. Jang and S.U.S. Choi, "Effects of Various Parameters on Nanofluid Thermal Conductivity," accepted for publication in the ASME *Journal of Heat Transfer*, 2006.
3. H.B. Ma, C. Wilson, and Q. Yu, S.U.S. Choi, and M. Tirumala, "An Experimental Investigation of Heat Transport Capability in a Nanofluid Oscillating Heat Pipe," accepted for publication in the ASME *Journal of Heat Transfer*, 2006.
4. W. Yu and S.U.S. Choi, "Influence of insulation coating on thermal conductivity measurement by transient hot-wire method," *Review of Scientific Instruments*, 77 (7), 076102, 2006.
5. S.K. Das, S.U.S. Choi, and H.E. Patel, "Heat Transfer in Nanofluids-A Review," *Heat Transfer Engineering*, 27 (10), pp. 3-19, 2006.
6. H.B. Ma, B. Borgmeyer, C. Wilson, K. Park, Q. Yu, S.U.S. Choi, and M. Tirumala, "Effect of Nanofluid on the Heat Transport Capability in an Oscillating Heat Pipe," *Applied Physics Letters,* 88, 143116, 2006.
7. S.P. Jang and S.U.S. Choi, "Cooling Performance of a Microchannel Heat Sink with Nanofluids," *Applied Thermal Engineering,* 26, pp. 2457-2463, 2006.

II.C. Erosion of Materials in Nanofluids

Principal Investigator: J.L. Routbort (co-workers: D. Singh, Cinta Lorenzo-Martin, O. Ajayi, R.K. Smith, and Gang Chen)
Argonne National Laboratory
9700 S. Cass Avenue, Argonne, IL 60439-4838
(630) 252-5065, e-mail: routbort@anl.gov

Technology Development Manager: Lee Slezak
(202) 586-2335, e-mail: Lee.Slezak@ee.doe.gov

Contractor: Argonne National Laboratory
Contract No.: W-31-109-Eng-38

Objective

- Determine if the use of fluids containing a variety of nanoparticles result in erosive damage to radiator materials.
- Develop models to predict the erosive damage.

Approach

- Develop an experimental apparatus to measure erosive loss.
- Conduct experiments to study erosive damage of fluids containing various types and sizes of nanoparticles on typical radiator materials.
- Develop methods to analyze the results.

Accomplishments

- Baseline data on aluminum using 50/50 mixture of ethylene and water and tricholoroethylene glycol established that no erosive damage at impact angles of 30, 50, and 90° occurred for velocities up to 10 m/s.
- Initial experiments using tricholoroethylene containing 0.01% Cu nanoparticles indicate that erosive damage at radiator velocities is negligible.

Future Direction

- The erosion of fluids containing a variety of well-characterized nanoparticles will be tested on typical radiator materials, varying both the angle and velocity of impact, volume percent of nanoparticles, and temperature.
- Initial friction and wear tests using nanofluids as lubricants.

Forward

There is no doubt that the important nanofluid effort at ANL was hurt because of the decrease in funding, the demise of the Energy Technology Division and the subsequent reorganization, and the reduction in staff from about 7 to less than 2. This has hindered the liquid erosion work because the supply of nanofluids was very limited. Furthermore, future efforts will be shifted into development of techniques to produce nanofluids that can be scaled up for industrial applications. Hence, a great deal of effort will be focussed on production and characterization of nanofluids, as well as thermal property measurements. As well-characterized nanofluids become available, liquid erosion tests will be performed.

Introduction

Many industrial technologies face the challenge of thermal management. With an ever-increasing thermal loads due to trends toward greater power output for engines and exhaust gas recirculation for diesel engines, cooling is a crucial issue in transportation. The conventional approach for increasing cooling rates is use of extended surfaces such as fins and microchannels. Reducing radiator size will reduce the frontal area and hence the aerodynamic drag. However, current designs have already stretched this approach to its limits. Therefore, an urgent need exists for new and innovative concepts to achieve ultra-high-performance cooling. Nanofluids seem to show enormous potentials as a coolant for radiators. Choi, et al. have shown that fluids containing 1 vol.% Cu nanoparticles increases thermal conductivity by 40% [1] while 1 vol.% carbon nanotubes increase thermal conductivity by 250% [2].

In order for the enhanced thermal conductivity to be utilized it must be shown that liquid erosion of typical radiator materials will be tolerable. Hence, the Office of FreedomCar and Vehicle Technologies funded a program on liquid erosion of radiator materials using nanofluids.

Results and Discussion of Erosion

An apparatus was built and calibrated as described in the FY05 annual report. The initial measurements were performed on a typical radiator material, aluminum 3003 using a tricholoroethylene glycol not containing any nanoparticles. Both 30 and 90° angles of impact were used. Typical fluid velocities in radiator tubing is about 1m/s, but velocities of 7.6 and 9.6 m/s were used to accelerate the damage process. It would be expected that the damage would be proportional to the square of the velocity. The results are tabulated in Table 1.

Table 1. Weight-loss measurements of 3003 aluminum using trichloroethylene glycol at 30 and 90° angles at velocities up to 9.6m/s

Impact Angle	Velocity (m/s)	Time (hrs)	Weight Loss (mg)
90°	7.6	238	0 ± 0.2
30°	7.6	263	0 ± 0.2
90°	9.6	242	0 ± 0.2
30°	9.6	307	0 ± 0.2

As can be seen from table 1, no erosive damage (during the several hundred hours of each test) occurs using this fluid that doesn't contain nanoparticles.

Results of using 0.01 vol.% Cu nanoparticles in trichloroethylene glycol are shown in Table 2. It is realized that the loading of the Cu nanoparticles was much lower than one would use in an application, however, we were using a nanofluid that had previously been produced and characterized.

While it would appear that no damage occurs up to approximately 300 hours of the test, longer-term test results are shown in Fig. 1.

Table 2. Results of erosion of 3003 aluminum using 0.01 vol. % Cu nanoparticles in trichloroethylene glycol

Impact Angle	Velocity (m/s)	Time (hrs)	Weight Loss (mg)
90°	4.0	217	0 ± 0.2
30°	4.0	311	0 ± 0.2
90°	7.6	341	0 ± 0.2
30°	7.6	335	0 ± 0.2
30°	9.6	336	0 ± 0.2

Fig. 1. Indicates that some steady-state weight loss occurs under the most extreme conditions (maximum kinetic energy transferred) tested using this fluid, after several hundred hours of testing. In order to calculate the erosion rate one needs to measure the impact area. A surface of the 3003 aluminum was painted on impacted at various velocities and angles and the impact area was measured. A typical impact area is shown in Fig. 2. Using the impact area, the steady-state erosion rate was calculated to be $3.5\text{x}10^{-6}$ g/h. If one assumes that the damage is proportional to the kinetic energy, V^2, the erosion rate at 1 m/s is $3.5\text{x}10^{-8}$ g/h.

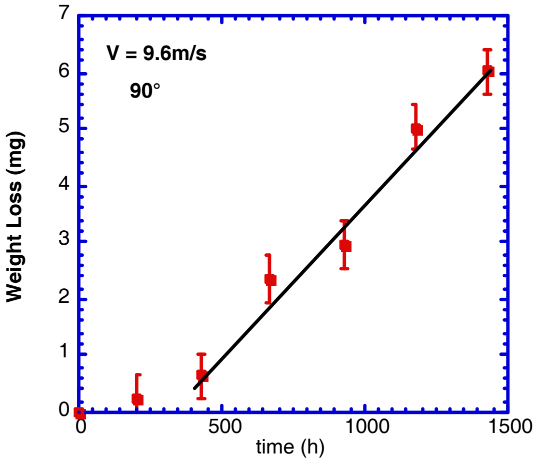

Figure 1. Weight loss for 3003 aluminum versus time measured at 90° and 9.6m/s using 0.01 vol.% Cu nanoparticle in trichloroethylene glycol

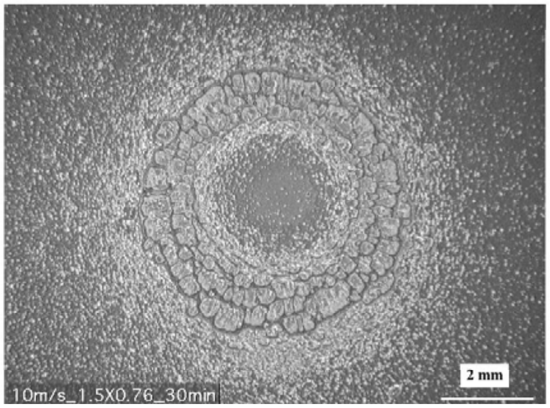

Figure 2. Area of a painted surface resulting from a fluid jet impacting at 10m/s at 90°

Based on 2500 h/year of engine operation, this would result in a recession rate of 0.065 mils/year. The recession rate should be compared to the corrosion rate of steel in water that is approximately 2 mils/year, or two orders of magnitude smaller than the erosion rate.

We must admit that the loading of the Cu nanoparticles was very low and that nanofluids containing higher loadings could cause more damage. However, these were initial tests were performed using the available nanofluid and the results are encouraging.

Friction and Wear Results

It is possible that the higher thermal conductivity of nanofluids would make them good candidates for lubricants in a sliding environment because they could remove heat more quickly than conventional lubricants. We have, therefore, performed some preliminary friction and wear tests using nanofluids as the lubricant.

Two concentrations of alumina nanoparticles (25-40 nm) in water, 0.5 and 1.5 vol.%) were used in the Ball-on-Disk Tribotester with a 4400 steel disk and a 5210 steel ball. The trichloroethylene glycol containing 0.01% Cu nanoparticles was also used. The latter nanofluid containing Cu nanoparticles had little effect on the coefficient of friction while the wear rate increased about a factor of 3. The absolute wear rate was still considered mild, about 6x10^{-7}mm^3/m-N. It is believed that the Cu nanoparticles probably oxided and the resultant CuO was more abrasive than pure Cu.

Friction results for the nanofluid containing alumina are shown in Fig. 3. The alumina-containing nanofluid has a slightly lower coefficient of friction than the pure fluid. Wear results are shown in Fig. 4. The relative wear rate is somewhat lower for the nanofluids than for water, but, as expected , the absolute wear rate is higher for the alumina containing nanofluids than for the CuO containing nanofluids. The nanofluid containing alumina nanoparticles polished the steel surfaces.

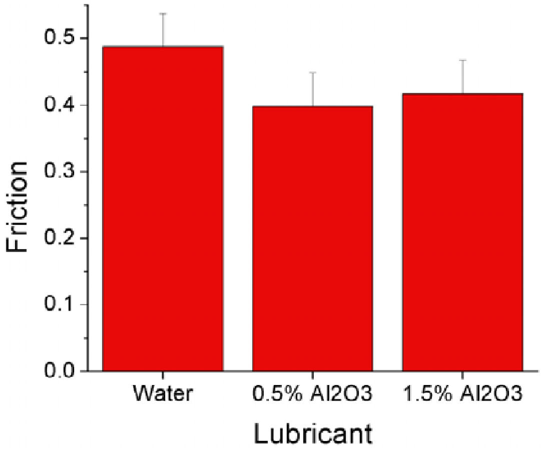

Figure 3. Coefficient of friction of 4400 steel on 5210 steel using water and water containing alumina nano particles as the lubricant

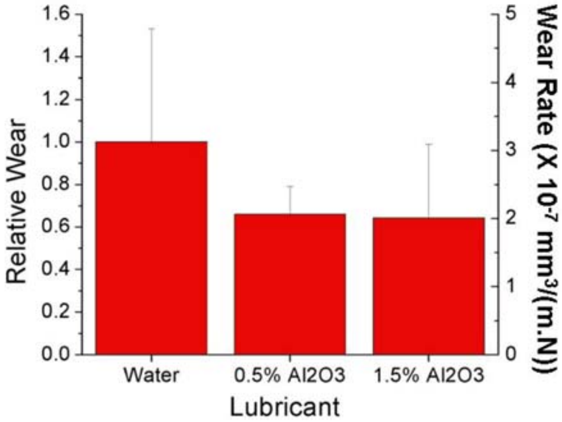

Figure 4. Wear rate for 4400 steel on 5210 steel using water and water containing alumina nanoparticles as the lubricant

Issues & Future Direction

Understanding mechanism(s) of weight loss of target metal is vital to developing pre-dictive models to describe the erosion behavior from nanofluids. At the present time, it appears that erosion behavior by nanofluids is not servere. However, it is not conclusive because we have not tested a wide-variety of nanofluids containing well-characterized, and controlled volumes of larger percentages of nanoparticles.

Furthermore, a parallel study to investigate the wear properties using nanofluids has been explored. Friction and wear behavior yielded interesting results that show that proper selection of nanofluids might reduce wear. This work will continue using the same nanofluids as used in the liquid erosion investigations.

Conclusions

Baseline data indicates that no erosion of Al3003 occurs using ethylene glycol and water (50-50), and trichlorethylene glycol for 90°-30° impact angles with velocities as high as 10 m/s. However, when 0.01 vol.% Cu was added to the trichlorethylene glycol, erosion began to occur at long times under the most extreme conditions (90°, and 10m/s). However, the erosion rates were very small, about 2 orders of magnitude less than the corrosion rate of steel in water. It remains to be seen how the erosion rate varies with type, size, size distribution and volume percent of nano particles in the fluid.

References

1. J. A. Eastman, S. U. S. Choi, S. Li, W. Yu, and L. J. Thompson, "Anomalously Increased Effective Thermal Conductivities of Ethylene Glycol-Based Nano-Fluids Containing Copper Nano-Particles," *Applied Physics Letters*, **78**, 718-720 (2001).

2. S. U. S. Choi, Z. G. Zhang, W. Yu, F. E. Lockwood, and E. A. Grulke, "Anomalous Thermal Conductivity Enhancement in Nano-tube Sus-pensions," *Applied Physics Letters*, **79**, 2252-2254 (2001).

3. D. Wong, L. Swette, and F. H. Cocks, "Aluminum Corrosion in Uninhibited Ethylene Glycol-water Solutions," J. Electrochem. Soc., **126**, 11-15 (1979).

II.D. Diesel Engine Underhood Thermal Analysis

Principal Investigators: Jimmy Chang and Tanju Sofu
Argonne National Laboratory
9700 S. Cass Avenue, Argonne, Illinois 60439
(630) 252-7547, fax: (630) 252-3361, e-mail: chang@anl.gov, tsofu@anl.gov

Field Project Manager: Tanju Sofu
Argonne National Laboratory
9700 S. Cass Avenue, Argonne, Illinois 60439
(630) 252-9673, fax: (630) 252-4500, e-mail: tsofu@anl.gov

Technology Development Area Specialists: Lee Slezak
(202) 586-4819, fax: (202) 586-2476, e-mail: lee.slezak@ee.doe.gov

Field Technical Manager: Lee Slezak
(202) 586-4819, fax: (202) 586-2476, e-mail: lee.slezak@ee.doe.gov

---

Contractor: Argonne National Laboratory
Contract No.: W-31-109-ENG-38

Objective

This work is to develop a simulation technique based on combined use of 3-D computational fluid dynamics (CFD) and 1-D thermal-flow models. This technique can be used to predict diesel engine thermal performance and identify potential hot-spots in engine compartments of diesel trucks. Optimizations of engine thermal system and cooling package are also critical to improve energy efficiency of heavy vehicle systems.

Approach

In this CRADA, ANL has focused on developing a conjoined 1-D thermal-fluid model and 3-D CFD model for diesel engine underhood thermal system. In the second year, Cummins will provide test data needed for the model validation. The end product will be a validated truck underhood thermal model to predict engine compartment temperatures, flow field distribution, and engine thermal performance. An optimal design of vehicle thermal system is important for energy efficiency since less than one-third of the total fuel energy provides useful mechanical work and the remainder is lost through the exhaust system and heat rejection. Determination of accurate temperature distributions in an engine is critical to achieve fuel efficiencies through cooling system optimization and radiator size reduction.

Accomplishments

So far, a 1-D network thermal-fluid model of a diesel Cummins engine with exhaust recirculation system (EGR) has been developed with assistance from Cummins engineers using the commercial software Flowmaster. The 1-D thermal-fluid model was developed to manage the underhood thermal control and enhance the cooling performance. The developed 1-D model includes engine metal structure, underhood air, lubrication oil, and machine cooling packages (cabin heater, EGR, and radiator subsystems). This 1-D model is a representation of engine internal flow loops combined with a lumped-parameter approach to characterize the thermal interactions between them through the engine structure as the major conduction paths. It simplifies the complex engine system by discretization based on known heat transfer paths under equilibrium conditions and predicts the complete thermal system performance and calculates thermal energy balance.

Future Direction

The 1-D model developed will be conjoined with the 3-D CFD model for a comprehensive underhood thermal analysis of a diesel engine. Both CFD and thermal-fluid systems models on their own have inherent limitations: CFD model is computationally prohibitive for simulations of the entire system and 1-D network model oversimplifies multi-dimensional flow and heat transfer. Combined use of CFD and network models offers unique advantages: Network model accounts for thermal energy balance and heat distribution inside the engine through 1-D network of flow loops and CFD model addresses multi-dimensional flow and heat transfer wherever needed. The combined model will include exhaust-gas recirculation, radiator-fan, and cabin heater systems to form a complete cooling analysis.

Introduction

As the diesel engine emission regulations becomes increasingly stringent, emission control technologies such as cooled exhaust gas recirculation (EGR) and after-treatment devices are applied. As a result, the engine heat rejection to both coolant and air increases substantially, causing generally higher underhood temperatures with potential hot spots. In addition, warm air from the radiator can further heat up as it passes over heat generating component surfaces. The combination of these effects can compromise the durability of certain temperature sensitive components under the hood, leading to reduced vehicle life, especially under extended driving conditions. To remedy the situation, OEMs often overdesign their cooling packages resulting in reduced energy efficiency. To address these challenges and shorten the design cycle, ANL has partnered with Cummins, Inc. under a CRADA to develop an integrated simulation technique for underhood thermal analysis and cooling package optimization for a conventional diesel engine.

Modeling Development

The 1-D thermal-fluid software Flowmaster is used to account for overall energy balance and simulate cooling system response. The CFD model Fluent is used to determine underhood air flow paths and component surface heat transfer. The Flowmaster will be conjoined with the Fluent to manage the underhood thermal control and enhance the cooling performance. The developed 1-D model is composed of engine structure, air, oil, and coolant loops. The coolant loop includes exhaust gas recirculation, radiator-fan, and cabin heater subsystems to form a complete cooling package.

Summary

A combined 1-D and 3-D simulation technique is being developed to predict the underhood thermal performance of a diesel engine with exhaust gas recirculation system. A predictive analytical capability can help redesign underhood configuration while meeting new energy efficiency and emissions requirements. An optimal design of vehicle thermal system is essential for energy efficiency since most of total fuel energy is thermally wasted. Significant fuel efficiencies can be expected from optimization of cooling system and reductions in radiator size through simulations.

III. FRICTION AND WEAR

III.A. Boundary Lubrication Mechanisms

Principal Investigators: O. O. Ajayi, J. G. Hershberger, C. Lorenzo-Martin,
J. Routbort, and G. R. Fenske
Argonne National Laboratory
9700 South Cass Avenue, Argonne, IL 60439
(630) 252-9021, fax: (630) 252-4798, e-mail: ajayi@anl.gov

Technology Development Manager: Lee Slezak
(202) 586-2335, e-mail: Lee.Slezak@hq.doe.gov

Technical Program Manager: Jules Routbort
(630) 252-5065, e-mail: routbort@anl.gov

Contractor: Argonne National Laboratory, Argonne, Illinois
Contract No.: DE-AC02-06CH11357

Objective

Develop a better understanding of the mechanisms and reactions that occur on component surfaces under boundary lubrication regimes with the ultimate goal of friction and wear reduction in oil-lubricated components and systems in heavy vehicles. Specific objectives are

- Determine the basic mechanisms of catastrophic failure in lubricated surfaces in terms of materials behavior. This knowledge will facilitate the design of higher power density components and systems.
- Determine the basic mechanisms of chemical boundary lubrication. This knowledge will facilitate lubricant and surface design for minimum frictional properties.
- Establish and validate methodologies for predicting the performance and failure of lubricated components and systems.
- Integrate coating and lubrication technologies for maximum enhancement of lubricated-surface performance.
- Transfer the technology developed to OEMs of diesel engine and vehicle components and systems.

Approach

- Characterize the dynamic changes in the near-surface material during scuffing. Formulate a material-behavior-based scuffing mechanism and prediction capability.
- Determine the chemical kinetics of boundary film formation and loss rate by in-situ X-ray characterization of tribological interfaces at the Advanced Photon Source (APS) of Argonne National Laboratory (ANL).
- Characterize the physical, mechanical, and tribological properties of tribo-chemical films, including the failure mechanisms.
- Integrate the performance and failure mechanisms of all the structural elements of a lubricated interface to formulate a method for predicting performance and/or failure. This task will include incorporation of surface coatings.
- Maintain continuous collaboration with OEMs of heavy vehicle systems to facilitate effective technology transfer.

Accomplishments

- Conducted extensive characterization of microstructural changes during scuffing of 4340 steel, using scanning electron microscopy (SEM) and X-ray analysis.
- For metallic materials, developed a model of scuffing initiation based on an adiabatic shear instability mechanism and scuffing propagation based on a balance between heat generation and heat dissipation rates.
- Characterized the mechanical properties and scuffing resistance of a graded nanocrystalline surface layer produced by severe plastic deformation resulting from the scuffing process.
- Conducted preliminary evaluation of scuffing mechanisms in ceramic materials.
- Using X-ray fluorescence, reflectivity, and diffraction at the APS, demonstrated the ability to characterize tribo-chemical films generated from model oil additives.
- Designed and constructed an X-ray accessible tribo-tester for in-situ study of boundary film formation and loss rates.

Future Direction

- Experimentally validate the comprehensive scuffing theory for various engineering materials, including ceramics.
- Develop and evaluate methods and technologies to prevent scuffing in heavily loaded oil-lubricated components and systems.
- Using X-ray based and other surface analytical techniques, continue to characterize tribochemical films formed by model lubricant additives.
- Characterize the physical, mechanical, and failure mechanisms of tribochemical films with nano-contact probe devices.
- Evaluate the impact of various surface technologies, such as coating and laser texturing, on boundary lubrication mechanisms.

Introduction

Many critical components in diesel engines and transportation vehicle subsystems are lubricated by oil. Satisfactory performance of these components and systems is achieved through the integration of materials, surface finish, and lubricant oil formulations. To that end, an Edisonian trial-and-error approach is often followed. Indeed, experience is likely the sole basis for new design and solutions to failure problems in lubricated components. With more severe operating conditions expected for component surfaces in advanced engines and vehicle systems, the trial-and-error approach to effective lubrication is inadequate and certainly inefficient. Departure from this approach will require a better understanding of the fundamentals of both boundary lubrication and surface failure mechanisms.

A major area of focus for the Department of Energy in the development of diesel engine technology for heavy vehicles is emission reduction. Some essential oil lubricants and diesel-fuel additives, such as sulfur, phosphorus, and chlorine, are known to poison the catalysts in emission-reducing after-treatment devices. Although reduction or elimination of these additives will make emission after-treatment devices more effective and durable, it will also render the surfaces of many lubricated components vulnerable to catastrophic failure. Many of the methods used to reduce diesel engine emissions may also render critical-component surfaces vulnerable to catastrophic failure, thereby compromising their reliability.

Increases in vehicle efficiency will require friction reduction and increase in power density in the engine and powertrain systems. Higher power density translates to increased severity of contact between many components. This, again, will compromise the reliability of various critical components, unless they are effectively lubricated. The efficacy of oil additives in reducing friction and in protecting component surfaces depends on the nature and extent of the chemical interactions between the component surface and the oil additives.

In addition to reliability issues, the durability of lubricated components also depends on the effectiveness of oil lubrication mechanisms. Components will eventually fail or wear out by various mechanisms and contact fatigue. Wear is the gradual removal of material from contacting surfaces, and it can occur by various mechanisms, such as abrasion, adhesion, and corrosion. Also, the repeated contact stress cycles to which component contact surfaces are subjected can initiate and propagate fatigue cracks and, ultimately, lead to the loss of a chunk of material from the surface. This damage mode is often referred to as "pitting." Wear and contact fatigue are both closely related to boundary lubrication mechanisms. Antiwear additives in lubricants are designed to form a wear-resistant protective layer on the surface. The role of lubricant additives on contact fatigue failure is not fully understood, although it is clear that the lubricant chemistry significantly affects contact fatigue. Again, lack of a comprehensive understanding of the basic mechanisms of boundary lubrication is a major obstacle to a reasonable prediction of the durability of lubricated components and systems.

Significant benefits would accrue by extending the drain interval for diesel engine oil, with an ultimate goal of a fill-for-life system. Successful implementation of the fill-for-life concept for the various lubricated systems in heavy vehicles requires optimization of surface lubrication through the integration of materials, lubricant, and, perhaps, coating technologies. Such an effort will require an adequate fundamental understanding of surface material behavior, chemical interactions between the material surface and the lubricant, and the behavior of material and lubricant over time.

Some common threads run through all of the challenges and problems in the area of surface lubrication of engine components and systems briefly described above. The two key ones are lack of adequate basic and quantitative understanding of the failure mechanisms of component surfaces, and lack of understanding of the basic mechanisms of boundary lubrication, i.e., how lubricant chemistry and additives interact with rubbing surfaces, and how this affects performance in terms of friction and wear. To progress beyond the empirical trial-and-error approach for predicting lubricated component performance, a better understanding is required of the basic mechanisms regarding the events that occur on lubricated surfaces. Consequently, the primary objective of the present project is to determine the fundamental mechanisms of boundary lubrication and failure processes of lubricated surfaces. The technical approach taken in this study differs from the usual one of posttest characterization of lubricated surfaces but, rather, will involve developing and applying in-situ characterization techniques for lubricated interfaces that will use the X-ray beam at the Advanced Photon Source (APS) located at ANL. Using a combination of different X-ray-based surface analytical techniques, we will study, in real time, the interactions between oil lubricants and their additives and the surfaces they lubricate. Such study will provide the basic mechanisms of boundary lubrication. In addition to surface chemical changes, the materials aspects of various tribological failure mechanisms will be studied.

Results and Discussion

Efforts during the past year (FY 06) were devoted to the study of scuffing mechanisms in ceramic materials, especially zirconia. Such study will provide significant input into the development of a comprehensive scuffing model that is applicable to all classes of engineering materials. Preliminary in-situ x-ray fluorescence analysis tests were also conducted with an X-ray accessible tribo-tester with model lubricant containing molybdenum dithiocarbamate (MoDTC) and zinc dialkyl diathiophosphate (ZDDP) additives.

Scuffing Zirconia Ceramic Material

In the past years, a scuffing theory was developed for metallic materials based on experimental observations from hardened 4140 steel. Scuffing initiation occurs when the rate of thermal softening as a result of heat generated by plastic deformation exceeds the rate of work hardening due to an increase in dislocation density associated with plastic deformation. Under such condition, the plastic deformation process becomes unstable and a severe localized plasticity ensues, accompanied by a large amount of heat generation – scuffing initiation. Progression of scuffing to a catastrophic stage is dependent on whether its propagation occurs or not. If the rate of heat dissipation from the initiation site exceeds the rate of heat generation from continued deformation, then scuffing does not propagate. If the rate of heat generation exceeds the rate of heat dissipation, scuffing will propagate into a run-away thermal process, ultimately resulting in a catastrophic failure.

Structural ceramic materials are currently being used in some tribological systems to address scuffing problems in the lubricated components of such systems. For example, zirconia (ZrO_2) ceramic plungers have been successfully used in fuel injector systems for heavy duty diesel engines, primarily to address scuffing failures in low-lubricity diesel fuels. Given the fact that scuffing, at least in metals, involves severe plastic deformation, and that ceramic materials in general do not plastically deform as easily as metals do, it is reasonable to assume that ceramics are less susceptible to scuffing. However, ceramic materials are capable of plastic deformation, and other material mechanisms may be involved in scuffing failure. For effective use of ceramic materials to address scuffing problems, it will be very instructive to assess if scuffing can occur in this class of material and what mechanisms are involved.

Two variants of Y_2O_3-stabilized ZrO_2 alloys were used for the scuffing study; single crystal cubic ZrO_2-$9Y_2O_3$ and tetragonal ZrO_2-$3Y_2O_3$. Scuffing tests were conducted with a block-on-ring contact configuration, with ZrO_2 as the block and steel as the ring. The block is held stationary and loaded against a rotating ring partially submerged in lubricant, thereby creating a fully flooded and well-lubricated contact interface. A three-axis load cell allows measurement of normal, lateral, and traction forces. Loading and unloading are done by a fast-response pneumatic system attached to the load cell, enabling fast unloading when scuffing occurs.

Figure 1 shows the frictional behavior during the test with cubic ZrO_2 material. In this material, phenomenological scuffing (i.e. a sudden rapid increase in friction) was observed in all the tests conducted at various speeds. Prior to the final failure, the friction coefficient for each test was nearly constant in the range of 0.1 to 0.15 with occasional perturbation, especially at load change points. The friction coefficients for tests conducted at higher speeds are slightly lower because of the formation of a lubricant fluid film with higher thickness. Although the friction behavior is typical of what is observed during scuffing tests with metals, the final failure occurred by fracture of the cubic ZrO_2 ceramic block, as opposed to the typical severe plastic deformation for metals. In all the tests with cubic zirconia, the sudden rise in friction at the end is always accompanied by the block specimen breaking into two pieces.

The frictional behavior during the test with tetragonal ZrO_2 blocks is shown in Figure 2. For this material, all the tests at various speeds usually started with a relatively high friction coefficient (about 0.2), but gradually decreased to a near steady value in the range of 0.05 to 0.07. Like the cubic material, occasional perturbations in the friction occurred at load changes, but unlike the cubic material, an irreversible sudden rise in friction was not observed at the end of the test to signify the occurrence of scuffing. Indeed, phenomenological scuffing did not occur in all the tests with tetragonal ZrO_2 material up to the maximum speed and load range of our test rig. Because of the high severity of contact in tests with tetragonal ZrO_2 material, a considerable amount of heat was generated, as indicated by the excessive smoking of the lubricant in all cases.

As shown in Figure 3, the cubic material exhibited extensive cracking, generally oriented perpendicular to the sliding direction. There was evidence of little or no plastic deformation. The tetragonal material, on the other hand, underwent significant plastic deformation and limited cracking (Figure 4). This difference is in spite of a significantly higher severity of contact during the test with tetragonal material. The observed plastic deformation of the tetragonal material reflects the operation of several possible deformation mechanisms during the progressively increasing contact severity that occurs in the scuffing test. At the initial stage of relatively low contact stress, ferroelastic domain switching by reorientation of tetragonal domains is responsible for plastic deformation. A crystal is ferroelastic if it has two or more stable orientation states that can be readily changed from one to another when subjected to mechanical stress. Single-crystal tetragonal ZrO_2-$3Y_2O_3$ has been shown to readily deform plastically by ferroelastic domain switching. At high contact stress, plastic deformation of tetragonal material can also occur by a phase transformation process, from tetragonal to monoclinic (t→m). This transformation-induced plasticity is stress induced and is accompanied by a volume increase that imposes compressive stresses, thereby suppressing cracking and fracture. This is indeed the mechanism for the transformation toughening of ZrO_2 or ZrO_2 containing structural ceramic materials and composites. In the present study, x-ray diffraction from the wear track and the non-contact areas of the tetragonal material showed the presence of monoclinic phase in the wear track (Figure 5). Thus, the plasticity observed in the tetragonal ZrO_2 material during scuffing test is partially due to t→m phase transformation in the contact area.

X-ray Characterization of Boundary Films

During the past year, the effort on boundary film characterization was devoted to the development of an x-ray accessible tribo-tester. Such a system is needed for in-situ characterization of boundary films at APS with various available x-ray-based surface analytical techniques.

Figure 6 shows a picture of the new x-ray accessible tribo-tester system, which combines a commercial pin-on-disc high-temperature test rig and an X-ray fluorescence (XRF) detector. A new 30-kV X-ray source was integrated into the system. XRF analysis can be conducted concurrently with friction and wear testing. Both the XRF analysis and the friction data collection are done by the same computer, making it possible to correlate friction behavior with surface chemical changes as indicated by XRF. A schematic of x-ray fluorescence analysis of the wear track during testing is shown in Figure 7.

Figure 8 shows a typical result of friction test with a model lubricant of poly-alpha olefin (PAO) with 1% MoDTC and ZDDP oil additives. The variations of the Zn and Mo atom concentration on the disc surface and the friction coefficient with test time are shown. Figure 9 is an optical image of the tribochemical films formed during the test.

Conclusions

During FY2006, the efforts on this project were focused on the study of scuffing mechanisms in ceramic materials. In the cubic zirconia material, “scuffing” occurred by a sudden catastrophic fracture, instead of the severe plastic deformation typical for metallic materials. The tetragonal zirconia material underwent no sudden catastrophic failure in spite of much higher contact severity during the test. This behavior is the result of sequential operation of several frictional stress dissipation mechanisms of plastic deformation. Ferroelastic domain switching occurred at lower loads, followed by tetragonal to monoclinic phase transformation and finally deformation by slip at elevated temperatures toward the end of the test. Based on the results of the present study, materials with multiple sequential dissipation mechanisms are expected to exhibit higher scuffing resistance.

In the area of tribochemical film characterization, a new X-ray accessible tribo-tester system was designed and constructed. In initial tests with the new rig, the variation of Zn and Mo atom concentration in the surface film as a function of test time was determined concurrently with the friction coefficient. This in-situ test system will be used to determine the boundary film formation and loss rates during sliding contact of a lubricated surface.

Publications

1. O. O. Ajayi and J. Hershberger, “In-situ characterization of boundary films by X-ray,” Presented at International conference on Frontiers in Boundary Lubricating Films, Lyon, France, April 9-14, 2006.

2. J. Hershberger, O. O. Ajayi, and G. R. Fenske, “X-ray accessible tribo-tester as a surface engineering tool”, Presented at STLE Annual Meeting, Calgary, Canada, May 7-11, 2006.

3. O. O. Ajayi, “Assessment of scuffing resistance of sliding surfaces,” Presented at STLE Annual Meeting, Calgary, Canada, May 7-11, 2006.

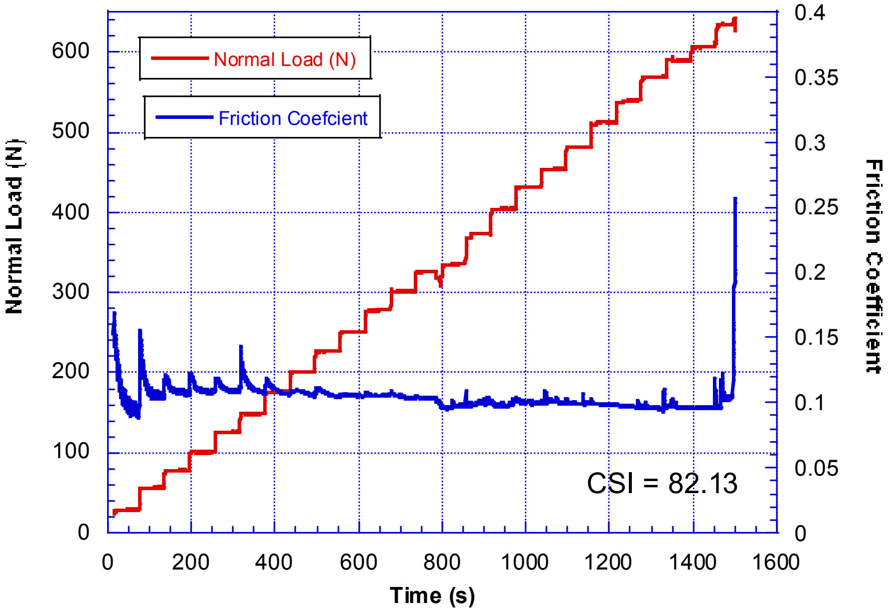

Figure 1. Friction variation during scuffing test with cubic zirconia

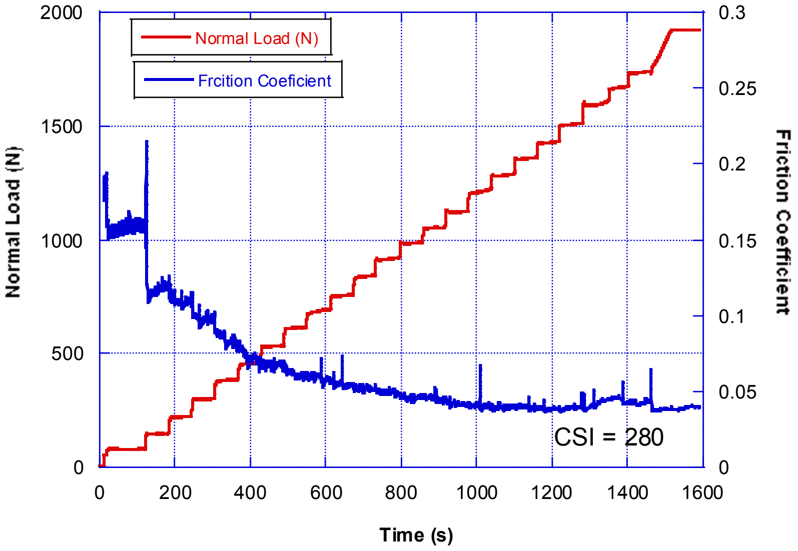

Figure 2. Friction variation during scuffing test with tetragonal zirconia

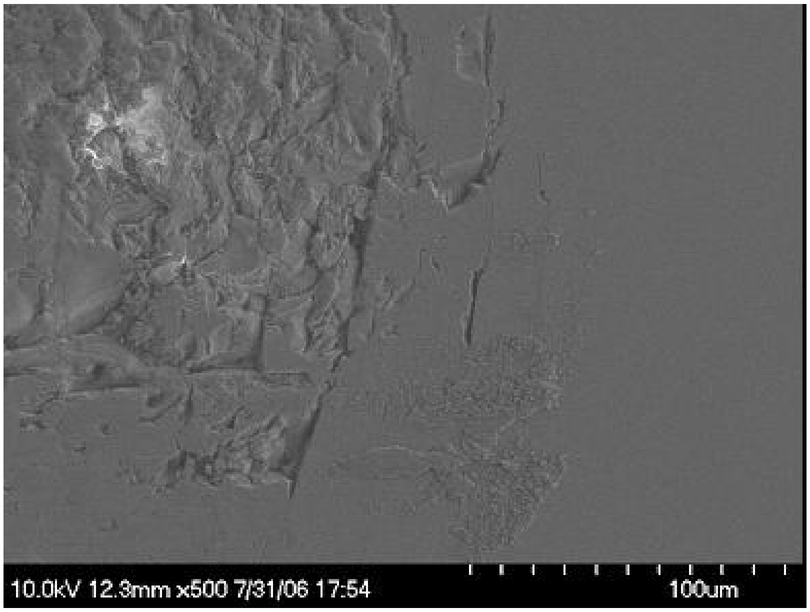

Figure 3. SEM micrograph of scuffed surface of cubic zirconia

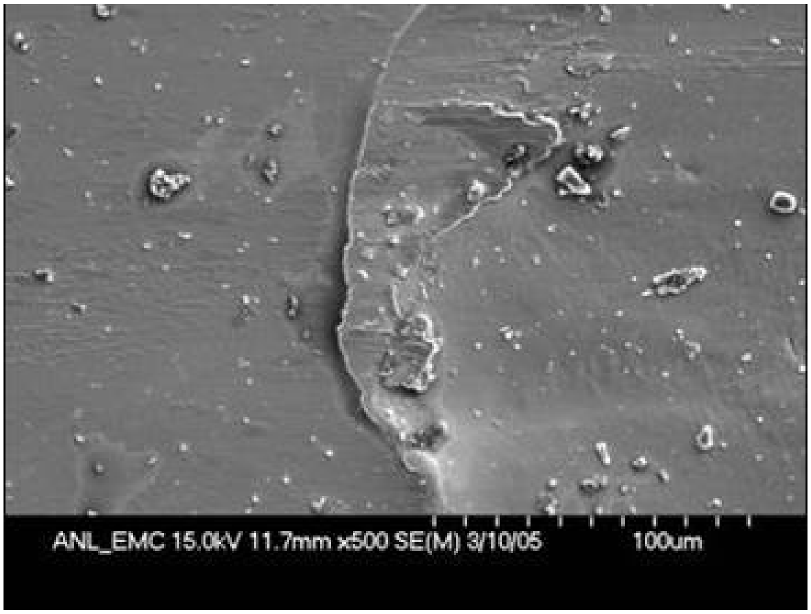

Figure 4. SEM micrograph of scuffed surface of tetragonal zirconia

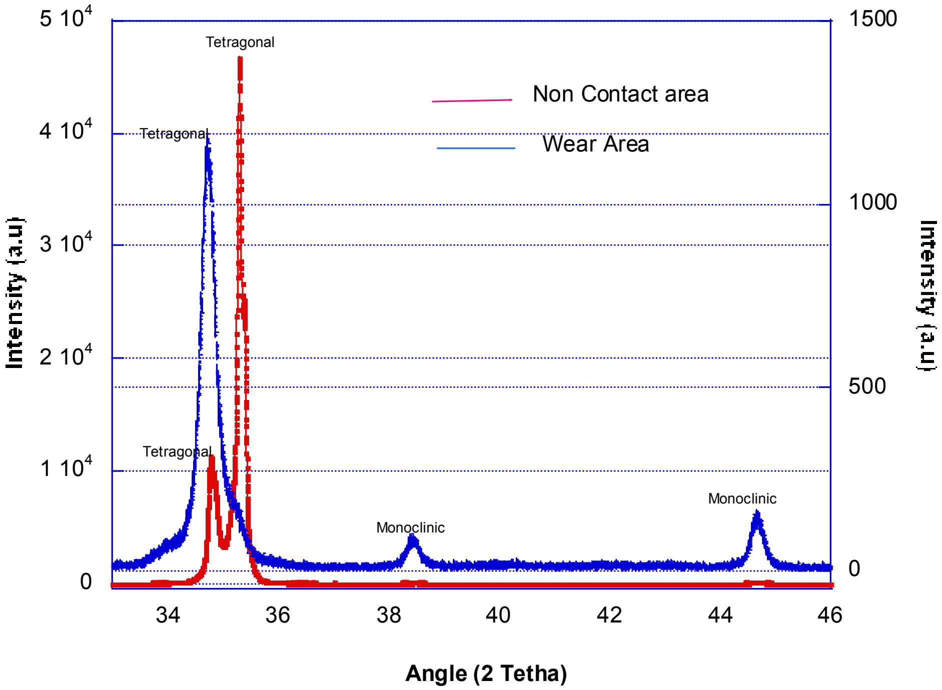

Figure 5. X-ray diffraction spectra for tetragonal zirconia showing phase transformation after scuffing test

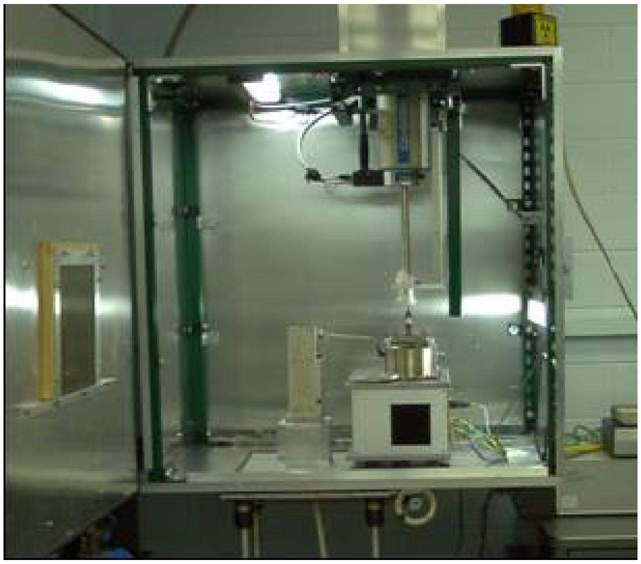

Figure 6. Picture of x-ray accessible tribo tester system

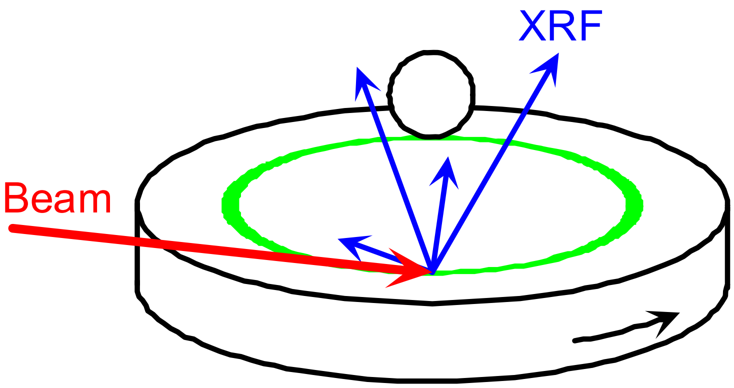

Figure 7. Schematic diagram of in-situ x-ray fluorescence analysis during tribo testing

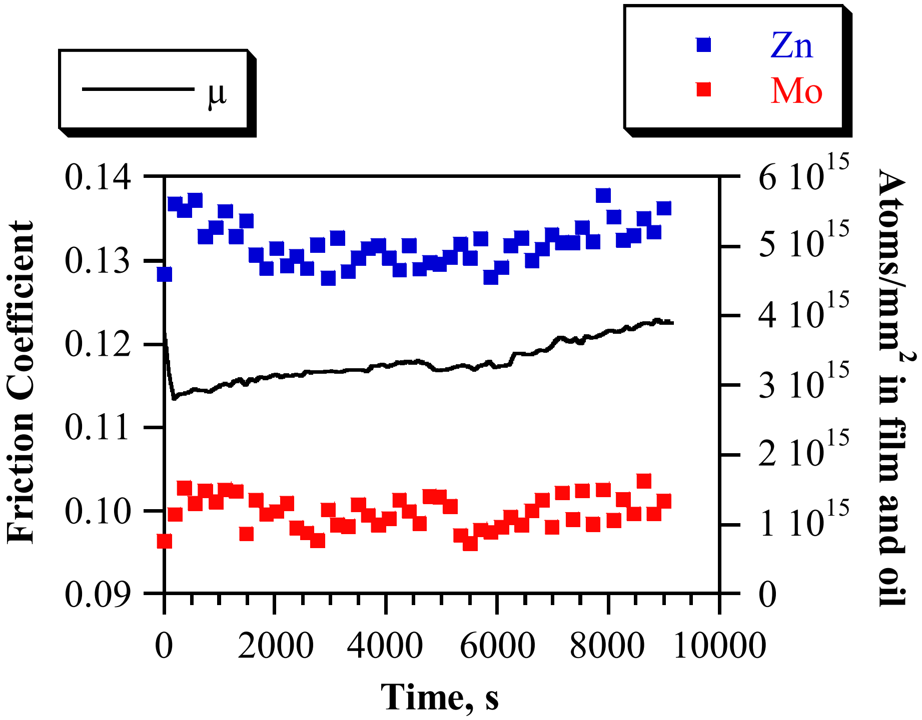

Figure 8. Variation of friction coefficient and Zn and Mo atom concentration during tribo testing with model lubricant

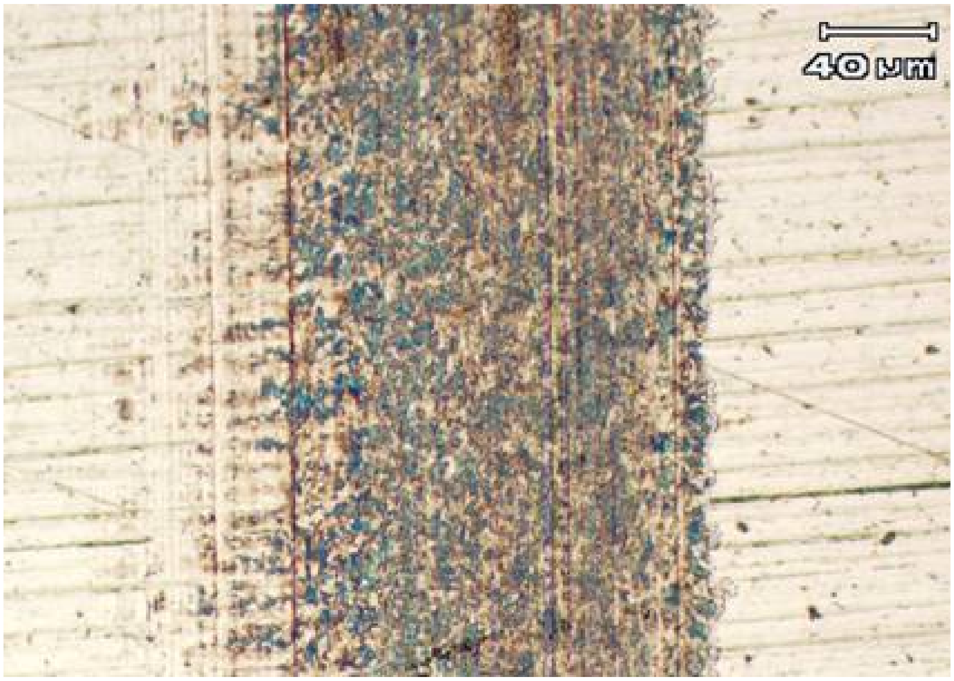

Figure 9. Optical micrograph of tribo-chemical film formed on disc surface during test with a model lubricant

III.B. Parasitic Engine Loss

Principal Investigators: George Fenske, Robert Erck, Ali Erdemir, and Layo Ajayi
Argonne National Laboratory
Argonne, IL 60439
(630) 252-5190, fax: (630) 252-4798, e-mail: gfenske@anl.gov

Technology Development Area Specialist: Lee Slezak
(202) 586-2335, fax: (202) 586-2476, e-mail: Lee.Slezak@hq.doe.gov

Field Project Manager: Jules Routbort
(630) 252-5065, fax: (630) 252-4798, e-mail: routbort@anl.gov

Participants
Robert Erck, Argonne National Laboratory
Layo Ajayi, Argonne National Laboratory
Ali Erdemir, Argonne National Laboratory
James Kezerle, Ricardo Engineering
Lee Oberto, Ricardo Engineering
Zoran Fillipe, University of Michigan

Contractor: Argonne National Laboratory
Contract No.: DE-AC02-06CH11357

Objective

- Develop and integrate mechanistic models of engine friction and wear to identify key sources of parasitic losses as functions of engine load, speed, and driving cycle.
- Develop advanced tribological systems (lubricants, surface metrology, and component materials/coatings) and model their impact on fuel efficiency with a goal to improve vehicle efficiency by 3% in FY12. Develop engine component maps to model the impact on fuel efficiency for use in analytical system toolkits.
- Develop database of friction and wear properties required for mechanistic friction and wear models –coatings, lubricant additives, and engineered surface textures.
- Validate mechanistic models by performing instrumented, fired-engine tests with single- and cylinder engines to confirm system approaches to reduce friction and wear of key components.
- Integrate models into vehicle system codes (PSAT).

Approach

- Predict fuel economy improvements over a wide range of oil viscosities using physics-based models of asperity and viscous losses.
- Model changes in contact severity loads on critical components that occur with low-viscosity lubricants.
- Develop and integrate advanced low-friction surface treatments (e.g., coatings, surface texturing, and additives) into tribological systems.
- Measure friction and wear improvements on advanced lab rigs and fired engines to confirm model calculations.
- Develop component maps of parasitic energy losses for heavy-vehicle system models.

Accomplishments

- Modeled the impact of low-friction coatings and low-viscosity lubricants on fuel savings (up to 4%) and predicted the impact of low-viscosity lubricants on the wear/durability of critical engine components.
- Developed experimental protocols to evaluate the friction and wear performance of advanced engine materials, coatings, and surface treatments under prototypical/piston/ring/environments.
- Initiated lab testing of surface modified ring and liner components to optimize treatments for single-cylinder engine tests.

Future Direction

- Apply superhard and low-friction coatings on actual engine components and demonstrate their usefulness in low-viscosity oils.
- Optimize coating composition, surface finish, thickness, and adhesion to achieve maximum fuel savings.
- Evaluate the impact of advanced lubricant additives on asperity friction.

Introduction

Friction, wear, and lubrication affect energy efficiency, durability, and environmental soundness of critical transportation systems, including diesel engines. Total frictional losses in a typical diesel engine may alone account for more than 10% of the total fuel energy (depending on the engine size, driving condition, etc.). The amount of emissions produced by these engines is related to the fuel economy of that engine. In general, the higher the fuel economy, the lower the emissions. Higher fuel economy and lower emissions in future diesel engines may be achieved by the development and widespread use of novel materials, lubricants, and coatings. For example, with increased use of lower viscosity oils (that also contain lower amounts of sulfur- and phosphorus-bearing additives) the fuel economy and environmental soundness of future engine systems can be dramatically improved. Furthermore, with the development and increased use of smart surface engineering and coating technologies, even higher fuel economy and better environmental soundness will be feasible.

Integration of advanced lubricant chemistries, textured/superfinished surfaces, and advanced component materials and coatings necessitates a systems approach. Changes in one system component can readily change the performance of other system components. For example, application of a hard coating on a liner to improve its durability may decrease the durability of the mating rings. Also, lowering the viscous drag will cause certain components (e.g., bearings) to operate under boundary lubrication regimes not previously encountered, resulting in accelerated degradation. A systems approach is required to not only identify what are the critical components to address in terms of energy savings, but also to identify potential pitfalls and solutions.

The main goal of this project is to develop a suite of software packages that can predict the impact of smart surface engineering technologies (e.g., laser dimpling, near frictionless carbon, and superhard coatings) and energy-conserving lubricant additives on parasitic energy losses from diesel engine components. The project also aims to validate the predictions by comparison with experimental friction and wear data from Argonne National Laboratory. Such information will help identify critical engine components that can benefit the most from the use of novel surface technologies, especially when low-viscosity engine oils are used to maximize the fuel economy of these engines by reducing churning and/or hydrodynamic losses. A longer-term objective is to develop a suite of computer codes capable of predicting the lifetime/durability of critical components exposed to low-viscosity lubricants.

Since FY 2003, Argonne and Ricardo, Inc., have collaborated to identify engine components that can benefit from low-friction coatings and/or surface treatments. The specific components considered included rings, piston skirt, piston pin bearings, crankshaft main and connecting rod bearings, and cam bearings. Using computer codes, Ricardo quantified the impact of low-viscosity engine oils on fuel economy. Ricardo also identified conditions that can result in direct metal-to-metal contacts, which, in turn, can accelerate engine wear and asperity friction. Efforts were also initiated to identify approaches to validate the predictions under fired conditions.

Argonne also worked on the development and testing of low-friction coatings under a wide range of sliding conditions using low- and high-viscosity engine oils. These coatings (such as near frictionless carbon) as well as laser-textured surfaces were subjected to extensive friction tests using bench-top rigs. The test conditions (i.e., speeds, loads, and temperatures) were selected to create conditions where direct metal-to-metal contacts will prevail, as well as situations where mixed or hydrodynamic regimes will dominate. Using frictional data generated by Argonne, Ricardo estimated the extent of potential energy savings in diesel engines and identified those components that can benefit the most from such low-friction coatings and/or surface treatments. Argonne developed a test rig to simulate engine conditions for piston rings sliding against cylinder liners – one of the major sources of parasitic energy losses identified in Ricardo's studies. Wear data generated by Argonne can be used to develop models and computer codes that predict the lifetime/durability of diesel engine components. Several techniques were surveyed to validate the models. A fired, single-cylinder, fixed-sleeve technique available at the University of Michigan was selected to provide in-situ friction force measurements between the cylinder liner and the piston/piston ring assembly – a major source of friction losses. Efforts also progressed on the development of a benchtop ring-on-liner rig for testing in the tribological conditions under which advanced surface treatments and additives optimally function.

During FY 2006, Ricardo and the University of Michigan completed design of the single-cylinder test bed and initiated fabrication of components necessary to measure combustion chamber friction forces under fired conditions. In addition, Argonne initiated benchtop tests on experimental and commercial-engine lubricant additives.

Results

Phase I and Phase II activities for this project focused on modeling the impact of low-friction surfaces and low-viscosity engine lubricants on friction losses and fuel economy. Figure 1 [1] summarizes the results of Ricardo's calculations on the impact of boundary friction and engine lubricant viscosity on the fuel economy of a heavy-duty diesel-powered vehicle. These curves are based on detailed calculations of the friction mean effective pressure (FMEP) for the piston rings and skirt, valve-train components, and engine bearings under a range of driving conditions. The results predicted fuel savings up to 4-5%, depending on lubricant viscosity grade and asperity friction.

Plans were established for a Phase III activity to validate the calculations using measurements with a fired diesel engine. Several approaches were considered, including a) direct fuel consumption measurements in a running, mass-production, diesel engine, b) friction force measurements in a running, mass-produced engine, and c) friction force measurements in a running, single-cylinder test engine. The last approach was selected due to considerations of simplicity and ability to accurately measure friction forces.

Three different methods were considered to measure forces during operation. A force-difference method based on cylinder-pressure and connecting-rod strain measurements and a floating liner method based on load cell measurements of liner forces were ruled out due to large statistical errors associated with the first method and gas leakage and structural vibration issues associated with the second method. In the end, a fixed-sleeve method (Figure 2) was chosen. The fixed-sleeve method employs strain gauges applied to a rigidly supported cylinder liner to measure the friction forces transmitted to the cylinder liner from the piston skirt and rings.

The fixed-sleeve method will be used with a Ricardo Hydra test engine installed at the University of Michigan. To this end, a sliding sleeve will be inserted inside a modified Hydra cylinder liner. The sleeve will be fixed radially near its top by a supporting wire and will be restrained axially by a locknut at its bottom. Axial forces on the sleeve will be transmitted through the locknut joint to the liner. Friction forces will be calculated from the measured liner strain.

The contract with Ricardo and the University of Michigan has been established, and Phase III activities are underway. The first task of Phase III involves adapting the Hydra engine to accept an instrumented fixed sleeve (strain gauges and thermocouples). Figure 3 shows a photograph of the Hydra engine mounted on the Cussons-dyno test stand at the University of Michigan. Current activities for this task are focused on design, fabrication, and instrumentation of combustion chamber components (in collaboration with Ricardo and Mahle). The second task will involve establishing a baseline to compare the engine to obtain friction measurements at different engine conditions (speeds and loads) and lubricant viscosities. Part of this task will involve in-situ friction measurements of unformulated basefluids (at two viscosities) with and without low-friction additives. Subsequent tasks will concentrate on measurements using low-friction technologies (e.g., low friction coatings, superfinishing, textured surfaces, and low-friction additives).

Experimental activities at Argonne concentrated on the development of a ring-on-liner rig to measure friction in an effort to confirm/validate asperity friction values used in the Ricardo models, to measure the boundary friction of advanced low-friction technologies on prototype ring and liner components, and to integrate/optimize advanced technologies for rings, liners, and pistons. The test system uses segments of rings and liners obtained from standard rings and liners, currently 137- mm and 145-mm diameter liners – comparable to those modeled by Ricardo. The system is capable of applying loads up to 2000 N, speeds up to 10 Hz, strokes up to 37 mm, and temperatures to 300°C. Data recorded during the tests include friction forces, temperature, ring position, and contact resistance (between the ring and liner) at rates in excess of 2000 Hz. High data acquisition rates (above 2000 Hz) are used to obtain “flash shots” of the friction, position, and contact resistance during each stroke. Such information provides detailed data required to determine which lubrication regime (boundary, mixed, or hydrodynamic) is dominant during the stroke.

Figure 4 shows the friction as a function of time for a stock CrN-coated ring sliding against a stock liner with a commercial, formulated 10W-30 synthetic lubricant (top) and a concentrated commercial additive package (bottom). The tests in Figure 4 were performed with a load of 150 N at a reciprocating speed,15 rpm, sufficiently low to ensure boundary lubrication over the entire travel or the baseline lubricant (top curve). At the point of stroke reversal where the speed is near zero with the baseline fluid, boundary lubrication is dominant with a friction coefficient around 0.12 to 0.15. As the velocity increased (near midstroke), the friction of the top curve remained high, indicating that the lubrication was dominated by boundary friction. The bottom curve in Figure 4 shows a significantly lower friction behavior than that of the baseline fluid – at reversal, the friction is around 0.09, but them rapidly decreases to around 0.05. The difference can be attributed to the high viscosity of the additive package (bottom curve). The high viscosity resulted in a rapid transition to mixed/hydrodynamic lubrication, thus providing lower friction. Overall, the friction was reduced by approximately 60 %. At higher speeds (150 rpm), the friction was also reduced by 60 % [2].

Other Phase III activities involve cost/benefit studies of treating specific engine components. Figure 5 shows cost/benefit analysis based on the Ricardo models. Fuel savings on the order of 100 gallons per 1000 hours of operation can be realized by using technologies (e.g., a low friction coating, low-friction additive, or surface texturing) that reduce boundary friction by 90% and a low-viscosity (e.g., SAE 20 wt) engine lubricant. At a price of $3/gallon, one would realize a cost savings of $300 per 1000 hours of operation, which should more than offset the cost of many low-friction coating treatments.

Summary

Computer simulation of parasitic energy losses in diesel engines indicate that fuel savings up to 5 % can be achieved through the use of low-viscosity engine lubricants and low-friction surface treatments. Work is underway to experimentally validate the models by tests with a fired, single-cylinder diesel rig outfitted with an instrumented fixed -sleeve to measure the friction forces continuously as a function of crank angle.

A rig-on-liner test rig was developed and brought on-line to validate the friction coefficient data used to model the parasitic friction losses, as well as to optimize advanced surface modification technologies for engine applications. Tests are underway to evaluate two technologies: a boric-acid based lubricant additive and a surface texturing technique. Both technologies, in addition to the use of low-friction coatings, will be further examined and optimized in FY07 in preparation for fired engine tests on the instrumented Hydra test engine in FY08. Cost/benefit analysis indicated a saving at about $300 per 1000 hours of operation with advanced tribological systems.

References

1. Fox, I., Numerical Evaluation of the Potential for Fuel Economy Improvement due to Boundary Friction Reduction within Heavy-Duty Diesel Engines, ECI International Conf. on Boundary Layer Lubrication, Copper Mountain, CO, Aug. 2003.

2. George Fenske, Parasitic Energy Loss Mechanisms: Impact on Vehicle System Efficiency, 2006 U.S. Department of Energy Heavy Vehicle Systems Review, April 18-20, 2006, Argonne National Laboratory, Argonne, Illinois.

Acknowledgements

Argonne is managed by UChicago Argonne, LLC, for the U.S. Department of Energy under contract DE-AC02-06CH11357.

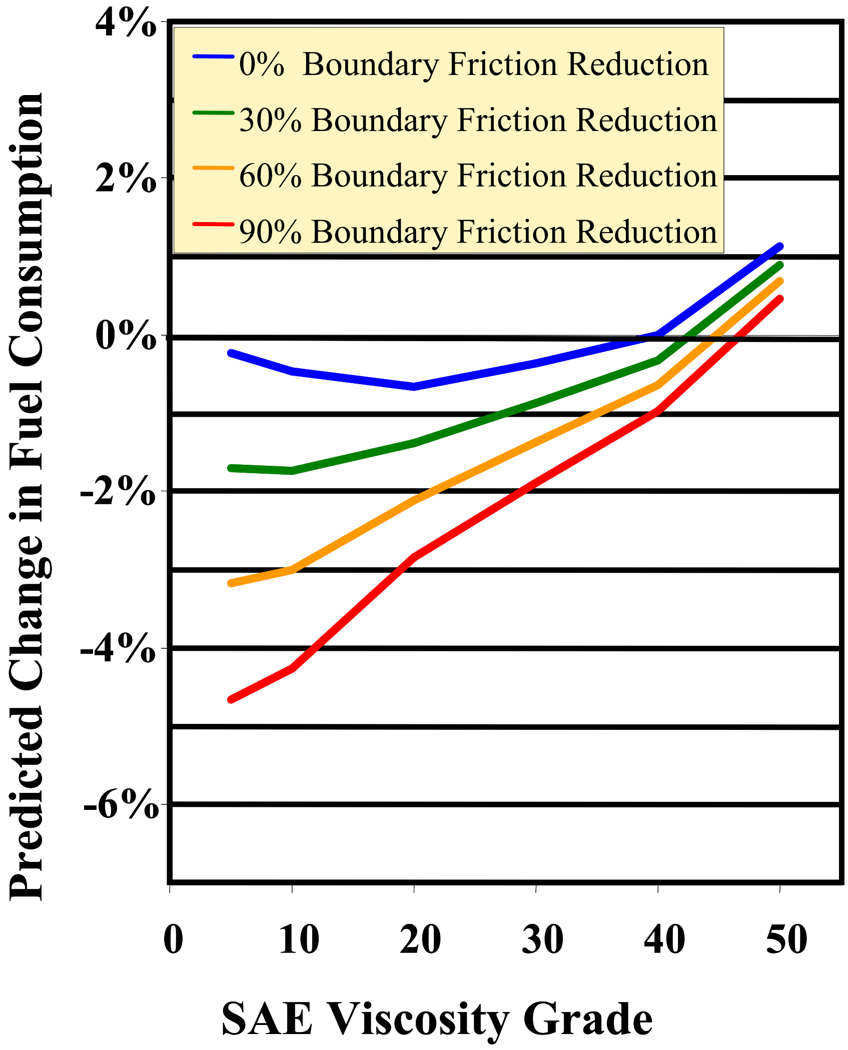

Figure 1. Predicted change in fuel economy as a function of engine lubricant viscosity and boundary friction

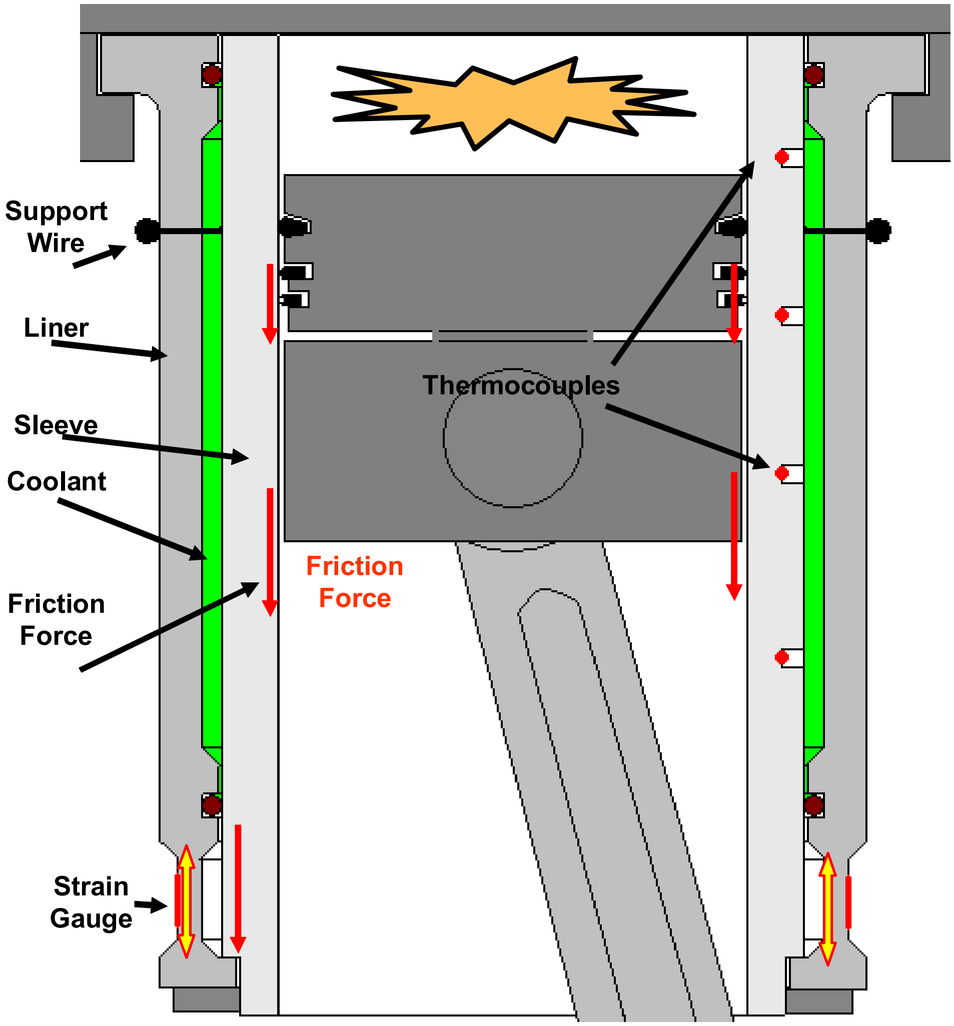

Figure 2. Schematic of fixed-sleeve method. This method will be used to continuously monitor friction forces during fired operation of a single-cylinder diesel engine.

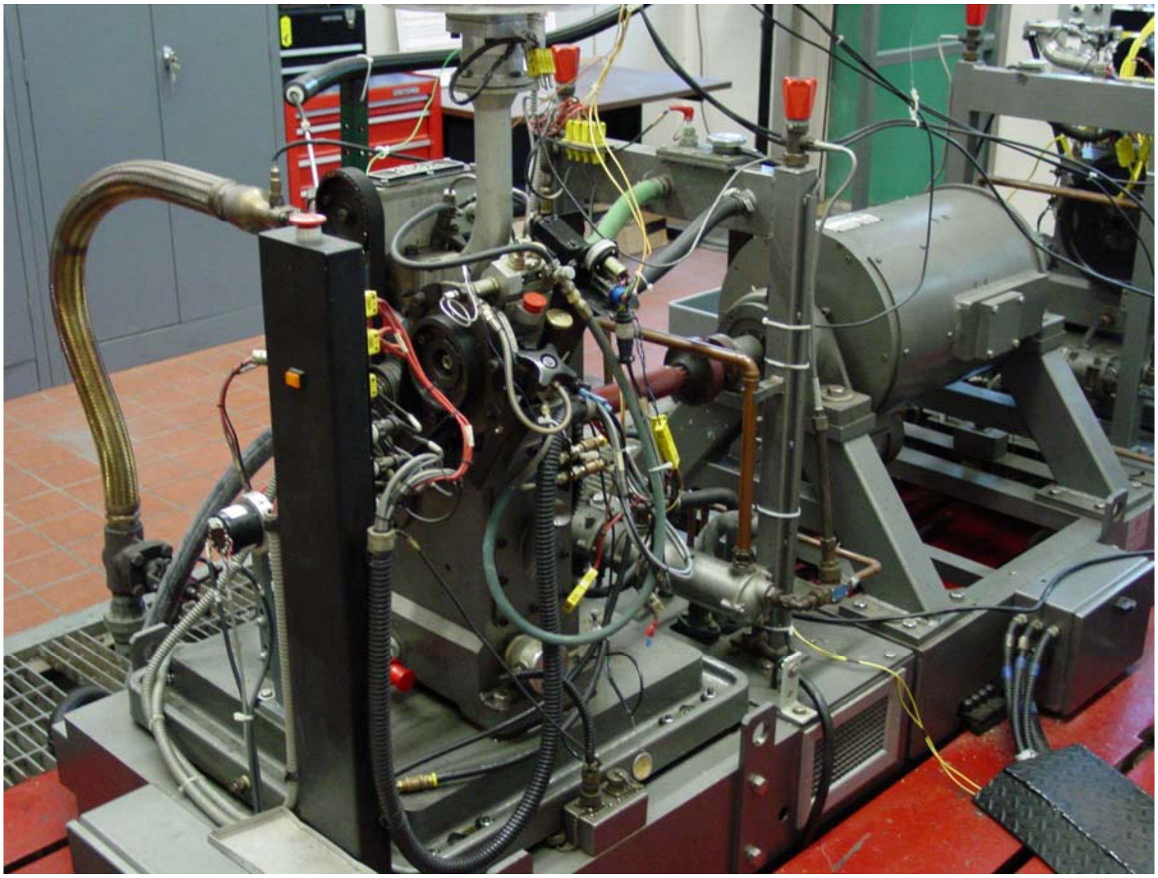

Figure 3. Photograph of the Ricardo hydra engine under modification for in-situ friction measurements (University of Michigan)

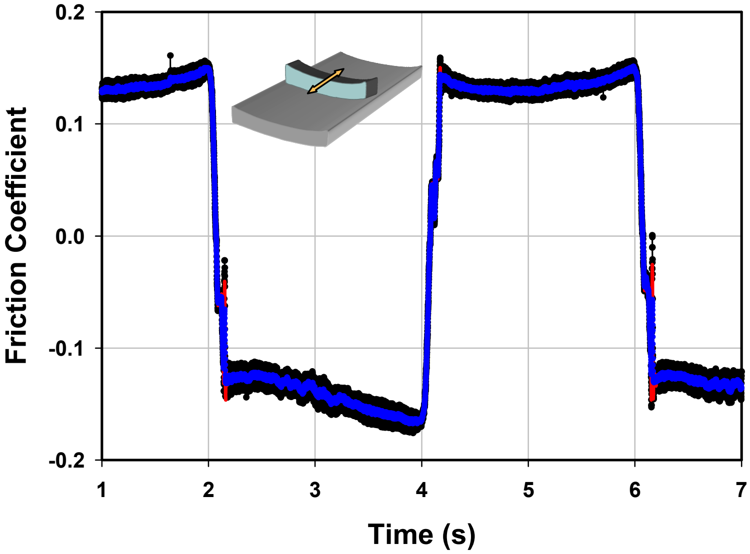

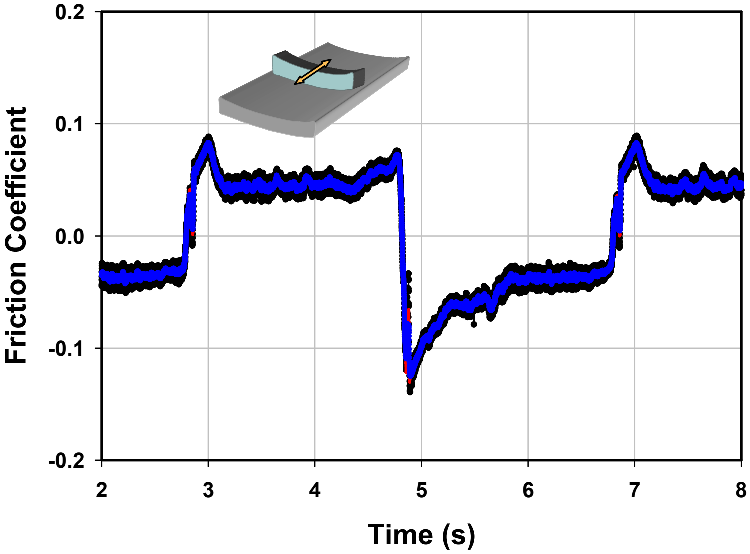

Figure 4. Friction as a function of time obtained from high-speed ring-on-liner lab tests (15 rpm, 150 N Load): Top - baseline - formulated 10W-30 synthetic, Bottom - commercial low-friction additive

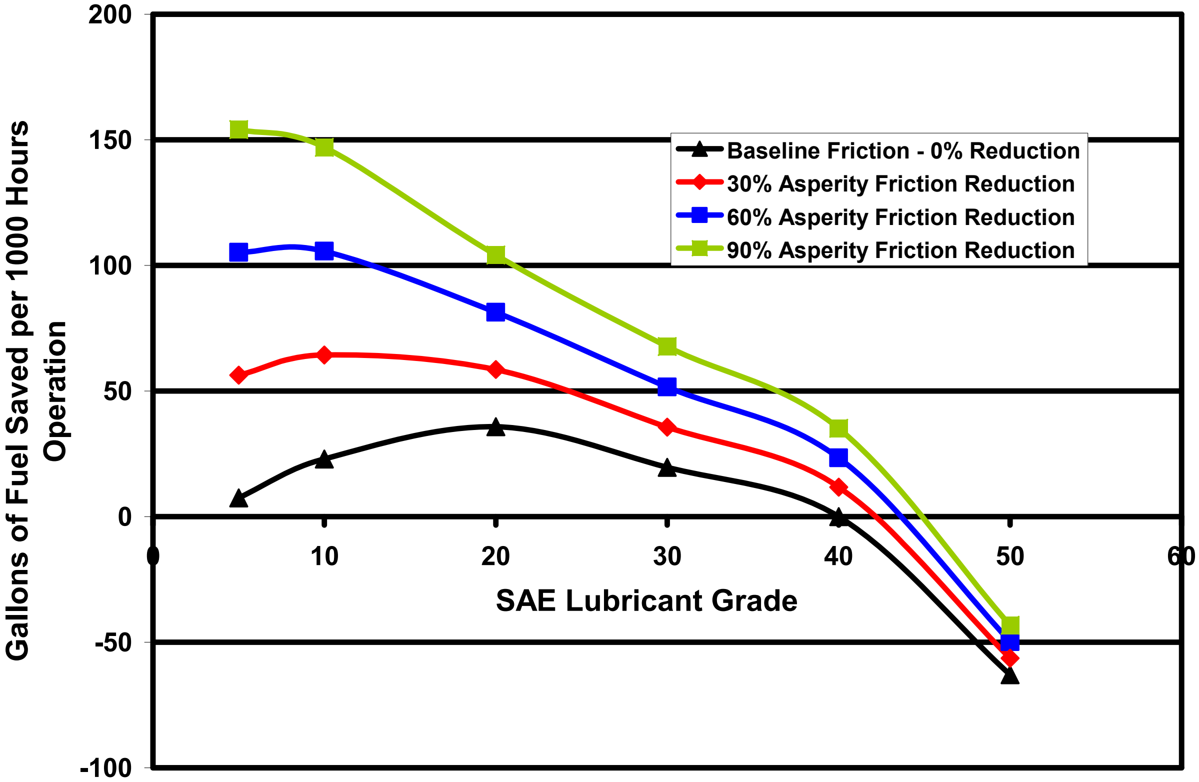

Figure 5. Fuel saved by reducing boundary friction of piston skirts as a function of lubricant viscosity

III.C. Efficiency Improvement Through Reduction of Friction and Wear in Powertrain Systems

Principal Investigator: Bohdan Lisowsky
Eaton Corporation
Innovation Center
26201 Northwestern Highway
Southfield, MI 48037
(248) 226-6219, fax: (248) 226-7166, e-mail: bohdanlisowsky@eaton.com

DOE Project Officer: John Jason Conley
National Energy Technology Laboratory
Morgantown, WV 26507-0880
(304) 285-2023, fax: (304) 285-4403, e-mail: John.Conley@netl.doe.gov

DOE Technology Development Area Specialist:
Lee A. Slezak
Office of FreedomCAR and Vehicle Technologies
U.S. Department of Energy
1000 Independence Ave., S.W.
Washington, D.C.
(202) 586-2335, fax: (202) 586-2476, e-mail: lee.slezak@ee.doe.gov

Field Technical Manager: Jules L. Routbort
(630) 252-5065, fax: (630) 252-4289, e-mail: jules.routbort@anl.gov

Participants
Jian Zhang, Diann Hua, Tom Beveridge, Caterpillar Inc.
Oyelayo Ajayi, George Fenske, Ali Erdemir, Jeff Hershberger, Argonne National Laboratory
Jane Wang, Leon Keer, Northwestern University
Dong Zhu, Zahedul Huq, Eaton Corporation, Innovation Center.

Contractor: Eaton Corporation4201 North 27th Street, Milwaukee WI 53216
Contract No.: DE-FC26-04NT42263

Objective

- To reduce friction and parasitic energy loss by 30-50% in truck transmissions and axles used in class 3-8 trucks by conducting research and development resulting in an integrated procedure for component design and analysis for minimizing friction and oil churning losses without compromise in performance and durability.
- During the first three (3) years, develop computer simulation tools for various contact geometries to predict friction, interface temperatures, wear, and other performance parameters for gears, bearings, seals, and oil churning losses. These simulation tools will be calibrated and validated utilizing coupon fixture testing and component bench testing.
- During the following two (2) years, to integrate the various simulation tools into a design procedure and prove its utility by designing specific components for transmissions and axles and conducting limited testing on dynamometers and vehicles.

- Identify potential commercialization strategies for efficiency improvement methods in transmissions and axles.

Approach

- Reduction of boundary friction through development of boundary film technologies, which involves low friction materials, coatings and lubricant additives. (see Figure 1)
- Reduction of hydrodynamic friction and churning loss via advanced lubrication technologies, improved system design, lubricant properties and surface texturing;
- Optimization of design parameters, operating conditions and surface finish processes to minimize the severity of surface contact and maximize hydrodynamic lubrication effectiveness through next-generation integrated design and analysis tools;
- Development of surface failure analysis and prediction tools and their correlation with experimental data to improve the component design for longer life and higher reliability.

Accomplishments

- Developed models to predict friction and wear of rough surface contacts and conducted limited verifications. A model for virtual texturing was also developed and results were judged appropriate based on limited experimental testing. A model for coated surfaces was developed to predict contact pressure and friction as a function of coating modulus and thickness. This model needs verification. Modeling of boundary lubrication will be done on experimental basis only as a “look-up” table to be used with other models.
- Using coupon bench testing, determined that although surface topography changes over time, significant reductions in friction could be achieved by improving original surface roughness. Surface texturing can have either positive or negative effect on friction, so careful texture design is required. Gear efficiency was evaluated using an FZG equipment and impact of additives was investigated.
- Low friction coatings tested to date have not demonstrated required durability, thus requiring further evaluations regarding optimum sub-surface characteristics, coating modulus, and thickness.
- Fuel efficiency simulations indicate that the 2.5% fuel savings can be met.

Future Direction

- Integrate all modeling modules into a design capability for prediction of friction and durability of contacting surfaces.
- Complete coupon testing and begin component testing to verify selection of specific surfaces, coatings, lubricants and additives for friction reduction without adverse effect on durability.
- Conduct limited dynamometer and field tests to verify energy efficiency gains of a selected truck driveline and develop required durability data.
- Develop commercialization approaches for the best value surface treatments and lubricant conditions.

Introduction

This report is a second annual report on the project. The FY2005 Annual Report described the current technologies utilized in truck powertrains regarding gears, bearings and seals. The sources of parasitic losses in drivetrains had been identified as:

- Gear tooth contact friction: 25-70%
- Oil churning: 15-35%
- Bearings and thrust washers: 10-25%
- Seals/other parts (as shift yoke/shaft): 10-20%

The FY2005 Annual Report also documented the project structure, project team, and team members’ roles for this project, which remained unchanged for FY2006. The technical progress was reported under specific headings, which focused on the effect of various parameters on friction reduction. These same headings are used in this report to document progress in FY2006 and allow for easy and continuous tracking of technical progress achieved in the FY2006.

This progress report uses same topical areas for progress presentation and allows for easy and continuous tracking of technical progress achieved since the start of the project. Each topic combines theoretical and experimental results, as appropriate, to help the reader to easier comprehend and integrate project activities and results.

Effect of Surface Topography and Surface Texture on Friction

The work conducted in FY2006 concentrated on the effect of running time and resultant wear on friction. Also, modeling of texture effect was initiated and some textured and engraved surface effects were experimentally evaluated in sliding as well as in rolling contact fatigue (RCF), which allows for simultaneous sliding and rolling conditions at contacting surface, typical of gear tooth contact.

Figure 1 shows the effect of running time on friction and the resultant change in topography due to wear. Similar effect has been observed in lubricant testing using the Wedeven friction testing, as the rest required a minimum of 3 “break-in” runs for the friction to stabilize. Therefore, the modeling efforts required ability to account for that change in topography due to wear. This is reported in the next section. Texture effects can also have impact on friction. Experiments with macro-texturing, such as engraving and shot peening, did not show significant improvements, but the effect of texture directionality with respect to rolling and sliding direction is critical. The effect of laser micro-texturing was reported in the previous year-end report. The results of modeling regarding dimple characteristics are shown in Figure 2. This approach allows for generation of ‘synthetic’ dimples and studying their effect on friction and on durability, which is impacted by contact ration resulting in contact stress.

$$D = \frac{dW}{dt} = k\frac{p_C V}{H} = k\frac{(pW_C)V}{H}$$

Effect of Surface Topography on Durability

In order to generate a commercially meaningful integrated model, surface durability must be incorporated so that optimization of the low friction and high durability can be achieved. In the 2005 report, a simplified model was described based on the approach of knowing the maximum stress location and magnitude is known, then the crack formation and growth is predicted using the FATG3D model, previously developed at Northwestern University, which yields an accurate analysis of intensity factors and it is capable of dealing with multiple cracks and their coalescence into larger cracks or one large crack. However, contact surface topography changes as a function of running time, thus requiring new input data for the FATG3D model. Therefore, a wear model development was initiated. The wear model incorporates only the effects of topography and the wear rate coefficient is a combination of various effects, such as lubricant effects, boundary layer effects, and thermal effects. The total wear is on a surface is expressed in the following equation:

Where:

$W_C = f(\lambda) = f(h/\sigma)$ (contact load ratio)
H - surfaces hardness (Gpa)
k - wear coefficients for the surface
V – rolling speed (mm/s)
p – Contact load (Gpa)
σ – composite surface roughness (μm)
h – lubricant film thickness (mm)

Figure 3 shows the change in surface topography as well as the resultant change in friction, contact ratio, amount of wear, and dimensionless film thickness. The contact conditions for this simulation are shown in the figure.

Some initial calibration of the model was done using three-ball-on-ring testing and measuring scar dimensions. That test showed that the assumed wear coefficient was about a factor of 14 greater than actual wear. So actual measurement of the wear scar could be used for model calibration. However, it must be recognized that the wear coefficient is specific to the conditions of the test, including lubricant, loads, speeds, and other parameters. Therefore, specific selections of surface topography, and other conditions will be made for future evaluations and modeling. Figure 4 shows the result of this calibration test.

Also, residual stress effects due to localized plastic deformation of contacting asperities will influence the stress state of the contacting surfaces. Residual stress distribution prediction model has been developed and a typical result of sub-surface distribution is shown in Figure 5 along with the 3-D distribution of plastic deformation due to rough contact with a mating surface.

Lubricant Effect on Friction and Power Loss

There is a significant potential to reduce contact friction by developing new formulations. In the 2005 report, the effect of lubricants on friction and use of specific additives was described. In 2006, specific lubricant selection was conducted and the effect on power loss measured using an instrumented FZG standard gear testing machine. Eighteen lubricants with three surface conditions were evaluated. Figure 6 shows reduction in power loss as a function of pinion speed. It is noted that there is a strong function of speed as well as a particular lubricant selection.

Regarding the boundary film modeling, a decision was made during 2006 project year, that this task is too complex for theoretical modeling and that a “look-up” tables will be developed for specific few lubricants of interest at selected test conditions of interest for transmissions and axles. The development of these look-up tables was initiated. In addition, 4-ball testing was conducted using some commercially available antiwear and antifriction commercial additives under mild wear conditions. Of he additives tested, Molyvan L, which has Mo, S, and P as additives, was best for wear resistance. Figure 7 shows a summary of results.

Low Friction Coatings

A number of coatings were evaluated on the modified “pin-on-disc” test using line contact condition and stepped loading condition. Argonne leads this technological area and provided ring samples coated with ‘near-frictionless coating’ (NFC) and nano-composite coating. The results are shown in Figure 8 with an unusual behavior of the nano-coating as load changes occurred, which exhibited lowest friction. However, rolling contact fatigue testing was not successful as the coatings failed by scuffing under 25% sliding condition. These failed rings are under investigation to determine if the failure was due to delamination or some other effect, such as lack of boundary film formation.

Modeling of friction and contact pressure as a function of coating thickness and modulus difference with substrate was developed for smooth surfaces. These relationships are shown in Figure 9.

The assessment is that use of high modulus coatings will result in least friction but there may have durability issues, especially for asperity contact in real rough surfaces of different hardnesses.

Fuel Economy Modeling

Preliminary fuel economy modeling was conducted using a US-1 route and applying engineering judgments as to potential efficiency improvements in axles and transmissions as a function of speed and load represented by the terrain of US-1. Figure 10 indicates that the fuel economy target of 2.5% is possible based on the conservative, likely, and optimistic efficiency improvements. The literature survey conducted in 2006 did not result in any reported correlations of friction reduction on efficiency of truck transmissions or axles. Future project years will evaluate and correlate these effects.

Summary

Highlights of the progress during FY 2006 are:

1. Rough surface contact models were extended to include texturing, residual stress, and wear prediction.

2. Experimental testing supported model predictions and limited calibrations of the models were initiated

3. Modeling of boundary lubrication films will be based don “look-up” tables to be developed for specific tribological conditions only.

4. Testing of coated surfaces identified shortcomings in coating durability, but friction reduction has potential.

5. Four quarterly reports, and six deliverables reports were submitted on time. Two Phase I Reviews were conducted at DOE Headquarters.

Conclusions

Surface contact models to predict friction have been developed, but require more calibration. Boundary film modeling will be done by developing experimental look-up tables for selected lubricants and contact conditions. Also, a model for prediction of sub-surface residual stress distribution will enhance pitting fatigue modeling. Models for coated surfaces and textured surfaces are under development with encouraging initial results. Preliminary wear models show much promise, but wear coefficients are a function of complex variables, which need to be experimentally verified. Because of that, only selected conditions will be used for experimental testing in future years.

Experimental results support model predictions for friction and wear, but more statistical data needs to be accumulated for model verification and better assessments of friction differences among various surface/lubricant/texture/roughness conditions.

Coatings have not yet demonstrated reliable behavior either as friction reduction or durability enhancers. More study is required, as the test results to date show potential for friction reduction. Modeling of coated surface contacts (friction and stress) conditions will be instrumental in proper selection of both the coating and its thickness for optimization.

Initial fuel economy simulations indicate that a project goal of 2.5% savings is attainable. Experimental work in future years will validate that model result.

Future work in FY 2007 will be focused on development of boundary film look-up tables, development of specific wear coefficients, and integration of all model modules into a preliminary predictive tool. Specific model calibration and validation will be done by first using them for prediction purpose and then conducting selected testing to obtain predicted results. Also, additional experimental work will be done for the purpose of sump fill optimization to minimize churning losses.

Publications

Publications and submissions for publications, and presentations, partially funded by this project, are identified below:

1. Bair, S., Liu, Y. and Q. Wang, "The Pressure-Viscosity Coefficient for Newtonian EHL Film Thickness with General Piezoviscous Response," Journal of Tribology.

2. F. Wang, L. M. Keer, and Q. J. Wang, "Analysis of 3D Elastic-Plastic Contact with Machined Rough Surfaces," submitted to Journal of Tribology

3. Liu, S., Chen, W.W, Hua, D., and Wang, Q., "Tribological Modeling: Application of Fast Fourier Transform," submitted to Tribology International.

4. Wang, F., Keer, L.M., and Wang, Q., "Analysis of 3D Elastic-Plastic Contacts with Machined Rough Surfaces," Journal of Tribology.

5. Martini, A., Velter, G., Keer, L.M., and Wang, Q., "Maximum Stress Prediction for Rough, Sinusoidal and Textured Surfaces," Tribology Letters.

6. Liu, Y., Wang, Q., Hu, Y., Wang, W., and Zhu, D., "Effects of Differential Schemes and Mesh Density on EHL Film Thickness in Point Contacts," Journal of Tribology.

7. He, B., Chen, W., and Wang, Q., "Friction and Wettability of A Micro-Textured Elastomer: Poly(dimethylsiloxane) (PDMS)," Tribology Letters.

8. Xiong, S., Wang, Q., Lin, C., Liu, W., Zhu, D., "A Local Enrichment Approach for Texturing Journal-Bearing Surfaces," Journal of Tribology.

9. Liu, Y., Zhang, Y., Zhu, D., and Wang, Q., "EHL Experimental Techniques and Experimental-Numerical Result Comparisons," J. of Tribology.

Presentations:

1. D. Zhu, "Numerical simulation of sliding wear in mixed EHL contacts," Frontiers in Boundary Lubricating Films" during April 9-14, 2006, in Lyon, France

2. D. Hua "Running-in phenomena and the role of antiwear additives," Frontiers in Boundary Lubricating Films" during April 9-14, 2006, in Lyon, France

3. J. Wang "MD-EHL Characterization of Thin Film Lubrication", Frontiers in Boundary Lubricating Films" during April 9-14, 2006, in Lyon, France

4. O.Ajayi "Boundary lubricating films analysis and their functions", Frontiers in Boundary Lubricating Films" during April 9-14, 2006, in Lyon, France

5. A.Erdemir "Promise and pitfalls of boron and its derivatives as alternative boundary lubrication" Frontiers in Boundary Lubricating Films" during April 9-14, 2006, in Lyon, France

6. M. Z. Huq, B. Lisowsky, M. P. Bujold, Effect of surface texturing on friction reduction under lubricated conditions, STLE Annual Meeting (2006), Calgary, Canada.

7. Liu, Y., Wang, Q., Wang, W., Hu, Y., and Zhu, D., "Experimental Verification of a Mixed Lubrication Model," STLE Annual Meeting (2006), Calgary, Canada.

8. Dong Zhu, Bo Lisowsky, Ashlie Martini, Wenzhong Wang and Yuanzhong Hu, Numerical Simulation of Sliding Wear in Mixed EHL Contacts, STLE Annual Meeting (2006), Calgary, Canada.

9. Martini, A., Liu, Y, Snurr, R., and Wang, Q., "MD Characterization of the Combined Effects of Shear Thinning and Oscillation on Thin-Film Viscosity for EHL Simulation," STLE Annual Meeting (2006), Calgary, Canada.

10. M. Z. Huq, B. Lisowsky, M. P. Bujold, poster on "Effect of surface texturing and lubricant chemistry on friction reduction under fluid lubricated condition, Frontiers in Boundary Lubricating Films" during April 9-14, 2006, in Lyon, France.

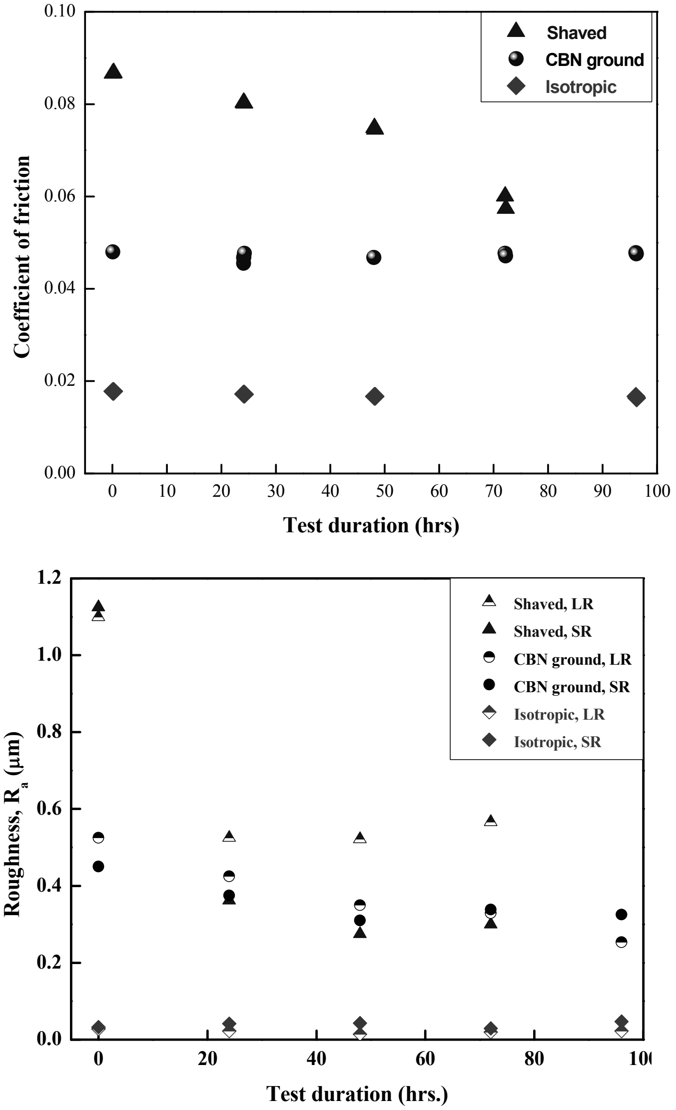

Figure 1. Left: Friction as a function of running time on the RCF test for common gear surface roughness. Right: Corresponding surface roughness change as a function or funning time for large and small rollers.

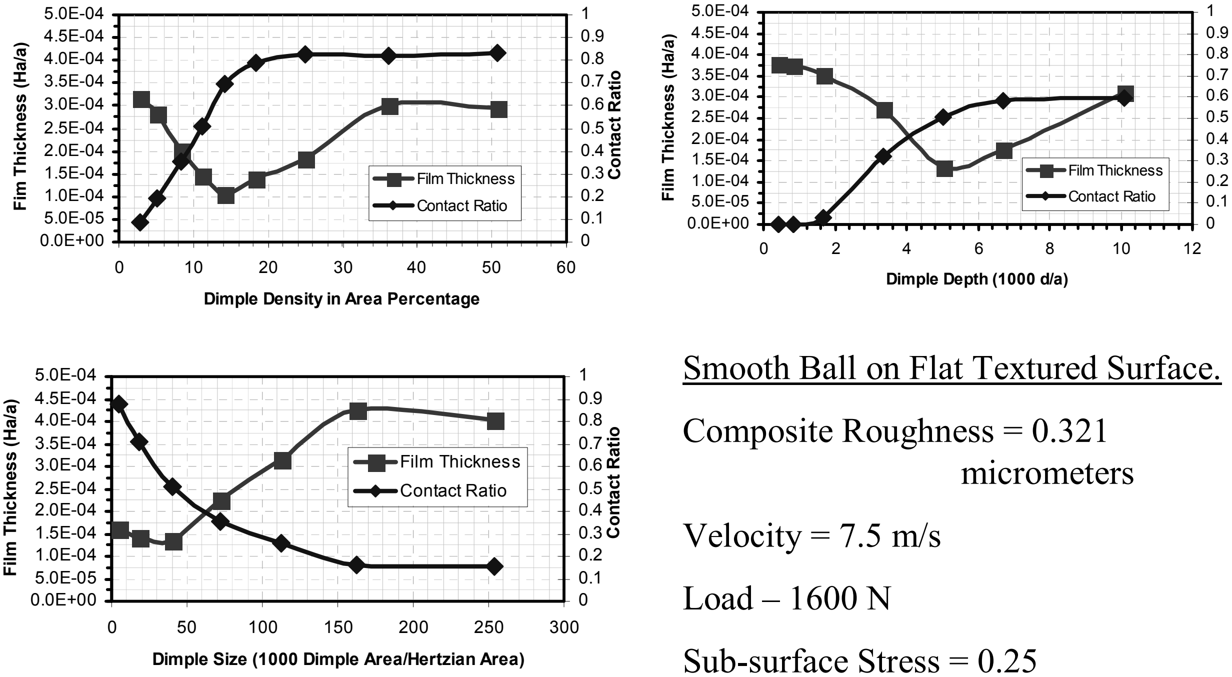

<u>Smooth Ball on Flat Textured Surface.</u>

Composite Roughness = 0.321 micrometers

Velocity = 7.5 m/s

Load – 1600 N

Sub-surface Stress = 0.25

Figure 2. Effect of dimple parameters on lubricant film thickness (friction) and on contact ratio (percent of surface supporting contact load). Optimization of both, film thickness and contact ratio is possible to generate lowest friction and assess surface durability.

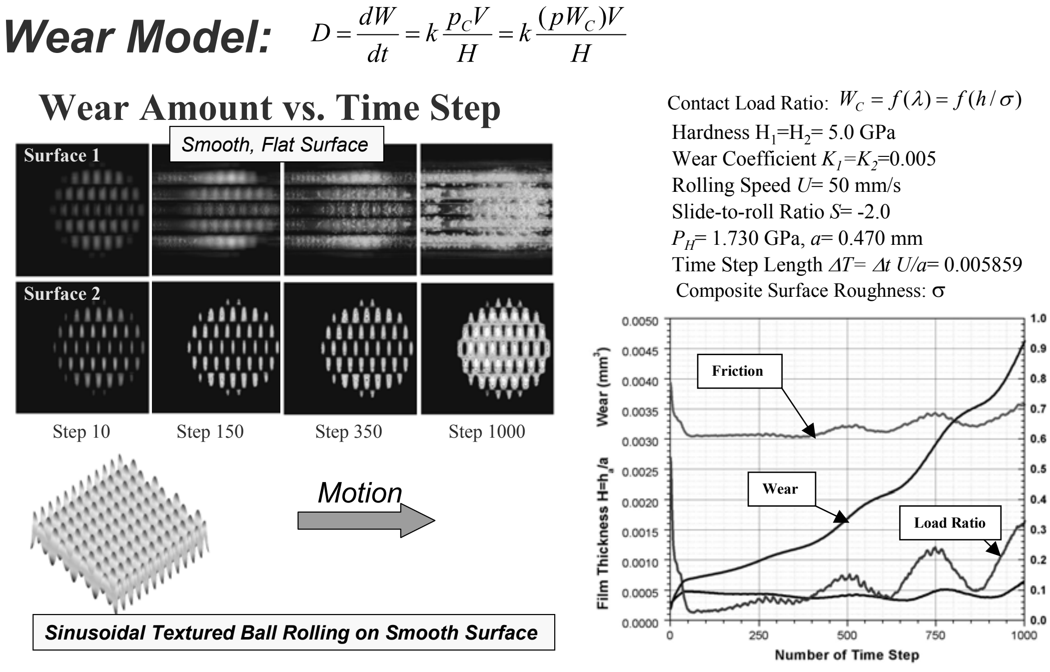

Figure 3. Wear model results showing change in mating surface wear as a function of time steps and changes in friction, load ratio, and lubricant film thickness for a sinusoidal textured ball sliding on a flat surface

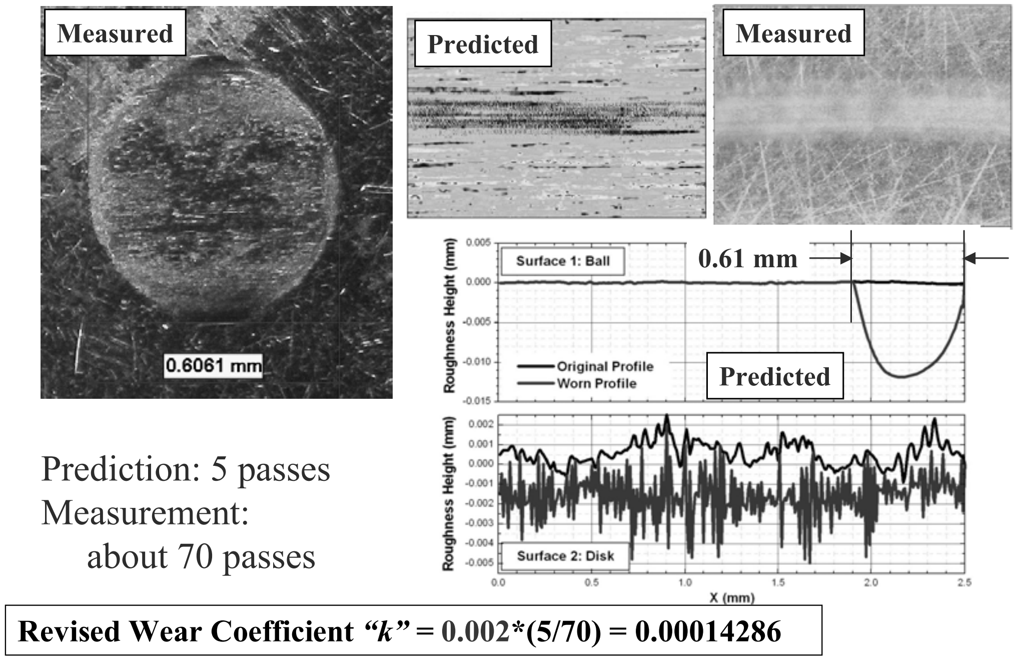

Figure 4. Computed 'transition load" form surface to subsurface as a function of surface roughness for specific tribological conditions of rough surface contact. (RMS = Root Mean Square)

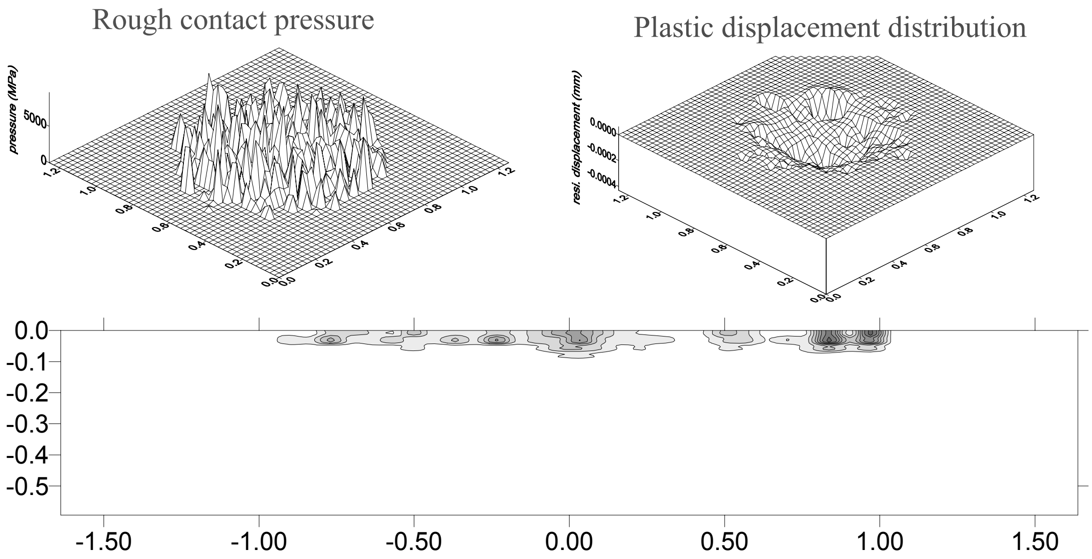

Figure 5. Residual stress subsurface distribution modeling results due to rough surface contact pressure (upper left) and resultant plastic deformation (upper right)

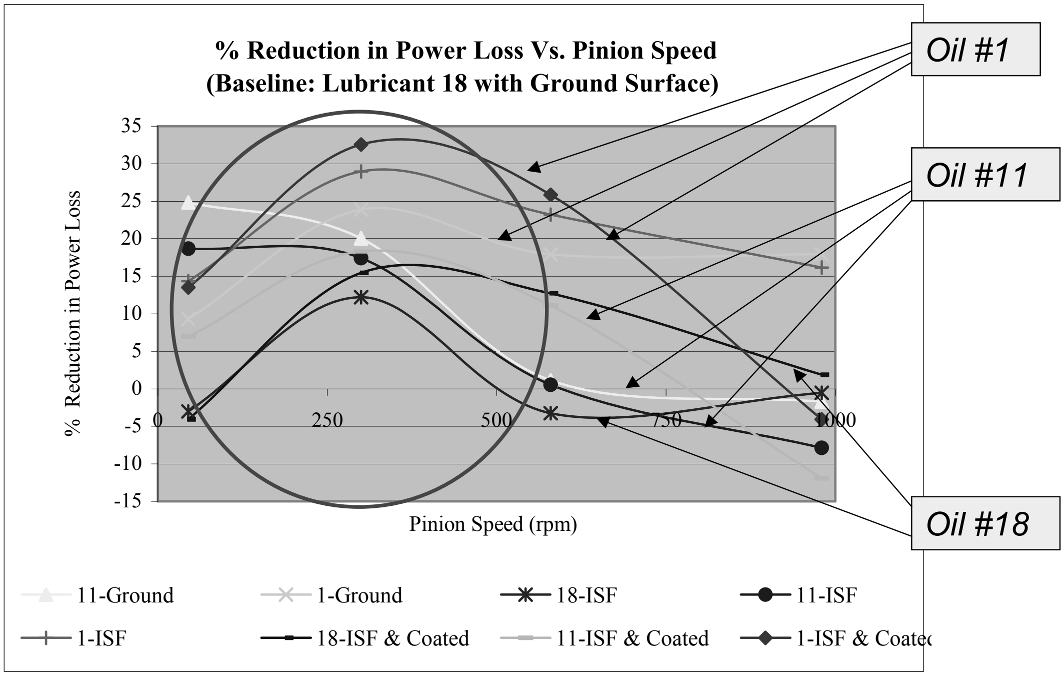

Figure 6. Reduction of power loss as a function of pinion speed in the FZG machine for straight spur gear configuration for three selected oils from 18 oils tested on the Wedevan machine in 2005

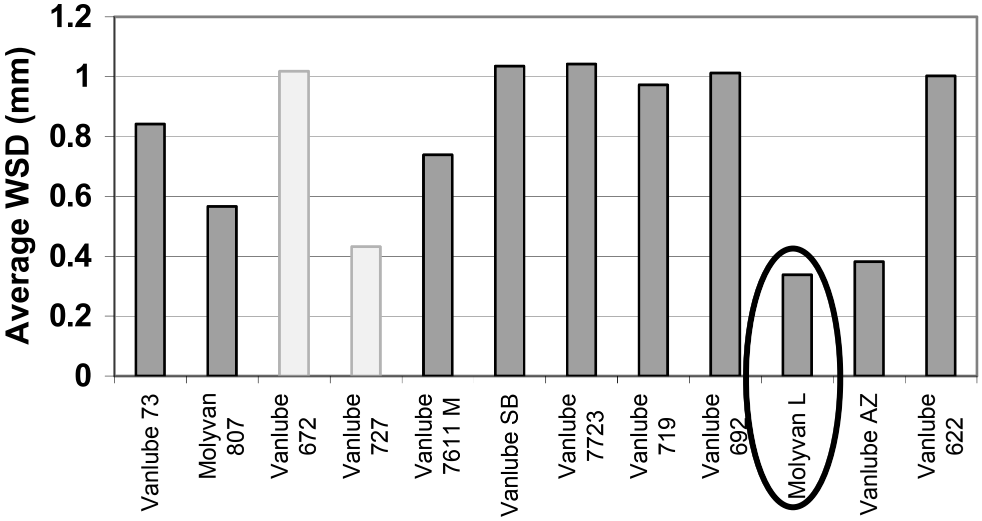

Figure 7. Effect of lubricant additive on wear. "WSD" is the wear scar diameter on three stationary balls in the 4-ball test rig.

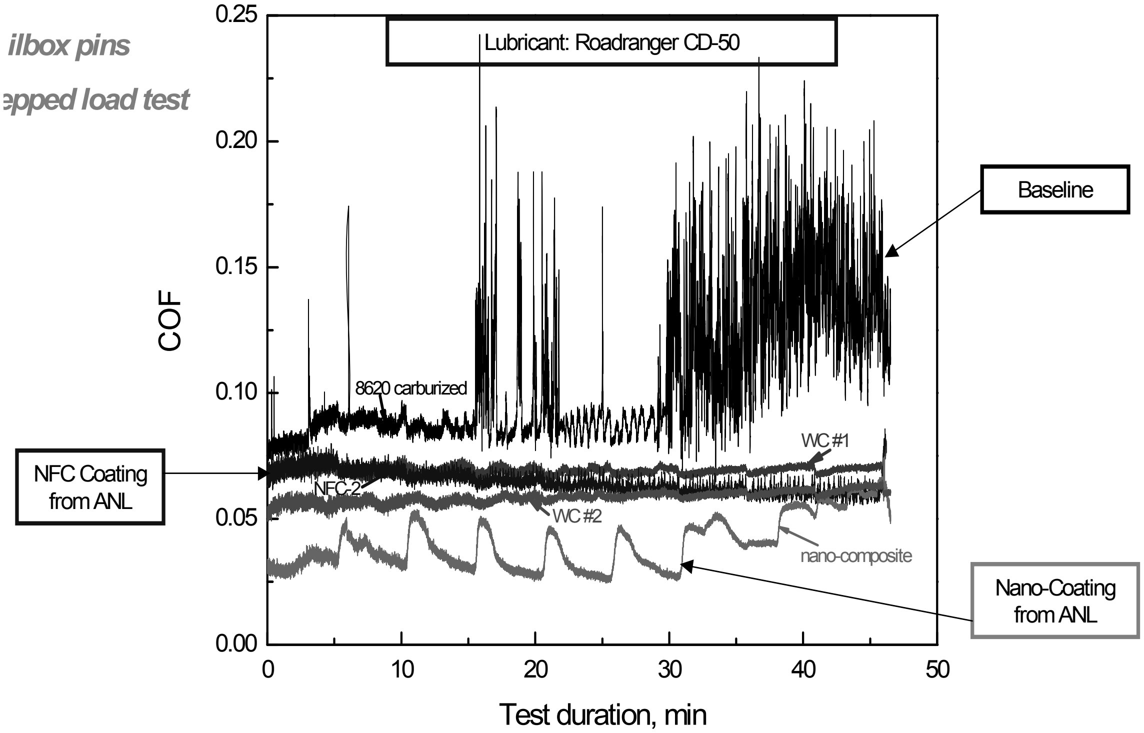

Figure 8. Coefficient of friction for coated surfaces using stepped energy Falex pin-on-disc test with line contact in standard transmission oil

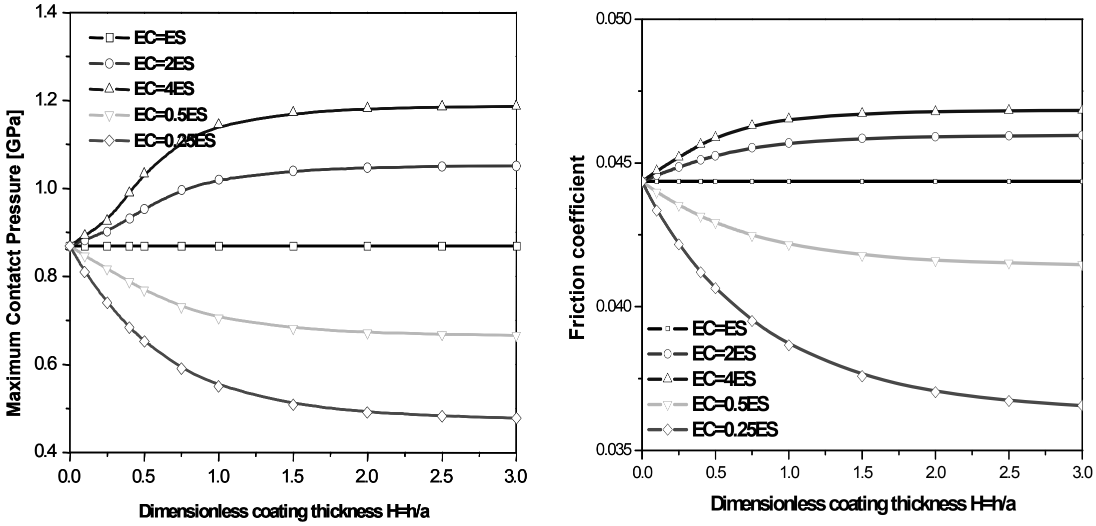

Figure 9. Effect of coating modulus on maximum contact pressure and friction coefficient for smooth surfaces as a function of coating thickness

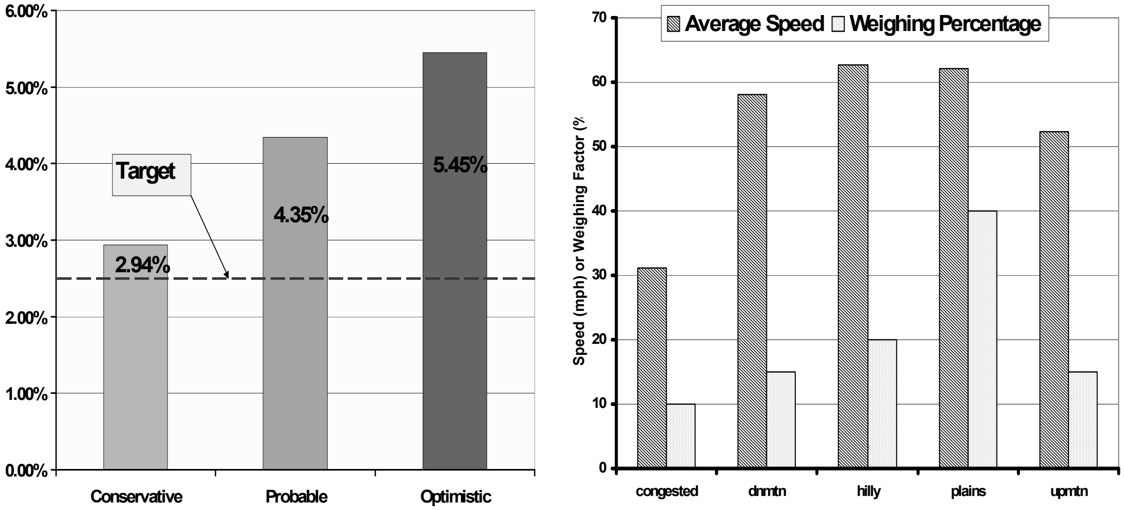

Figure 10. Fuel economy impact simulation results (left) using US-1 route (right)

III.D. Superhard Coatings

Principal Investigators: A. Erdemir, L. Ajayi, and O. Eryilmaz
Affiliation: Argonne National Laboratory
Address: Energy Systems Division, Argonne, IL 60439
(630) 252-6571, fax: (630) 252-4798, e-mail: erdemir@anl.gov

Technology Development Area Specialist: Lee Slezak
(202) 586-2335, fax: (202) 586-2476, e-mail: Lee.Slezak@hq.doe.gov

Field Project Manager: Jules Routbort
(630) 252-5065, fax: (630) 252-4798, e-mail: routbort@anl.gov

---

Contractor: Argonne National Laboratory
Contract No.: DE-AC02-06CH11357

Objective

- Design, develop, and optimize low-friction, superhard, nano-composite coatings.
- Demonstrate their durability and energy-saving benefits in actual diesel engine systems.
- Elucidate their friction and wear-reducing mechanisms.
- Explore large-scale production of such coatings in commercial-scale deposition systems.
- Implement demonstrated technology in engine systems in collaboration with industrial collaborators.
- Confirm performance under severe running conditions of fired engines.

Approach

- Obtain test samples and components and prepare for coating deposition.
- Optimize and employ deposition protocols that can consistently produce superhard coatings on these samples and components.
- Characterize coating adhesion, thickness, and uniformity and surface roughness.
- Optimize the superhard coatings to provide the lowest possible friction and wear coefficients and longest wear life.
- Test and demonstrate their superior friction and wear performance under a wide range of conditions using bench-top test machines and actual engines.
- Analyze test data and examine sliding surfaces.
- Determine friction and wear mechanisms.
- Prepare reports.

Accomplishments

- During FY06, we further optimized our physical vapor deposition conditions and successfully produced a range of superhard coatings on test samples and components using a commercial-scale CemeCon sputter ion plating system.

- We optimized the bonding, thickness, and surface finish of these coatings by effectively controlling the deposition conditions.
- Using coated test samples, we demonstrated that they possessed extreme resistance to scuffing (exceeded the load limits of our bench-top test systems), dramatic reductions in friction under boundary-lubricated sliding regimes, and near-zero wear.
- We tested the performance of optimized superhard coatings on cut segments of piston rings and cylinder liners. Significant reductions in friction were achieved on these parts. Furthermore, these coatings virtually eliminated the wear of the components.
- We used time-of-flight secondary ion mass spectrometry and x-ray photoelectron spectroscopy to determine the lubrication mechanisms of these coatings.
- Several companies (Bekaert, Hauzer, and CemeCon) are interested in licensing and mass-producing these coatings for large-scale engine applications.
- Several engine companies and OEMs (GM, Burgess-Norton, Eaton, and Caterpillar) are interested in testing the performance of these coatings on sliding and rolling engine components.

Future Direction

- Explore new coating compositions based on MoN-Sn, MoN-Sb, and MoN-C while finalizing the current deposition protocol for the MoN-Cu system and transitioning this technology to coating manufacturers and engine companies.
- Continue to test the friction and wear performance of these new coatings with bench-top ring-liner and block-on-ring test machines.
- Determine the coating friction and wear behavior as a function of temperature under lubricated sliding conditions.
- Perform surface analytical studies characterization on as-deposited and friction- and wear-tested surfaces to understand the fundamental tribological mechanisms behind the superlow friction and wear of superhard coatings.
- Increase collaboration with Eaton, Caterpillar, GM, Federal Mogul, and Burgess-Norton. Have some of the tests run in their engine test systems. We held several meetings with representatives of these companies in recent months, and they are extremely interested in this technology.

Introduction

Increasing demands for higher power density and reduced emissions in future diesel engines are pushing current materials and lubricants to their limits. In particular, higher loads and speeds and other harsh operating conditions are rendering current materials and lubricants essentially useless. Therefore, the development of novel materials (including hard coatings) and lubricants is extremely important for satisfying the increasingly more stringent application conditions of future engine systems. One of the major goals of this project is to design, develop, and optimize novel superhard and low-friction coatings for use in critical diesel engine parts and components that are subject to severe operating conditions. Another important goal is to optimize and apply these coatings in engines to improve their performance, efficiency, and durability even under the most stringent operating conditions.

Synthesis of Superhard Coatings

The superhard coatings used in our experiments were synthesized in a commercial-scale sputter ion-plating system (CemeCon, Model # CC800/9XL). They are made of two distinct phases: MoN and Cu. The choice of these two phases is based primarily on the fact that they could tribochemically react with the oil and its additives during sliding and result in a boundary film that can provide low friction and wear. To prevent wear under lubricated sliding conditions, we felt that such coatings must have sufficient hardness; thus, we optimized the proportion of each phase in the coating to achieve superhardness while still maintaining low friction.

The sputter ion plating system consists of two sputtering targets. One of these targets is made of Cu and used as the minor alloying phase during the production of superhard coatings. We felt that Cu was critical for achieving a high degree of chemical compatibility with, or response to, lubricating oils. Specifically, CuS_x, which may result from reactions with sulfur-bearing additives in formulated oils, can provide easy shear to sliding surfaces. It has a strong affinity toward, or chemical reactivity with, additives in oils and thus can provide a low-friction, high-scuff-resistant boundary film during sliding. The MoN phase is very hard and hence can increase resistance to wear.

During our deposition trials, we tried a range of Cu concentrations (1 wt.% to 10 wt.%) in nano-composite coatings. Depending on the concentration, we were able to produce films with hardness values as low as 30 GPa and as high as 50 GPa. To improve their adhesion to the substrate surface, we had to remove organic contaminants from the surfaces by means of chemical solvents in an ultrasonic bath. After loading these ultrasonically cleaned substrates into the deposition chamber, we had to perform an Ar ion etching step to remove remaining contaminants and most of the natural oxide layers from the substrate surface. Earlier trials had shown that preparation of such atomically clean surfaces was important for attaining very strong bonding to the superhard coatings. To further help adhesion, we always deposited a pure Mo bond or transition layer that can provide a smooth transition from the base steel to the superhard coating. Finally, the appropriate plasma deposition conditions were established, and the deposition of superhard coatings on steel substrates was started. In most cases, we produced 2- to 3-µm-thick coatings on substrate surfaces.

Tribological Tests

Tribological testing of superhard coatings was carried out with two types of test machines: a pin-on-disk tribometer for screening tests and a block-on-ring test machine for scuffing studies. All of the tests were performed under heavy loads and relatively low sliding velocities to create a boundary-lubricated sliding regime where direct metal-to-metal contacts occur.

Figure 1 compares the typical friction coefficients of control and superhard-coated test pairs under lubricated sliding conditions. These tests were performed in the pin-on-disk tribometer. The lubricant used was an SAE 15W-40 grade formulated engine oil. As evident in Fig. 1, after the initial low-friction run-in period, the friction coefficient of the control test pair increases rapidly and stabilizes at around 0.09. The friction coefficient of the superhard coated test pair is initially high but decreases steadily and finally stabilizes at around 0.04 for the rest of the test. Such a reduction in friction is expected to result in increased fuel savings in actual engines.

In addition to impressive friction test results, the wear of superhard coated surfaces was so low as to be hard to measure, while a very large wear scar and track had formed on the control test samples.

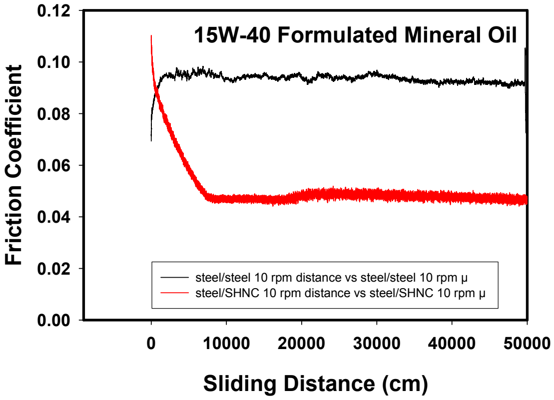

Figure 1. Typical friction coefficients of uncoated (control) and superhard-coated steel test samples under boundary-lubricated sliding conditions of a pin-on-disk tribometer

Using the block-on-ring test machine, we performed a series of scuffing tests on control and superhard coated steel samples. Scuffing is a catastrophic failure of a lubricated surface subjected to severe loading and/or inadequate lubrication. It is a major problem in heavy duty engines. Figure 2 shows the scuffing performance of a superhard coated sample in the block-on-ring test machine where the contact load was increased stepwise until a sudden increase in friction was observed. When such a test was run on uncoated or control samples, scuffing always occurred between 650 and 700 N loads. However, for a superhard coating on the surface of the rubbing steel samples, scuffing did not occur even up to the load limit (1700 N) of this machine. Overall, the superhard coatings developed under this program possessed exceptional resistance to scuffing. Such a property would be extremely useful for engine applications involving severe loading, high temperatures, low viscosity oils, and/or starved lubrication conditions.

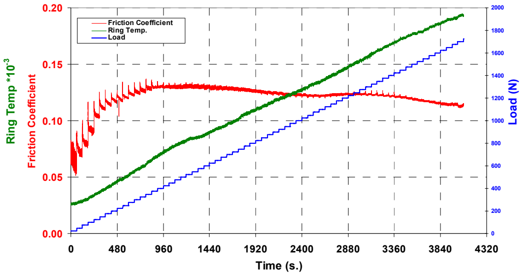

Figure 2. Scuffing performance of superhard coated steel sample in block-on-ring test machine

Surface Analytical Studies

During FY06, we conducted numerous surface analytical studies on the sliding surfaces of superhard coated test samples. The main motivation was to elucidate the fundamental tribological mechanisms controlling the friction, wear, and scuffing behavior of these coatings. One of the tools we used was a time-of-flight secondary ion mass spectrometer (or ToF-SIMS), which is well-known for its surface sensitivity (capable of providing chemical information from surface layers that are a few Angstroms thick). In support of the ToF-SIMS, we also used x-ray photoelectron spectroscopy (XPS).

ToF-SIMS images of the sliding surfaces clearly show high phosphorus and sulfur concentrations within the wear track, while in the area away from it these species were not evident. As is well known, both sulfur and phosphorus are integral parts of the formulated engine oils, and they exist in most boundary films. XPS study of the same sliding surfaces yielded supporting information. Specifically, it suggested that sulfur existed in at least two reacted forms: MoS_x and CuS_x. Some FeS_x was also found on the sliding surfaces.

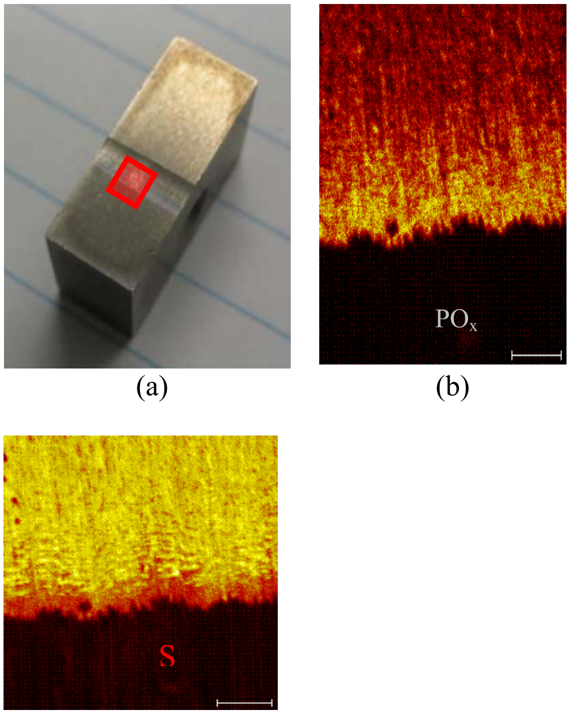

(a) (b)

(c)

Figure 3. (a) Superhard-coated block sample used in a block-on-ring test and ToF-SIMS chemical images for (b) PO_x- and (b) S in a region covering both the undisturbed and sliding contact portions of the sample surface

Conclusions

During FY06, we produced superhard coatings on test samples using a commercial-size deposition system. We performed systematic studies on their friction, wear, and scuffing performance. Friction and wear tests in a pin-on-disk machine confirmed more than 50% reduction in friction, while wear was reduced to unmeasurable levels. These superhard coatings drastically improved the resistance of steel samples to scuffing. Using a block-on-ring test machine, we could not scuff these surfaces up to the load limit of this machine. Detailed surface analytical studies with ToF-SIMS and XPS revealed high concentration of MoS_x and CuS_x (and some FeS_x) within the wear track, suggesting that these species were perhaps responsible for the exceptional scuffing resistance of these coatings.

Patents and Publications

During FY06, we filed one provisional patent and published and/or presented three new papers on the work that was performed under this project.

1. "Design of Novel Nanocomposite Films For Improved Boundary Lubrication and Scuff Resistance," A. Erdemir, O. L. Eryilmaz, O. O. Ajayi, M. Urgen, and K. Kazmanli, presented at the Annual Meeting of the Society of Tribologists and Lubrication Engineers, Calgary, Canada, May 7-11, 2006.
2. "Multifunctional Nanocomposite Hard Coatings for Improved Boundary Lubrication," A. Erdemir, invited keynote paper presented at Joint COST 532 & U.S. Dept. of Energy Conf. on Triboscience & Tribotechnology, Porto, Portugal, Oct. 12-14, 2005.
3. "Development of Multifunctional Nanocomposite Coatings with Extreme Resistance to Wear and Scuffing under Boundary Lubricated Sliding Conditions," A. Erdemir, O. L. Eryilmaz, O. O. Ajayi, M. Urgen, and K. Kazmanli, presented at Intl. Conf. on Metallurgical Coatings & Thin Films ICMCTF 2006, San Diego, May 1-5, 2006.

III.E. Residual Stresses in Thin Films

Principal Investigator: J. L. Routbort (co-workers: D. Singh and Gang Chen)
Argonne National Laboratory
9700 S. Cass Avenue, Argonne, IL 60439-4838
(630) 252-5065, e-mail: routbort@anl.gov

Program Manager: Lee Slezak
(202) 586-2335, e-mail: Lee.Slezak@ee.doe.gov

Contractor: Argonne National Laboratory
Contract No.: W-31-109-Eng-38

Objective

- Measure residual stresses in thin films and coatings as a function of film thickness and relate stresses to film properties such as hardness, fracture toughness, and adhesion energy to relate to film processing variables and to predict durability

Approach

- Develop X-ray technique to measure change of lattice parameter as a function of depth and hence to calculate the lattice strains and stresses
- Develop indentation technique to measure hardness, fracture toughness, and adhesion energy of films and coatings
- Relate stresses, properties, and processing conditions to durability

Accomplishments

- Advanced Photon Source (APS) used to measure stresses in 3–µm thick thin films of nanocrystalline MoN as a function of depth using the established “wire” technique, and a new “cross sectional technique”
- Stresses are sensitive to deposition conditions and thermal annealing
- Software modified to calculate lattice spacing from diffraction patterns
- Initial results accepted for publication in Applied Physics Letters
- Invention report filed on cross section technique

Future Directions

- Continue to refine and improve resolution of X-ray technique
- Develop indentation technique to measure film adhesion
- Investigate stresses in superhard, nanocrystalline MoCuN films as a function of deposition conditions and Cu concentration

Introduction

Because of their unusual structural, mechanical, and tribological properties, superhard, nanocrystalline coatings can have an immediate and far-reaching impact on numerous advanced transportation applications including FreedomCar and 21st Century Truck Programs of DOE by reducing parasitic friction losses (hence increasing fuel economy) and wear (hence increasing durability/reliability). They can also be used to overcome toxic emission problems associated with exhaust gas recirculation in diesel engines. Durability of hard coatings is a critical property. The durability is determined by the surface adhesion energy, but is the result, in a large part, of the residual stresses that form as a result of materials, and processing parameters such as bias voltage, ion flux, and temperature.

Using high-brilliance X-rays produced by the Advanced Photon Source at Argonne National Laboratory, and a microfocus beam, we have preformed initial measurements of the residual stresses of MoN thin films as a function of depth from the surface through the interface to the substrate. Results have been correlated to processing and growth conditions in the sections that follow.

Experimental

MoN/Mo bilayer films were prepared by physical vapor deposition (PVD) using magnetron sputtering. A 99.5% pure molybdenum plate was used as sputtering target. The substrate was p-type (100) single-crystal silicon wafer (cleaved into 3 cm × 3 cm × 0.1 cm pieces) with native oxide layer. The substrates were rotated and heated during deposition with an estimated temperature between 250 and 300°C. A Mo bond layer was first deposited on the Si substrate, followed by deposition of a MoN layer. For the Mo layer deposition, the argon gas pressure was 0.15 Pa, and the substrate bias was -300 V. For the MoN layer, the partial pressure of argon and nitrogen was 0.22 and 0.78 Pa, respectively, and the substrate bias was -200 V. The deposition rates for MoN and Mo were 0.22 and 0.45 Å/s, respectively. After deposition, some of the films were annealed at 500°C in vacuum for one hour. The as-deposited and annealed films were fractured along Si {110} planes to create smooth cross sections. Figure 1 is a scanning electron microscopy (SEM) micrograph of the cross section of an as-deposited MoN/Mo film. The Mo and MoN layers show a dense columnar structure.

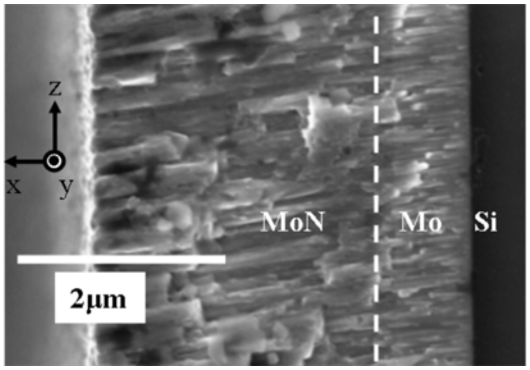

Figure 1. Cross-sectional scanning electron micrograph of a MoN/Mo bilayer film deposited on a Si substrate

X-ray microdiffraction was performed on beamline 34-ID-E at the Advanced Photon Source (Argonne National Laboratory) [1]. The x-ray beam was focused by Kirkpatrick-Baez mirrors down to 0.4 (horizontal) × 0.6 (vertical) μm^2. The angle between the x-ray beam and the sample cross-section plane was 45°. A high-resolution charged coupled device (CCD) x-ray detector was placed 30 mm above the sample to collect x-ray diffraction (XRD) patterns from the x-ray microbeam with an energy of 8.9 keV (1.39308 Å). Before the XRD patterns were taken, the sample was aligned by an x-ray fluorescence method so that the film surface (i.e., the yz plane in Figure 1) was parallel to the x-ray beam. The position of the x-ray beam was scanned along the film normal (x in Figure 1) direction with a step size of 0.25 µm.

Figures 2a and 2b show typical polycrystalline XRD patterns from the MoN and the Mo layers, respectively. The MoN film is a hexagonal phase with fiber texture such that the c axis is parallel to the film surface. The Mo film is a cubic phase with <110> fiber texture. Some of the films were scraped off the Si substrate using a diamond scriber and ground into a powder for determination of the strain-free lattice parameter. For the as-deposited and annealed hexagonal MoN, the measured strain-free lattice parameters are a = 5.763 Å, c = 5.6242 Å, and a = 5.7268 Å, c = 5.6204 Å, respectively. For the as-deposited and annealed cubic Mo, the parameters are

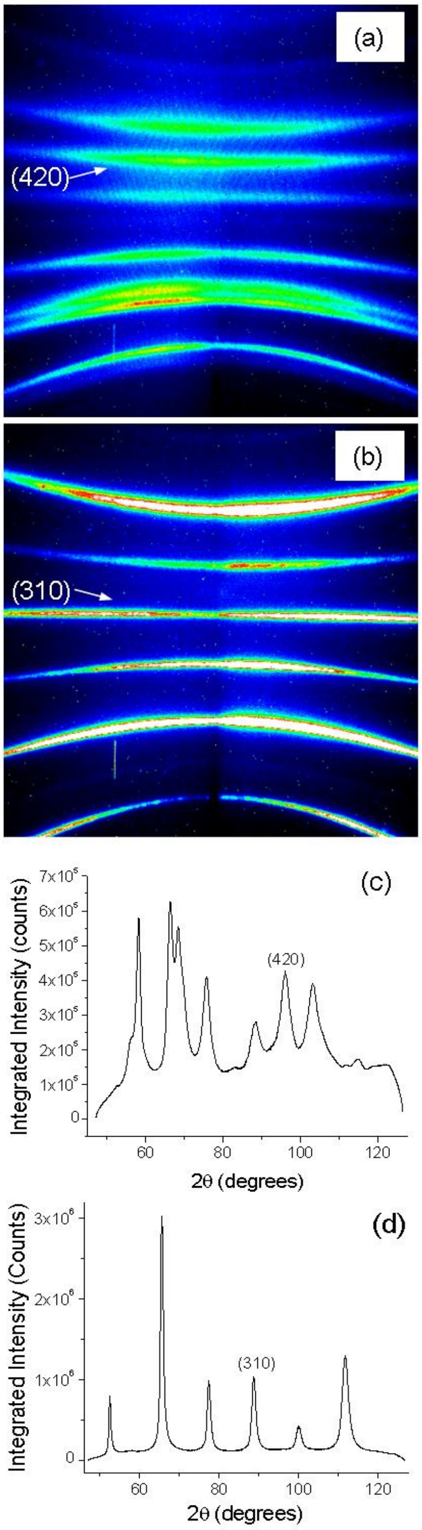

Figure 2. Two-dimensional x-ray diffraction patterns of the MoN layer (a) and the Mo layer (b); (c) and (d) are integrated 1-D patterns from (a) and (b), respectively

a = 3.1516 Å and a = 3.1549 Å, respectively. Figure 2c and 2d are the 1-D patterns of MoN and Mo derived from the 2-D patterns shown in Figure 2a and 2b, respectively. The (420) peak of MoN and (310) peak of Mo were selected for data analysis to have scattering vectors close to the normal of the cross-sectional plane (i.e., y in Figure 1). Assuming isotropy in the plane of the film, this approach measures the in-plane lattice parameters, from which the in-plane strain can be determined. The XRD peaks were fit by using an asymmetric pseudo-Voigt function, and the strain and the full width at half maximum (FWHM) of the diffraction peaks were derived as a function of depth from the film surface. Using the Scherrer formula [2], the average grain sizes for the MoN and Mo layers were found to be 5 and 20 nm, respectively. The cross-sectional point-by-point scanning was repeated at different x positions along the sample to determine the variation of measured strain along the x direction.

Results and Discussion

Figure 3a shows depth-resolved strain (ε_y) profiles for the as-deposited and annealed MoN/Mo films. The thicknesses of the MoN and Mo layers were 2.7 μm and 0.8 μm, respectively. For the as-deposited film, the MoN layer was under in-plane compression, and the magnitude of the in-plane strain (ε_y) increased almost linearly with the depth. The maximum strain reached 0.005 at the MoN/Mo interface. The Mo layer was found to be under in-plane compression also, but the strain magnitude decreased with increasing depth. The maximum strain of 0.003 in the Mo layer appeared at the MoN/Mo interface.

After annealing, the strain in the Mo film changed little and was still under in-plane compression. However, for the MoN layer, the overall strain magnitude decreased dramatically. The strain had its maximum of 0.0012 at the MoN surface and decreased linearly to essentially zero at the MoN/Mo interface. Figure 3b is a plot of the FWHM as a function of depth for both as-deposited and annealed films. For the as-deposited film, the FWHM of the MoN layer varied little with depth, while the diffraction width of the Mo layer increased with increasing depth. The FHWM of the MoN layer decreased slightly with annealing, but it was still

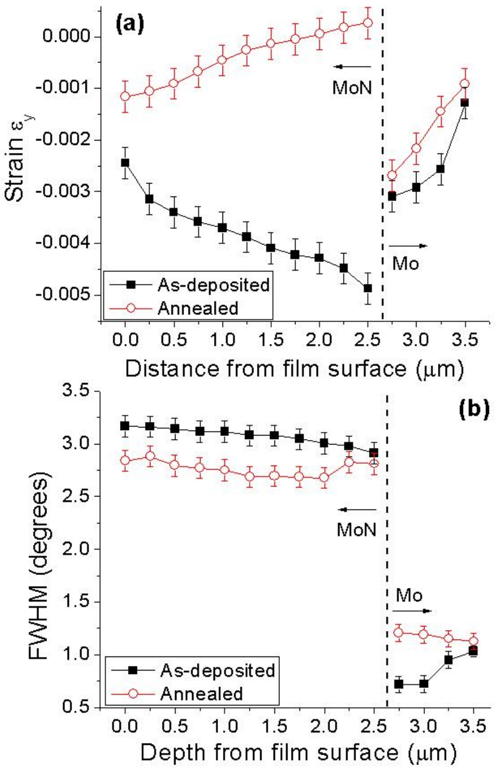

Figure 3. Depth-resolved residual strain (a) and FWHM (b) for as-deposited and annealed MoN/Mo bilayer films

relatively constant as a function of depth. For the Mo layer, the FWHM increased near the MoN/Mo interface, but there was almost no change near the Mo/Si interface.

Residual strains in PVD coatings are very complex because they include both intrinsic and extrinsic strains [3]. The intrinsic strains are related to the microstructure of thin films, which varies with material as well as with film deposition conditions. Extrinsic effects here refer to thermal strain caused by the thermal expansion coefficient mismatch between film and substrate. The differential thermal strain in the Mo and MoN layers of as-deposited and annealed films was estimated to be less than 10^{-3}; this value is much smaller than the residual strains observed in the films and will be neglected in further discussion.

In PVD films, the intrinsic residual strain is strongly affected by deposition conditions and is very difficult to model. Nonetheless, it is believed that compressive strains in thin films that have been subjected to ion or atom bombardment are caused by atomic peening [4], which is enhanced by low sputtering gas pressure and high substrate bias during deposition [3]. The strain profile observed in the Mo layer is similar to the near-surface strain profiles in shot-peened bulk metals [5], i.e., both have high compressive strain near the surface, and the magnitude of strain decreases as the depth increases. Since strain profiles in PVD films may be complicated by defects, voids, trapped gas ions, impurities, and dislocations introduced during film deposition [3], there should be differences between these two peening processes. However, the similarity in strain profiles suggests that the bombardment of the film by atoms/ions during its growth may be partially responsible for the observed strain profile in the Mo layer. The case of the MoN layer is more complicated since N_2 was introduced during the film growth to form the metal nitride. The maximum residual strain in the MoN layer is at the MoN/Mo interface, decreasing sharply as the film surface is approached. It is possible that the decrease is the result of a relaxation process during growth. As shown in Figure 1, the Mo layer has a dense columnar structure, and the MoN columns are also dense near the MoN/Mo interface. However, as the MoN layer grows, the columns start to regroup into large clusters, and voids start to appear between the clusters. Therefore, some strain relaxation may occur as the MoN columns attempt to fill the voids.

In the MoN layer of the as-deposited film, the FWHM of the diffraction peak is independent of the film depth (Figure 3b). This relationship implies that strain in the MoN layer is uniform at different depths since uniform strain does not change the peak width [2]. For the Mo layer, the FWHM of the diffraction peak is larger at the Mo/Si interface than at the MoN/Mo interface. This difference implies that the Mo grain size is smaller and/or the grains are more defective near the Si interface than near the MoN/Mo interface. After annealing, the FWHM of the MoN layer was observed to decrease, accompanied by a significant relief of the residual strain (Figure 3a). In comparison, an increase in the FWHM of the Mo layer accompanied a slight relief of the strain. Note that the melting temperatures of MoN and Mo are 1750°C and 2623°C, respectively [6]. These temperatures indicate that the annealing temperature (500°C) is probably not high enough to initiate recrystallization or grain growth. Therefore, the decrease in the FWHM of the MoN layer could be caused by the reduction of defects, which may include crystallite defects, trapped gas ions and molecules, and voids. For the Mo layer, the increase in the FWHM after annealing probably means an increase in the defect concentration near the MoN/Mo interface. From these analyses, we conclude that annealing relieves strain and alters defect concentrations in the MoN and Mo layers.

Since the microstructure of films is sensitive to defects in general, annealing-induced changes in defect concentration might be expected to change the microstructure. This hypothesis was confirmed by examining the SEM micrographs of the MoN film before and after annealing. In the as-deposited film (Figure 4a), there are large clusters with diameters of a few hundred nanometers, and the boundary around these clusters can be clearly seen. Each cluster consists of many very small columns (Figure 1). After annealing (Figure 4b), the microstructure changed significantly: the boundary between clusters was no longer well defined, and the grains in the clusters could be seen clearly.

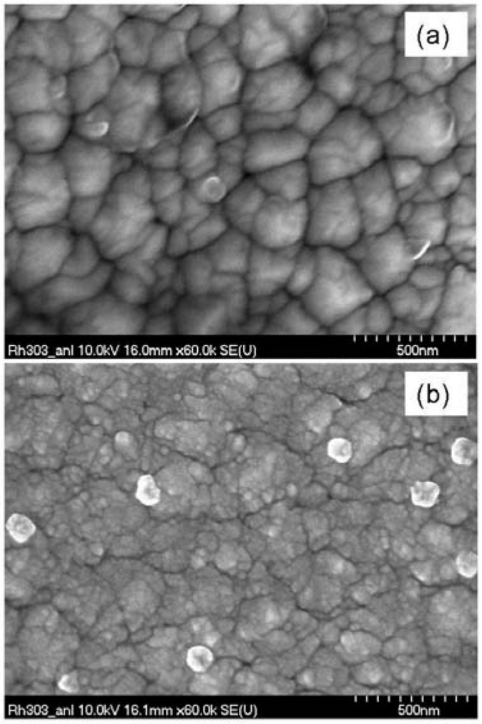

Figure 4. Scanning electron micrographs of the surface of the MoN layer before (a) and after (b) annealing at 500°C for one hour

Therefore, annealing significantly changed the microstructure of the MoN layer, as is consistent with the observed large relief of strain in the annealed MoN layer.

In conclusion, we have applied cross-section x-ray microdiffraction to study depth-resolved residual strain in magnetron-sputtered MoN/Mo bilayer films. The MoN and Mo layers in the as-deposited film were found to be under in-plane compression, with large strain gradients as a function of depth. The observed strain profiles were explained in terms of atomic peening and void-induced strain relaxation. Annealing of the film causes significant strain relief and defect reduction in the MoN layer. In contrast, residual strain in the Mo layer is only slightly relieved, and the defect concentration increases after annealing. This study provides insights into the annealing effect on the depth-dependent structure and property of magnetron-sputtered nano-crystalline MoN/Mo films.

Measurement of Thin Film Adhesion Energy

An indentation technique is used to measure adhesion of residually stressed MoN thin film deposited on silicon substrate. Vickers indent on the film causes formation of lateral cracks at the film/substrate interface. The delaminated film bulges out as shown in Figure 5. Surface profilometer is used measure the size of the lateral crack. This procedure is conducted at various indentation loads. By measuring the lateral crack length as a function of applied load and using a fracture mechanics model, interface toughness or a adhesion energy of

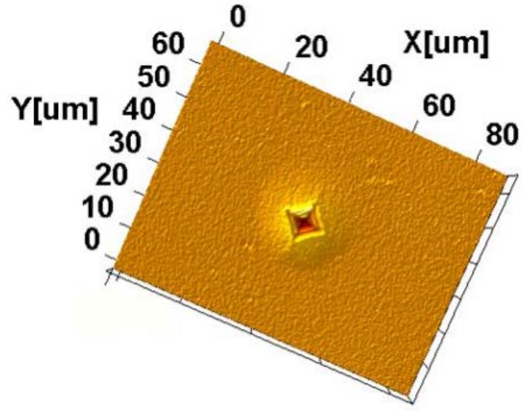

Figure 5. Vickers indent on a MoN film on Si substrate as imaged on a surface profilometer

the film can be determined. As part of the future effort, the role of residual stresses on the adhesion energy of the film will be investigated.

Future Direction

Residual stresse measurements will be extended to superhard, nanocrystalline MoCuN thin films and to commercial films, namely Ni_3B. The indentation technique will be exploited to measure the thin film or coating properties and the adhesion energy. The stresses and adhesion energy will be related to the film deposition conditions.

References

1. G. E. Ice, B. C. Larson, W. Yang, J. D. Budai, J. Z. Tischler, J. W. L. Pang, R. I. Barabash, and W. Liu, J. Synchrotron Rad. **12**, 155 (2005).
2. B. D. Cullity and S. R. Stock, *Elements of X-ray Diffraction, 3rd ed.* (Prentice Hall, Upper Saddle River, NJ, 2001), pp. 170-176.
3. A. Misra and M. Nastasi, *Engineering Thin Films and Nanostructures with Ion Beams*, edited by Emile Knystautas (Taylor & Francis, Boca Raton, FL, 2005), Chapter 7.
4. H. Windischmann, Crit. Rev. Solid State Mater. Sci. **17**, 547 (1992).
5. A. Ezeilo, *Analysis of Residual Stresses by Diffraction using Neutron and Synchrotron Radiation*, edited by M. E. Fitzpatrick and A. Lodini (Taylor & Francis, London and New York, 2003), p.260.
6. *CRC Handbook of Chemistry and Physics, 78th ed.*, edited by D.R. Lide (CRC Press LC, Boca Raton, FL, 1997-1998), p.4-71.

IV. ANALYSIS

IV.A. Powertrain System Analysis Toolkit (PSAT) Heavy Duty Development

Aymeric Rousseau (project leader)
Argonne National Laboratory
9700 South Cass Avenue
Argonne, IL 60439-4815
(630) 252-7261, e-mail: arousseau@anl.gov

DOE Technology Manager: Lee Slezak
(202) 586-2335, e-mail: Lee.Slezak@ee.doe.gov

Objectives

- Expand the utility of the Powertrain Systems Analysis Toolkit (PSAT) by developing and integrating heavy duty vehicle modeling capabilities.

Approach

- Gather data and information from 21st Century Truck Partners to develop model specifications and needs.
- Modify the PSAT GUI and the initialization files to separate data in to either the light duty class or the heavy duty class.
- Modify the GUI to add multiple non-drive axles.
- Modify the building algorithms to accommodate braking on multiple non-drive axles.

Accomplishments

- The GUI can present light duty or heavy duty data based on the user choice.
- The user can select any number of non-drive axles from the GUI.
- The building algorithm can build a vehicle with any number of drive axles.

Future Directions

- Collection and integration of more component and vehicle data.
- Allow the user to select any number of drive axles

Introduction

Observing the success of PSAT as a light duty vehicle model for the FreedomCAR program, the 21st Century Truck Program would like to have the same success with a vehicle model that is tailored to meet their heavy duty needs. Thus, modifications of the existing light duty platform of PSAT have begun in order to create a heavy duty vehicle module.

Before starting the development of the heavy duty version of PSAT, several meetings were held with key heavy truck manufacturers to review the current capabilities and list the ones that should be developed specifically for Heavy Duty applications.

This input was disseminated and prioritized in order to establish which features should be implemented first.

Results

Figure 1 shows the new start screen developed for the PSAT 6.1 release. Shown here is the option for the user to select either light duty vehicle applications, or the newly implemented heavy vehicle models.

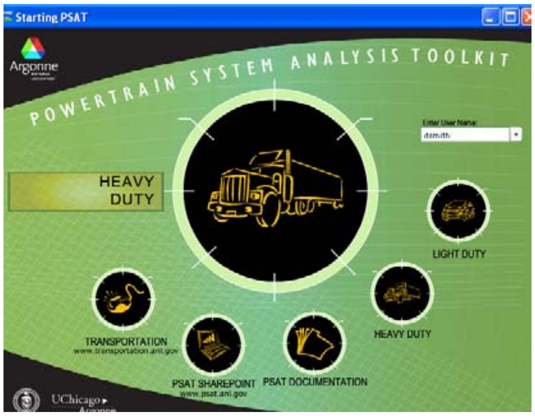

Figure 1. Launch Screen for Heavy Duty PSAT

Figure 2 shows the new PSAT 6.1 graphical user interface with a block diagram representation of a heavy vehicle that adds passive axles to the drivetrain.

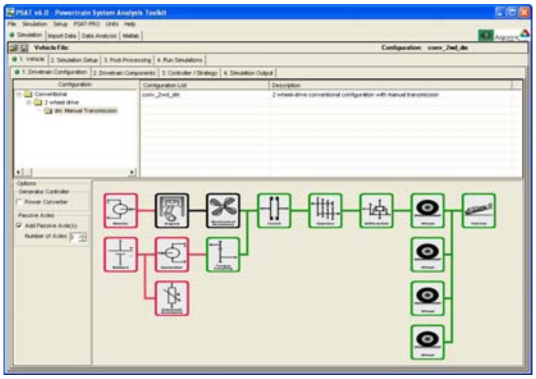

Figure 2. PSAT main screen depicting heavy vehicle powertrain with multiple passive axles

Figure 3 shows an actual SIMULINK model of a heavy duty vehicle powertrain with 2 passive axles and 1 driven axle.

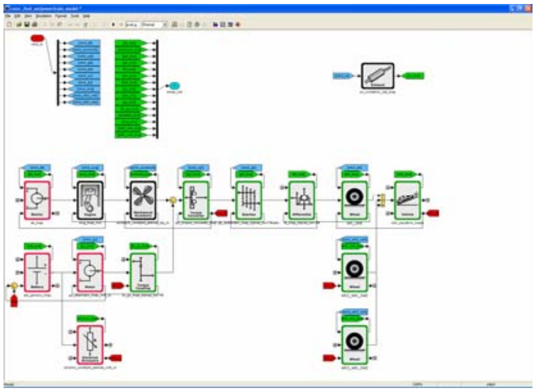

Figure 3. PSAT heavy duty vehicle model using one driven axle and two passive axles

To fulfill the requests from our heavy duty 21st Century Truck partners, a hydraulic hybrid configuration and generic hydraulic component models were added to PSAT. Two entirely new component models were defined in PSAT: the hydraulic pump and the hydraulic energy storage system, also known as the accumulator.

This new configuration was developed to support an on-going project within a truck manufacturer.

Non-disclosure agreements have been signed to allow the exchange of proprietary component models and data.

Conclusions

Preliminary modifications leading towards a heavy duty version of PSAT have been implemented. PSAT is ready to do basic heavy duty simulation; however more work can be done in incorporating special heavy duty models, controls and most importantly component and vehicle data. Configurations with additional drive axles can also be incorporated into PSAT.

Collaborations have planned with national laboratories and universities to validate component models using test data.

Publications / Presentations

1. Heavy Duty Powertrain System Analysis Toolkit (PSAT - HD) – presentation: Aymeric Rousseau, Phil Sharer, Glenn Keller, Shane Halbach, Sylvain Pagerit

IV.B. Development of Medium- and Heavy-Duty Truck Systems Sub-Models

K. Dean Edwards (Principal Investigator)
Oak Ridge National Laboratory
National Transportation Research Center
2360 Cherahala Boulevard, Room L-04
Knoxville, TN 37932-6472
(865) 946-1213, e-mail: edwardskd@ornl.gov

DOE Program Manager: Lee Slezak
(202) 586-2335, e-mail: Lee.Slezak@ee.doe.gov

Objectives

- To support the Office of FreedomCAR and Vehicle Technologies Heavy Vehicle Systems activity and 21st Century Truck Partnership through the establishment of an updated medium and heavy truck dedicated model platform for PSAT-type simulations and evaluations.

Approach

- Engine maps for PSAT are being developed using dynamometer data from heavy-duty diesel engines.

Accomplishments

- Engine dynamometer data necessary to produce the engine maps has been obtained from four, 2004 emissions compliant, heavy-duty diesel engines.
- A technique has been developed for producing the PSAT engine maps from the engine data.
- PSAT engine maps for one of the engines have been completed.

Future Directions

- Completion of the PSAT engine maps for the 2004-compliant engines.
- Re-configure aftertreatment models developed for light-duty vehicles for the heavy-duty PSAT application and explore the development of simulated engine maps to predict the impact of advanced combustion technologies.

Introduction

Accurate systems simulations of the fuel efficiency and environmental impact of advanced vehicle propulsion and emissions control technologies are vital for making informed decisions about the optimal use of R&D resources and DOE programmatic priorities. One of the key modeling tools available for making such simulations is the Powertrain System Analysis Toolkit (PSAT) maintained by Argonne National Laboratory (ANL). A distinctive feature of PSAT is its ability to simulate the transient behavior of individual drive-train components as well as their combined performance effects under realistic driving conditions. However, the accuracy and usefulness of PSAT simulations ultimately depend on the accuracy of the individual component sub-models or maps and the variety of systems which can be modeled.

Oak Ridge National Laboratory (ORNL) is collaborating with ANL in this endeavor and is specifically tasked with providing data and sub-models that augment PSAT's capabilities.

Specifically, ORNL's role has focused on the experimental measurement of performance data from advanced diesel engines and emission control components and the incorporation of that data in the form of maps or low-order transient models into PSAT.

In addition to considerable effort on light-duty systems, in FY2006, ORNL has begun efforts to expand PSAT capabilities on the heavy-duty side by providing engine maps for heavy-duty diesel engines. The maps are based on dynamometer data from four, 2004 emissions compliant engines.

Approach

The PSAT engine maps are generated from a small subset of data that is obtained through the evaluation of the actual engine using an engine dynamometer. Data is collected at a number of speed and load points with the engine operating under steady state conditions. Clearly, the accuracy of the maps is dependent upon the extensiveness of original engine data. It is important to have data that covers the entire speed-load range of the engine and that defines the torque curve.

The PSAT engine maps consist of m x n lookup tables with inputs of engine speed and torque. To generate the matrix used to populate the lookup table for each map, the experimental engine dynamometer data is fed into a Matlab routine which uses interpolation to fill in the missing regions of the speed-load range. The regions of the matrix that lie above the torque curve of the engine (where the engine cannot operate but which must be filled in with "dummy" values to complete the lookup tables) are filled in vertically using a "nearest-neighbor" extrapolation technique.

Results

The first set of PSAT engine maps have been completed for one of the four, 2004-compliant heavy-duty diesel engines. Graphical representations of the maps are shown in Figure 1. The set of maps for this engine includes 12 look-up tables for fuel and exhaust flow rates, intake pressure and temperature, exhaust temperature, and emission levels of NOx, total hydrocarbons (THC), O_2, CO, CO_2, and particulate matter (PM). These parameters were chosen to provide information about the engine performance and to supply the necessary exhaust conditions to the aftertreatment models.

Future Directions

Future efforts will contribute to the development of additional PSAT sub-models that will enable simulating the efficiency of medium- and heavy-duty truck configurations operating on prescribed duty cycles. Tasks for FY 2007 include:

- Completion of the PSAT engine maps for the 2004-compliant engines.
- Re-configure aftertreatment models developed for light-duty vehicles for the heavy-duty PSAT application and explore the development of simulated engine maps to predict the impact of advanced combustion technologies.

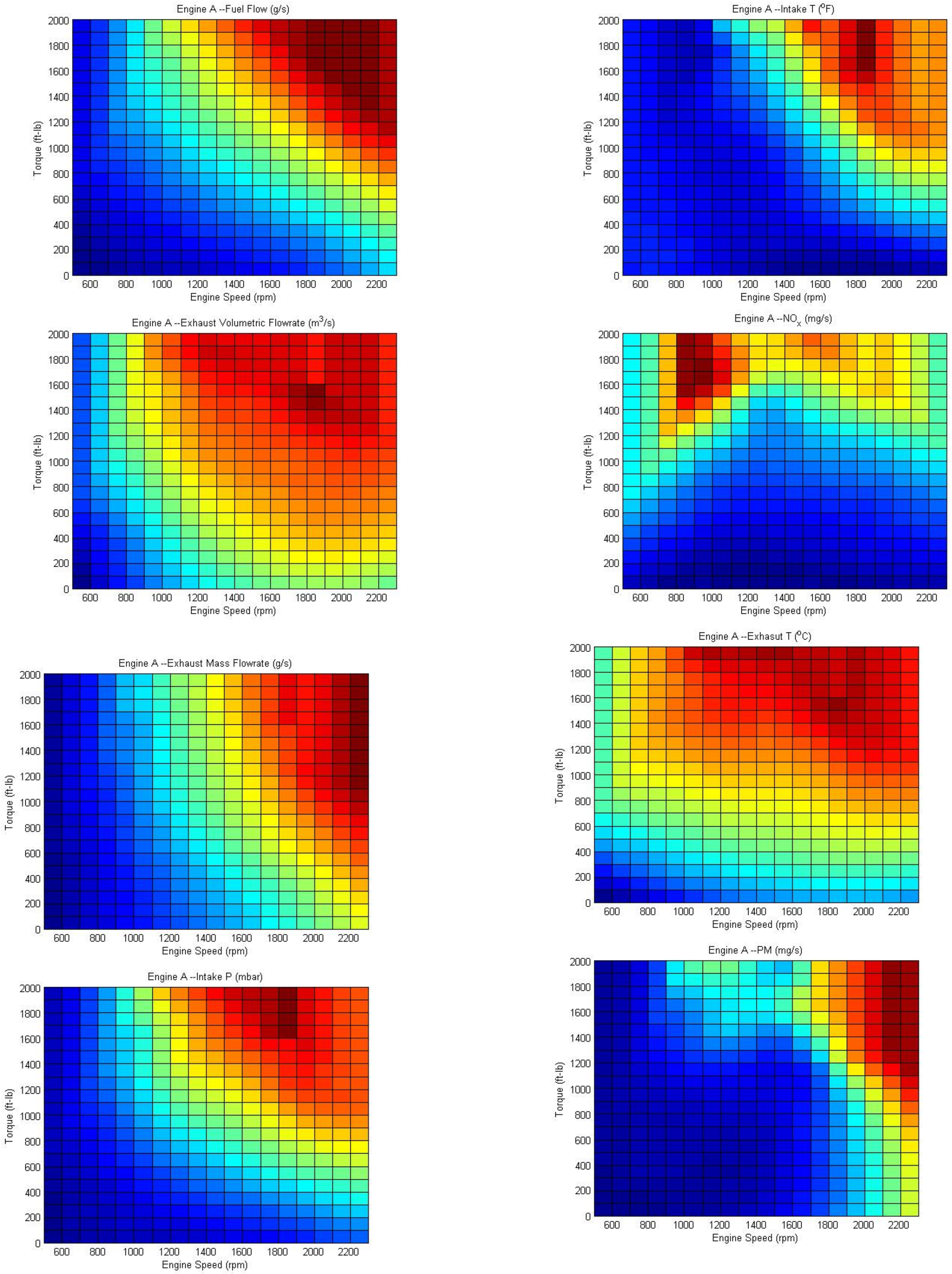

Figure 1. Graphical representation of the PSAT maps for the first of four, 2004-compliant, heavy-duty diesel engines

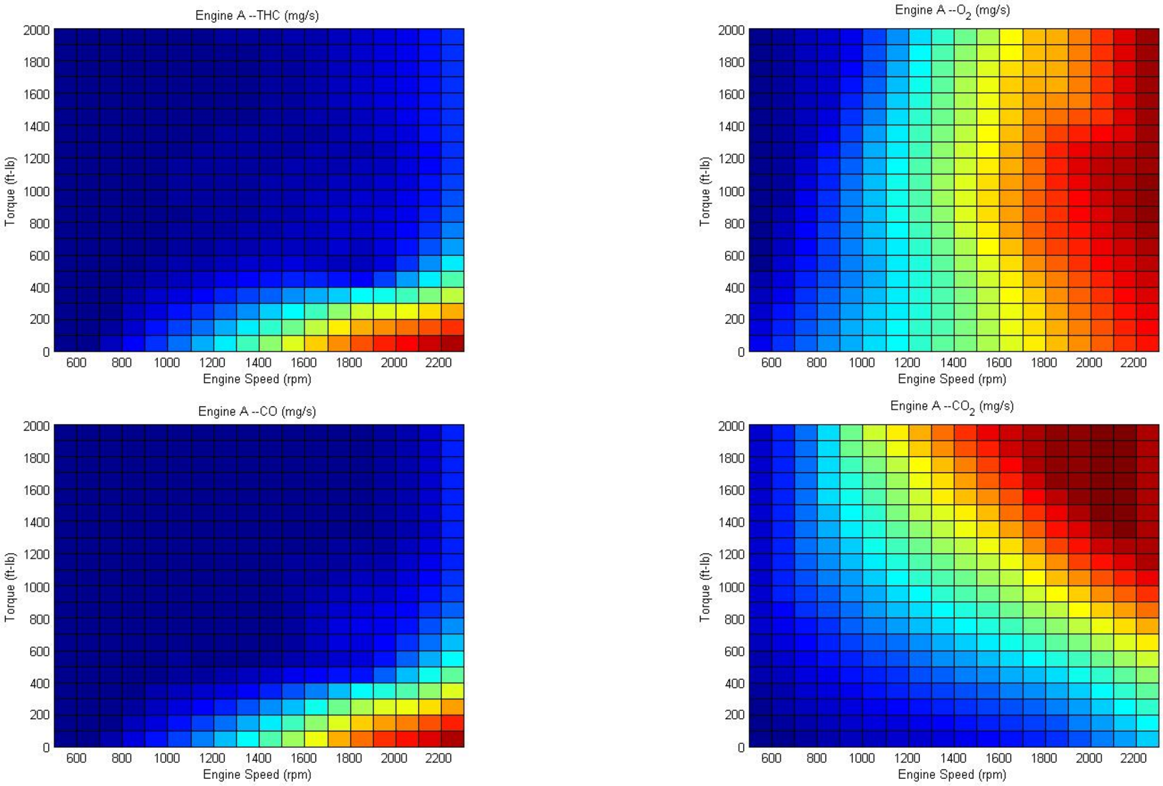

Figure 1. (cont.) Graphical representation of the PSAT maps for the first of four, 2004-compliant, heavy-duty diesel engines

V. OFF-HIGHWAY

V.A. Hybrid Energy Storage and Fuel Optimization

Principal Investigator: Lembit Salasoo
General Electric Global Research
1 Research Circle, Niskayuna NY 12309
(518) 387-5000, fax: (518) 387-6675, e-mail: salasoo@crd.ge.com

Field Project Manager: Steve Cooke
National Energy Technology Laboratory
Morgantown, WV 26507-0880
(304) 285-5437, e-mail: Steve.Cooke@netl.doe.go

Technology Development Manager: Lee Slezak
(202) 586-4819, e-mail: Lee.Slezak@ee.doe.gov

Participants
Paul K. Houpt, General Electric Global Research

Contractor: General Electric Global Research
Contract No.: DE-FC04-2002AL68284

Objective

- Develop and demonstrate locomotive system technologies targeting gross fuel efficiency gains
- Demonstrate a modular energy storage system for hybrid locomotive system on a hybrid locomotive platform
- Develop optimization software for minimizing fuel consumption in both hybrid and non-hybrid locomotives, and demonstrate the consist optimizer on the test track
- Demonstrate the combination of modular energy storage system and fuel optimizer on a hybrid locomotive with full-scale energy storage system

Approach

- Specify and develop advanced modular energy storage units and lab test prototype modules
- Design and bench test advanced hybrid locomotive energy management system (EMS) controls and demonstrate on a hybrid locomotive on a test track
- Develop suitable models for dynamic optimization of fuel use
- Develop practical robust fuel use optimization algorithms capable of locomotive implementation
- Demonstrate fuel use optimization algorithms in off-line interactive simulation environment
- Complete field demonstrations of selected fuel saving algorithms
- Fabricate and bench test full-scale energy storage modules and associated controls
- Integrate full-scale energy storage modules to hybrid locomotive
- Design, fabricate and bench test hybrid fuel optimizer controls

- Integrate fuel optimizer controls on hybrid locomotive, demonstrate on test track
- Measure and verify fuel savings benefit

Accomplishments

- Modular advanced battery system cold energization testing and evaluation
- Modular advanced battery system vibration design and initiate proof-of-principle module fabrication
- Demonstrated, in revenue service, near-optimal fuel-saving driving plans
- Enhanced real-time Consist Manager and Trip Optimizer simulation platform and operator interface

Future Direction

- Fabricate and evaluate locomotive-worthy hybrid energy storage modules
- Design the integration of hybrid energy storage system to the hybrid locomotive platform
- Fabricate full locomotive set of hybrid energy storage modules, integrate system to the hybrid locomotive and track test
- On-locomotive test of hybrid fuel optimization controls
- Fuel performance of combined system will be measured and verified

---

Introduction

The 21st Century Locomotive Technology project was proposed by GE to improve locomotive efficiency with energy management and optimization technologies, and to develop advanced fuel injection and turbomachinery technologies for an emissions-compliant and fuel efficient power plant. The energy management and optimization technologies are projected to produce a combined 20% reduction in total fuel consumption with emissions at the baseline or lower. This annual report applies in particular to the progress for the two locomotive systems technologies of hybrid energy storage and fuel optimization.

At this point, the construction of a vibration-hardened hybrid locomotive energy storage battery module is underway, and the electrical sensitivities of a cold battery have been elucidated. A hybrid locomotive system model has been added to the fuel optimizer and upcoming work will extend the optimization techniques to cover a train consist that includes hybrid locomotives. These are necessary steps towards the project objective of demonstrating a hybrid locomotive fuel optimizer.

Benefits for Locomotives and Road Vehicles

The rail modality carries approximately 40% of US freight on a ton-mile basis, and in 2003 the Class 1 railroads consumed 3.85 billion gallons of fuel to move this freight. Application of the energy management and optimization technologies developed in this project to the whole locomotive fleet will save approximately 770 million gallons of fuel annually. Further, as fuel prices rise and global oil supply tightens, increasing railroad fuel efficiency makes transfer of freight transportation mode from less fuel-efficient modalities to rail increasingly attractive on an economic basis, producing significant impact on the national strategic imperative to reduce dependence on foreign oil. That is, the increase in railroad fuel efficiency will naturally provide the market-based signals to transfer freight transportation to rail from modalities with significantly lower fuel efficiency.

Reducing the energy expended in completing a mission reduces fuel use and emissions production. Optimization algorithms developed manage how the train is driven to meet travel time objectives, subject to track and train constraints, with the least fuel possible. While the precise variability is still being quantified, savings exceeding 4% have been demonstrated in several test runs. The advanced fuel optimizer and modular hybrid energy storage technologies developed in the 21st Century Locomotive Technology project have the potential to be applied for fuel efficiency improvement of on-the-road vehicles.

Advanced Modular Energy Storage System

A hybrid locomotive will store otherwise-wasted locomotive braking energy and reuse this energy for traction, thereby reducing fuel consumption 10-15%, while keeping emissions at the baseline or lower. The energy storage system (ESS) is the core part of the overall hybrid locomotive system. In previous years, sodium nickel chloride technology was selected for the hybrid locomotive, battery module voltage was set and an upgraded battery module cooling system design was developed. Three accelerated vibration tests were performed on the existing module design to identify failure modes to be addressed by locomotive-specific module redesign. A test program was started to quantify the effects of connecting a cold battery to the locomotive system.

In FY2006, the vendor, together with GE Transportation consultation, has developed a more robust battery module design to address the premature vibration failures identified in testing of the existing module design. The vendor has begun manufacture of an instrumented “mockup” battery to validate the vibration performance of the improved design. Once delivered, the mockup battery will be tested under an accelerated vibration regime in a cold and unenergized condition. The complexity of the vibration redesign has pushed out the delivery schedule of advanced modular battery systems for the 21st Century Locomotive Technology project well into 2007.

Testing was performed to assess the effects of connecting a cold battery to the locomotive system. While a frozen battery is in a high internal resistance state, it still has an internal EMF and can deliver low currents to a load. Cell-level tests were performed to assess the effects of such energization. It was found that application of a reversed voltage to a cell produced internal cell damage (of unknown nature) that resulted in premature failure of the cell when it was heated to operating temperature and. In addition a low, microamp-level discharge of a cell resulted in voltage reversal given sufficient time. An operating limit of 1 mAh cold discharge was developed to avoid damage. The locomotive system design will have to ensure that cold battery leakage currents stay below such limits.

Develop Fuel Optimizer Systems and Demonstrate Consist Fuel Optimizer

The goal was to develop and demonstrate control strategies to save fuel initially in freight trains using conventional (non-hybrid) diesel-electric locomotives for propulsion. A methodology was developed to bring benefit to non-hybrid locomotives, and then extended to hybrid locomotives. The key systems developed in the effort are referred to as Consist Manager and Trip Optimizer. Focus has been: to develop the required algorithms to compute fuel optimal trips in numerically robust ways including new ways to simplify a complex optimization problem; to develop a means to follow the optimal plans in a coaching or closed loop fashion; to provide for a means to re-plan a partially completed trip in an efficient fashion; to develop a simulation means to prototype a real-time interactive system to demonstrate the concepts; and finally to demonstrate the system on a revenue service locomotive.

The Consist Manager has been described in detail previously; it saves fuel by distributing power requested by the driver among the locomotives in the most fuel-efficient fashion. This system was shown to be simple to implement and is transparent to operations, and was demonstrated to save 1-2% fuel when used in typical duty cycles. Consist Manager is now a product sold by GE Rail for both DC and AC locomotives and is undergoing field trials at two Class 1 Railroads in the US.

Trip Optimizer provides an integrating framework for energy management in completing a freight haul from a mission perspective. Information provided by dispatch on the logistics of the load to be carried, starting point and destination, route to follow, power (locomotive) configuration, together with models and parameter values of associated models, are together used to synthesize the best way to drive the train to arrive at a specified time with the least fuel consumption. Trip Optimizer synthesizes the optimal speed to drive and the associated throttle setting, which minimizes fuel and satisfies speed restrictions (limits) along the route. The optimal "recipe" or plan for driving the train can be provided as coaching cues to the driver or executed closed-loop with feedback of certain locomotive variables plus GPS-derived track location coordinates. With Trip Optimizer, the onboard crew has a tool to manage the journey in a completely novel way, by allowing explicit tradeoffs between journey completion time and the fuel used as opposed to operating at or near the speed limit all the time when given a track authority. For this increase in mission complexity, a crew with suitable incentives can save more than 4% fuel in a typical mission, for the same travel time, compared to manual operation.Where even a small amount of slack time is available, additional fuel savings exceeding 8% are feasible.

Planning Architecture

Trip Optimizer planning is the process that builds on the driving recipe of throttle and speed to carry out a typical trip. In particular, it provides the analysis and decision framework to start a journey, adjust a plan for changes that occur in route and when required, to develop a completely new plan when conditions preclude a simple fix.

This architecture has been implemented, including the following elements:

- Data structures to represent the plan elements and system parameters
- An 'engine' to compute a plan based on parameters and objectives
- An algorithm to break the plan into single or multiple parts (segments)
- A means to execute the plan in both an advisory (i.e. operator controls throttle) and closed loop (system controls the throttle)
- A means to track projected arrival times and performance compared to the plan

Field Demonstration of Trip Optimizer

The non-hybrid trip optimizer was implemented in a development environment similar to the Consist Manager demonstration conducted in 2004. A throttle-only non-braking version of Trip Optimizer was used: whenever braking was required to stay on the fuel optimial plan, control was handed off to the driver, who then re-engaged the system when throttle only control was feasible. In this case, all real-time algorithms were hosted on an industrial strength PC that runs all the GPS navigation and speed regulation functions. Separate linked laptops provided planning and operator interfaces, and a setup and engineering interface to the display seen by the driver. Figure 1 shows the setup in a GE Dash 9 Evolution locomotive. A digital interface to the master control throttle and the locomotive computer was also provided. The entire system requires no changes to the locomotive software and can be installed in a few hours, including a serial data interface to acquire various locomotive signals. Using this setup, Trip Optimizer was tested on over 3000 miles of track, in live revenue service on a Class 1 and a regional railroad. It took about 15 minutes or less to show the crews how to operate the system, and the system was operational on average more than 70% of the miles traveled

Using data from more than six months of manually driven runs, fuel use data was compared to more than 30 different crews with similar train makeups. Savings exceeding 4% (in some cases double digit percentages) were observed among the test runs. Feedback from road-foreman and crews was consistently positive on the performance compared manual operation with respect train handling. Additional tests for fuel saving and train handling performance are planned for late 2006.

Conclusions

The GE project team looks forward in FY2007 to receiving and evaluating locomotive-hardened advanced hybrid energy storage modules and fully developing fuel optimization technology that utilizes the additional degrees of freedom presented by locomotive hybridization. The combination of these technologies will yield double-digit percentage reduction in fuel usage in freight haulage applications, a significant benefit to one of the dominant US freight transportation modalities.

Monitor and host laptop computers

Driver display (upper left) and control keyboard

Figure 1. Cab setup for trip optimizer demonstration

V.B. Advanced Hybrid Propulsion and Energy Management System for High-Efficiency, Off-Highway, 320-Ton-Class, Diesel Electric Haul Trucks

Principal Investigator: Tim Richter
GE Global Research, 1 Research Circle, EP110C, Niskayuna, NY 12309
(518) 387-5670, fax: (518) 387-6675, e-mail: tim.richter@ge.com

Technology Development Area Specialist: Lee Slezak
(202) 586-2335, fax: (202) 586-1610, e-mail: slee.slezak@ee.doe.gov

Field Project Manager: Sam Taylor
(304) 285-4681, fax: (304) 285-4469, e-mail: samuel.taylor@netl.doe.gov

Participants
Sean Huang, GE Global Research
Kevin Gavel, GE Global Research
Gary Kilinski, GE Global Research
Dwight McCormick, GE Global Research
Henry Young, GE Rail
Bertrand Bastien, GE Rail
Allen Randolph, GE Rail
Rafael Santana, GE Rail
Tim Brown, GE Rail
Joe Currie, GE Rail
Kim Byard, Komatsu America Corp.
Cord Dustmann, MES-DEA

Contractor: GE Global Research
Contract No.: DE-FC04-2002AL68080

Objective

The objective of this project is to reduce the fuel consumption of off-highway vehicles, specifically large tonnage mine haul trucks, as shown in Figure 1 at the end of this report. A hybrid energy storage and management system will be added to a conventional diesel-electric truck that will allow capture of braking energy normally dissipated in grid resistors as heat. The captured energy will be used during acceleration and motoring, reducing the diesel engine load, thus conserving fuel.

Approach

The project will work towards a system validation of the hybrid system by first selecting an energy storage subsystem and energy management subsystem. Laboratory testing at a subscale level will evaluate these selections and then a full-scale laboratory test will be performed. After the subsystems have been proven at the full-scale lab, equipment will be mounted on a mine haul truck and integrated with the vehicle systems. The integrated hybrid components will be exercised to show functionality, capability, and fuel economy impacts in a mine setting.

Accomplishments in FY 2006

- Battery enclosure design and construction completed
- Full-scale lab evaluation hybrid system operational with full hybrid control:
  - 700kW discharge
  - 450kW charge
- Major components have been installed on the vehicle:
  - 4-pack battery enclosure
  - Inductors
  - Power Electronics
  - Controls

Future Direction

- The current accomplishments are leading to a final on-truck system validation currently scheduled for May 2007. Upon completion of the hybrid systems and testing, a demonstration of vehicle performance and technical review is planned at the Komatsu Proving Ground near Tucson, AZ. Until then, the GE and Komatsu teams will be working to finalize the truck integration and hybrid controls on the vehicle. This will also enable validation of the system modeling work performed earlier in the project.
- Following the on-truck system validation, battery performance and life can be investigated. While great care has been taken to evaluate and select batteries with regard to performance characteristics, it is also necessary to better understand the mechanical life of the battery systems in high vibration installations. The batteries used in the system validation testing will be electrically characterized to measure resistance rise, one primary indication of service life. Several of these batteries will be torn down and analyzed for excessive wear and mechanical damage. Other batteries will be further exercised electrically and mechanically to better understand failure modes and performance characteristics.
- Beyond the current project, work could continue to better investigate the primary commercialization paths and next generation energy storage systems. Beyond improving fuel economy, the use of hybrid technology for reducing emissions would also be developed. By considering the energy storage system and related hybrid components during design, the next generation hybrid mine haul truck will provide increased benefits in many aspects of mining operations.

Introduction

The conventional mine haul truck, also referred to as an Off-Highway Vehicle (OHV), uses a diesel engine to turn an alternator that generates alternating current (AC) electricity. The electricity is rectified to DC voltage that is applied to the main electrical bus called the DC Link. Power electronics convert the DC link voltage to variable frequency, 3-phase AC that drives the wheel motors during motoring. When braking is required, the wheel motors function as generators and electrical power is directed to the Braking Grid Resistors, also known as the “Grid Box,” to be dissipated as heat. In addition to traction motors, the diesel engine must power auxiliary loads such as radiator cooling fans, operator air conditioning, steering, hydraulics, and control circuits. These auxiliary loads are powered by mechanical means and with a smaller, second alternator connected to the vehicle’s 24V battery system. Figure 2 shows a block diagram of the hybrid vehicle system. Three primary components will be added to the conventional OHV: Hybrid Vehicle System Controls, Energy Management System, and Energy Storage System. Each component plays a specific role in the recovery of braking energy.

The Hybrid Vehicle System Controls perform the high-level supervisory functions of the hybrid vehicle, primarily controlling the balance of engine power, grid dissipation and battery charging or discharging. Performing these functions requires intimate connections to all of the truck systems.

The Energy Management System (EMS) acts to convert electrical power on the DC link into levels compatible with the Energy Storage System. The EMS is essentially a high power DC-DC converter. The Energy Storage System (ESS) consists of the batteries and manual disconnects, fuses and related safety and protective components.

The hybrid system can enable additional power to be supplied as additional motoring power available at the wheels resulting in a faster speed-on-grade. The higher speed-on-grade is important when considering the impact of hybrid system weight on productivity. Any hybrid system weight must be subtracted from the working payload of the truck to maintain the same gross vehicle weight (GVW). Because the truck is already moving downhill as fast as possible, productivity, expressed in tons/hour, can only be maintained by decreasing the uphill haul time. The hybrid system enables this improvement while saving fuel.

Full-scale Laboratory Evaluation

GE Transportation Systems (GETS) operates a 3500hp dynamometer for functional and performance testing of OHV propulsion systems. The facility can emulate all vehicle systems in a controlled environment allowing instrumentation of the system for analysis and troubleshooting. The entire battery system, with all control components and software, was assembled for evaluation prior to the truck integration.

The full-scale battery test facility consists of twelve batteries connected with a CAN communication system. Each battery has a management controller on the CAN network and is capable of communicating status messages, such as temperature and state-of-charge (SOC), and receiving commands from the system controller. The GETS team has fully integrated and tested CAN communication between all components, including the high voltage batteries. Galvanic isolation was installed on the CAN bus from the batteries to prevent damage or hazards in the control groups.

The power electronics unit found on production trucks is used to provide wheel motor and braking grid power control, as well as perform some hybrid power management. The standard propulsion system controller has been adapted to interface with the hybrid controller to enable smooth response of diesel engine and battery power to the wheels based on driver commands.

The full-scale laboratory evaluation achieved 700kW discharge rates and 450kW charge rates into the hybrid battery pack. Because the lab evaluation system is configured to match the on-truck system, confidence in battery voltage ripple estimates and inverter stability has been confirmed.

Vehicle Integration

The primary milestone of this project is to validate the performance of the hybrid system on a truck in actual mining conditions. In support of this milestone, significant progress has been made in FY 2006 with the construction and mounting of major hybrid components on the vehicle. The smoothing reactors, or inductors, hybrid control group and 4-pack battery enclosure have all been installed on the truck. The last major component, the 8-pack battery enclosure, is currently being assembled in Erie, PA and is scheduled for installation by the end of this calendar year.

While the OHV is a big truck, mounting an 8,000+ pound battery enclosure and other hybrid components requires careful consideration and design. Komatsu America Corp provided design guidance and made modifications to reinforce and add mounting structures for hybrid components. Four primary hybrid equipment groups are located on the vehicle: two battery enclosures (box 2 & 3), one hybrid control group (box 1), and one inductor group (box 4), shown in Figure 4.

The batteries are mounted in two separate enclosures. These enclosures mount on the right-front upper deck and front bumper. The front bumper enclosure includes receptacles for off-truck battery charging and monitoring, when needed. Each enclosure is isolated from the truck's vibration to minimize the risk of mechanical battery failure. The battery enclosures also host appropriate support components, such as disconnect switches and cooling fans.

The battery enclosures are designed to be compact, reducing weight overhead and affording visibility for the driver when possible. Visibility is certainly a concern for the enclosure on the upper right-front deck. Two visual aids, additional mirrors and a camera system, are planned to compensate for obstruction caused by the battery enclosure. The enclosures are air-cooled using filtered air and include means to quickly charge one or more batteries using off-board factory chargers to verify SOC and other diagnostic features.

The front bumper mounted battery pack houses four of the twelve total batteries. Komatsu has designed, fabricated and installed a mounting extension to the front bumper and the enclosure is installed. Since being installed, the truck has been driven and performance of the vibration isolators and mounts is good.

The Hybrid Control Group (HCG) contains support and interface components for hybrid equipment and was one of the first components installed. It is located behind the operator’s cab and houses power supplies (DC-DC converters), fuses, contactors and other auxiliary equipment. Reinforcements to the deck were designed and provided by Komatsu to shore up mounting locations for the HCG.

Smoothing reactors have been mounted between the frame rails in the rear of the vehicle. Komatsu supplied modifications to support the two iron-core inductors with a simple cross-member type mounting structure. A sheet metal cover provides protection from water and excessive dirt.

Final integration of all components is expected to complete in January 2007. A check of sub-scale hybrid operation using the 4-pack battery enclosure is expected in October 2006 and this will provide a check of proper operation prior to the build-up and installation of the 8-pack enclosure. The 8-pack is planned for installation in December. Following installation of the 8-pack enclosure, final wiring and installation details will be completed and power-up can begin.

On-vehicle System Validation

With an operational hybrid system, the team will begin running functional and performance tests on the hybrid OHV. Data collected will provide insight into hybrid / truck interactions and allow validation of the system model developed earlier in the project. The primary impact expected from the system is a reduction in fuel economy, though the system could also be used to provide a power-up function wherein the diesel engine power is supplemented by hybrid assist. This would increase on-grade speed and increase productivity. Both fuel economy and productivity are important to mines and the system validation will help bring actual quantification of hybrid impact to these metrics.

Several tests will be considered for the Komatsu Proving Grounds, shown in Figure 5. One test will subject the hybrid truck to a real mine haul. The haul is approximately 1.6 miles in length and 750 feet in elevation change. During the downhill, the vehicle will charge the batteries, reducing the amount of dissipation in the retard grid. During the uphill climb, the vehicle will pull power from the battery to reduce the loading on the diesel engine, saving fuel. A mode of operation wherein the engine is still operated at full power and supplemented by the hybrid system will also be investigated using the 10% constant grade track.

In May 2007, GE expects to hold a technical review and demonstrate hybrid system operation and show test results and measured performance. This review will also serve as a third go/no-go milestone in the project to determine next steps on battery tear down and future plans for the hybrid truck.

Battery Testing

Last year, sub-scale battery testing was performed to help understand the performance and life of the batteries as subjected to expected hybrid operational modes. Cells can electrically “fail” in two ways: complete failure or degraded performance. GE is primarily concerned with degraded performance in the form of increased resistance of cells. As a cells ages, the resistance generally increases, requiring higher voltages to drive charging current. For all chemical cells, there are voltage limits that, when exceeded, greatly reduce the life of the cell.

For the hybrid OHV application, the most demanding operating point is peak charging. Truck speeds are usually high (>20MPH) and the wheel motors generate megawatts of power. To create an effective hybrid system, the batteries must capture as much of this generated power as possible. During the debug and system validation task in early 2007, the batteries will be exercised in-situ and be exposed to non-laboratory conditions such as dirt, vibration, and solar heating loads. A follow-on task of battery analysis is planned to follow the system validation testing.

Beyond electrical cell failure, mechanical failure due to vibration is also a concern. Heavy-duty diesel-powered vehicles are known for vibrations and resonance points. Last year, vibration tests were performed on an off-the-shelf battery and life estimates were made based on this testing. Using vibration isolators, battery life is expected to be significantly long for the demonstration period, however, the limited vibration data and lack of mechanical life information results in high uncertainty for the impact on commercial life of the battery system. Accumulated testing will help better define performance of the battery system in terms of life – a key driver of hybrid system life cycle cost.

Conclusions

The full-scale laboratory evaluation has been completed. Successful battery tests achieved charging at 450kW and discharging at 700kW. Also confirmed in the lab evaluation were hybrid controls, inverter stability, and battery voltage ripple.

Nearly all hybrid components have been mounted on the truck. The inductors, hybrid control group and 4-pack battery enclosure are fully mounted and significantly wired and tested. The 8-pack battery enclosure is planned for build-up and final installation by December 2006.

GE and Komatsu will soon finalize modifications to the truck and begin component power-up, debug, and initial testing. 2007 will be the final year for the project and GE and Komatsu are looking forward to utilizing the developments from this project to steer and enable future direction of hybrid off-highway vehicles.

Figure 1. Komatsu 830E-AC at Las Vegas Mine Expo

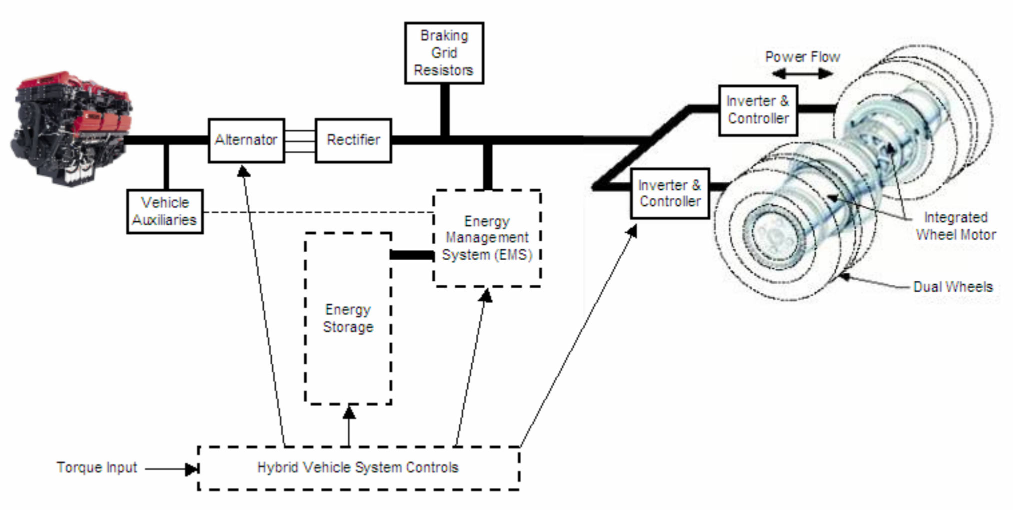

Figure 2. Hybrid electric system block diagram

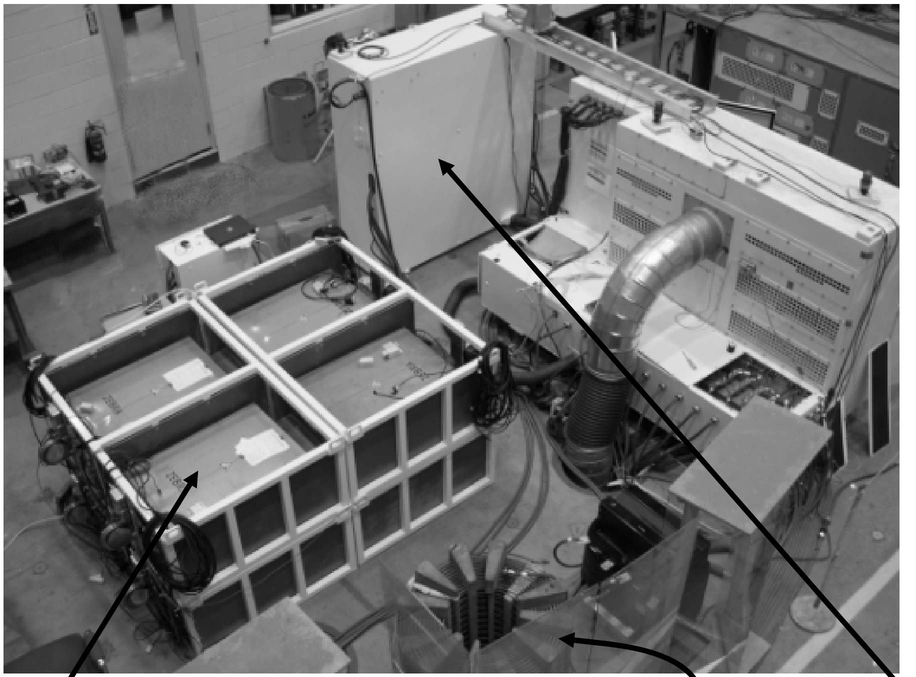

Figure 3. Full-scale test configuration

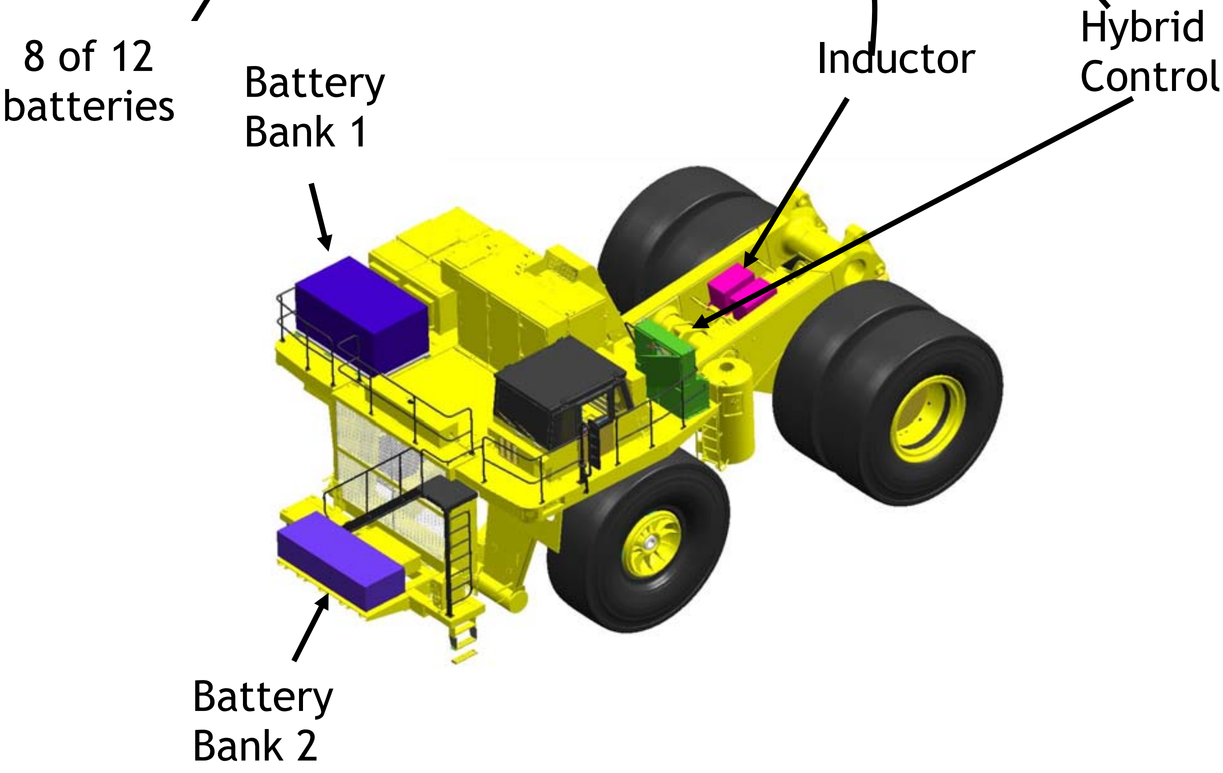

Figure 4. Hybrid equipment groups

Figure 5. Komatsu Proving Grounds, Green Valley, AZ

VI. BRAKE SYSTEMS

VI.A. Advanced Brake Systems for Heavy-Duty Vehicles

Project Manager: Glenn J. Grant
Pacific Northwest National Laboratory
P.O. Box 999, Richland, WA 99352
(509) 375-6890, e-mail: glenn.grant@pnl.gov

Technology Development Manager: Lee Slezak
(202) 586 4819, e-mail: Lee.Slezak@ee.doe.gov

Field Technical Manager: Jules Routbort
(630) 252-5065, fax: (630) 252-4798, e-mail: routbort@anl.gov

Participants: Yngve Naerheim
Tribomaterials LLC
(805) 496 8371, e-mail: ynaerheim@verizon.net

Contractor: Pacific Northwest National Laboratory
Contract No.: DE-AC06-76RL01830

Objective

The objective of this project is to assess the potential of alternate disc brake designs and technology concepts to achieve the goals of increased energy efficiency, higher performance, and an increased level of safety and system control in heavy vehicle braking systems. System and material optimization will lead to increased energy efficiency, reduced environmental impact, and improved life cycle costs.

Approach

- Develop a new high efficiency, low inertia, and lightweight braking system for heavy vehicles and future heavy-hybrids that will meet performance, durability, and economic metrics, as well as assisting in achieving 21CT and FCVT energy efficiency program goals. The application of a lightweight disc brake system could impact vehicle fuel economy by reducing fuel consumption an estimated 0.8% for vocational Class 6-8 vehicles, and 0.5% for line-haul trucks.[1] If fully implemented across Class 6-8 vehicles, the energy savings is estimated to be $3x10^{13}$ BTU/yr, or roughly equivalent to 5.3 million barrels of oil per year.[2]
- Develop numerical computational tools to evaluate new brake designs, and novel vehicle speed attenuation concepts, as well as wheel-well air flow that impacts braking cooling and vehicle performance. The intent is to develop these computational tools so that they can be incorporated into a module for a PSAT-like efficiency model for heavy vehicles, and enhance the vehicle performance simulations capability.
- Explore new friction materials and brake designs that will:
  - Facilitate energy efficiency (light weight)
  - Increase safety, decreased stopping distance, and increase controllability (high and stable friction coefficient)

---

[1] US DOT FHA Highway Statistics – www.ops.fhwa.dot.gov/freight/freight_analysis
[2] Annual Energy Outlook 2005 DOE/EIA-0383(2005)

  - Increase operational efficiency (low life cycle cost by high wear resistance)
- In conjunction with Truck OEM and a Tier 1 brake supplier, use the computational tools to design and implement a full-scale lightweight brake system and initiate instrumented truck field trials to validate designs and generate wheel-well pressure field data.

Accomplishments

- CFD and FEA models have been developed that track braking energy transients and heat generation and convective cooling in a conventional heavy vehicle brake design. The model can input material properties and system geometries, allowing it to be used to predict the effects of materials and designs on the brake surface temperature and resulting heat transfer through the entire vehicle corner module.
- Five candidate new and innovative brake material friction pairs were evaluated for friction, wear, mechanical, and thermal performance at PNNL , Tribo Materials LLC, and Rockwell Scientific. These materials include cermets, novel SiC-C-Cu composites, and Friction Stir Processed materials.
- Material options were downselected to two new materials that show significant increase in wear resistance while maintaining appropriate friction coefficients. One of these materials shows significant weight savings and thermal conductivity improvement over baseline cast iron systems.

Future Direction

- Initiate design study with brake system suppliers with the goal of developing a full scale rotor/pad systems that can be tested for performance and durability.
- Investigate multi-disc brake rotor arrangements and other new design concepts and determine benefits and sensitivity of each to braking performance, energy efficiency , reduced mass, and barriers to implementation.
- Identify alternate energy absorption/conversion and heat management/rejection methods for potential system concept redesign.
- Evaluation of system response to noise-vibration-harshness (NVH) for friction pair combinations.
- Further down selection of friction materials based on wear rate, thermal stability, friction characteristics, NVH, and cost.
- Evaluate new software tools and new materials for application to weight-optimized heavy hybrid vehicles.

Introduction

The objective of this project is to assess the potential of alternate disc brake designs and technology concepts to increase the performance, energy efficiency, and safety of heavy vehicle braking systems. For the last 50 years heavy vehicle braking systems have remained largely unchanged; heavy, cast iron drum brakes actuated by air or hydraulic systems. These brakes have been refined over the years by changes in actuator geometry, and with the addition of automatic slack adjusters and ABS, but in terms of overall stopping efficiency and system design, cast iron/phenolic pad drum brakes have reached a technological plateau. In the last decade, a strong pull to increase the efficiency and performance of these systems has emerged both from the regulatory side (FMVSS 121 decreased stopping distance and control) and from the operational cost side including the need for decreased life cycle costs, and increased energy efficiency. In addition to the pulls from the economic and regulatory side, the current braking systems are being subjected to increasing demands from:

- Higher speeds
- Higher GVW
- 30% decrease in the vehicle drag from parasitic loss (aerodynamics and other)[1]
- 19% reduction in engine braking force[3]

These trends will eventually push the current cast iron / phenolic pads systems beyond their capabilities to shed the energy required to stop

---

[3] (NRC-CNRC Technical Report TP 13892E, 2002)

efficiently and safely. The consequence of using current designs and materials in future heavy vehicles will be poor and unreliable performance, excessive wear, increased wear debris, and increased energy consumption on the manufacturing side for required replacement materials. This leads to increased environmental impact, higher maintenance costs, and ultimately lower safety and productivity. Optimizing and improving the current braking system will lead to a completely different paradigm (lightweight, high-temperature systems, electro-mechanical actuation, electrification of existing mechanical and compressed air based systems, small diameter multi disk, etc.).

The current braking systems are also heavy. A typical cast iron drum weighs 112 lbs (50.8kg). Weight reduction alone has a demonstrable effect on fuel consumption for a heavy vehicle, especially those with severe stop-and-go duty cycles, like urban delivery and transit buses (due to high rotational inertia in a heavy vehicle brake). It has been estimated that these high duty cycle heavy vehicles will see a 3.4% reduction in fuel consumption per 2204 lb weight reduction.[1] The new materials proposed in this study, in a disc brake configuration, are estimated to be in the 25lb to 30lb range, representing a savings of up to 87 lbs per brake for the braking surface component alone (not including other scaled down components such as lighter weight calipers and hubs.) For a typical 6-brake urban delivery or bus (Class 6-7-8) this is a potential weight savings of 522 lbs, leading to a projected fuel consumption reduction of about 0.8%. In 2002 these vehicles accounted for 10,305 million gallons of fuel.[4]

Although the fuel savings from weight reduction has less of an effect on long haul Class 8 trucks (1.2% change in consumption per 2200 lb weight reduction[1]) their total energy consumption is much higher than buses: 2.13 million barrels per day oil equivalent. Energy savings (reduction in fuel consumption) due to weight reduction in the braking system for a typical 10-brake Class 8 could be as high as 0.5%. In 2002 Class 8 long haul tractor trailers consumed 26,451 million gallon of fuel. The 2002 US energy consumption for commercial light truck, transit buses, and Class 8 trucks (urban delivery and long haul) was 5.21 Quads (Quadrillion BTUs). [5] Energy savings due to brake system optimization could be as high as (0.0058)(5.21)=0.0302 Quads or $3\text{x}10^{13}$ BTUs. (about 5.3 million barrels per year oil equivalent).

Next generation, lightweight brake systems will have an opportunity to contribute to the goals of increased energy efficiency, performance, and safety. The challenge is integrating new systems and designs into the current truck platforms. A major concern of both truck manufacturers and customers is how new brake systems will interface with existing systems. Of particular concern is the balance between potential new tractor brakes and older legacy air based systems on trailers. Concern also exists about upsetting the stability and balance that has been achieved over the last 10 years with ASC and ABS. Any new system envisioned by this program must take a systems optimization approach, and not one that simply seeks to replace cast iron with something new.

With the need to improve braking performance and durability beyond the 500,000 mile minimum expected life of the vehicle, new friction materials will be required. However, direct material substitution is not likely to be effective from current drum brake systems to advanced disc brake geometries. As such, disc brake design and system packaging is critical to achieving the project objectives.

Approach

The project approach is to develop tools that can help identify new brake system designs and materials. A primary problem being investigated is thermal management. The trend in advanced braking systems is toward higher temperature operation. New brake materials being considered include cermets and high temperature surface modified materials that deviate greatly in their thermal properties from conventional phenolic pad / cast iron braking systems. These materials may require fundamentally different ways to deal with heat rejection or conduction. For this reason, a primary focus of the project is on developing a generalized

---

[4] US DOT FHA Highway Statistics – www.ops.fhwa.dot.gov/freight/freight_analysis

[5] Annual Energy Outlook 2005 DOE/EIA-0383(2005)

thermal/mechanical predictive models to describe heat flow and heat rejection in an advanced braking system. This focus uses linked computational fluid dynamics and solid mechanical modeling to predict how heat will be managed in a potentially higher temperature braking system. The models developed in the last two years will require calibration by experimental testing of new material friction pairs, and will need to be validated by field trials and on-vehicle testing before practical implementation.

The approach can be broken into three main task areas:

Task 1 – Development of Thermal / Structural Models and Brake System Design

This task focuses on developing and evaluating innovative disc brake designs, with the emphasis on enhanced thermal management. Modeling tools in development include computational fluid dynamic approaches (STAR CD and RADtherm) and coupled stress analysis. These tools are used to assist in the design and evaluation of novel disc geometries and system components. The goal of the modeling is to develop a functional solid model and utilize predictive tools to simulate the performance (thermal and fluid profiles, as well as stress analysis) of the proposed disc brake systems.

Some of the brake system design concepts that need to be explored include, but are not limited to, floating single or twin rotors, full phase pad/rotor, and mechanical/electric actuation.

Task 2 – Friction Pair Development

This task involves experimental testing and characterization of the five candidate friction materials outlined in FY04 and FY05. Candidate materials are evaluated for wear and durability in conditions that simulate typical braking scenarios for on-highway and vocational heavy-duty vehicles. Testing includes thermomechanical tests on the bulk materials (CTE, Cp, Emissivity, Conductivity, as well as compressive strength and modulus), tests of the friction, wear , and durability characteristics (on instrumented subscale rotor/pad test equipment), and surface characterization (SEM SEM-Auger, optical profilometry) of the tested pairs to establish the chemical and physical nature of the transfer layer, an important surface layer that determines friction coefficient, heat generation, wear performance and NVH characteristics.

Bulk thermomechanical testing and surface characterization was done at PNNL and the subscale friction testing was done by Tribo Materials at Rockwell Scientific Company (RSC). This data helps to delineate the safe operating envelope of the materials, and is needed by the brake designers to determine where and how the new materials can be employed for current and next generation braking systems.

The outcome of this task will provide the thermal models and the brake designers with relevant data on new materials to enable them to explore new brake concepts, which until now have not been possible with currently available cast iron and phenolic-binder friction materials.

Task 3 – Concept Feasibility of Alternate Braking Technologies

The third task is generally focused on analyzing specific concepts that may be employable for brake systems to either enhance braking efficiency, improve thermal management of friction surfaces, or recovery and storage of waste heat that can be utilized at a later time to drive an electrical loads.

Task objectives will be achieved through evaluation of emerging braking system concepts to scrub kinetic energy from a moving vehicle, such as the use of inductive / regenerative braking, or mechanical (hydraulic) energy recovery. In addition, thermal management is critical in brake system durability and maintaining adequate friction performance. Waste heat is available throughout the braking cycle and is possibly recoverable through energy management devices or energy harvesting methods such as thermoelectrics or piezioelectic generators attached to brake system components. Methods which show promise will be presented to brake suppliers and OEMs, and investigated further as appropriate.

Results

Task 1 – Development of Thermal / Structural Models and Brake System Design

A model was developed for a simplified disc brake rotor geometry that consists of a solid disc and brake pad. This model was created to predict the fluid distribution (air flow) around the brake assembly, and the thermal profile and stress analysis. This will be used to establish design limits (bounding loads) in new disc brake designs. The thermally induced stresses are proportional to spatial and temporal gradients in temperature that develop during braking and cooling.

The analysis and CFD simulation predicts disc temperatures and heat flux during a maximum braking stop from highway speed. This analysis includes essential features of the vehicle wheel well airflow that determine convective cooling rates at the disc surface. Full vehicle CFD simulations from manufacturers and other FreedomCAR projects will be used, as available, as guidance for the convective cooling portion of this model. Radiation heat transfer is also expected to significantly effect disc cooling. Conduction from the rotating disc to the caliper, hub and wheel components is also accounted for in this simulation. If brake temperatures in next generation braking systems are significantly higher than current systems then it will be very important to be able to predict the temperature effects on adjacent components like aluminum wheels and hub bearings.

The simulation utilizes a two step approach, in order to minimize time and computing requirements. StarCD was selected for the CFD part of this application. This software has been used by Volvo for a similar disc brake cooling application. Since the CFD analysis is a time consuming transient simulation, selected results from StarCD are used to form inputs to an additional thermal analysis tool that can be used efficiently for preliminary/scoping sensitivity analyses. The tool selected for this purpose is RadTherm, as it is widely used for brake thermal analysis by industry.

RadTherm is typically used to predict component temperature distributions during repetitive braking test sequences. This package is capable of simulating simple radiation heat transfer from surfaces and also includes the capability of simulating conduction through solids. The efficiency with this tool is realized by not solving for cooling air flow, but by applying convective heat transfer as surface heat transfer coefficients. These heat transfer coefficients are obtained from the preceding StarCD CFD simulation. Sensitivity to parameters such as disc thickness, thermal radiation emissivities, or thermal contact resistances can be investigated with this software to better define the bounding conditions for the stress analysis.

Computer models provide a means of evaluating response of new brake materials, from both a thermal and structural standpoint. Thermal stresses induced during a panic stop and hold or those due to repeated start-stop transients are the limiting performance measures for these components. Both of these events can be effectively modeled to provide, at a minimum, a qualitative comparison between possible materials, and in many cases accurate estimates of peak temperatures and stress states. Accurate knowledge of material properties is a key to the modeling process. In this report initial comparisons of the temperature rise during a braking transient for two rotor materials will be presented: a “reaction-processed” cermet material and the baseline gray cast iron.

Calculations were performed with Adapco’s StarCCM+ code to compare thermal behavior of two heavy truck disc materials during braking. A simplified model is used for this comparison, consisting of a rotating solid disc and hub in air. The wheel, brake caliper and pads are left out, as is the dust shield. The solid mesh is shown in Figure 1. Because the hub and disc model lacks the airflow blockage imposed by the wheel and the dust shield, predicted temperatures are not quantitatively accurate, however they are useful for relative values and trends and in particular, when comparing between candidate rotor materials. Actual

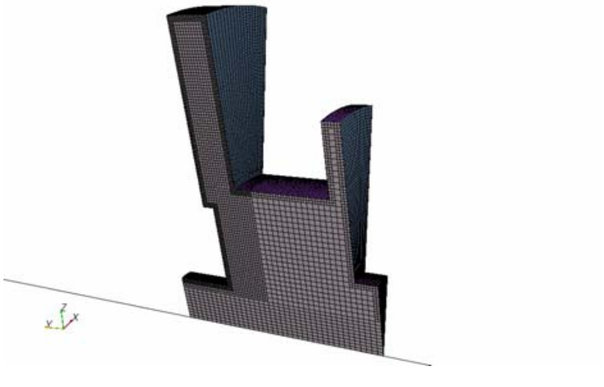

Figure 1. Solid mesh for modeled section of disc and hub

temperatures and rates of temperature increase would be slightly higher.

The two materials being compared are grey cast iron, typical of current commercial truck brakes, and an innovative cermet material. Thermal conductivity of the cermet is roughly 1/10 that of the cast iron, while density and heat capacity are half and twice that of cast iron, respectively. A 300 K (27 C) ambient is assumed for the calculations. Predicted temperatures are shown in Figures 2 and 3 for a steady state calculation with a low heat generation rate typical of continuous light braking to maintain speed (45 mph) on gentle descent (1 degree grade). For the cast iron disc and hub, the maximum temperature on the friction faces are roughly 25 C lower than the peak for the cermet. The model also predicts for these materials that although the rotor face temperatures are higher for the cermet, the hub temperatures are lower, a logical effect of the lower conductivity of the cermet.

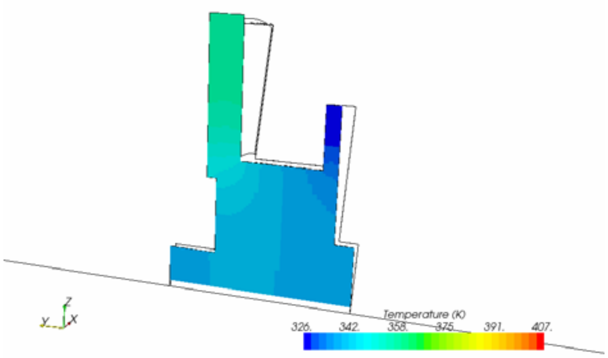

Figure 2. Steady state temperature for cast iron during constant descent

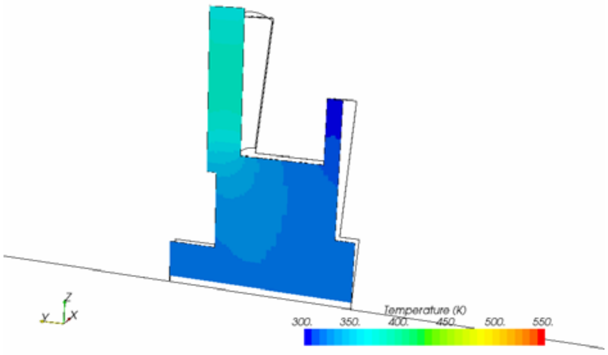

Figure 3. Steady state temperature for low-k material during constant descent

The stopping transient simulation predicts temperature rise following an instantaneous increase in braking force. The constant rate descent steady state is used as the starting point with frictional heating increased by 100 times. This heating rate is typical of what would occur under a constant deceleration stop from 45 mph in 6 seconds. Temperatures are compared after the first three seconds of this transient in Figures 4 and 5. The peak temperature in the cast iron case is roughly 100 C while the peak in the cermet material is 250 C over ambient. The temperature gradients across the cermet material are noticeably higher. Hub temperatures, however, are significantly lower in the cermet rotor simulation.

Although we again emphasize that these temperature magnitudes are dependent upon the simplifying assumptions, the difference in the peak temperature and temperature gradient is significant. In

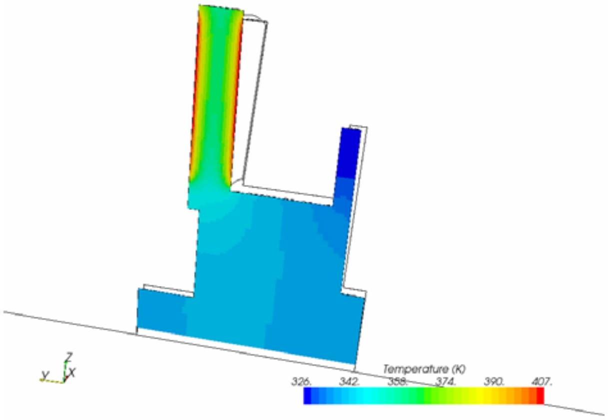

Figure 4. Temperatures at 3 s in stopping transient for cast iron

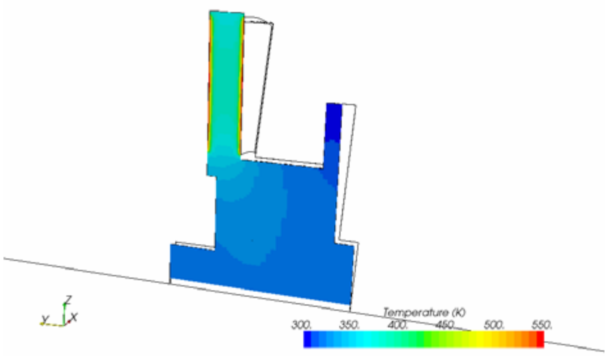

Figure 5. Temperatures at 3 s during stopping transient for low-k material

particular, the temperature gradient will result in a high local stress state due to differential thermal expansion. However this also leads to a situation where the rotor face is hotter but the temperatures in the hub and bearings will be lower than cast iron, a feature that could be important if the brake friction surface is to go to higher temperatures in future designs. Heat generation and flow could be very different in new brake designs, low conductivity rotors may force changes in heat rejection that will be beneficial to some components and detrimental to others. Modeling and simulation tools like the one being developed in this program will be necessary to systems design and optimization.

A detailed FEA model, using the general finite element code ANSYS® 9.0, is currently being developed to explore the structural response of the brake rotor materials and designs to the potentially new thermal environments. The system geometry is shown in Figure 6 with an example finite element mesh. A detailed view without the tire and caliper head is shown in Figure 7. The model currently features a standard diameter tire (43.4), Alcoa® style wheel (24.5”), and a proportionately sized rotor (15.1”). However, the model was constructed such that geometric modifications can be rapidly implemented by simply altering relative dimensions and rebuilding. By using this approach, parametric sensitivity evaluations will be simple to perform.

Task 2 – Friction Pair Development

An integral part of the development of new braking systems is the development of new friction pair materials. It is probable that future demands on the breaking system and the needs for increased operational and energy efficiency will drive the brake friction pair materials away from cast iron and phenolic pad systems. Friction pair development is a rich research area with data available from numerous sources including commercial material suppliers as well as government funded research.[6] For this study a survey of was conducted of friction pair materials, which included commercial and emerging materials options, as well as those still in the research and development phase by various vendors. Over twenty friction material options and vendors were surveyed and based on the technology readiness level and cursory economic considerations, four were down-selected. These four friction materials were tested along with a baseline cast iron rotor material. Friction pairs were assembled from various combinations of these basic material as the rotor, and either these same materials as the pad, or other pad materials. The baseline system was a well optimized cast iron with an Arvin Meritor disc brake pad: R705. The four candidate new materials are outlined below, and described more fully in the FY04 DOE OFCVT Vehicle Systems Annual Report.[7] The friction materials include examples of C/SIC, reaction-processed cermets, and friction stir processed surface engineered materials.

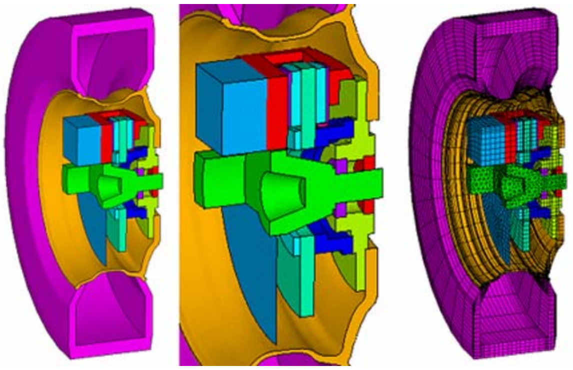

Figure 6. System geometry and sample mesh for detailed thermal-structural

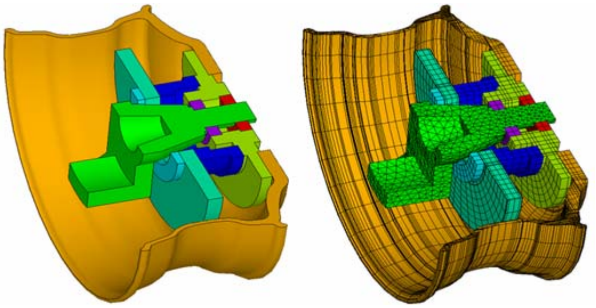

Figure 7. Model and mesh detail without tire and caliper head

1. Reaction Processed Cermet from Excera Materials Group - 50SiC/35Al_2O_3/W1461-XBr
2. C/SiC from Starfire Systems polymer-based ceramic reinforced with chopped PAN carbon fibers

---

[6] PJ Blau, *Advanced Materials for Friction Brakes*, DOE OFCVT 2004 HSWR Annual Report http://www.eere.energy.gov/vehiclesandfuels/pdfs/hswr_2004/fy04_hswr_6.pdf

[7] http://www.eere.energy.gov/vehiclesandfuels/pdfs/program/2004_hv_optimization.pdf

3. C/SiC-copper composite from MER Corp. - Composite of pitch-based graphite cloth in SiC matrix, in-situ attached to high temperature copper core.
4. Surface engineered cast iron - Cast Iron with TiB2 particles incorporated into the surface by friction stir processing. PNNL/SDSMT designed.

All the brake materials selected are currently more expensive than the baseline cast iron, but all are fabricated by methods that could be translated to bulk processing and reduced part cost at high volume. Current estimates of market conditions suggest that 20% of the heavy vehicle market is very sensitive to weight reduction. It has been estimated that in this specialty market, the premium paid for weight reduction could be as high as 3$/lb.[8] In the total truck market this number may be closer to $1.50/lb, indicating any new material proposed will be subjected to very stringent demands on cost differential if weight reduction alone is the only consideration. However, another factor that may play heavily into the economics of looking at advanced material replacements of cast iron is the life cycle cost and performance. Many materials provide combinations of high friction coefficient, particular heat transfer characteristics or increased wear life that can favorably affect system life cycle cost. A 50% increase in wear life for instance will double to interval between rotor change-outs and can affect the economics for those vehicle sensitive to down time.

Experimental investigations into the performance of new brake materials included studies of the friction pair wear performance and durability, thermomechanical testing, and surface characterization. Friction pair testing was done at Tribomaterials LLC and Rockwell Scientific. Four inch diameter discs of each of the down selected rotor material were fabricated and tested for wear performance in an instrumented test apparatus (Figure 8). The tests were run at constant torque for a fixed time, and rotor temperatures were maintained by a water-cooled backing plate. Pads of different manufacture and composition were tested against each rotor material and loads required to maintain torque were measured. From this data friction coefficient can be calculated. Post-test weights were taken of the rotor and pads material to determine wear rate and wear performance. Two conditions were tested in this program. Condition 1 is designed to simulated light braking as might be needed in a gradual decent or in a light snub from freeway speeds. These tests were conducted at a 60 MPH equivalent rotational speed, 100 psi rotor/pad contact pressure and a constant temperature of 200°C. The second condition was more aggressive and designed to simulate slow speed braking at high brake pressure like might be expected in a mountain descent. These conditions were 30 MPH equivalent, 700 psi rotor pad contact pressure, and 600°C rotor temperatures.

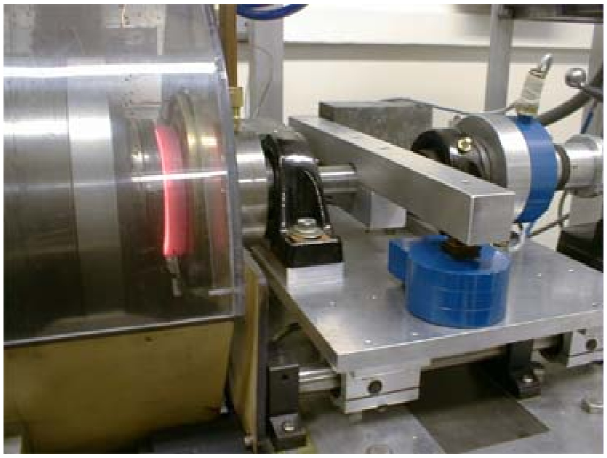

Figure 8. Subscale wear/durability tester at Rockwell Scientific

Figures 9 an 10 illustrate a subset of the tested materials and show the wide range of wear rates and friction coefficients that are possible with the down selected friction pairs. Friction pair development and optimization is an iterative process. One pad material may show high wear rates against one rotor material but when run against another rotor might cause the rotor to wear. Optimization of the friction pairs is not in the scope of this program so data in Figures 9 and 10 is generated only to expose the basic frictional and thermal conduction characteristic of these new materials. Several new material pairs performed very well against the baseline cast iron / phenolic pad showing friction coefficients as high or higher (0.31 to 0.37 on subscale tester) than the

---

[8] NRC-CNRC Technical Report TP 13892E, 2002

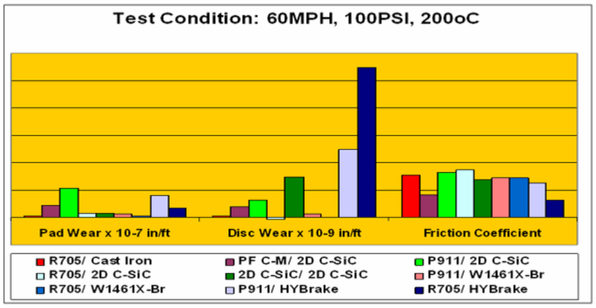

Figure 9. Friction pair performance at low load snubs

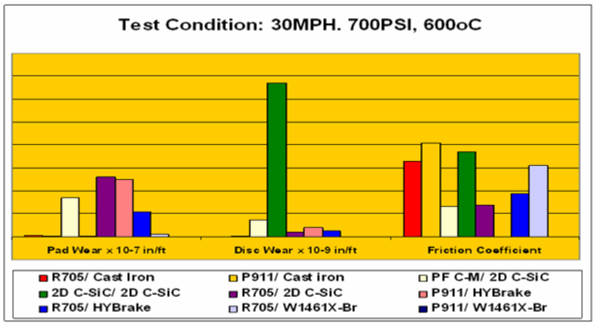

Figure 10. Friction Pair performance at high load transient

optimized cast iron rotor running a current commercial Arvin Meritor pad (R705). Some rotor materials (like the C-SiC at low load condition 1, and the reaction processed cermet rotor at condition 1 and 2) showed wear rates far below cast iron suggesting that these materials may show very low life cycle cost (potentially life of vehicle parts).

Two of the most promising materials are cast iron that has had its surface modified by friction stir processing (FSP) [1], and the reaction processed cermet from Excera Group [2]. The FSP processed materials are fabricated by taking a quantity of TiB2 powder, placing it on the surface of a plate of Class 40 grey cast iron and using a friction stir tool, driving the powder into the plate through severe plastic deformation. This process leaves behind a mixed layer up to 0.25 inches thick in our experiments on the surface of the cast iron that is composed of very fine grained ferrite with dissolved carbon and ultra fine grained TiB2 and in situ formed TiC dispersed in the processed region. This modified cast iron does not have any weight savings advantages but is interesting from the life cycle cost point of view since it has greater than 50% increase in wear resistance.

The second material of interest is the reaction processed cermet. This material showed a greater wear resistance than cast iron, but has half the density. Also, heat capacity was twice that of cast iron. These thermomechaical properties, in combination with the wear and friction performance indicates that this material has good potential to be an appropriate choice for a next generation brake rotor material. Further work is needed to characterize durability and cost structure, but materials such as these show promise to achieve higher performance and higher energy efficiency over current systems.

Conclusions

System modeling tools developed during this program will help to define if some of these wear resistant, high temperature friction pairs can be applied to the specific demands of heavy vehicle brake systems.

Future work should focus predominately on brake rotor geometry design, thermal management, and simulation activities in support of system design considerations. Designs such as multi-disc brake rotor geometries are particularly attractive for thermal and braking performance. Other new design concepts need to be investigated to determine what benefits they may provide, as well as the sensitivity of each on braking performance. In addition, alternate energy absorption/conversion and heat management/rejection methods should be investigated for their potential as primary or secondary methods to control vehicle speed.

A critical next step for this project will be model calibration and validation. Full scale testing needs to be initiated with the collaboration of a truck OEM/Tier 1 brake supplier. These efforts should be directed towards instrumented on-vehicle tests of heat generation and rejection in current braking systems to help refine the current model's predictions on heat generation and wheel well airflow. As new friction pairs and brake designs are developed, full scale testing (dyno and on-vehicle testing) will be required to verify new material durability, designs, and concepts.

Brake system and material optimization will lead to increased energy efficiency, reduced environmental impact, and improved life cycle costs. Lightweight, high performance braking systems have an opportunity to contribute directly to the 21CT and Vehicle Systems goals of increased energy efficiency, decreased parasitic losses through mass reductions, improved knowledge of vehicle undercarriage and wheel-well aerodynamic flow, and improving truck safety through the development and optimization of technologies for better stability, control and braking performance.

Acknowledgements

The principal investigators would like to acknowledge the valuable contributions of James Fort and Harold Adkins of the Pacific Northwest National Laboratory for their work associated with the developing the brake model and simulations.

References

1. Ramasubramanian,U., Arbegast, W.J., Stone, G.A., Grant,G.J., Friction Stir Processing of Class 40 Grey Cast Iron, in Friction Stir Welding and Processing III, Edited by K. V. Jata, et al., TMS (The Minerals, Metals & Materials Society), 2005

2. Daehn, G.S. and Breslin, M.C., Co-Continuous Composite Materials for Friction and Braking Applications, in Journal of Materials, vol.58, no. 11, pp 87-91, TMS, 2006

VII. EFFICIENCY IMPROVEMENTS FOR HEAVY VEHICLES

VII.A. Truck Essential Power Systems Efficiency Improvements for Medium-Duty Trucks

Principal Investigator / Technical Manager: Larry M. Slone
Caterpillar Inc. – Technology & Solutions Division
(309) 578-0243, fax: (309) 578-6285, e-mail: Slone_Larry_M@cat.com

Program Manager: William H. Lane
Caterpillar Inc. – Technology & Solutions Division
(309) 578-8643, fax: (309) 578-2984, e-mail: Lane_William_H@cat.com

Assistant Contract Administrator: Pamela J. Breen
Caterpillar Inc. - New Technology Division
(309) 578-9955, fax: (309) 578-2834, e-mail: Breen_Pamela_J@cat.com

Technology Development Manager: Lee Slezak
U.S. Dept. of Energy - Office of the FreedomCAR and Vehicle Technology Program
(202) 586-2335, fax: (202) 586-2476, e-mail: Lee.Slezak@hq.doe.gov

---

Contractor: National Energy Technology Laboratory
Contract No.: DE-FC26-04NT42258

Objectives

The goals of the Truck Essential Power Systems Efficiency Improvements for Medium Duty Trucks (TEPS) project are:

1. Develop a medium duty generator package and energy storage system for sales to a broad, medium-duty (Class 4-7) truck market.
2. Develop electrical alternatives to the use of the belts and gears in the medium truck engine compartment.
3. Develop a computer supervisory controller and algorithms to demonstrate fuel savings by taking advantage of electrification.
4. Demonstrate reduction of fuel consumption during idle conditions and evaluate the possibility of charging the energy storage system during vehicle braking.
5. Provide electricity for auxiliary equipment use in the field.

Approach

The team has finished the design of the components and systems based on the truck specifications cited in earlier reports. Briefly these attributes include:

- A Caterpillar® C7 engine
- A medium duty chassis equipped as follows:
  - Class 6 Gross Vehicle Weight Rating (GVWR)
  - Utility truck body

  - Automatic transmission

In the next period, the TEPS team will be focused on integrating the TEPS components into the chassis and testing the components once integrated.

Accomplishments

- Electrical architecture and energy storage specified
- Detailed model and simulations developed
- Supervisory control algorithms written
- ISG assembled and bench tested
- Electro-hydraulic power steering (EHPS) system assembled and bench tested
- Contract with Argonne National Lab for PSAT analysis ratified
- Chassis procured and instrumented
- Caterpillar® CX28 transmission installed
- Baseline on-road fuel economy testing completed

Future Work

- Baseline thermal performance testing
- Vehicle integration
- Prototype testing
- Final reports

Introduction

During budget period 2 (BP2), the team has brought closure to the design and specification work of Task 101 (Specifications, Concepts, and Designs) while simultaneously embarking on the bench testing and procurement work outlined by Task 102 (Bench Testing). The team completed the remaining concept and design items during the first two quarters of the year. Building on the "Best" concept developed during 2005, the chassis specifications for the truck platform were finalized early in the year and a Ford F-750 chassis was procured. The purchased chassis is a close match to the target specifications identified. Even though truck chassis procurement did not meet the initial target date, the majority of tasks have remained on schedule with only the baseline testing encountering delays from the belated truck chassis delivery. While awaiting the chassis, the team requested and received quotes from aerial device suppliers ("body builders"). The aerial device is now on order for integration onto the test vehicle during 2007.

Previous contractual challenges with Argonne National Laboratory have been resolved and PSAT analysis is in process. Likewise, the team at Caterpillar has continued to refine their existing plant models and recently received baseline testing data to aid in incorporating additional fidelity into the model. The minor delays in truck delivery and PSAT modeling have not encumbered progress on component development and testing. The team has worked to transform the concepts of Task 101 into reality during BP2. As necessary, components and hardware have been purchased throughout the period. Many of these items are currently on-hand at Caterpillar and have successfully completed bench testing. A few components remain in the hands of key sub-contractors, undergoing final refinement and tuning. All components are expected to be available as necessary for the transition to Task 103 (Vehicle Integration and Testing). Component integration will begin shortly after the completion of baseline testing and the return of the truck chassis to Caterpillar. As noted in prior reports, the substantial changes to the vehicle architecture suggest that implementation of the TEPS components will last several months. System tuning follows the component installation, as overall vehicle operation is refined prior to the second round of vehicle testing. The second round of testing will mimic the baseline testing to quantify the improvements yielded by the integration of the TEPS components. As such, both on-road and dynamometer testing will be employed to enable system optimization and demonstrate the fuel economy gains of the enhanced chassis. The project remains on schedule to meet all original deliverables by December 2007.

Design and Development

ISG Design – The heart of the electrification effort is the integrated starter/generator (ISG), a switched reluctance machine packaged in the flywheel housing of a Caterpillar® C7 engine. The ISG starts the engine, serves as the lone electrical generator, and provides motive power to the driveline. This machine operates at approximately 90% efficiency across the operating range of the engine. Compared to conventional alternators, which operate at 45-55% percent efficiency,[1] the ISG represents a substantial improvement in power generation efficiency. The ISG is rated for 20 kW of generating power above 1300 RPM. Conversely, the machine is capable of delivering 12 kW of motoring power across most engine operating speeds.

The design of the ISG is based on an earlier, larger machine design that has been proven in extensive vehicle testing.[1] Like the previous design, the TEPS ISG operates around a nominal bus voltage of 340 VDC when charging. The stator is liquid cooled and can be suitably cooled with jacket water from the engine up to temperatures of 100°C. Nevertheless, this new design represents a refinement of the earlier design – incorporating lessons learned from earlier projects. In particular, the cables now exit from the transmission end of the ISG – facilitating assembly on an engine. Furthermore, no rotor-position sensors are required as sensor-less position detection algorithms are used in the control system. The machine characteristics have also been designed to deliver not only engine starting power, but also a useful power curve for providing some additional propulsive power.

ISG Machine – The ISG machine components have been manufactured and winding and assembly of the machines is complete, as shown in Figure 1. Design and fabrication of the test bench components necessary to allow dynamometer testing of the rotor/stator assemblies is complete. With the test bench ready, the first casting of the flywheel housing underwent a successful test fitting to a C7 engine and was sent to Switched Reluctance Drives (SRDL) for testing.

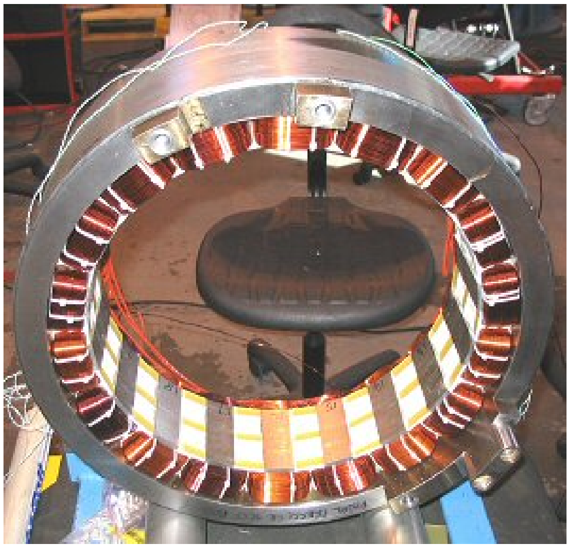

Figure 1. Wound stator assembly for ISG

ISG Power Converter – Among the enhancements to the TEPS unit in comparison to the prior unit are improvements to both the controller board and power conversion hardware. Both units have benefited from several years of technological advancements. This iteration represents a near 40% reduction in size compared to the controller produced previously.

The power converter hardware was assembled (as shown in Figure 2) and tested against an existing machine while the TEPS machine was being fabricated. As such, the converter hardware and software were successfully demonstrated before the TEPS machine was complete. Once the TEPS machine fabrication was complete, final bench testing and tuning began. General functionality and sensor-less algorithms will be tuned prior to the unit being shipped to Caterpillar.

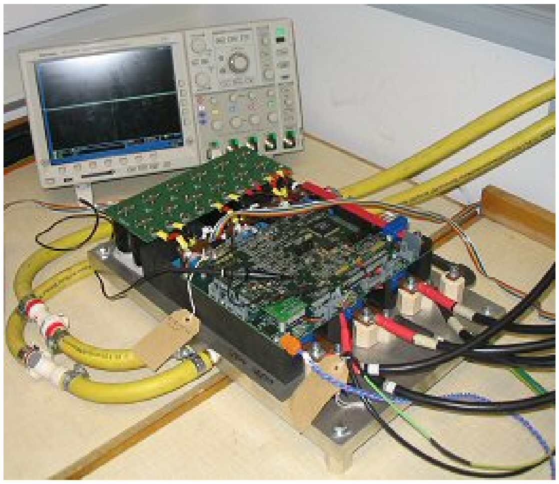

Figure 2. Power converter on test bench

Electrified Power Steering – A typical parasitic load on the engine is the power steering pump. While power-assisted steering can be essential for low speed maneuvering, the additional boosting is not generally required once the vehicle is underway. Low vehicle and engine speed conditions, such as static steering, generally dictate the size of power steering pumps. Consequently, in conventional systems, these pumps often prove to be substantially oversized at elevated engine and vehicle speeds. Cruising conditions, for instance, produce increased flow that cannot be utilized and is wasted as a result.^{2}

The TEPS project seeks to demonstrate the benefits of an electro-hydraulic power steering architecture by utilizing an electrically driven (high voltage) power steering pump. This pump operates on the same nominal 340 VDC that the ISG outputs, yielding an efficient unit that can be run "on-demand." The pump uses a brushless motor and pump combination that represents an integrated, managed solution. Communications to the pump are achieved via the CAN bus employed throughout the vehicle. Assembly of the first power steering unit was completed at the beginning of the year. Throughout the year, the unit underwent bench testing (test bench shown in Figure 3) and further development at the Dana Corporation's facility, focusing on optimizing the power output of the unit.

TEPS Baseline Testing – A Caterpillar® CX28 transmission was installed on the TEPS test truck platform (shown in Figure 4) prior to the baseline fuel economy testing. The CX28 replaced the transmission that was originally installed on the truck from the factory. A truck similar to the specifications of the TEPS test truck platform was acquired later in the year to serve as a control vehicle for testing. The control truck will be used to compare fuel economy at each stage of the test truck's lifecycle.

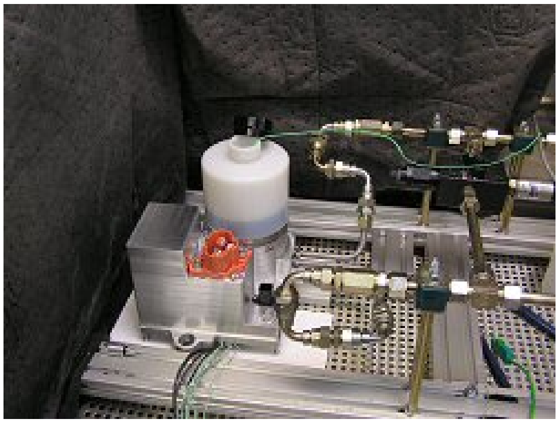

Figure 3. Assembled power steering test bench

Figure 4. TEPS test truck platform at TRC

Both trucks were sent to the Transportation Research Center (TRC) in Ohio for fuel economy and thermal testing. Road testing, per SAE Recommended Practice J1321, was performed to establish baseline fuel consumption on a representative medium-duty truck cycle. Both trucks were ballasted with a gross weight of 19,200 lbs and tested on the 7.5-mile test track. The fuel tanks were weighed and changed before and after every half-cycle (a cycle is 6 laps of the track plus 60 minutes of idling time). The trucks averaged a speed of 13.5 mph with wide-open throttle acceleration. Coastdown and chassis dyno testing will be completed during the fourth quarter of 2006.

Cooling Module - The cooling module as defined for this application includes the pumps, fans, and heat exchangers employed by both the powertrain and electrical systems for vehicle operation. The cooling module represents an ideal location to utilize the availability of electricity for driving accessories. Conventionally, cooling module components are primarily driven mechanically from the engine. These mechanical connections are prime candidates for independent, on-demand operation rather than operating points dictated by engine speed. Independent operation improves the efficiency of the entire system and removes unnecessary parasitic loads from the engine. In addition to the reduction in parasitic loads, electric configurations offer opportunities for simplified packaging as well as improvements in heat management and emissions.

The TEPS truck will comprise two coolant circuits, one high temperature and one low temperature loop. The major components of the high temperature loop are the engine, transmission, and ISG stator. The heat load of this circuit is approximately 150kW. The low temperature loop, on the other hand, cools the power electronics for all of the devices as well as the energy storage system. The heat load of this circuit is approximately 10kW.

The TEPS cooling module components operate directly from the 340 VDC produced by the ISG, yielding the best system efficiency from the ISG. An electric water pump will be installed for pumping duties. Road test results from a previous project suggest that the electric coolant pump, for instance, may reduce coolant pumping power consumption by 40% or more.[1] An array of electric fans will also replace the traditional, single engine-driven fan. Finally, an electronically controlled thermostat valve replaces the conventional wax-type thermostat. These components provide a system with fine levels of control and excellent efficiency.

Electrical Architecture – As procurement and bench testing tasks accelerated during the year, several components were ordered and received. Orders were placed for the power inverter and DC/DC converter. The DC/DC converter has already been received and bench tested while the power inverter is expected late in 2006. The laboratory testing includes performance and cooling analysis to enable optimization of both systems. Meanwhile, the supervisory controller has arrived and been tested against existing components in the laboratory. The ignition interface, high voltage protection, and electronic control unit (ECU) interface printed circuit boards were received. Bench testing of the printed circuit boards resulted in updated designs for each. Hardware for the latest electric air conditioning system has arrived, passed testing, and awaits installation on the chassis.

Simulation Results – The project team has exercised extensive analysis in the concepts and component designs for the truck. As previously mentioned, much of the simulation work focused on the selection of the appropriate energy storage system. After the energy storage system was selected, the focus shifted to refinement of the supervisory control algorithms and analysis of driving cycles.

Bearing in mind that the components developed during the TEPS effort are designed to be readily applicable to a wide variety of medium duty applications (Class 4 to Class 7), analysis for a variety of vocations has been considered. Two such examples are illustrated.

A general pick up and delivery cycle was selected to represent a variety of medium duty applications. The cycle features a top speed of approximately 49 MPH, an average speed of about 19 MPH, as well as some brief idling periods.

Figure 5 highlights the results of the pick up and delivery simulations. The divergent lines for fuel consumption portray the improvements offered by the TEPS components. The simulations suggest fuel consumption reductions of approximately 10% on this cycle.

After careful analysis of several medium duty applications, the TEPS team decided to build this demonstration platform as a utility truck. The utility truck represents an ideal platform for showcasing the advanced technologies of the TEPS project. Utility trucks operate under cycles that may involve extended idling periods as well as a need for field

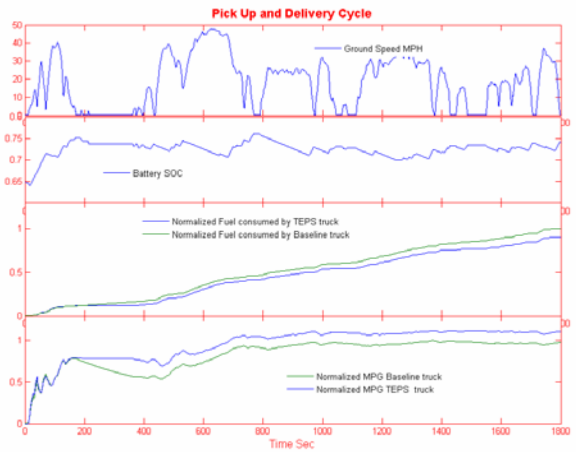

Figure 5. Pick up and delivery cycle results

power. These operational requirements offer exceptional opportunities to demonstrate the features of the TEPS components.

In the absence of a “standard” utility truck operating cycle, a cycle was constructed to simulate utility truck activities. The cycle consists of road driving speeds up to approximately 38 MPH, stops at traffic lights, and a job site idle period of about 90 minutes. Accessory loads simulating the use of a bucket and/or tool are included in the plant model. Figure 6 shows that operation of these tools leads to a discharging of the batteries. When the minimum state of charge (SOC) is reached, the engine restarts to charge the batteries. In this simulation, idle recharging conditions occur twice, once near 2500 seconds into the route and again at approximately 6000 seconds. These two instances can easily be seen as the jumps in engine speed and SOC during the job site idling. The simulation results for this profile yield fuel consumption reductions of approximately 40%, with savings during the idle periods topping 50%.

Conclusion

The TEPS project will demonstrate an integrated system of electric accessories and truck electrification to improve fuel economy. The heart of the system is the ISG, which starts the engine and generates all on-board electric power. The ISG machine presents a significant improvement in efficiency compared to a conventional alternator and offers an opportunity to provide additional power to the driveline. Progress on the ISG during the year has resulted in the fabrication of the machine and power electronics. Furthermore, bench testing is nearly complete at SRD’s facility. Upon completion of the bench testing, the machine will be ready for installation into the test chassis.

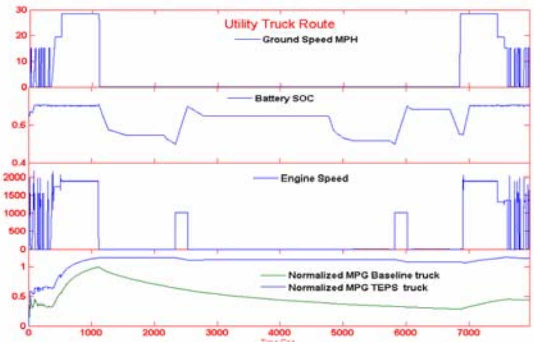

Figure 6. Utility truck cycle results

ISG power generation to the 340 VDC bus enables the use of high voltage, high-efficiency electric accessories. The accessories can operate in a more “on-demand” or variable fashion and offer more efficient operation in addition to packaging flexibility. Partner providers Engineered Machined Products, Inc. (EMP) and Dana Corp. are poised to deliver the electric accessories for the TEPS vehicle. The Caterpillar team has also procured and bench tested a wide array of components and systems to support the electrified architecture.

Extensive supervisory control algorithms harness the capability of the ISG, energy storage, and electric accessories. Simulation results were obtained by coupling a dynamic plant model with the control algorithms. These simulations suggest significant fuel consumption reductions are achievable for a variety of medium duty applications or driving cycles, particularly those with extended idle periods.

A chassis has been procured and baseline testing commenced during September 2006. On-road fuel economy testing is complete and provides the requisite standard for a quantitative analysis of the impact of the TEPS components. After the conclusion of baseline testing, implementation of the ISG, electric accessories, and other advanced components will begin and last into 2007. The TEPS truck, complete with all appropriate components, will be tested and evaluated during 2007 to yield detailed information about the fuel economy improvements afforded by truck electrification.

References

1. Algrain, M.C., W.H. Lane, D.C. Orr, "A case study in the electrification of Class-8 trucks," Electric Machines and Drives Conference, 2003. IEMDC'03. IEEE International, Volume 2, 1-4 June 2003 Page(s): 647 - 655 vol.2

2. Warinner, D.K., E.L. Sailor, W.A. Szabela, K.A. Sherwin, "Hybrid Electric Vehicle Steering System," 2005-01-3533, SAE International, Warrendale, PA, 2005.

VII.B. Advanced Electric Systems and Aerodynamics for Efficiency Improvements in Heavy-Duty Trucks

Principle Investigator: Kris W. Johnson
Caterpillar Inc. – Technology & Solutions Division
(309) 578-4890, fax: (309) 578-6285, e-mail: johnson_kris_w@cat.com

Caterpillar Program Manager: William H. Lane
Caterpillar Inc. – Technology & Solutions Division
(309) 578-8643, fax: (309) 578-2984, e-mail: lane_william_h@cat.com

Project Manager: Ralph D. Nine
National Energy Technology Laboratory
(304) 285-2017, fax: (304) 285-4469, e-mail: ralph.nine@netl.doe.gov

Technology Program Manager: Lee A. Slezak
U.S. Dept. of Energy - Office of the FreedomCAR and Vehicle Technology Program
(202) 586-2335, fax: (202) 586-2476, e-mail: lee.slezak@hq.doe.gov

---

Contractor: Caterpillar Inc.
Contract No.: DE-FC26-04NT42189

Purpose

Improve fuel efficiency of heavy-duty trucks through improvements in cooling system performance, air system management, and advanced power management. Prototype components will be developed and integrated for fuel economy, thermal, and functional performance testing on the Kenworth T-2000 More Electric Truck (MET) platform.

Objectives

- Analyze, design, build, and test a cooling system that provides a minimum of 10% greater heat rejection in the same frontal area with no increase in parasitic fan load.
- Develop an intelligent vehicle air management system, whereby the vehicle air system compressor is decoupled from the engine and is incorporated into an air system supply module.
- Realize fuel savings with advanced power management and acceleration assist, utilizing the Integrated Starter Generator (ISG) and energy storage devices.
- Quantify the effect of aerodynamic drag due to the frontal shape mandated by the area required for the cooling system.

Major Accomplishments - 2006

- ISG stop/start assist algorithms were completed.
- Fabrication and assembly of a modular engine cooling system for the truck platform were completed. The system consists of a main radiator core, electric cooling fan, engine oil auxiliary radiator, and high temperature charge air cooler.
- Prototype high efficiency cooling fan blades and shroud were designed, fabricated, and performance tested in a lab setting.

- Truck underhood computational fluid dynamics (CFD) cooling analysis was completed.
- An energy storage system consisting of NiMH batteries, high voltage bus interconnect, liquid cooling loop, and CAN communication was procured. The design for integration of the system into the truck platform was completed and mounting brackets were fabricated.
- Break-in and baseline dynamometer performance testing for a 2007 C15 engine was performed.
- A 2007 emissions-compliant engine coupled with an integrated motor generator (IMG) and diesel particulate filter (DPF) was installed in the MET platform.

Introduction

This program effort, currently in year two of a three-year project, focuses on areas that will primarily benefit fuel economy and improve heat rejection while driving over the road. This year's effort consisted primarily of bench testing individual components for efficiency and operation, developing designs to integrate the components into the truck platform, and fabricating necessary mounting hardware. Integration of the components on the vehicle platform and performance testing with regard to fuel economy and heat rejection of the system as a whole will be performed in the third and final year of the project.

Emission control measures for heavy-duty engines have resulted in increased engine heat loads, thus requiring added parasitic engine cooling loads. Truck electrification, in the form of thermal management, offers technology solutions to mitigate or even neutralize the effects of this trend. Thermal control offers opportunities to avoid increases in cooling system frontal area and forestall reduced fuel economy brought about by additional aerodynamic vehicle drag.

Advanced power management, in the form of continuously optimized and controlled power flow between electric components, offers additional fuel economy benefits to the heavy-duty trucking industry. Control software for power management offers additional value to the power distribution and energy storage architecture on board a truck with electric accessories and integrated starter generator.

The research team has built upon a previous truck electrification project, formally, "*Parasitic Energy Loss Reduction and Enabling Technologies for Class 7/8 Trucks,*" *DE-FC04-2000AL6701,* where the fundamental concept of electrically-driven accessories replacing belt/gear-driven accessories was demonstrated on a Kenworth T2000 truck chassis. The electrical accessories, shown in Figure 1, are controlled to provide "flow on demand" variable-speed operation and reduced parasitic engine loads for increased fuel economy. These accessories also provided solutions for main engine idle reduction in long haul trucks. The advanced components and systems of the current project are being integrated into the same Kenworth T2000 truck platform.

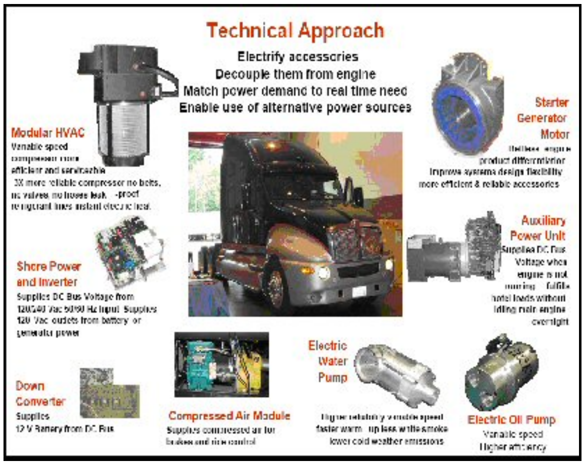

Figure 1. More Electric Truck

Reducing parasitic engine loading by decoupling accessory loads from the engine and driving them electrically is a central concept of this project. Belt or gear-driven engine accessories, such as oil pump, water pump, air conditioning compressor, or air compressor, are necessarily tied to whatever engine rpm the operator demands at any given time from the engine for operating and load conditions. The accessory pumps may need to be sized to provide adequate flow or pressure at low idle or peak torque speeds, resulting in excess flow or pressure at cruising or rated speeds, so that the flow is diverted through a pressure relief valve or other device to minimize peak pressure. This bypassing through a relief valve results in excess, or wasted, energy to drive the pump, and inefficient operation of the accessory, resulting in increased parasitic load to the engine, leading to loss of usable output power and decreased fuel economy.

Using variable-speed electric motors to drive accessory pumps and controlling the speed to provide only the required flow or pressure of a particular accessory system can provide significant increases in fuel economy to a commercial vehicle. Motor loads at relatively high power levels (1 – 5 kW, or higher) can be efficiently provided current from high-efficiency generators or batteries with system voltages in the range of 250 to 360 volts DC.

In the previous project, the electric accessories could be powered from one of three sources: an AC voltage source (“shore power”), an on board diesel generator (auxiliary power unit), or an integrated starter generator (ISG) located in the flywheel housing and driven by the main engine. The electric accessories and power sources, including the ISG, have remained in place for the current upgrade of the research platform vehicle.

The transition to broad commercial applications of these technologies in the trucking industry will lead to significant gains in performance, reliability, serviceability, and system design flexibility. The Class 8 truck sector will benefit the most due to their higher average speed, the large number of vehicles produced yearly, and the high number of miles per year accumulated by each vehicle. Better fuel economy can accompany emissions reduction and will encourage customers to purchase the vehicles as an improved capital investment. These technology enhancements are also directly beneficial to mobile construction equipment, a variety of commercial and marine engine markets, and powertrains used by a wide variety of U.S. military mobile equipment as well.

Analysis and Design

In alignment with the project goal of controlled thermal management for cooling system performance improvements, the electric cooling fan, radiator coolant bypass control valve, and oil cooler were identified as having the potential to increase cooling system heat rejection and improve fuel economy. Simulation analysis showed the AES cooling system with thermal management is capable of 300 kW heat rejection under worst case ambient condition of 43°C for both peak torque and rated speed conditions.

Electric Cooling Fan

Typical engine cooling fans on heavy-duty trucks range in size from about 28 inches to 32 inches in diameter and can consume up to 55 kW under conditions of full engine speed and low vehicle speed, especially as engine-to-fan belt pulley speed ratios have increased to about 1.4:1. The fan is belt driven through an on-off clutch on the front of the engine. For a long haul truck, average fan on-time as a percentage of truck operation is about 6 percent with half of that time attributable to air conditioning demands. The cooling fan is typically sized to deliver adequate cooling air flow at a peak torque engine speed of 1200 rpm resulting in excess air delivery at higher engine speeds with a cubic exponential increase in parasitic power draw from the engine. Electrification of the fan allows fan speed to be matched proportionately to cooling system load.

For the electric cooling fan, the space constraints for installation in the current platform were a determining factor in the decision to use puller-type fans, as hood profile and mounting considerations of truck frame rail ends would require a difficult redesign of major structural components. Future designs using electric pusher fans, having the electric motor in front of the heat exchangers, have potential to benefit from increased fan efficiency due to the fan blades blowing colder, denser air. Air-cooling of the fan motor may also be more feasible with a pusher design, as the motor would be located in cooler air upstream from the heat exchangers.

For the current puller design, fan motor power was specified to 20 kW continuous at 2000 rpm. Due to thermal issues of the fan motor residing downstream of the heat exchangers and being subjected to air temperatures as high as 80°C and coolant fluid temperatures of 100°C, fan design dimensions from engine installation space claim constraints limited fan motor continuous power to about 20 kW. This matches the 20 kW mechanical fan power at 1800-rpm engine speed and 30 mph ram air for a conventional belt-driven fan. With a higher efficiency fan and shroud, the same fan power will give more airflow and higher heat rejection. Figure 2 shows the mechanical power required to drive the conventional fan of the research platform. The fan is 31.25 inches in diameter and is driven at a 1:1 fan-to-engine speed ratio. The fan has a 1-inch tip-to-shroud clearance and utilizes a knife-edge shroud. The plotted data from 600 to 1400 rpm was acquired using fuel data during fan on and off states and calculating the power delta between states from brake-specific fuel consumption values for a Caterpillar® C-15 engine. The plotted data from 1500 to 2300 rpm was derived from fan curves. The solid red line in the plot shows a third-order polynomial fit typical of a cubic exponential power draw of an axial fan.

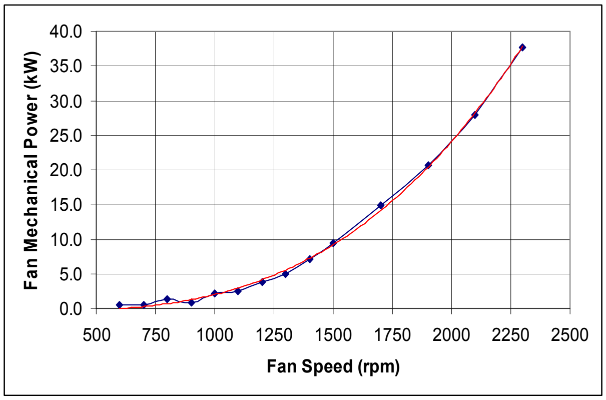

Figure 2. Conventional mechanical fan power

Switched Reluctance Drives Ltd, a subsidiary of Emerson Electric Co., designed, developed, and tested the prototype motor for the electric fan shown in Figure 3. The motor design is switched reluctance technology with an 18/12-stator/rotor pole structure and peak continuous power rating of 20 kW at 2000 rpm. Motor operation allows the reversal of the fan, perhaps unneeded in an on-highway application but potentially useful in an off-highway machine, to facilitate cleanout of debris from the heat exchangers. Motor physical size is approximately 300 mm in diameter by 200 mm in axial length. Electric current commutation is provided by position sensors mounted to the motor front, interfacing with slotted tabs on the fan hub. Fan motor / drive efficiency of over 90 percent was demonstrated in dyno testing over most of its operating speed and power range.

Figure 3. 20kW cooling fan motor

Primary cooling of the motor stator windings is accomplished with engine coolant, while secondary rotor / stator cooling is provided by aft-to-fore air-cooling stream through openings in the motor endplates. Radial vanes on the fan hub provide a negative pressure zone at the motor front, enabling cooling airflow through the rotor.

The fan hub, Figure 4, was designed to wrap around the motor and provide mounting for the base of nine individually-molded blades. This wraparound design allows the fan blade leading edge to be located 100 mm from the radiator core, improving efficiency of the airfoil shaped blades and permitting space for the inlet radius of a type II shroud. Centrally locating the fan relative to the radiator core and tight tip to shroud clearance have allowed a fan diameter design of 864mm.

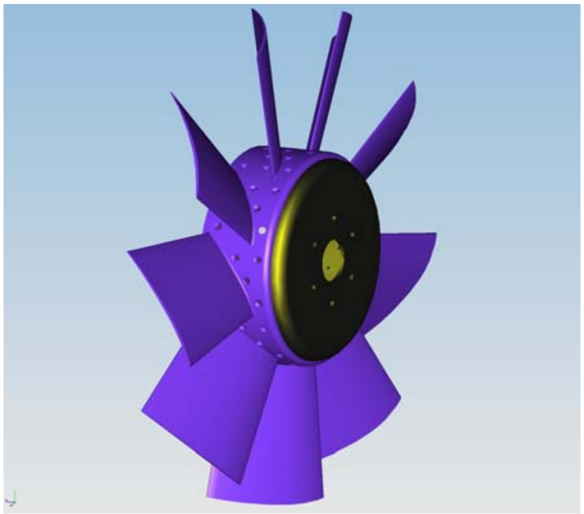

Figure 4. Fan hub and blade design

The electric cooling fan and motor were designed to integrate with the cooling module through cross frame tubing supports mounted to each corner of the radiator frame. Mounting to the radiator frame allows close tip-to-shroud tolerance (8mm) since engine movement on flexible mounts does not have to be accounted for. Mounting the cooling fan and motor to the radiator frame also allows for a completely modular cooling package for easy assembly and service.

System controller / fan motor drive communications is J1939 spec CAN over a proprietary data link. Supervisory control algorithms for speed control of the cooling fan motor were developed to provide the temperature differential across both radiator and engine to within an 8°C range. The fan only operates when the bypass valve is fully diverting all coolant to the radiator. This ensures the diverter valve primarily controls coolant temperature, as this is the control actuation with the least energy cost. The fan then operates in variable speed mode to control the temperature differential across the radiator.

CFD analysis for underhood cooling airflow was performed for both the OEM-configured conventional cooling components and the new AES components. Results of the underhood computational fluid dynamics (CFD) cooling analysis using AES components showed an overall 14-33% efficiency gain (fan power (kW) per fan flow (kg/s)) with the AES fan and shroud design. The range stems from analysis at different design points with variable fan and vehicle speeds. Most significant is the 33% efficiency gain at the worst case cooling point of full fan speed (2000 rpm) and low ram air speed (30 mph) where the fan delivers 10.3 kg/s airflow with a mechanical input power of 28.9 kW (power to flow ratio 2.81). This compares to analysis of the vehicle baseline fan (belt driven) delivering 12.0 kg/s at 2520 rpm with an input power of 50.0 kW (power to flow ratio 4.17).

Lab airflow tests were conducted with the newly fabricated fan blades, hub, and type II venturi shroud. The results show a 7% increase in airflow at the design point and an 8% increase in efficiency with the new design vs. the OEM fan.

Operation of the fan mounted to the radiator frame was validated to 1500 rpm and 15 kW. System control and control communications with the fan drive were verified. The fan was tested for excessive vibrations at natural frequencies that could cause damage to the fan or frame. The design and mounting were found to be robust and ready for integration to the vehicle with no excessive vibrations throughout the operational speed range.

Radiator Coolant Bypass Control Valve

An electrically-actuated valve was provided by Engineered Machined Products, Inc. to control the coolant flow between the radiator and radiator bypass loop of the coolant circuit. Replacement of a conventional wax-type thermostat allows for variable set point temperatures of engine coolant. During periods of light to moderate engine load, the reference temperature can be increased, thus allowing less heat absorption by the coolant from the engine and permitting higher exhaust temperatures for better passive regeneration of diesel particulate filter. The increased exhaust energy can also be used to power more boost from the turbocharger. Higher coolant temperature can also result in elevated cylinder wall temperature, increasing combustion efficiency. As engine load increases, the temperature set point can be decreased to provide adequate cooling of exhaust ports and other areas of high heat flux.

Figure 5 shows the valve installation in the research platform integrated with the C-15 engine. The control valve consists of a linearly-actuated flow diverter contained in a cylindrical nylon and aluminum housing driven by a stepper motor. A small drive electronics box with CAN communication and drivers for the valve motor / actuator runs from 12 V power. The 2.4-inch valve with 1-inch bypass will deliver 100 gpm with 1-psi pressure drop, 300 gpm with 5-psi pressure drop, and goes from closed to full open in 16 seconds. The valve is electrically powered from the vehicle 12 V system. Communication between the supervisory system controller and the valve electronics is established with over a controller area network (CAN) using SAE J1939 specifications and proprietary network IDs.

Figure 5. Radiator coolant bypass valve installation

Auxiliary Oil Cooler

The elevated engine coolant temperature made possible by the radiator coolant bypass control valve necessarily results in increased radiator outlet temperature, or bottom tank temperature, since a temperature differential of 8°C or less must be maintained across the engine. Since it is the coolant from the radiator outlet that is used to absorb heat in the oil cooler (oil to coolant heat exchanger), an increase in the bottom tank temperature may result in an inadequate temperature gradient across the oil cooler to effectively cool the engine oil. Figure 6 shows a design concept for an additional coolant loop (light blue) and heat exchanger to provide auxiliary cooling of the coolant entering the oil cooler. The liquid-to-air heat exchanger is integrated into the vehicle cooling module with the radiator and charge air cooler.

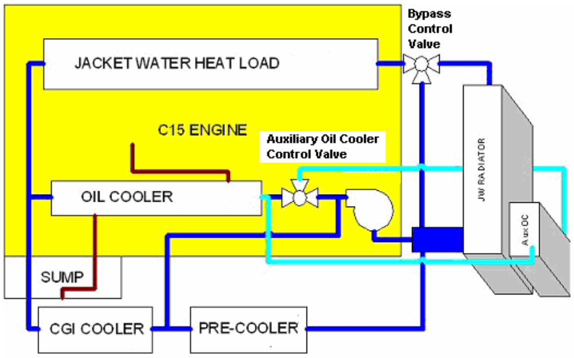

Figure 6. Oil cooling system

The auxiliary oil cooler control valve shown in the schematic of Figure 6 provides control over the temperature of the coolant entering the oil cooler. Using the proportional flow control valve, the engine oil temperature, and ultimately the temperature dependent viscosity of the oil, can effectively be controlled. In this way, during times of light to moderate engine loading and especially at low ambient temperatures, the oil temperature can be increased to reduce oil viscosity and parasitic friction. For periods of high engine loading, the oil temperature can be decreased to provide adequate oil pressure for journal bearing flotation and critical cooling of engine components by the engine oil.

The increased heat rejection per unit of frontal area made possible by the AES components of the cooling system described in the preceding pages may allow truck OEMs the vehicle design option of reducing the frontal area of the engine hood. Aerodynamic analysis using computational fluid dynamics (CFD) will be performed to determine the fuel efficiency opportunity for a heavy-duty vehicle. Overall vehicle drag coefficients will be determined using parametric width and height deviations of hood frontal area from baseline geometry made possible from proposed cooling system changes.

Advanced Power Management

Advance power management of electrified accessories and exploration of hybrid operation with electric energy storage and integrated motor generator (IMG) is being explored for potential in class 7 and 8 short and long haul trucks. Vehicle acceleration and deceleration assist with IMG and regenerative storage of braking energy has potential to increase fuel economy significantly depending on the drive cycle the vehicle undergoes. Power management during vehicle operation on hilly terrain, where energy is captured and stored during downhill runs and then utilized to power electric accessories on the uphill run, also has potential for fuel savings dependent on the slope and length of the terrain.

Sensorless control algorithms for the ISG were developed by Emerson’s Switched Reluctance Drives (SRD) Division for motoring operation over the 0 to 2400 rpm range. Peak torque of 1200 Nm was achieved from 0 to 160 rpm and constant power of 25-26 kW was achieved from 500 to 2400 rpm with 84 percent to 90 percent efficiency. The ISG motoring functionality was developed to facilitate engine stop/start and acceleration assist modes of operation.

Motoring capability, which allows the integrated starter generator (ISG) to propel the truck under certain conditions, was added to the AES truck's ISG. An algorithm to simultaneously launch and start the engine during periods of frequent stop-and-go traffic was refined and demonstrated on the truck. This new functionality permits idle stop, or shutdown of the engine, saving fuel and reducing emissions. In addition to restarting the engine, the ISG also provides initial propulsion of the truck as soon as the driver pushes the accelerator pedal. The algorithm was then expanded to allow acceleration assist under other driving conditions when increased vehicle speed is desired. When tested with a fully loaded trailer on level ground, the ISG provided acceptable acceleration.

Based on the acceleration-assist code, cruise-assist capability was next added to the power-management algorithm. Cruise assist switches the ISG from generating to motoring to help maintain a constant travel speed during times of increased engine load, such as when going uphill. Previous simulation work indicated that fuel savings of 1-4% were possible with a cruise-assist control, depending on the spacing and steepness of the hills.

The plot in Figure 7 shows an engine off stop/start operation with the ISG. With the sizeable peak torque capability of the ISG, simultaneous engine starting and vehicle launch from a vehicle stop is possible, even with a fully loaded trailer and GVW of 80,000 lbs. Idle stop and launch assist for heavy-duty applications have the potential to provide increased and smooth vehicle acceleration and to reduce clutch wear. Engine load transients can be reduced during launch assist, providing possible reduction in emissions. Collateral benefits such as these may increase the customer value of an ISG, stepping up acceptance of the technology, while also providing critical fuel savings.

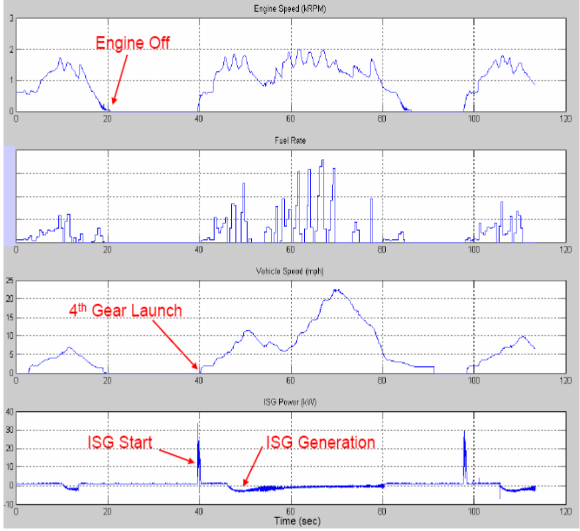

Figure 7. ISG plots showing engine stop/start assist

An energy storage system with Nickel-Metal-Hydride batteries was specified and procured for the MET platform. This system has a capacity of 4.8 kW-Hrs, of which approximately 1 kWHr will be utilized by a 20% depth of discharge limit to optimize life of the battery pack. The 1 kWHr is equal to 100 seconds of acceleration or deceleration.

Because the ISG and other MEI components draw power from the batteries while the ISG is motoring, an algorithm monitors the state of the charge of the batteries to ensure that the system is not overdrawn. If the voltage or state of charge of the battery system falls below the allowed limit, then the ISG is switched back to the generating mode.

Engine Upgrade

A 2007 emissions-compliant, pre-production Caterpillar® C15 engine has been procured and installed in the T2000 vehicle test platform. This C15 ACERT^{TM} engine, rated at 550 HP and 1850 ft-lb of torque, includes a diesel particulate filter (DPF) and a Caterpillar regeneration system (CRS). The decision to upgrade to the ACERT® C15 rated at 550 HP and 1850 ft-lb torque was made in order to demonstrate the electric accessory and power management technology on an engine with 2007 representative heat loads and heat load splits.

System Supervisory Control

Systems control is managed through a central electronic supervisory controller, utilizing digital and analog input / output, as well as serial CAN communication. All algorithms are developed in block diagram format and then auto-coded using rapid controls prototyping hardware and software.

Conclusion

During 2007, the team will continue exploration of hybrid operation with the ISG including refining control algorithms such as regenerative braking and cruise assist in on–road testing.

The team will complete integration of the electric cooling fan, stainless steel aftercooler, and energy storage system into the MET platform and perform baseline thermal performance testing on the newly installed 2007 engine. After refining and optimizing control algorithms for the above components, the team will perform on-road and lab performance testing and compare the results to the baseline.

This project effort, with analysis and design, followed by fabrication and integration, of electric truck accessory components into a prototype research platform vehicle is a critical step to understanding the potential fuel economy, thermal management, and functional benefits provided to an electrified Class 8 truck. Validation of the concepts presented and an understanding of the component and system costs of these advanced systems is crucial to then move on to the next step of technology commercialization, which is where the real benefits to fuel savings can be realized by truck customers. An essential element for truck electrification is an overall systems-oriented approach where each component is optimized for operation within the system as a whole.

VIII. ULTRALIGHT TRANSIT BUS SYSTEM

VIII.A. The Vehicle System Optimization of a Lightweight Stainless Steel Bus

Principal Investigator: J. Bruce Emmons
Autokinetics Inc
1711 West Hamlin Road
Rochester Hills, MI 48309-3368
(248) 852-4450, fax: (248) 852-7182, e-mail: jbemmons@autokinetics.com

Technology Development Managers: Sid Diamond and Lee Slezak
(202) 586-2335, fax: (202) 586-2476, e-mail: Lee.Slezak@hq.doe.gov

Field Technical Manager: Jules Routbort
(630) 252-5065, fax: (630) 252-4798, e-mail: routbort@anl.gov

---

Contractor: Argonne National Laboratory
Contract No.: 4F-02161

Objective

- The intent of this project is to perform the integration and optimization of a hybrid or battery/electric propulsion system, and various vehicle subsystems into a lightweight bus body.
- Autokinetics will use as much off the shelf technology as possible. Optimization of the propulsion and vehicle systems will primarily be through careful selection of appropriately sized components.
- This project will result in a single “Proof-of-Concept” prototype bus, suitable for testing and evaluation of performance under controlled conditions.
- A further objective of the project is to identify one or more paths to rapid commercialization of the technology.

Approach

- Conduct ADVISOR and GREET computer simulations of a number of different types of propulsion systems to predict performance and energy efficiency.
- After identifying the most promising propulsion system architecture, use computer simulations to evaluate and select the individual components with the best combination of performance and affordability.
- Design, integrate and install the propulsion system.
- Design or select optimized vehicle subsystems such as seats, glass, air conditioning, etc.
- Purchase or fabricate and install all vehicle subsystems.
- Evaluate the performance and make modifications, if necessary.
- Perform initial testing.

Accomplishments

- Fabricated and installed windows and glass
- Fabricated and installed emergency exits.

- Fabricated and installed driver's station.
- Purchased energy storage system.
- Installed energy storage system.
- Fabricated and installed soft start unit.
- Installed propulsion system.

Future Direction

- Design, fabricate and install vehicle subsystems.
- Test the propulsion system.
- Perform FMEA (failure modes and effects analysis).
- Perform limited testing and development of the complete vehicle.
- Continue commercialization efforts.

Introduction

The intent of this project is to perform the integration and optimization of a hybrid or battery/electric propulsion system and various vehicle subsystems into a lightweight bus body. Off the shelf technology will be used wherever possible. Optimization of the propulsion and vehicle systems will primarily be through careful selection of appropriately sized components.

This project will result in a single "Proof-of-Concept" prototype bus, suitable for testing and evaluation of performance under controlled conditions. The design will not necessarily be ready for mass production, nor will it include trim and appearance items.

The completed prototype will include the primary body structure, suspension, glazing, driver's station, electric wheel motors, inverters, and energy storage system. It will also include regenerative braking, limited lighting, bumpers, and full seating.

Fabricate and Install Windows and Glass

Laminated glass was chosen for all glazing positions because it provides a number of benefits over tempered glass. During this reporting period, Fox Fire Glass (Pontiac, Michigan) completed fabrication and delivered the prototype glass for all side windows and the two-part windshield.

The fixed position glass was installed by Troy Auto Glass Inc. (Troy, Michigan), a local automotive glass installer. The installation was accomplished using standard processes and materials. The first few pieces of glass and their installation were covered under a separate project to provide an opportunity for evaluation. The side and rear window glass installation is shown in Figure 1. The balance of the side glass and the two-piece windshield shown in Figure 2, were completed as a deliverable for this project.

It is interesting to note, a couple of windows were installed prematurely and had to be removed to allow access for other operations. The installer removed these windows using industry standard equipment and reinstalled them when appropriate.

Figure 1. Installation of side and rear windows

Figure 2. Windshield installation

This exercise provided the opportunity to evaluate the glass replacement procedure. It was found that replacement of the bonded side glass could be accomplished quickly and efficiently using only standard equipment, materials, and processes.

Fabricate and Install Emergency Exits

In addition to the two doors, five windows located throughout the bus are designated as emergency exits. One such window is shown in Figure 3. Since the vehicle structure incorporates bonded in place side glass, the five exit windows required a different attachment and sealing approach. These windows are of a frameless design and are attached to the structure through a standard "piano" type hinge bonded to the upper edge of the glass. The body side of the hinge is bolted rather than spot-welded to aid replacement. A standard profile bulb seal pressed onto the flanges around the perimeter of the window opening provides the sealing function as well as protection from the raw edges of the sheet metal.

A latch-bar, which carries the two side position latches, was then bonded to the inside of the glass panel. This joining procedure uses the same bonding material as the standard glass installation. The use of a latch-bar allows for subassembly of the latch system, greater dimensional control, and a wide distribution of the stress imposed by the latch. A detail of this arrangement is shown in Figure 4.

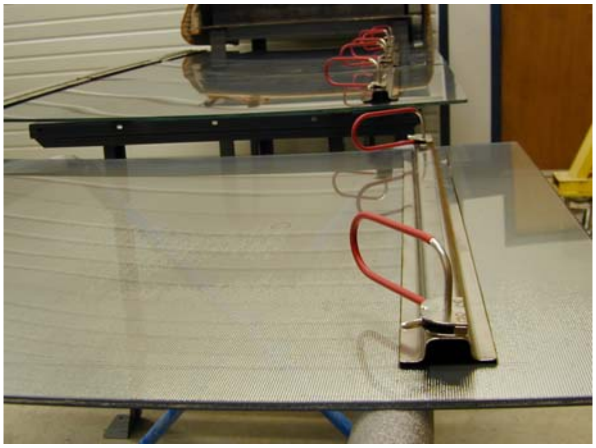

Figure 3. Emergency exit window latch detail

Figure 4. Installed emergency exit window

Fabricate and Install Driver's Station

A driver's station mock-up produced under separate project was used as a basis for evaluation and development of the driver's station design task of this project. During this reporting period, the ergonomic and packaging considerations were finalized and supporting structures for the steering column, instruments, and operator's seat were designed, constructed, and installed into the prototype. The completed driver station is shown in Figure 5.

Figure 5. Driver's station

Purchase Energy Storage System

As described in the FY2005 report, Autokinetics reviewed the currently available battery technologies, and selected Zebra batteries as best suited for a battery dominant, plug-in hybrid bus, or a pure battery electric bus. Nine batteries were purchased from the manufacturer, MES-DEA in Stabio, Switzerland. This order included all the necessary support equipment, including battery management interfaces, cooling fans, on-board chargers, and a multi-battery server.

Install energy storage system

A securement system for the batteries was designed and fabricated. The Zebra battery operates at a high (300°C) internal temperature. Heat loss is minimized by a layer of foam insulation inside of a stainless steel shell in which the air has been evacuated. Cooling is provided by internal air passages and an external fan. It is necessary to provide for a small amount of air circulation around the battery to prevent the heat flux from causing elevated temperatures. Also, because it is possible to lose the vacuum seal, which greatly increases the heat flux, the securement system must be made of heat resistant materials. The finished installation uses simple stainless steel sections, spot-welded together to form support frames and clamping frames. Strips of silicone foam rubber tape, applied to the inside surfaces of the frames, are used to cushion the batteries. Seven batteries were mounted on the roof as shown in Figure 6. An additional two batteries were mounted ahead of each rear wheel well, along with the power electronics, as shown in Figure 8**.**

Figure 6. Roof mounted energy storage system

Fabricate and Install Soft Start Unit

The UQM CD40-400L Inverter/Controller has a large array of capacitors on the high voltage input. These capacitors must be "softly" charged before the high current path from the energy storage unit is completed. Our soft start unit consists of two Tyco EV200AAANA contactors rated at 500+ amps and 900VDC. One contactor is in series with a 225 watt resistor and is closed first to charge the capacitors. The vehicle controller monitors the voltage and the second main contactor is closed when the capacitor voltage reaches at least 90% of the energy storage voltage. A 400 amp semiconductor main fuse protects the UQM Inverter/Controller.

There are two soft start units mounted on stainless steel plates and installed on the Zebra batteries located at each rear wheel well to keep the high current paths as short as possible. One of these units is shown in Figure 7.

Install Propulsion System

There was a significant amount of engineering required to solve the technical challenges involved in the installation of the propulsion system.

Figure 7. Motor soft start unit

The cables from the UQM inverter/controller to the motor were shielded with a tinned copper braid to minimize EMI/RFI. This includes the hall effect cable. The four shielded cables are grounded at both ends. A stainless steel strap with cable clamps on each end is mounted between the inner wheel well and the motor, with the cables, cooling hoses and an 8awg ground securely tied to it. This strap minimizes the radius of the bends and supports the cables and hoses during the full excursion of the suspension. The cables enter the wheel well through a 4 up sealed port. The cooling hoses continue inside through brass fittings mounted to the wheel well. The ground strap is bolted to a copper rivet mounted to the wheel well. The traction motor with its shielded cables is shown in Figure 8.

On the inside of the bus the key components of the propulsion system are mounted just forward of the two rear wheel wells. These components are strategically located here to minimize the high current paths to the wheel mounted motor. A passenger seat is located in this position so care was taken to make sure all the components fit in the space required. One each of a Zebra battery, a Zebra charger, Zebra harnesses, fuses, cooling fan, a UQM inverter/controller, and a soft start unit were securely mounted to the bus floor at each wheel well with a unique securement system. One of these assemblies is shown in Figure 9.

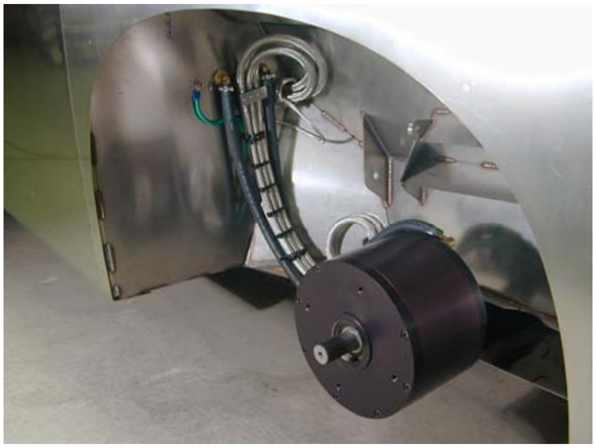

Figure 8. Traction motor and cables

Figure 9. Installed propulsion system

Conclusions

Several major high-risk milestones were successfully completed in FY2006. In particular, the physical integration of the propulsion system and batteries has greatly reduced the number of uncertainties in achieving the overall project goals. The remaining project tasks, scheduled to be completed by June 30, 2007, primarily involve lower risk subsystems such as seats, HVAC, doors, and ADA compliance. In light of this, Autokinetics continues to be confident that the improvement in fuel economy for this vehicle will be at least 300%, as predicted. It is anticipated that performance testing of the completed vehicle in the not too distant future will bear this out.

IX. PLASMA-BASED ION-MOBILITY NO$_X$ SENSOR

IX.A. Plasma-based Ion-mobility NO$_x$ Sensor

Principal Investigator: Shuh-Haw Sheen
Argonne National Laboratory
9700 S Cass Ave., Argonne, IL 60439
(630) 252-7502, fax: (630) 252-3250, e-mail: sheen@anl.gov

Technology Development Area Specialist: Lee Slezak
(202) 586-4819, fax: (202) 586-1600, e-mail: Lee.Slezak@ee.doe.gov

Field Technical Manager: Jules Routbort
630-252-5065, e-mail: routbort@anl.gov

Participants
Hual-Te Chien, Argonne National Laboratory
Eric B. Andrews Cummins, Inc. 1900 McKinley Ave. Columbus, IN 47201

Contractor: Argonne National Laboratory
Contract No.: 49C34

Objective

- Develop a low-cost, fast-response NO$_x$ sensor based on negative-ion mobility measurement for heavy-vehicle engine combustion control and in-stream emission monitoring.

Approach

- Establish a Cooperative Research and Development Agreement (CRADA) with Cummins, Inc.
- Develop a corona/spark discharge negative ion source.
- Evaluate temperature and moisture effects on negative ion formation.
- Develop a laboratory prototype of ion-mobility sensor.
- Evaluate the prototype sensor in a diesel engine exhaust line.
- Document sensor performance and draw a go/no-go decision.

Accomplishments

- Established a CRADA with Cummins, Inc.
- Evaluated spark-discharge ion-source geometries.
- Conducted tests to assess flow, temperature and moisture effects.

Future Direction

- Conduct sensor tests at a diesel-engine combustion facility.
- Analyze sensor performance data and deliver a technical report.

Introduction

This project is a Cooperative Research and Development Agreement (CRADA) between Argonne National Laboratory (ANL) and Cummins Inc. The goal of this project is to develop and test a low-cost and fast-response NO_x sensor based on an ion-mobility spectrometry (IMS) technique for engine combustion control, in-stream monitoring of the after-treatment catalysts and on-board diagnostics. The ANL-IMS sensor uses a spark-discharge ionization source operating under the ambient conditions. Electrons emitted from the discharge source can either ionize gases of low electron affinity to produce positive ions (such as NO) or be captured by gases of high electron affinity to form negative ions (such as NO_2). Preliminary results [1] show that the predominant negative ions produced in NO_x/dry-N_2 under spark discharge are negative NO_2 ions and the peak amplitude is proportional to NO_2 concentration. The same IMS can be used to detect NO concentration if operating under positive ion mode.

Sensor Requirements and Proposed Development

An inline NOx sensor requires a sensitivity better than 5% and response time less than 200 ms, can detect both NO and NO_2, and can function under wide ranges of temperature (38°C to 760°C) and flow rate (0 to 4 m/sec). The proposed work therefore covers IMS sensor design and optimization, packaging of control electronics, and critical performance tests. However, prior to the engineering development, some technical issues that determine the go/no-go decision must be evaluated. The major issues are (a) oxygen and water interference (b) stability over the operating temperatures and flow rates, and (c) cross sensitivity and (d) capability of detecting both NO and NO_2.

Because the complexity of the ion chemistry generated by spark discharge in air, the go/no-go decision of this project depends on positive identification of negative NO_2 ions produced by spark discharge in the air/ NO_2 mixture with high moisture content.

Results and Discussion

A laboratory IMS prototype [1] was used for the sensor tests conducted in FY 2006. The tests focused on sensor performance under variations of gas flow, temperature and moisture content. The gas flow tests involve variations of flow rate and flow direction. Two flow directions, cross and parallel to the spark direction, were examined. Results, given in Figure 1, show that the peak amplitude decreases exponentially as flow rate increases but flow affects less for the parallel flow geometry. Effects of gas temperature on IMS were examined by locally heating up the gas-water mixture before entering the IMS. No significant variation in ion peaks was detected over the tested range from room temperature to 100°C.

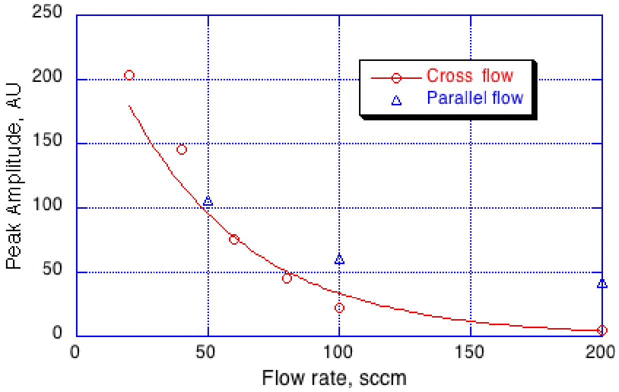

Figure 1. Peak amplitudes of negative ions versus flow rate for two flow directions

Moisture interferes the IMS performance primarily in altering the ion chemistry. Negative ions such as O_2^-, $OH^-(H_2O)_n$, and $O_2^-(H_2O)_n$ have been identified [2] under corona discharge. Inevitably, the formation of NO_2^- must compete with the water chemistry. We observed that the NO_2^- peak was gradually replaced by a broader peak at a higher drift time when moisture was introduced in the gas stream. And as moisture accumulated inside the IMS the negative ion peak diminished completely. To retrieve the ion peak, we turned off the ion-extracting electronics and thus trapping ions in the ion source for a few seconds. Figure 2 shows the retrieved ion peaks for different gas compositions.

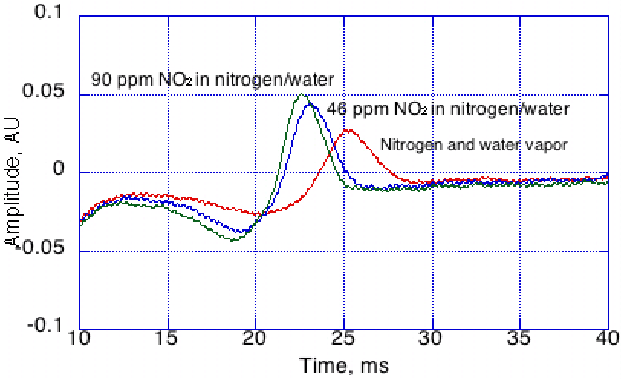

Figure 2. Negative ion peaks of NO_2/N_2/water mixtures

Conclusions and Future Plan

We have conducted sensor performance tests to examine the effects on the sensor sensitivity and stability due to variations of gas flow, temperature, and moisture content. Both drift time and amplitude of the ion peak are sensitive to flow rate and flow direction, smaller flow rates producing more ions that reach the detector. Variation of gas temperature up to 100°C has little effect on ion peak. However, the data is not sufficient to project the effect at exhaust-line temperature (>700°C). Because the present IMS is designed for operation under ambient- or high-pressure environment, the ion spectrum lacks of peak resolution; only one peak is resolved. Therefore the presence of moisture or oxygen in the gas stream causes measurement uncertainty and reduces the detection sensitivity.

To reach the go/no-go decision, we will re-evaluate the sensor design and conduct tests in a realistic environment. Specific tasks planned are:

(1) Ion source development with emphases on flow management and pressure reduction in the drift tube.
(2) Realistic diesel-engine exhaust-line tests using both IMS and a commercial NO_x sensor provided by Cummins, Inc.

References

1. S. H. Sheen, H. T. Chien, and A. C. Raptis, “Advanced sensors for real-time control of advanced natural-gas reciprocating engine combustion,” Argonne National Laboratory Publicationn ANL-03/26, October, 2003.

2. T. W. Carr, “Negative ions in plasma chromatography-mass spectrometry,” Anal. Chem. Vol. 49, NO.6, pp.828-831, 1977.

Printed on
recycled
paper

For more information contact:
EERE Information Center
1-877-EERE-INF (1-877-337-3463)
www.eere.energy.gov